Geographia Technica

Technical Geography
an International Journal for the Progress of Scientific Geography

Volume 21, Geographia Technica No. 3/2026

www.technicalgeography.org

Cluj University Press

Geographia Technica

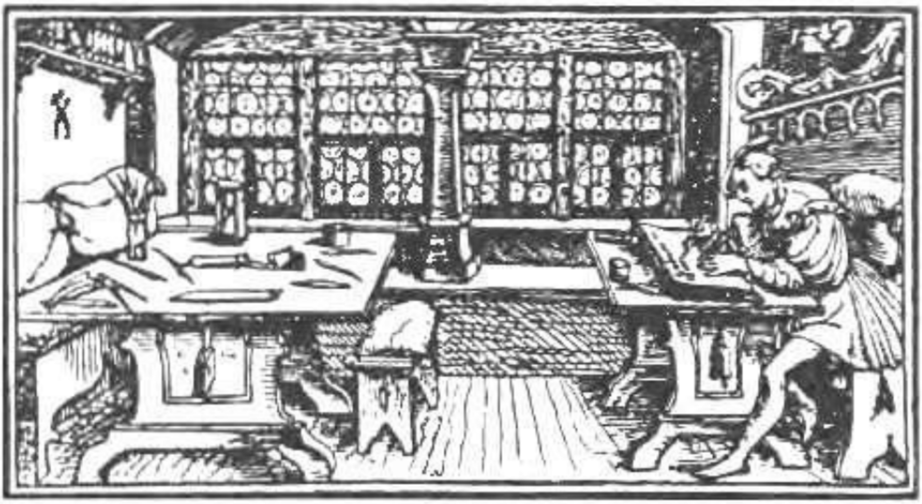

Technical Geography

an International Journal for the Progress of Scientific Geography

2026 – No. 3

Cluj University Press

ISSN: 1842 - 5135 (Printed version)
ISSN: 2065 - 4421 (Online version)

Universitatea Babeş-Bolyai
Presa Universitară Clujeană
Director: Codruța Săcelean
Str. B.P. Hasdeu nr. 51
400371 Cluj-Napoca, România
Tel./fax: (+40)-264-597.401
E-mail: editura@ubbcluj.ro
http://www.editura.ubbcluj.ro/

Asociatia Geographia Technica
2, Prunilor Street
400334 Cluj-Napoca, România
Tel. +40 744 238093
editorial-secretary@technicalgeography.org
http://technicalgeography.org/

C o n t e n t

Geographia Technica

Volume 21, Issue 3, summer 2026
An International Journal of Technical Geography
ISSN 2065-4421 (Online); ISSN 1842-5135 (printed)

TOURISM REVENUE DYNAMICS IN XINJIANG: A SPATIO-ECONOMETRIC ANALYSIS OF SCALE, MOBILITY, AND REGIONAL STRUCTURE

Imanaly AKBAR [1,2,*], ***Bahaerguli NULAHEMAIT*** [3], ***Gulnar KUBESSOVA*** [4,*], ***Altynbay SAULEMBAYEV*** [5], ***Zabira MYRZALIYEVA*** [5], ***Zhannat ALIYEVA*** [1], ***Bauyrzhan PAZYLKHAIYR*** [1] **&** ***Gulden YRYSBAY*** [1]

DOI: 10.21163/GT_2026.213.01

ABSTRACT

Against the backdrop of China's rapid economic development, Xinjiang's tourism sector has experienced substantial growth, emerging as an important engine of regional development. This study employs a theory-grounded econometric model to systematically evaluate the key determinants of tourism revenue in Xinjiang using annual data from 2009 to 2020. Integrating tourism demand theory and destination competitiveness frameworks, the analysis examines Total Tourism Revenue (Y) in relation to five explanatory variables: Tourist Volume (X_1), Passenger Traffic (X_2), Tourist Person-Days (X_3), Tourist Mobility Intensity (X_4), and Inbound Overnight Visitors (X_5). Initial regression diagnostics reveal severe multicollinearity among the explanatory variables, which is addressed through a stepwise regression approach. The refined model identifies Tourist Volume ($\beta = 1.108$, $p < 0.001$) and Tourist Mobility Intensity ($\beta = 0.409$, $p < 0.001$) as the dominant and statistically significant predictors of tourism revenue, jointly explaining 91% of the variance (Adjusted $R^2 = 0.91$). These findings indicate that Xinjiang's tourism economy remains primarily scale-driven and mobility-dependent. However, the results also expose critical structural inefficiencies. While tourist arrivals increased by 89.8% between 2009 and 2019, tourist person-days declined sharply by 71.5%, reflecting significantly shortened stays and weakened visitor engagement. Moreover, the observed negative correlation between tourism revenue and passenger traffic suggests potential infrastructural pressures and inefficiencies in transport utilization. Together, these patterns reveal a fundamental contradiction between quantitative expansion and qualitative depth, raising concerns regarding environmental pressure and limited per-capita value capture. The study concludes that Xinjiang must transition from a volume-based tourism growth model toward a quality-centered development pathway. This shift requires optimizing transport efficiency, extending visitor stays through enhanced cultural and ecological experiences, diversifying tourism products, and promoting sustainable tourism practices to support resilient, inclusive, and long-term regional development.

Keywords: *Econometric Modeling, Structural Transformation; Tourism Revenue; Tourist Mobility; Spatial Interaction; Regional Heterogeneity; Xinjiang.*

---

[1]*Al-Farabi Kazakh National University, Almaty, Kazakhstan.* akbar.imanaly@kaznu.kz* *(IA),* aliyeva.zhannat@kaznu.kz*(ZA),*Bauyrzhan.Pazylkhaiyr@kaznu.edu.kz*(BP),*yrysbay_gulden1@live.kaznu.kz*GY)*

[2]*UC Davis Continuing and Professional Education, University of California, Davis, CA, USA.* iakbar@ucdavis.edu *(IA)*

[3] *School of Mathematics and Statistics, Yili Normal University, Xinjiang, China,* gulnara@sdxiehe.edu.cn *(BN)*

[4] *K. Zhubanov Aktobe Regional University, Aktobe, Kazakhstan,* gkubessova@zhubanov.edu.kz * *(GN)*

[5]*South Kazakhstan Pedagogical University named after Uzbekali Zhanibekov, Shymkent, Kazakhstan.* saulembayev.altynbay@okmpu.kz *(AS),* myrzaliyeva.zabira@okmpu.kz *(ZM)*

[*]*Corresponding author email:* akbar.imanaly@kaznu.kz, gkubessova@zhubanov.edu.kz

1. INTRODUCTION

Tourism has become a central driver of regional transformation, economic diversification, and social development across emerging destinations. Globally, tourism research recognizes the sector as a catalyst for income generation, employment growth, infrastructure development, and cross-cultural exchange (Farid et al., 2016; Meyer & Meyer, 2015). In China, these dynamics are especially evident in western regions where national initiatives, such as the Western Development Strategy and the Belt and Road Initiative (BRI), have stimulated large-scale tourism investment and accelerated destination development (Ahmad & Ullah, 2023). Within this context, the Xinjiang Uyghur Autonomous Region has rapidly emerged as one of China's fastest-growing tourism destinations due to its distinctive natural landscapes, Silk Road heritage, ethnic diversity, and expanding transport infrastructure.

Over the past decade, Xinjiang has experienced sustained increases in tourist arrivals, tourism revenue, and mobility flows, supported by improved highways, airport expansion, and the growth of high-speed rail (Jiao et al., 2020; Kaijun et al., 2023). Despite this remarkable expansion, tourism development in Xinjiang faces persistent structural challenges, including short visitor stays, uneven regional development, infrastructure bottlenecks, and constrained service capacity (Wu & Wang, 2024). These issues highlight the importance of understanding the determinants of tourism revenue to support sustainable planning and effective policy design.

Although numerous studies have examined Xinjiang's tourism patterns, much of the existing work remains descriptive, lacking rigorous econometric assessment or a strong theoretical foundation. Previous research has highlighted tourism competitiveness (Liu et al., 2022), transport infrastructure (Zhang & Zhang, 2022), destination risks (Ding & Wu, 2022; Zhang et al., 2024), and ecological constraints (Jiang et al., 2025), yet few studies integrate these factors into a comprehensive, theory-grounded empirical model of tourism revenue. Additionally, the tourism mobility nexus, widely emphasized in international tourism demand literature (Song et al., 2019), remains understudied in Xinjiang.

This study addresses these gaps by developing a theoretically informed econometric model to examine how tourism volume, mobility, stay duration, and inbound visitation influence revenue in Xinjiang. Drawing on tourism demand theory, destination competitiveness frameworks, and transport-tourism interactions, the analysis evaluates annual data from 2009 to 2020 using multicollinearity diagnostics and stepwise regression. The goal is to identify the most influential drivers of tourism revenue and highlight structural constraints limiting high-quality, experience-based, and sustainable growth.

The findings contribute to tourism literature by (1) demonstrating how scale-driven growth dominates Xinjiang's tourism economy; (2) revealing the role of internal mobility in shaping revenue patterns; and (3) identifying the limitations linked to short stays and low conversion from mobility to spending. The study also offers evidence-based recommendations for extending visitor stays, improving transport efficiency, diversifying tourism products, and transitioning from quantity-driven to quality-driven development. These results provide valuable insights for tourism scholars, planners, and policymakers seeking to support sustainable tourism development in western China.

2. LITERATURE REVIEW

2.1. Tourism Development and Regional Transformation

Tourism is widely recognized as a significant driver of economic restructuring and regional development, particularly in peripheral or emerging regions (Farid et al., 2016; Meyer & Meyer, 2015). Tourism-led development frameworks emphasize the role of the sector in creating employment, generating local income, stimulating service industries, and improving public infrastructure. In China, large-scale regional strategies such as the Belt and Road Initiative have further accelerated tourism growth, especially in western provinces where tourism is positioned as a core engine of socioeconomic transformation (Ahmad & Ullah, 2023).

Xinjiang, characterized by vast landscapes and cultural diversity, has increasingly leveraged tourism as a strategic development priority. While visitor numbers have risen rapidly, research suggests uneven development, infrastructure gaps, and regional disparities (Liu et al., 2024). Understanding the determinants of tourism performance is therefore crucial for effective planning and management.

2.2. Tourism Demand Theory and Revenue Determinants

International tourism demand research provides a theoretical foundation for analyzing visitor flows, spending behavior, and revenue generation. Tourism demand models emphasize economic factors (income, prices, exchange rates), socio-cultural motivations, destination attributes, and accessibility as major determinants (Altinay & Kozak, 2021; Song et al., 2019). Within this framework, variables such as tourist volume, length of stay, transport efficiency, and mobility patterns are central components shaping tourism performance.

The length of stay, often measured through tourist person-days, is particularly important because longer visits generate higher per-capita revenue and greater engagement with local services. However, in many emerging destinations, including Xinjiang, visitor stays remain relatively short, limiting economic benefits (Wu & Wang, 2024). Tourism scholars argue that insufficient diversification of tourism products, inadequate service quality, and limited destination experience depth constrain stay duration (Assaf & Josiassen, 2016).

Similarly, transport accessibility and connectivity influence tourism by shaping mobility costs, convenience, and perceived travel barriers (Li et al., 2023). Efficient transportation can increase tourist arrivals and enhance spatial tourism flows. However, research also shows that when transportation infrastructure is congested, inefficient, or poorly integrated with tourism services, increased mobility may not translate into higher tourism revenue (Chen et al., 2022).

2.3. Destination Competitiveness and Mobility Dynamics

Destination competitiveness theory offers additional insights for assessing how infrastructure, service quality, cultural assets, and environmental factors influence tourism performance (Crouch, 2011). The role of spatial structure is particularly pronounced in regions like Xinjiang, where spatial fragmentation, core-periphery structures, and long travel distances mediate tourism flows, economic linkages, and destination competitiveness. Xinjiang's competitive advantages include its unique desert-steppe environments, Silk Road heritage, and ethnic cultural diversity. However, challenges such as seasonal fluctuations, vast geographic scale, environmental vulnerability, and service inconsistency weaken destination competitiveness (Ding & Wu, 2022; Zhang et al., 2024).

The mobility dimension has recently gained prominence in competitiveness and tourism flow research. Studies emphasize that intra-destination mobility, the extent to which tourists move within a region, affects expenditure levels, attraction visitation, and local economic linkages (Zhang & Zhang, 2022). Tourist Mobility Intensity (measured in kilometers traveled) thus provides insight into consumption potential beyond simple arrival numbers.

In Xinjiang, high geographic distances and dispersed attractions mean that mobility efficiency is essential. Poorly coordinated transport services or long travel times can reduce visitor satisfaction and spending opportunities (Chen et al., 2022). This necessitates examining mobility indicators in econometric models of tourism revenue.

2.4. Empirical Studies on Tourism in Xinjiang

Numerous studies have analyzed tourism growth, spatial patterns, and policy frameworks in Xinjiang. These include assessments of tourism resource distribution (Chen et al., 2022), tourism–ecology interactions (Jiang et al., 2025), tourism efficiency (Yang et al., 2022), tourist risk perception (Yingzhi et al., 2020), and tourism development under environmental constraints (Wang et al., 2023). Although valuable, most studies rely on descriptive data or qualitative assessments, with limited application of advanced econometric techniques.

Only a few studies apply regression-based approaches, and they often analyze narrower sets of variables or aggregate macroeconomic indicators (Li & Hou, 2025). Further, existing econometric studies seldom address multicollinearity among tourism variables or link empirical findings to tourism theory in a meaningful way. This gap limits both academic contributions and practical implications.

2.5. Research Gap and Contribution

The literature reveals three major gaps: Limited theory-driven empirical research on tourism revenue determinants in Xinjiang; Insufficient integration of mobility indicators, despite their theoretical importance; and Lack of models addressing multicollinearity, which is common among tourism indicators (tourist volume, person-days, tourist mobility intensity). To sum up, these gaps point to a limited understanding of how Xinjiang's distinctive geographical structure, its vastness, dispersal of attractions, and reliance on long-distance mobility, fundamentally shapes the relationship between tourism scale, movement, and revenue generation. This study contributes by: developing a theoretical framework grounded in tourism demand and destination competitiveness; applying a rigorous econometric model with multicollinearity diagnostics and stepwise selection; evaluating the combined effects of volume, stay duration, mobility, and inbound tourism; providing insights for policy, planning, and sustainable tourism development in western China.

2.6. Research Area Overview: Geographical Context and Primary Tourism Resources of Xinjiang

The Xinjiang Uyghur Autonomous Region, situated in northwestern China, constitutes the nation's largest provincial-level administrative division. It shares borders with eight countries, including Kazakhstan, Kyrgyzstan, Tajikistan, Pakistan, and Mongolia, granting it a strategic position at the heart of Central Asia and along the historic Silk Road corridors (Toops, 2013).

The region's physiography is defined by a pronounced mountain-basin system, wherein the east-west trending Tianshan Mountain range bisects Xinjiang into two distinct macro-regions: Northern Xinjiang (Dzungarian Basin) and Southern Xinjiang (Tarim Basin). This structure is further framed by the Altai Mountains to the north and the Kunlun Mountains to the south (Wang et al., 2022).

As depicted in **Fig. 1.**, the spatial distribution of Xinjiang's principal tourism resources exhibits a strong correspondence with this underlying physical geography and regional structure. The Tianshan Mountains serve as a fundamental natural boundary, profoundly influencing tourism patterns and resource allocation.

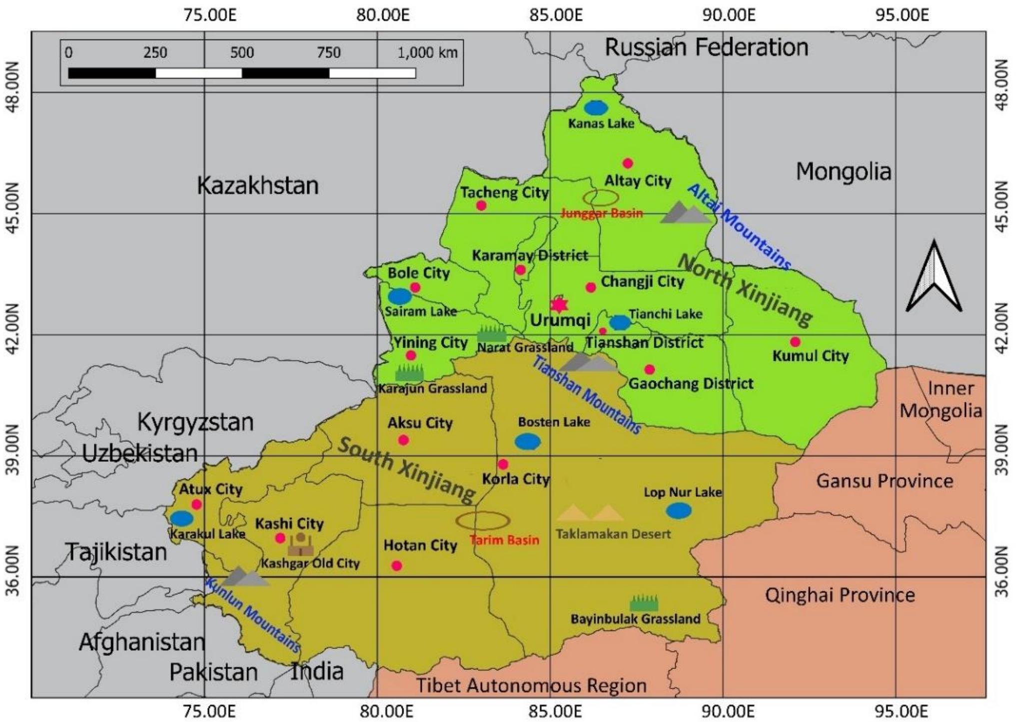

Fig. 1. Spatial Distribution of Major Tourism Resources and Physiographic Structure of Xinjiang Uyghur Autonomous Region, China.

3. DATA AND METHODS

3.1. Research Design

This study adopts a quantitative, theory-grounded research design to examine the determinants of tourism revenue in Xinjiang over the period 2009-2020. The analytical framework is informed by tourism demand theory and destination competitiveness models, emphasizing market scale, accessibility, visitor behavior, and mobility as key drivers of tourism revenue.

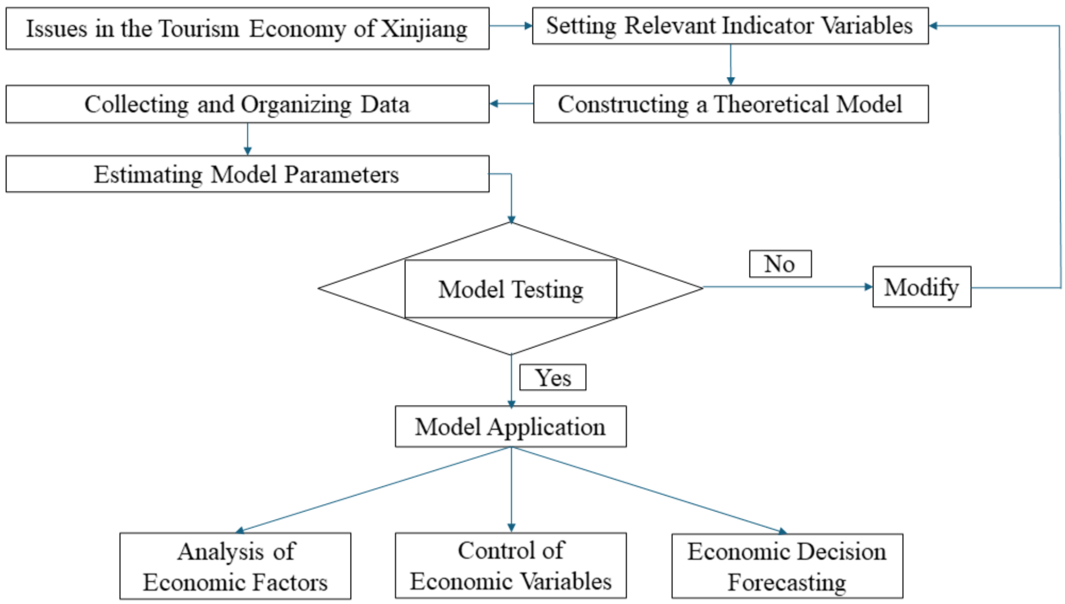

Fig. 2. Conceptual framework of tourism revenue determinants in Xinjiang.

Fig. 2. presents the conceptual framework of the study, illustrating the hypothesized relationships between tourism revenue and its key determinants, including tourist volume, passenger traffic, tourist person-days, tourist mobility intensity, and inbound overnight visitors.

Throughout this manuscript, terms such as “predictor,” “associated with,” and “related to” are used to describe statistical relationships identified through regression analysis. These expressions should not be interpreted as implying causal effects, given the observational design, limited sample size, and potential omitted variables.

3.2. Data and Variable Selection

Annual regional-level tourism data for 2009 – 2020 were obtained from the Xinjiang Tourism Bureau and the National Bureau of Statistics of China. All variables are officially published and reported on an annual basis.

Total tourism revenue (Y) is measured in 100 million yuan at current prices. Explanatory variables include tourist volume (X_1; total tourist arrivals, 10,000 persons), passenger volume (X_2; total passenger traffic, 10,000 persons), tourist person-days (X_3; cumulative days spent by tourists), tourist mobility intensity (X_4; billion passenger-kilometers traveled by tourists across all transport modes within Xinjiang), and inbound overnight visitors (X_5; foreign tourists staying at least one night, 10,000 persons).

Tourist mobility intensity captures the spatial extent of tourist movement within the region rather than simple arrival counts. It is derived from observed transport statistics aggregated across road, rail, and air modes and reflects realized rather than modeled mobility.

3.3. Analytical Procedures

Given the limited time-series length (12 annual observations), model parsimony was prioritized to reduce overfitting risks. A two-stage analytical strategy was adopted. First, a full multiple regression model was estimated to assess overall explanatory power and diagnose multicollinearity. Second, stepwise regression was employed as a variable-selection and diagnostic tool to identify the most stable predictors under severe collinearity constraints.

Although stepwise regression has recognized limitations, it remains a pragmatic approach in small-sample regional studies when complemented by robustness checks. Accordingly, sensitivity analyses were conducted using alternative model specifications, exclusion of the COVID-19 year, and predictive validation.

To account for the exogenous shock associated with the COVID-19 pandemic, a dummy variable for 2020 was introduced in an alternative specification. In addition, all core regressions were re-estimated excluding 2020. Results remained qualitatively consistent, with tourist volume and tourist mobility intensity retaining statistical significance, indicating that the findings are not driven by pandemic-related outliers.

3.4. Model Specification and Validation

Model Specification. Given the multifactor nature of tourism revenue, this study employs regression analysis to quantify the relationship between tourism revenue and its key determinants. Multiple linear regression is applied to examine the effects of tourist volume, passenger traffic, tourist person-days, tourist mobility intensity, and inbound overnight visitors on tourism revenue in Xinjiang. The objective is to assess the statistical significance, magnitude, and direction of these effects, thereby supporting forecasting and evidence-based policymaking.

Independent variables were selected based on tourism demand theory and destination competitiveness frameworks and are supported by consistent annual data for the period 2009-2020. To ensure model validity, diagnostic tests were conducted, including unit root tests for stationarity, variance inflation factors (VIFs) for multicollinearity, Durbin-Watson statistics for autocorrelation, and normality tests of residuals.

The simple linear regression model (Sen & Srivastava, 2012) is expressed as:

$$y = \beta_0 + \beta_1 x + \varepsilon \tag{1}$$

where: y is the dependent variable, x is the independent variable, β_0 and β_1 are unknown parameters and ε is the random error term. Parameters are estimated using the ordinary least squares method.

Multiple Linear Regression Model (Sen & Srivastava, 2012) which extends the simple model to multiple explanatory variables, is specified as:

$$y = \beta_0 + \beta_1 x_1 + \beta_2 x_2 + \ldots + \beta_p x_p + \varepsilon, \tag{2}$$

where: y denotes tourism revenue, x_1, x_2, ..., x_p represent explanatory variables, β_0 is the intercept, β_1, ..., β_P are regression coefficients, ε is the error term.

In the context of this study, a predictive model for tourism development in Xinjiang is constructed using tourism revenue, tourist volume, and tourist person-days as core variables. Holding other factors constant, the estimated coefficients measure the marginal effect of each explanatory variable on tourism revenue. Positive coefficients indicate that increases in tourist volume or tourist-days are associated with higher tourism revenue, consistent with theoretical expectations.

The regression modeling procedure follows a structured sequence, including variable definition, correlation analysis, model estimation, and comparison of predicted and observed values to assess model performance. These steps are summarized in **Fig. 2**, which presents the logical flow of the regression modeling process applied in this study.

Model Validation. Model adequacy was assessed using unit root tests for stationarity, variance inflation factors (VIFs) for multicollinearity, Durbin–Watson statistics for autocorrelation, and residual normality tests. Heteroskedasticity was examined using the Breusch–Pagan test, and influential observations were assessed using Cook’s distance.

Predictive performance was evaluated using mean absolute error (MAE) and root mean squared error (RMSE) under leave-one-out cross-validation. Models including tourist mobility intensity consistently produced lower prediction errors, confirming its additional explanatory value.

4. RESULTS AND EMPIRICAL ANALYSIS

4.1. Data and Variable Specification

This study conducts an empirical analysis of the determinants of tourism development in Xinjiang using annual data from 2009 to 2020 obtained from the Xinjiang Tourism Bureau and the National Bureau of Statistics of China. Variable selection is guided by tourism demand theory and destination competitiveness frameworks, capturing key dimensions of tourist activity, infrastructure, and destination appeal.

Total tourism revenue (Y), measured in 100 million yuan, serves as the dependent variable. The explanatory variables include tourist volume (X_1; 10,000 persons), representing market scale; passenger volume (X_2; 10,000 persons), reflecting transport infrastructure capacity; tourist person-days (X_3), capturing visit depth and duration; tourist mobility intensity (X_4; billion passenger-kilometers), measuring the spatial extent of tourist movement within the region and it is derived from observed transport statistics aggregated across road, rail, and air modes and reflects realized tourist mobility rather than modeled distances.; and inbound overnight visitors (X_5; 10,000 persons), indicating international tourism capacity.

Table 1.

Factors affecting tourism development in Xinjiang.

Year	y	x_1	x_2	x_3	x_4	x_5
2009	186.08	2133.49	29886	969.611	386.68	350
2010	281	3100	31937	2227.224	420.82	510
2011	351	3078.57	35130	1110.346	488.53	560
2012	576	4860	38331	1539.582	535.81	620
2013	673.24	5205.59	40926	1846.55	544.46	690
2014	830	4952.69	37176	1529.808	500.00	540
2015	985	6097	35948	1265.487	477.29	530
2016	1340	8102	32148	1971.213	458.06	580
2017	1751.6	10725.51	27083	1936.617	428.54	770
2018	2579.71	15024.89	21204	946.982	405.76	990
2019	3593.5	21329.54	20276	859.446	414.53	350
2020	991.03	15811.46	6960	276.1	184.97	320
Data Source: *Department of Culture and Tourism of Xinjiang Uygur Autonomous Region (https://wlt.xinjiang.gov.cn/) and the National Bureau of Statistics of China (https://www.stats.gov.cn/).*						

Table 1 presents annual data (2009-2020) for six major tourism indicators in Xinjiang, including revenue, tourist numbers, and passenger volume. Most indicators rise steadily until 2019, reflecting sustained sector growth, followed by a sharp decline in 2020 due to pandemic-related travel disruptions. This dataset underpins the study’s econometric analysis.

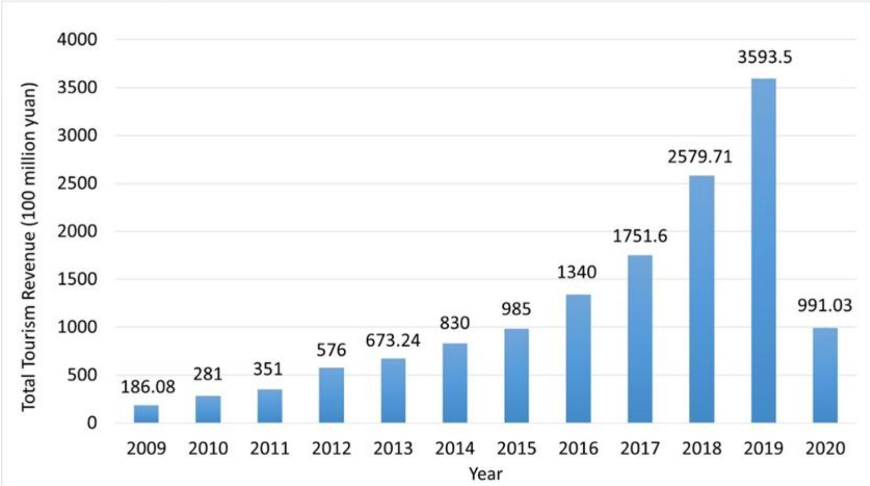

Fig. 3. Xinjiang's Total Tourism Revenue from 2009 to 2020.
Data Source: Department of Culture and Tourism of Xinjiang Uygur Autonomous Region (https://wlt.xinjiang.gov.cn/) and the National Bureau of Statistics of China (https://www.stats.gov.cn/).

Fig. 3. illustrates Xinjiang's annual tourism revenue from 2009 to 2020. Revenue shows a steady and significant increase from 2009 to 2019, peaking in 2019, followed by a sharp decline in 2020 due to COVID-19 disruptions. The figure highlights both long-term growth and short-term external vulnerabilities in the tourism sector.

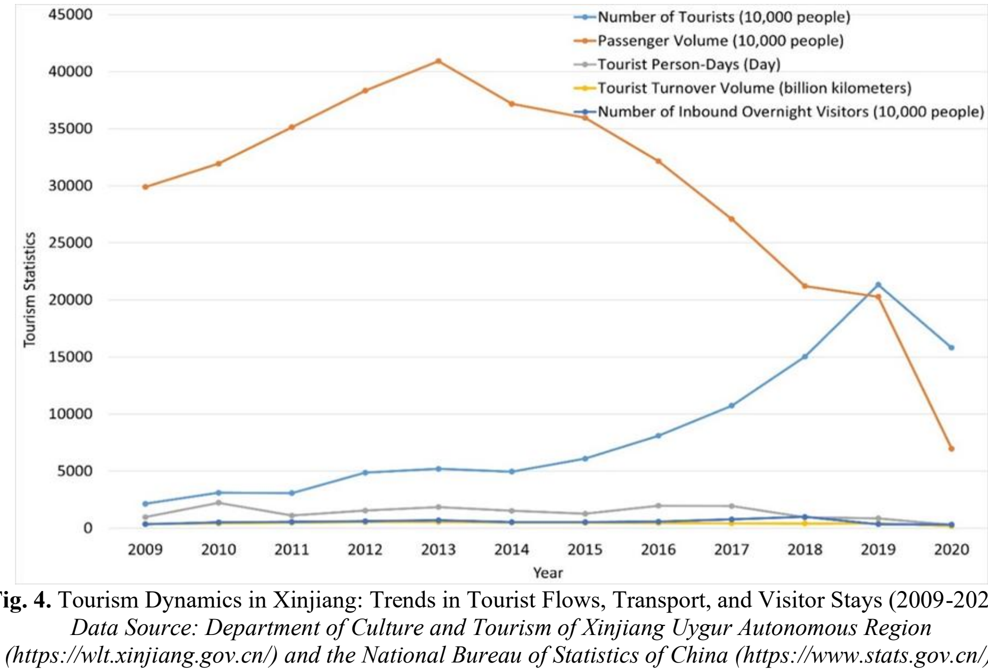

Fig. 4. Tourism Dynamics in Xinjiang: Trends in Tourist Flows, Transport, and Visitor Stays (2009-2020).
Data Source: Department of Culture and Tourism of Xinjiang Uygur Autonomous Region (https://wlt.xinjiang.gov.cn/) and the National Bureau of Statistics of China (https://www.stats.gov.cn/).

Fig. 4. illustrates trends in five key tourism indicators in Xinjiang (2009-2020): tourist numbers, passenger volume, tourist person-days, tourist mobility intensity, and inbound overnight visitors. Most indicators rise steadily over the decade, reflecting growing tourism activity and mobility, followed by sharp declines in 2020 due to pandemic restrictions, highlighting interconnected tourism dynamics over time.

4.2. Diagnostic Tests and Model Estimation

Pearson correlation analysis (**Table 2**) reveals a strong positive correlation between total tourism revenue (Y) and tourist volume (X_1) ($r = 0.897$, $p < 0.01$). Tourism revenue exhibits negative correlations with passenger volume (X_2: $r = -0.489$, $p = 0.106$), tourist person-days (X_3: $r = -0.271$, $p = 0.394$), and tourist mobility intensity (X_4: $r = -0.164$, $p = 0.610$); however, these correlations do not reach statistical significance at conventional levels. A weak positive correlation with inbound overnight visitors (X_5: $r = 0.200$, $p = 0.532$) is likewise not statistically significant.

Table 2.

Analysis Results of Pearson Correlation Coefficients.

	y	x_1	x_2	x_3	x_4	x_5
y	1 (0.000***)	0.897 (0.000***)	-0.489 (0.106)	-0.271 (0.394)	-0.164 (0.610)	0.2 (0.532)
x_1	0.897 (0.000***)	1(0.000***)	-0.779 (0.003***)	-0.51 (0.090*)	-0.518 (0.085*)	-0.005 (0.987)
x_2	-0.489 (0.106)	-0.779 (0.003***)	1 (0.000***)	0.68 (0.015**)	0.93 (0.000***)	0.236 (0.460)
x_4	-0.271 (0.394)	-0.51 (0.090*)	0.68 (0.015**)	1 (0.000***)	0.634 (0.027**)	0.362 (0.248)
x_5	-0.164 (0.610)	-0.518 (0.085*)	0.93 (0.000***)	0.634 (0.027**)	1 (0.000***)	0.401 (0.196)

Note: **** p < 0.01, ** p < 0.05, * p < 0.10. Values without asterisks are not statistically significant at conventional levels.*

Among the explanatory variables, several significant intercorrelations are observed. Tourist volume correlates negatively with passenger volume ($r = -0.779$, $p < 0.01$), tourist person-days ($r = -0.510$, $p < 0.10$), and tourist mobility intensity ($r = -0.518$, $p < 0.10$). Passenger volume correlates positively with tourist person-days ($r = 0.680$, $p < 0.05$) and tourist mobility intensity ($r = 0.930$, $p < 0.01$). These intercorrelations indicate potential multicollinearity, which is addressed in subsequent regression analysis.

Table 3 presents descriptive statistics and normality test results for all variables, including measures of central tendency and dispersion as well as skewness, kurtosis, and Shapiro-Wilk and Kolmogorov-Smirnov tests. Most variables satisfy normality assumptions, while tourist mobility intensity exhibits a significant deviation from normality. These diagnostics inform subsequent model specification and confirm the overall suitability of the data for linear regression analysis.

Table 3.

Normality test analysis results.

Variable name	Sample size	Median	Mean	Standard deviation	Skewness	Kurtosis	S-W test	K-S test
y	12	907.5	1178.18	1019.698	1.478	1.84	0.848 (0.034**)	0.239 (0.430)
x_1	12	5651.295	8368.395	6083.339	1.083	0.197	0.867 (0.060*)	0.229 (0.486)
x_2	12	32042.5	29750.417	9633.659	-1.278	1.632	0.896 (0.141)	0.173 (0.807)
x_3	12	1397.648	1373.247	569.968	-0.288	-0.457	0.965 (0.852)	0.13 (0.971)
x_4	12	443.3	437.121	94.324	-1.762	4.533	0.838 (0.026**)	0.213 (0.576)
x_5	12	550	567.5	190.412	0.785	1.004	0.93 (0.377)	0.141 (0.943)

Normality was assessed using the Shapiro-Wilk test, which is appropriate for small samples (N < 5000). The test results indicate that tourist volume (X_1), passenger volume (X_2; p = 0.060), tourist person-days (X_3; p = 0.141), and inbound overnight visitors (X_5; p = 0.377) do not significantly deviate from normality, as the null hypothesis of normal distribution cannot be rejected.

In contrast, tourist mobility intensity (X_4) exhibits a significant Shapiro-Wilk test result ($p < 0.05$), leading to rejection of the null hypothesis and indicating a departure from normality.

Table 4.

Linear regression analysis results (n=14).

Variable name	Sample size	Median	Mean	Standard deviation	Skewness	Kurtosis	S-W test	K-S test
y	12	907.5	1178.18	1019.698	1.478	1.84	0.848 (0.034**)	0.239 (0.430)
x_1	12	5651.295	8368.395	6083.339	1.083	0.197	0.867 (0.060*)	0.229 (0.486)
x_2	12	32042.5	29750.417	9633.659	-1.278	1.632	0.896 (0.141)	0.173 (0.807)
x_3	12	1397.648	1373.247	569.968	-0.288	-0.457	0.965 (0.852)	0.13 (0.971)
x_4	12	443.3	437.121	94.324	-1.762	4.533	0.838 (0.026**)	0.213 (0.576)
x_5	12	550	567.5	190.412	0.785	1.004	0.93 (0.377)	0.141 (0.943)

The initial multiple linear regression model including all explanatory variables (**Table 4**) exhibits strong explanatory power ($R^2 = 0.933$) and is statistically significant (F = 16.816, p = 0.002). The estimated regression equation is expressed as:

$$y = -2151.723 + 0.148 \times x_1 - 0.065 \times x_2 + 0.147 x_3 + 8.776 x_4 - 0.028 x_5 \quad (3)$$

Despite the good overall fit, the Variance Inflation Factor (VIF) values for tourist volume (X_1), passenger volume (X_2), and tourist mobility intensity (X_4) exceed the critical threshold of 10, indicating severe multicollinearity and reducing the reliability of individual coefficient estimates.

To address this issue, a stepwise regression procedure was applied. The resulting parsimonious model (**Table 5**) excludes collinear variables and retains only the most statistically robust predictors. The final model remains highly significant (F = 56.696, p < 0.001) and demonstrates excellent explanatory power ($R^2 = 0.926$; Adjusted $R^2 = 0.910$). Importantly, all VIF values in the refined specification fall below 10, confirming that multicollinearity has been effectively mitigated and that the coefficient estimates are more stable and credible.

Table 5.

Stepwise regression model results (n=14).

	Unstandardized coefficients and Standardized coefficients			*t*	*p*	VIF	R²	Adjustment R²	F
	B	Standard error	*Beta*						
Constant	-2311.11	596.315	-	-3.876	0.004***	-	0.926	0.91	F=56.696 P=0.000***
x_1	0.186	0.018	1.108	10.492	0.000***	1.366			
x_4	4.425	1.142	0.409	3.875	0.004***	1.366			
y: Dependent Variable									

Table 5 reports the final stepwise regression results, identifying tourist volume and tourist mobility intensity as the primary determinants of tourism revenue in Xinjiang. Both variables are statistically significant at the 1% level. Multicollinearity is effectively controlled, as all Variance Inflation Factor (VIF) values fall below the conventional threshold of 10. The model demonstrates strong explanatory power, as indicated by the high R^2 and adjusted R^2 values.

The overall model is highly significant (F-test, $p < 0.001$), leading to rejection of the null hypothesis that all regression coefficients are jointly equal to zero. These results confirm the statistical validity and robustness of the final specification.

4.3. Analysis of Empirical Findings

The stepwise regression results identify tourist volume and tourist mobility intensity as the primary determinants of tourism revenue in Xinjiang. Tourist volume (X_1) exerts a strong and statistically significant positive effect on tourism revenue ($B = 0.186$, standardized $\beta = 1.108$, $p < 0.001$), confirming that visitor arrivals remain the most influential direct driver of revenue growth. Tourist mobility intensity (X_4) also shows a significant positive impact ($B = 4.425$, $\beta = 0.409$, $p = 0.004$), underscoring the importance of internal tourist movement and associated economic activity within the destination.

The exclusion of passenger volume (X_2), which initially exhibited a negative association, suggests inefficiencies in transport infrastructure utilization. This result may reflect congestion effects and modal mismatches, whereby general passenger flows do not effectively translate into productive tourist mobility and may even generate disutility. Likewise, the insignificance of tourist person-days (X_3) and inbound overnight visitors (X_5) points to structural limitations in the tourism system, indicating a continued reliance on domestic visitor volume rather than high-value, long-stay, or diversified international markets.

Overall, the results demonstrate that Xinjiang's tourism revenue growth is primarily driven by visitor scale and internal mobility rather than stay duration or international demand. While this pattern explains recent revenue expansion, it also reveals structural vulnerabilities that must be addressed to support a more sustainable and resilient tourism development strategy.

5. DISCUSSION

The empirical results show that tourism revenue in Xinjiang is closely related to the volume of tourist flows and the intensity of internal mobility. In addition to scale effects, the statistical significance of mobility intensity suggests that spatial circulation within a region plays an important role in generating revenue. In geographically large and structurally fragmented destinations, revenue generation depends not only on the number of visitors but also on how tourists move between nodes. Spatially, Xinjiang's tourism system exhibits a core-periphery configuration built around major nodes, corridors, and last-mile connections (**Fig. 5**). Urumqi serves as the main central node, where transportation networks, accommodation capacity, and service aggregation are concentrated. Secondary nodes such as Turpan and Aksu function as regional hubs, and many small attractions are located along the corridors connecting these centers.

This configuration raises an important conceptual question: if many peripheral attractions are located along major mobility corridors, why do corridor flows not automatically generate significant spillover effects? The answer lies in the distinction between geographical proximity and functional integration in the tourism system.

Although many attractions are geographically close to major transport corridors, they often serve as transit points rather than destination nodes. Their peripheral status is determined not by physical distance but by their limited integration into the tourism value chain. Several mechanisms explain this functional marginality:

First, limited service capacity limits value capture. Many destinations located close to corridors lack adequate accommodation, catering, guide services, and interpretive infrastructure. As a result, visitors, although staying for short periods, do not generate significant overnight stays or spending.

Fig. 5. Conceptual spatial structure of tourism development and internal mobility in the Xinjiang Uygur Autonomous Region, China.

Second, despite proximity to the corridor, gaps in last-mile accessibility persist. Poor road signage, poor secondary road conditions, limited public transport connections and insufficient parking can all hinder meaningful travel.

Third, route structures in large areas often prioritize efficiency over depth. Tour operators and independent travelers who follow multi-destination itineraries may spend minimal time at peripheral destinations, creating “pass-through” tourism rather than deep consumption.

Fourth, information asymmetries reduce functional visibility. Without effective marketing and interpretation, geographically accessible destinations remain economically marginal.

This distinction is consistent with Friedmann (1966) core-periphery theory, which defines peripheral status not by absolute location but by asymmetric exchange relations with central regions. Brown et al. (2000) emphasize in their research that tourism development in peripheral regions depends not only on infrastructure but also on service capacity. They link the difference between transit points and destination nodes to the degree of service concentration. Song et al. (2013), developing the tourism value chain theory, argue that the economic exclusion of peripheral points occurs due to their incomplete integration into the value chain due to insufficient service infrastructure. Value accumulation, service concentration, and economic retention occur in central nodes, where tourism services are packaged and consumed. Although peripheral locations are located along corridors, they remain economically marginal if they function primarily as transit routes rather than as service-capable stops.

The policy message is that improving corridor infrastructure alone is not enough to integrate peripheral regions. Additional investments are needed in service development, last-mile connections, interpretive infrastructure, and route design to transform transit points into economically integrated destination hubs.

6. CONCLUSIONS

This study develops a theory-grounded econometric framework to examine the key drivers of tourism revenue in Xinjiang using annual data from 2009 to 2020. Integrating tourism demand theory, destination competitiveness frameworks, and rigorous diagnostic testing, the analysis provides clear evidence that tourism revenue formation in Xinjiang is primarily driven by two interrelated factors: tourist volume and tourist mobility intensity. These findings align with established tourism research while offering new insights into the spatial structure of tourism development in western China.

The results confirm that visitor scale remains the most influential determinant of tourism revenue, reinforcing theoretical perspectives that emphasize market size as a core driver of destination performance. At the same time, tourist mobility intensity, capturing internal movement and spatial travel, emerges as a significant contributor to revenue generation. This suggests that beyond attracting tourists, the circulation of visitors within the destination plays a critical role in stimulating spending and supporting regional economic linkages. In contrast, the insignificance of passenger volume, tourist person-days, and inbound tourism points to structural weaknesses, including short visitor stays, limited product diversification, and weak penetration of high-value international markets.

These findings carry important policy implications for sustainable tourism development. Xinjiang should move beyond a predominantly volume-driven growth model toward a quality-oriented strategy that emphasizes longer stays and higher per-capita expenditure. Enhancing experiential tourism products, such as nature-based, heritage, winter sports, and rural tourism, alongside improvements in internal mobility efficiency and last-mile connectivity, will be essential. Destination planning should also promote more balanced regional development by extending tourism benefits to rural, peripheral, and minority areas through community-based tourism and localized value creation.

From a theoretical perspective, the study demonstrates that tourism growth in large, emerging destinations like Xinjiang is shaped more by scale and mobility effects than by depth-of-experience effects. While this dynamic can generate rapid revenue growth, it may constrain long-term competitiveness unless experiential quality and stay duration are strengthened.

Despite offering meaningful insights, this study is subject to several limitations. The size of the annual time series ($n = 12$) limits the complexity of the model and does not allow for causal inferences. Annual aggregation may obscure seasonal and intra-regional heterogeneity. In addition, the mobility intensity indicator, although theoretically sound, aggregates different transport modes and is likely to contain measurement inaccuracies.

We believe that future research can extend this analysis in several directions: First, spatial network analysis could incorporate structural metrics such as node centrality, betweenness, and corridor itinerary length to quantify how destinations' positions within tourism networks influence revenue capture. Second, spatial econometric models (including spatial autoregressive models, spatial error models, and spatial Durbin models) could be estimated using travel-time-based or network-based spatial weights matrices. Such models would allow direct testing of corridor spillover effects and assessment of whether mobility-driven revenue concentrates in core nodes or diffuses to peripheral areas. Third, high-frequency mobility data derived from mobile positioning systems, GPS traces, or smart transport cards could enable fine-grained analysis of tourist movement patterns, dwell times at specific sites, and spatial expenditure linkages. Fourth, panel data across multiple regions would facilitate stronger causal inference and allow examination of spatial heterogeneity in mobility-revenue relationships. These extensions would provide a more rigorous empirical basis for evaluating how spatial structure mediates tourism value capture in large, corridor-based destinations.

In conclusion, although Xinjiang's tourism sector has experienced rapid growth, its long-term success will depend on improving experience quality, enhancing mobility efficiency, and diversifying high-value tourism offerings. Addressing these challenges will support a transition toward a more resilient, inclusive, and internationally competitive tourism economy.

REFERENCES

Ahmad, T., & Ullah, S. (2023). Development under belt and road initiative: Gains for tourism industry in participant countries. Journal of China Tourism Research, 19(4), 950-972. https://doi.org/10.1080/19388160.2023.2167895

Altinay, L., & Kozak, M. (2021). Revisiting destination competitiveness through chaos theory: The butterfly competitiveness model. Journal of Hospitality and Tourism Management, 49, 331-340. https://doi.org/10.1016/j.jhtm.2021.10.004

Assaf, A. G., & Josiassen, A. (2016). Frontier analysis: A state-of-the-art review and meta-analysis. Journal of travel research, 55(5), 612-627. https://doi.org/10.1177/0047287515569776

Brown, F., Hall, D. D., & Hall, D. R. (2000). Tourism in peripheral areas: Case studies (Vol. 2). Channel View Publications. https://search.library.ucdavis.edu/permalink/01UCD_INST/kueho9/alma9981238668103126

Chen, J., Li, M., & Xie, C. (2022). Transportation connectivity strategies and regional tourism economy-empirical analysis of 153 cities in China. Tourism Review, 77(1), 113-128. https://doi.org/10.1108/TR-03-2021-0134

Crouch, G. I. (2011). Destination competitiveness: An analysis of determinant attributes. Journal of travel research, 50(1), 27-45. https://doi.org/10.1177/0047287510362776

Ding, G., & Wu, J. (2022). Influence of tourism safety perception on destination image: A case study of Xinjiang, China. Sustainability, 14(3), 1663. https://doi.org/10.3390/su14031663

Farid, H., Hakimian, F., Nair, V., Nair, P. K., & Ismail, N. (2016). Trend of research on sustainable tourism and climate change in 21st century. Worldwide Hospitality and Tourism Themes, 8(5), 516-533. https://doi.org/10.1108/WHATT-06-2016-0032

Friedmann, J. (1966). Planning as innovation: The Chilean case. Journal of the American Institute of Planners, 32(4), 194-204. https://doi.org/10.1080/01944366608978495

Jiang, B., Zhang, C., Liu, Z., Wen, J., Zhu, J., Xu, L., & Wang, F. (2025). Tailoring an economic-ecological-tourism coupling framework for arid-region ski resorts: A PSR model-based case study of Xinjiang, China. Ecological Indicators, 178, 113881. https://doi.org/10.1016/j.ecolind.2025.113881

Jiao, Y., Zhang, Y., & Meng, Z. (2020). Tourism as development aid: Policies and challenges for tourism planning in Xinjiang, China. Tourism Planning & Development, 17(3), 335-354. https://doi.org/10.1080/21568316.2019.1597762

Kaijun, C., Ning, S., & Mimi, W. (2023). Spatial distribution pattern and accessibility analysis of the key rural tourism villages in the five northwestern provinces of China. Arid Land Geography, 46(7), 1196-1205. https://doi.org/10.12118/j.issn.1000-6060.2022.531

Li, G., Pu, K., & Long, M. (2023). High-speed rail connectivity, space-time distance compression, and trans-regional tourism flows: Evidence from China's inbound tourism. Journal of Transport Geography, 109, 103592. https://doi.org/10.1016/j.jtrangeo.2023.103592

Li, X., & Hou, J. (2025). Spatial Differentiation Characteristics and Influencing Factors of Public Cultural Facilities in Xinjiang. Sustainability, 17(11), 4994. https://doi.org/10.3390/su17114994

Liu, H., Chen, B., Xia, Q., Zabi, G., & Li, G. (2024). Study on the complex relationship of tourism-economy-ecological environment in arid zones: The case of Xinjiang, China. Frontiers in Environmental Science, 12, 1435660. https://doi.org/10.3389/fenvs.2024.1435660

Liu, H., Hasan, M., Cui, D., Yan, J., & Sun, G. (2022). Evaluation of tourism competitiveness and mechanisms of spatial differentiation in Xinjiang, China. PLoS One, 17(2), e0263229. https://doi.org/10.1371/journal.pone.0263229

Meyer, D., & Meyer, N. (2015). The role and impact of tourism on local economic development: a comparative study and leisure. African Journal for Physical Health Education, Recreation and Dance, 21(1.1), 197-214. https://hdl.handle.net/10520/EJC172415

Sen, A., & Srivastava, M. (2012). Regression analysis: theory, methods, and applications. Springer Science & Business Media. https://link.springer.com/chapter/10.1007/978-1-4612-4470-7_11

Song, H., Liu, J., & Chen, G. (2013). Tourism value chain governance: Review and prospects. Journal of travel research, 52(1), 15-28. https://doi.org/10.1177/0047287512457264

Song, H., Qiu, R. T., & Park, J. (2019). A review of research on tourism demand forecasting: Launching the Annals of Tourism Research Curated Collection on tourism demand forecasting. Annals of tourism research, 75, 338-362. https://doi.org/10.1016/j.annals.2018.12.001

Toops, S. W. (2013). Where Inner Asia Meets Outer China: The Xinjiang Uyghur Autonomous Region of China. In Eurasian Corridors of Interconnection (pp. 49-71). Routledge. https://www.taylorfrancis.com/chapters/edit/10.4324/9780203796443-4/inner-asia-meets-outer-china-stanley-toops

Wang, J. a., Liang, S., & Shi, P. (2022). The geography of contemporary China. Land degradation and ecological restoration, 183-213. https://doi.org/10.1007/978-3-031-04158-7

Wang, R., Wu, F., & He, Z. (2023). Tourism Development under Water-Energy Dual Constraints: A Case Study from Xinjiang Based on Different Emergency Scenarios. International Journal of Environmental Research and Public Health, 20(3), 2224. https://doi.org/10.3390/ijerph20032224

Wu, Y., & Wang, Y. (2024). An empirical study on the tourist cognitive evaluations of tourism public services in Xinjiang province, China. Sustainability, 16(5), 1712. https://doi.org/10.3390/su16051712

Yang, Y., Zhang, C., Qin, Z., & Cui, Y. (2022). The spatial-temporal pattern evolution and influencing factors of county-scale tourism efficiency in Xinjiang, China. Open Geosciences, 14(1), 1547-1561. https://doi.org/10.1515/geo-2022-0410

Yingzhi, G., Ningning, X., Huimin, T., & Jiaying, X. (2020). An empirical study on the impacts of tourist risk perception on tourist motivation and satisfaction in Xinjiang of China under the background of the Belt and Road Initiative. Journal of Tourism and Hospitality Management, 8(1), 14-34. https://doi.org/10.17265/2328-2169/2020.01.002

Zhang, J., & Zhang, Y. (2022). Tourism, transport infrastructure and income inequality: A panel data analysis of China. Current Issues in Tourism, 25(10), 1607-1626. https://doi.org/10.1080/13683500.2021.1928012

Zhang, K., Mei, X., & Xiao, Z. (2024). Spatio-temporal evolution of sports tourism industry integration: A empirical analysis of Xinjiang in China. PLoS One, 19(4), e0300959. https://doi.org/10.1371/journal.pone.0300959

GIS-BASED WILDFIRE RISK ASSESSMENT IN A MEDITERRANEAN PROTECTED AREA: A MULTI-CRITERIA ANALYSIS OF DAJTI NATIONAL PARK, ALBANIA

Sonila PAPATHIMIU [1]*, Adelajda HALILI [2] & Fioralba SULA [1]

DOI: 10.21163/GT_2026.213.02

ABSTRACT

Wildfires represent a major environmental threat in Mediterranean landscapes, particularly within protected mountainous areas where complex topography, vegetation patterns, climatic variability, and increasing human pressure interact. In this context, spatially explicit fire risk assessment is essential for effective prevention planning and sustainable ecosystem management. This study presents a GIS-based multi-criteria analysis for forest fire risk assessment in Dajti National Park, Albania. A comprehensive set of spatial factors was integrated, including terrain slope, aspect, land cover and land use, vegetation density derived from the Normalized Difference Vegetation Index (NDVI), temperature, rainfall, wind speed, and proximity to roads and settlements. Each factor was processed as a thematic raster layer and reclassified into standardized fire susceptibility classes ranging from very low to very high risk. The layers were subsequently combined using a weighted overlay approach to generate a composite wildfire susceptibility index. The resulting forest fire risk map reveals that moderate to high-risk zones dominate the study area, particularly in sectors characterized by steep terrain, dense or degraded vegetation cover, elevated temperatures, lower precipitation, higher wind exposure, and close proximity to infrastructure. Very high-risk zones are mainly concentrated along peripheral areas and access corridors, where anthropogenic influence overlaps with favorable natural conditions for fire ignition and spread. The results demonstrate the effectiveness of GIS-based multi-criteria analysis as a robust decision-support tool for forest wildfire susceptibility zoning in protected areas. The proposed methodological framework supports the identification of priority zones for fire prevention and management measures and is transferable to other Mediterranean and mountainous environments facing similar wildfire challenges.

Keywords: *Wildfire risk; GIS; Weighted overlay; NDVI; Multi-Criteria analysis; Protected areas; Disaster risk reduction.*

1. INTRODUCTION

Wildfires constitute one of the most critical natural hazards affecting Mediterranean regions, with severe consequences for ecosystems, human safety, and socio-economic systems. In recent decades, the frequency, intensity, and spatial extent of wildfire events have increased markedly, driven by the combined effects of climate change, land-use transformations, and the expansion of human activities at the wildland–urban interface (Bowman et al., 2009). Recent assessments indicate that Mediterranean Europe is experiencing longer fire seasons and an increasing likelihood of extreme wildfire events, underscoring the growing urgency of proactive and spatially informed risk reduction strategies (San-Miguel-Ayanz et al., 2021).

Mediterranean landscapes are particularly vulnerable to wildfires due to their climatic conditions—characterized by hot, dry summers—combined with complex topography and highly flammable vegetation types such as pine forests and shrublands (Pausas & Keeley, 2009).

----

[1] *Department of Geography, Faculty of History and Philology, University of Tirana, Albania. * Corresponding author: sonila.papathimiu@unitir.edu.al (SP), adela.halili@fgjm.edu.al (AH).*

[2] *Faculty of Geology and Mines/Department of Mineral Resources/Polytechnic University of Tirana, Tirana, Albania; fioralba.sula@fhf.edu.al (FS).*

In these environments, wildfires represent not only a recurrent ecological disturbance but also a major disaster risk capable of generating cascading impacts, including biodiversity loss, soil erosion, air pollution, and threats to nearby settlements and infrastructure (FAO, 2020). These risks are especially pronounced in protected areas, where conservation objectives increasingly intersect with recreational pressure, accessibility, and infrastructural development.

Geographic Information Systems (GIS) and remote sensing have become essential tools for wildfire risk assessment, enabling the integration and spatial analysis of heterogeneous environmental and anthropogenic factors (Chuvieco & Salas, 1996). Recent advances in spatial wildfire science emphasize the importance of combining vegetation characteristics, topographic conditions, climatic variables, and human influence to enhance susceptibility mapping and to support disaster risk reduction and land-management policies (Chuvieco et al., 2021). Among available approaches, GIS-based multi-criteria analysis (MCA), including weighted overlay techniques, remains widely applied due to its transparency, adaptability, and suitability for regions where long-term fire records or detailed calibration data are limited.

Despite substantial progress in wildfire risk modeling at global and continental scales, significant gaps persist in Southeastern Europe. In Albania, spatially explicit wildfire susceptibility assessments remain scarce, particularly for protected areas, even as wildfire occurrence and human pressure continue to intensify. This lack of localized risk mapping constrains prevention planning, limits the effectiveness of early warning systems, and reduces the capacity of authorities to prioritize mitigation measures in the most vulnerable zones. Dajti National Park, located adjacent to the metropolitan area of Tirana, exemplifies these challenges. The Park is characterized by steep terrain, diverse forest ecosystems, and intense seasonal visitation, factors that collectively increase the probability of wildfire ignition and rapid fire spread. Its position at the wildland–urban interface further amplifies potential environmental and socio-economic impacts. While European-level monitoring systems provide valuable large-scale fire information, site-specific susceptibility assessments remain essential for operational risk reduction, protected area management, and local decision-making (San-Miguel-Ayanz et al., 2021).

In this context, the present study aims to assess wildfire susceptibility in Dajti National Park using a GIS-based MCA framework. By integrating key natural and anthropogenic factors—including topography, land cover, vegetation density, climatic variables, and proximity to infrastructure—this research identifies spatial patterns of wildfire risk and delineates zones requiring priority intervention. The study contributes to disaster risk reduction by providing a reproducible and transferable methodological approach that supports evidence-based prevention strategies and the sustainable management of wildfire-prone protected areas in Mediterranean environments.

2. MATERIALS AND METHODS

2.1. Study area

Dajti National Park is located in central Albania, immediately east of the Tirana metropolitan area, and covers approximately 28,561.85 ha. The Park represents a mountainous protected landscape characterized by steep slopes, complex terrain morphology, and a high diversity of forest ecosystems. Following the 2022 boundary redefinition (Decision of the Council of Ministers No. 59, 26 January 2022), the park includes not only Mount Dajti itself but also parts of the adjoining Mali me Gropa–Bizë–Martanesh massif on its eastern side. The area is influenced by a Mediterranean–continental climate, with hot and dry summers and increased precipitation during the winter season.

The park's close proximity to urban and peri-urban settlements, combined with intensive recreational activities during summer months, places it within a pronounced wildland–urban interface. Such conditions are widely recognized as significantly increasing wildfire ignition probability and potential impacts, particularly in Mediterranean protected areas (Moreira et al., 2011; San-Miguel-Ayanz et al., 2021) **(Fig. 1).**

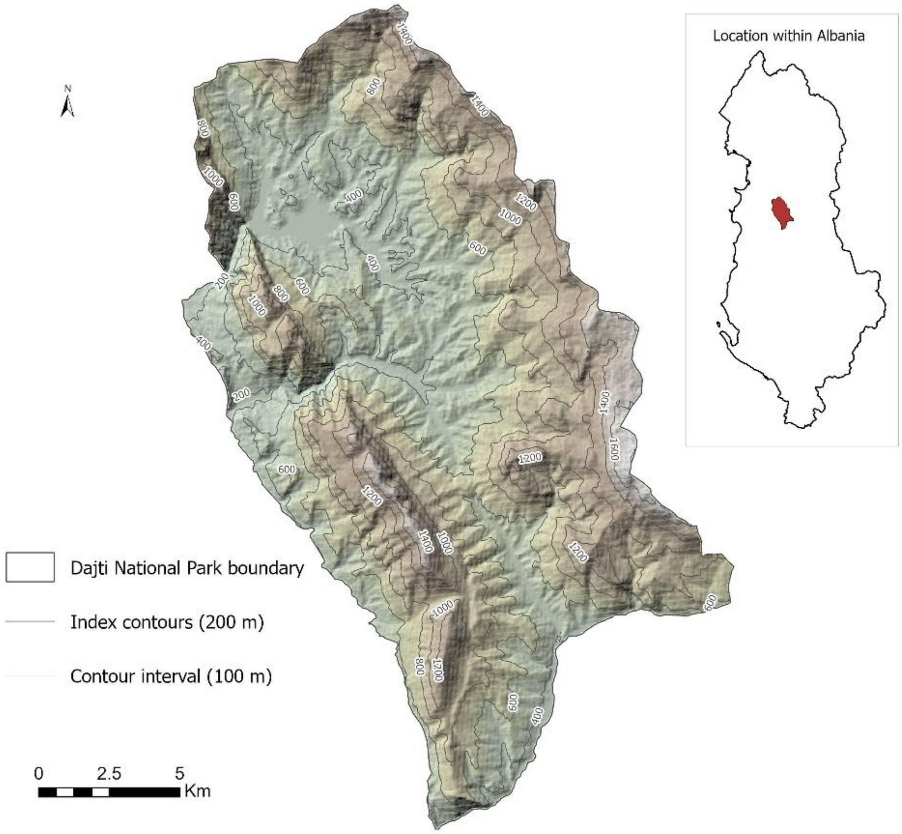

Fig. 1. Study area and topographic characteristics of Dajti National Park. The 30 m-resolution Digital Elevation Model (DEM) is displayed using a 100 m contour interval and 200 m index contours. Elevation ranges from 132 to 1,813 m above sea level (a.s.l.), with the highest values located in the eastern Mali me Gropa sector of the park. The coordinate reference system is WGS 1984 / UTM Zone 34 N.

2.2. Data sources and preprocessing

The wildfire susceptibility assessment was conducted using a GIS-based multi-criteria spatial analysis framework widely applied in wildfire hazard and environmental risk studies (Chuvieco et al., 2010; Pourghasemi et al., 2016). All spatial datasets were integrated into a unified geodatabase to ensure spatial consistency, geometric accuracy, and analytical reliability. Prior to analysis, all raster and vector layers were projected into a common coordinate reference system (WGS 1984 / UTM Zone 34N), resampled to a uniform spatial resolution of 30 m, and clipped to the boundary of Dajti National Park to ensure spatial alignment among all variables.

Topographic influence on wildfire susceptibility was represented by terrain slope derived from a 30 m DEM obtained from the United States Geological Survey (USGS) Earth Explorer database. Slope was calculated in degrees using standard terrain analysis tools within the GIS environment. Steeper slopes are known to accelerate fire spread and increase fire intensity due to enhanced heat transfer and fuel pre-heating processes (Sharples, 2009; Chuvieco et al., 2010).

Land use and land cover (LULC) information was derived from supervised classification of Landsat imagery obtained from the USGS Earth Resources Observation and Science (EROS) Center archive. Landsat imagery with 30 m spatial resolution was processed in ArcGIS Pro to generate land-cover classes representing the dominant surface types within the study area. Training samples were manually collected using the Training Samples Manager tool, and five land-cover classes were defined: water bodies, bare/urban surfaces, grasslands, shrublands, and forests.

The classification was performed using a Random Trees classifier, a machine-learning algorithm widely applied in remote sensing classification due to its ability to handle nonlinear relationships between spectral variables and land-cover categories. Following classification, a majority filter was applied to reduce isolated pixels and improve spatial coherence of the resulting LULC map. The final classified raster was subsequently clipped to the Dajti National Park boundary and used as an input variable in the wildfire susceptibility model. Landsat imagery is widely used for environmental monitoring and land-cover mapping due to its long-term temporal coverage and consistent spatial resolution (Wulder et al., 2019).
Vegetation density and fuel availability were represented using the NDVI derived from Landsat imagery. NDVI was calculated using the standard formula:

$$NDVI = \frac{(NIR - RED)}{(NIR + RED)}$$

where NIR represents near-infrared reflectance and RED represents red spectral reflectance (Rouse et al., 1974).

Multi-temporal NDVI layers derived from Landsat imagery for the period 2022–2024 were analyzed to represent vegetation density and fuel load conditions during the peak vegetation season. NDVI is widely used in wildfire studies as an indicator of vegetation biomass, fuel continuity, and vegetation health (Chuvieco et al., 2004).

Table 1.

Data sources and characteristics of spatial variables used in the wildfire susceptibility analysis.

Variable	Data Source	Spatial Resolution	Temporal Coverage	Data Format	Description
Elevation (DEM)	USGS Earth Explorer	30 m	Static	Raster	DEM used to derive terrain slope and aspect
Slope	Derived from DEM (USGS)	30 m	Static	Raster	Terrain slope calculated in degrees
Aspect	Derived from DEM (USGS)	30 m	Static	Raster	Terrain orientation influencing solar radiation and fuel drying
Land Use / Land Cover	Landsat imagery (USGS EROS)	30 m	2023	Raster	Supervised classification using Random Trees algorithm
NDVI	Landsat imagery (USGS EROS)	30 m	2022–2024	Raster	Vegetation density and biomass indicator
Temperature	ERA5 (ECMWF)	Resampled to 30 m	Multi-year average	Raster	Climatic variable influencing fuel drying
Precipitation	ERA5 (ECMWF)	Resampled to 30 m	Multi-year average	Raster	Climatic variable affecting vegetation moisture
Wind Speed	ERA5 (ECMWF)	Resampled to 30 m	Multi-year average	Raster	Climatic variable influencing fire spread
Distance to Roads	OpenStreetMap (OSM)	30 m	Current	Raster	Euclidean distance from road network
Distance to Buildings	OpenStreetMap (OSM)	30 m	Current	Raster	Euclidean distance from building points
Fire Occurrence Data	MODIS Active Fire (NASA FIRMS)	~1 km	2001–2023	Point	Used for wildfire susceptibility model validation

Climatic variables including temperature, precipitation, and wind speed were obtained from the ERA5 climate reanalysis dataset produced by the European Centre for Medium-Range Weather Forecasts (ECMWF). ERA5 provides globally consistent atmospheric and land-surface variables derived from data assimilation and numerical weather prediction models (Hersbach et al., 2020). Climatic variables were extracted for a multi-year period and interpolated to raster surfaces with 30 m spatial resolution using the Inverse Distance Weighting (IDW) interpolation method in order to match the spatial resolution of the other environmental variables used in the analysis. IDW interpolation estimates unknown values based on spatially weighted averages of surrounding observations and is commonly applied in environmental spatial modeling where station density is limited (Li & Heap, 2014).

Anthropogenic influence was incorporated through proximity analysis, reflecting the well-documented role of human activity as a dominant ignition source in Mediterranean wildfire regimes (Catry et al., 2010; Moreira et al., 2011). Vector datasets representing road infrastructure and building location points obtained from OpenStreetMap (OSM) were converted into Euclidean distance rasters. These layers were used to calculate distance-to-road and distance-to-building indicators, representing potential anthropogenic ignition sources. Areas located closer to infrastructure were assumed to have higher wildfire ignition probability due to increased accessibility and recreational pressure.

To enhance methodological transparency and reproducibility, a Data Source Summary Table (**Table 1**) is provided, presenting the source, spatial resolution, temporal coverage, and data format of all variables used in the analysis. This table clarifies the characteristics of each dataset used for wildfire susceptibility modeling and for validation using historical fire occurrence data derived from MODIS active fire detections (2001–2023).

2.3. Selection of fire risk factors and Reclassification of thematic layers

The selection of wildfire risk factors was guided by consulting the literature addressing wildfire susceptibility in Mediterranean and mountainous environments, where fire occurrence results from the interaction of topographic, vegetation, climatic, and anthropogenic drivers (Jaiswal et al., 2002; Chuvieco et al., 2010; Vilar et al., 2016; Pourghasemi et al., 2016). To capture these interacting influences, the analysis incorporated a combination of natural and human-related variables representing both fuel conditions and ignition probability.

Based on data availability and their documented influence on wildfire dynamics, nine factors were selected for the susceptibility assessment: terrain slope, aspect, land use/land cover (LULC), vegetation density derived from the NDVI, temperature, precipitation, wind speed, distance from roads, and distance from buildings (mostly representing settlements). These variables are widely recognized as key determinants of fuel availability, ignition likelihood, and fire spread behavior in Mediterranean ecosystems (Jolly et al., 2015; Abatzoglou & Williams, 2016). Because the selected variables differ in measurement units and value ranges, all thematic layers were standardized prior to integration. Each variable was reclassified into five ordinal susceptibility classes ranging from 1 (Very Low risk) to 5 (Very High risk). This standardization approach is commonly used in GIS based multi-criteria wildfire susceptibility modeling to enable the integration of heterogeneous spatial variables within a unified analytical framework (Jaiswal et al., 2002; Chuvieco et al., 2014).

The reclassification procedure combined three complementary criteria: the statistical distribution of each variable within the study area, the physical interpretation of its influence on wildfire ignition and propagation and threshold values reported in comparable wildfire susceptibility studies conducted in Mediterranean environments.

This approach ensures methodological consistency with established wildfire modeling practices while allowing thresholds to be adapted to local environmental conditions. Terrain slope was derived from the DEM and classified into five categories representing increasing potential for fire spread. Steeper slopes promote faster uphill fire propagation due to enhanced convective heat transfer and fuel pre-heating (Sharples, 2009). The slope-based susceptibility classification used five classes: 0–5, 5–15, 15–25, 25–35, and >35, corresponding to increasing fire spread potential (**Fig. 2**).

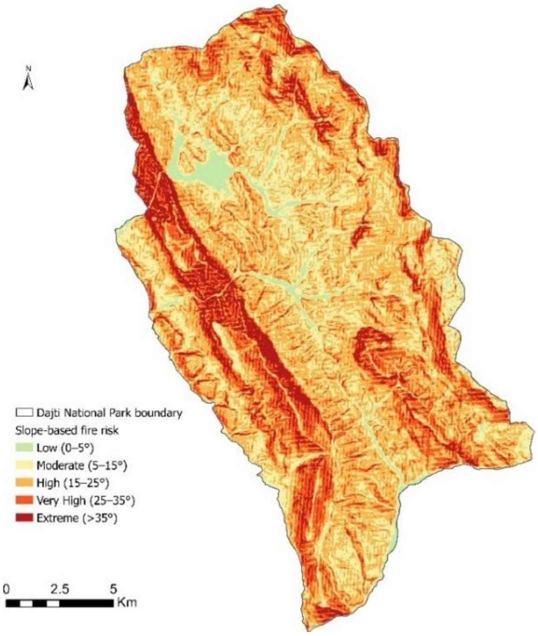

Fig. 2. Slope-based fire risk classification of Dajti National Park derived from a 30 m resolution DEM.

LULC classes were reclassified according to their potential fuel characteristics and combustibility. Grassland and shrubland formations were assigned higher susceptibility values due to greater fuel continuity and biomass accumulation, whereas water bodies and noncombustible surfaces were assigned lower susceptibility levels (**Fig. 3**).

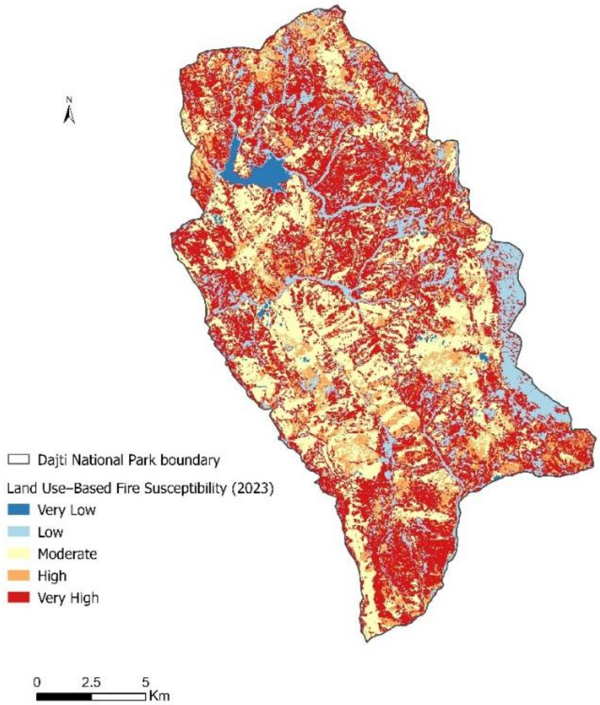

Fig. 3. LULC classes reclassified into five fire susceptibility levels (very low to very high) based on vegetation type and ignition potential. The resulting layer was used as an input factor in the weighted overlay model.

Vegetation density was further represented through NDVI values derived from Landsat imagery. Higher NDVI values indicate denser vegetation cover and therefore greater fuel availability, resulting in higher susceptibility classes (Chuvieco et al., 2004) (**Fig. 4**). The resulting reclassified layers represent spatially comparable indicators of wildfire susceptibility and constitute the input datasets for the subsequent multi-criteria overlay analysis.

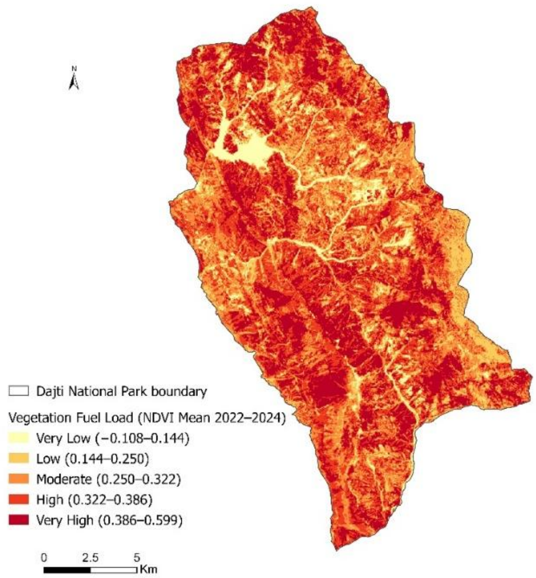

Fig. 4. NDVI-derived vegetation fuel load classes in Dajti National Park based on the multi-annual mean NDVI (2022–2024). NDVI values were classified into five categories using the Natural Breaks (Jenks) method and standardized to a 1–5 scale. Higher NDVI values indicate increased vegetation density and fuel availability. This layer was incorporated as the fuel component in the weighted overlay fire risk model.

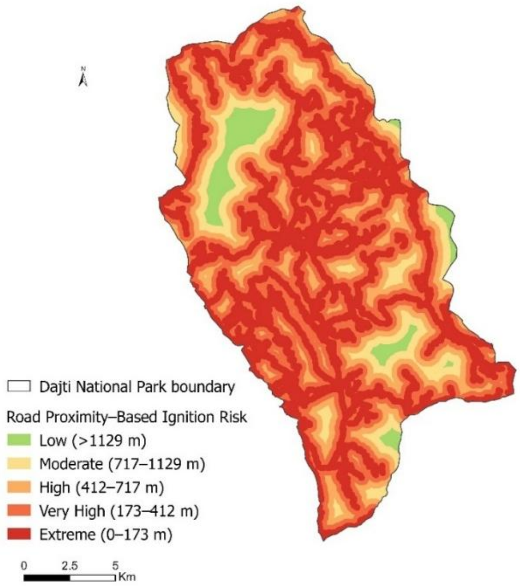

Fig. 5. Road proximity–based ignition risk map of Dajti National Park derived from Euclidean distance analysis (30 m spatial resolution). Distance values were classified using the Natural Breaks (Jenks) method and reclassified into five ignition risk categories, with areas closer to roads assigned higher ignition risk.

Climatic variables including temperature, precipitation, and wind speed were incorporated to represent environmental conditions influencing fuel moisture, ignition probability, and fire spread dynamics. Higher temperatures and stronger winds were associated with increased wildfire susceptibility due to enhanced fuel desiccation and fire propagation potential, while higher precipitation values were associated with reduced susceptibility due to increased fuel moisture (Jolly et al., 2015; Abatzoglou & Williams, 2016).

Anthropogenic factors were represented through distance-based indicators derived from road infrastructure and building location data. Proximity to roads and settlements is widely recognized as a key determinant of wildfire ignition in Mediterranean landscapes, where the majority of fires are human-induced (Catry et al., 2010; Moreira et al., 2011). Euclidean distance analysis was therefore used to generate distance-to-road (**Fig. 5**) and distance-to-settlement layers (**Fig. 6**). Areas located closer to infrastructure were assigned higher susceptibility values due to increased accessibility and human activity.

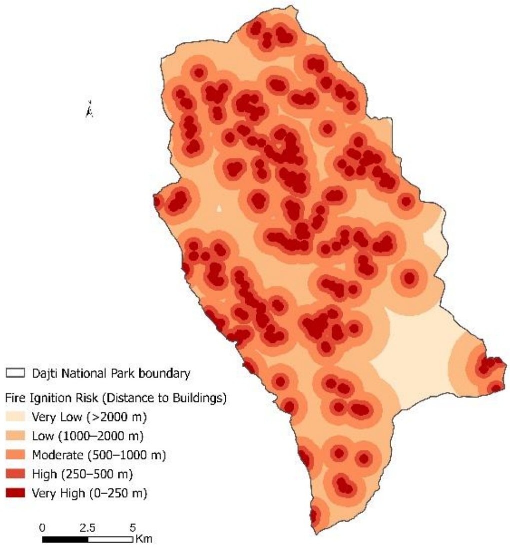

Fig. 6. Building proximity–based ignition risk map of Dajti National Park derived from Euclidean distance analysis (30 m spatial resolution). Distance values were calculated from building point locations obtained from OpenStreetMap (OSM) data and classified into five ignition risk categories (>2000 m, 1000–2000 m, 500–1000 m, 250–500 m, and 0–250 m). Areas located closer to buildings were assigned higher ignition susceptibility due to increased human presence and potential ignition sources.

The resulting reclassified layers represent standardized spatial indicators of wildfire susceptibility and constitute the input variables used in the subsequent weighted overlay analysis. To improve methodological transparency and reproducibility, the classification thresholds applied to each factor are summarized in **Table 2**, which presents the raw value ranges corresponding to each susceptibility class and the literature references supporting the adopted thresholds.

2.4. Weighting scheme, multi-criteria overlay analysis, and wildfire risk zoning

Following the reclassification of all thematic layers into a standardized wildfire susceptibility scale ranging from 1 (very low susceptibility) to 5 (very high susceptibility), the variables were integrated using a weighted overlay analysis within a Geographic Information System (GIS) environment. Weighted overlay analysis is a widely used approach in environmental risk assessment and spatial decision-support modeling because it enables the integration of multiple spatial variables with different units and value ranges into a single composite susceptibility index (Malczewski, 2006; Feizizadeh et al., 2014).

Table 2.

Reclassification scheme applied to wildfire susceptibility factors used in the weighted overlay model.

Factor	Class	Range / Category	Susceptibility Score
Slope (°)	Very Low	0–5	1
	Low	5–15	2
	Moderate	15–25	3
	High	25–35	4
	Very High	>35	5
Aspect	Low	North & Flat	1
	Moderate	East / West	3
	High	South	5
Land Use/Land Cover	Very Low	Water	1
	Low	Bare / Urban	2
	Moderate	Forest	3
	High	Shrubland	4
	Very High	Grassland	5
NDVI	Very Low	Lowest vegetation density	1
	Low		2
	Moderate		3
	High		4
	Very High	Highest vegetation density	5
Temperature (°C)	Very Low	Lowest values	1
	Low		2
	Moderate		3
	High		4
	Very High	Highest values	5
Precipitation (mm)	Very High	Highest rainfall	1
	High		2
	Moderate		3
	Low		4
	Very Low	Lowest rainfall	5
Wind Speed (m/s)	Very Low	Lowest wind speeds	1
	Low		2
	Moderate		3
	High		4
	Very High	Highest wind speeds	5
Distance to Roads (m)	Very High	0–173	5
	High	173–412	4
	Moderate	412–717	3
	Low	717–1129	2
	Very Low	>1129	1
Distance to Buildings (m)	Very High	0–250	5
	High	250–500	4
	Moderate	500–1000	3
	Low	1000–2000	2
	Very Low	>2000	1

In this study, each factor was assigned a specific weight representing its relative influence on wildfire ignition probability and fire spread potential. The weighting scheme was defined based on a review of wildfire susceptibility studies conducted in Mediterranean and mountainous environments, combined with the ecological interpretation of each variable within the study area. Factors representing human accessibility and ignition probability, such as distance to roads and distance to buildings, were assigned higher weights because human activities are widely recognized as the dominant ignition source in Mediterranean landscapes (Catry et al., 2010; Moreira et al., 2011; Vilar et al., 2016). Vegetation-related variables, including land use/land cover (LULC) and NDVI, were also given relatively high weights because they represent fuel availability and continuity, which strongly influence wildfire behavior and fire intensity (Chuvieco et al., 2004; Pausas & Keeley, 2009).

Topographic and climatic variables were incorporated with moderate weights reflecting their influence on fire propagation and fuel moisture conditions. Terrain slope affects fire spread rate and direction due to convective heat transfer and fuel preheating (Sharples, 2009), while climatic variables such as temperature, precipitation, and wind speed influence vegetation dryness, ignition probability, and fire spread dynamics (Jolly et al., 2015; Abatzoglou & Williams, 2016). Aspect was included with a lower weight because its influence is mainly indirect, affecting solar radiation exposure and local microclimatic conditions.

Based on these considerations, the following weighting scheme was applied in the weighted overlay model: distance to buildings (17%), distance to roads (17%), NDVI (14%), land use/land cover (14%), slope (12%), temperature (8%), precipitation (8%), wind speed (5%), and aspect (5%). The sum of all weights equals 100%, ensuring proportional contribution of each factor to the final susceptibility index.

The weighted overlay analysis was implemented using the Weighted Overlay tool in ArcGIS, which multiplies the standardized susceptibility score of each factor by its assigned weight and then sums the resulting weighted layers to generate a composite wildfire susceptibility index.

The resulting continuous wildfire susceptibility surface was subsequently classified into wildfire susceptibility zones using the Natural Breaks (Jenks) classification method, which groups values based on inherent statistical patterns in the data and maximizes differences between classes while minimizing within-class variance. The final wildfire susceptibility map was divided into five categories: very low, low, moderate, high, and very high susceptibility.

The resulting wildfire susceptibility map provides an integrated spatial representation of the combined influence of environmental conditions and anthropogenic pressures within Dajti National Park. Given the park's proximity to the Tirana metropolitan area and its intensive recreational use during the summer season, this susceptibility zones provide a valuable spatial framework for identifying priority areas for wildfire prevention, monitoring, and management within a wildland–urban interface context (Moreira et al., 2011; San-Miguel-Ayanz et al., 2021).

3. RESULTS AND VALIDATION

3.1. Historical wildfire occurrence patterns

An analysis of historical wildfire occurrence was conducted in order to identify spatial patterns of fire activity within the study area and to support the subsequent validation of the wildfire susceptibility model. Historical fire data were obtained from the MODIS active fire detection dataset available through the NASA FIRMS platform, covering the period 2001–2023.

The spatial distribution of fire detections indicates that wildfire events are not evenly distributed across Dajti National Park but tend to cluster in specific areas characterized by greater human accessibility and favorable environmental conditions for fire ignition. Several clusters of fire occurrences can be observed in areas located close to transportation corridors and settlement zones, highlighting the importance of anthropogenic factors in wildfire ignition.

To further analyze the spatial concentration of wildfire events, a Kernel density estimation (KDE) analysis was performed, to generate a continuous surface representing the density of fire occurrences across the study area, allowing the identification of zones with a higher frequency of wildfire events. The kernel density map (**Fig.7**) reveals clear hotspots of wildfire activity, particularly in areas located near the park boundaries and in zones with higher accessibility. These spatial patterns are consistent with wildfire regimes in Mediterranean protected areas where human activities represent a major ignition source.

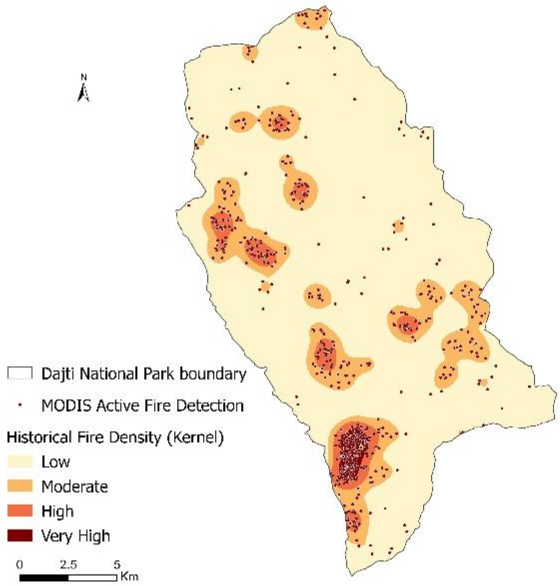

Fig. 7. Historical wildfire occurrences and kernel density distribution in Dajti National Park derived from MODIS active fire detections (2001–2023).

3.2. Spatial distribution of wildfire susceptibility

The GIS-based weighted overlay analysis produced a spatially continuous wildfire susceptibility surface representing the combined influence of topographic, vegetation, climatic, and anthropogenic factors within Dajti National Park (**Fig. 8**). The resulting wildfire susceptibility index was classified into five categories—very low, low, moderate, high, and very high—using the Natural Breaks (Jenks) classification method in order to preserve the natural distribution of the data.

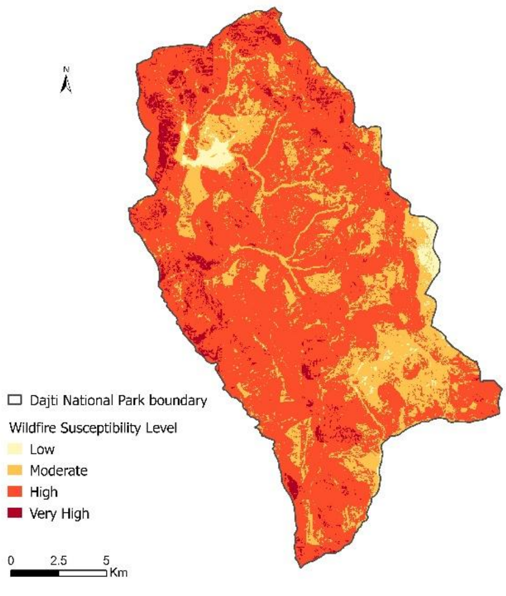

Fig. 8. Final wildfire susceptibility map of Dajti National Park derived from the GIS-based weighted overlay analysis integrating topographic, vegetation, climatic, and anthropogenic factors.

The final wildfire susceptibility map highlights a heterogeneous spatial distribution of wildfire risk across the park. Areas classified as high and very high susceptibility are mainly concentrated in zones characterized by dense vegetation cover, steep slopes, and close proximity to roads and settlements. These conditions facilitate both ignition probability and fire spread potential. Moderate susceptibility areas are distributed in intermediate zones where vegetation density remains relatively high but human accessibility is more limited. In contrast, low and very low susceptibility zones generally correspond to areas with limited vegetation cover, greater distance from infrastructure, or topographic conditions that reduce fire propagation potential. The spatial pattern observed in the susceptibility map reflects the interaction between environmental drivers and anthropogenic pressure within the study area. The proximity of Dajti National Park to the metropolitan area of Tirana and the high level of recreational use during the summer season contribute significantly to wildfire risk patterns within the park.

3.3. Validation of the Susceptibility Model Using Historical Fire Data

To evaluate the reliability of the wildfire susceptibility model, the spatial distribution of historical wildfire occurrences was compared with the predicted wildfire susceptibility classes. Fire occurrence data derived from MODIS active fire detections were overlaid with the final wildfire susceptibility map in order to assess the spatial correspondence between observed fire events and predicted risk zones. The results show that the majority of wildfire detections occurred within the moderate and high susceptibility classes, which together account for 97.37% of all recorded fire events. Specifically, 68.42% of fire occurrences were located in the High susceptibility class, while 28.95% were located in the Moderate class, indicating strong spatial agreement between the modeled wildfire risk and the observed fire activity. A smaller proportion of fires (2.32%) occurred within the Very High susceptibility class, which occupies a relatively small portion of the study area. Only 0.31% of fire detections were located within the Low susceptibility class, further supporting the ability of the model to distinguish between areas of lower and higher wildfire risk.

When normalized by area, the spatial distribution of fire occurrences reveals clear clustering patterns associated with zones of higher predicted susceptibility. These patterns are consistent with the influence of both environmental conditions and human activity on wildfire ignition and propagation. To statistically evaluate the relationship between wildfire occurrences and susceptibility classes, a Chi-square goodness-of-fit test was applied. The Chi-square goodness-of-fit test confirmed that wildfire occurrences are not randomly distributed across susceptibility classes (χ^2 test, $p < 0.001$), supporting the statistical validity of the wildfire susceptibility model (**Table 3**).

Overall, the strong correspondence between observed wildfire events and the predicted susceptibility classes demonstrate the effectiveness of the GIS-based multi-criteria model in identifying spatial patterns of wildfire risk within Dajti National Park.

Table 3.
Distribution of historical fire occurrences across wildfire susceptibility classes.

Risk Level	Raster Value	Number of Fires	Fire (%)
Low	2	2	0.31
Moderate	3	187	28.95
High	4	442	68.42
Very High	5	15	2.32

3.4. Quantitative Distribution of Wildfire Risk Classes and Identification of Priority Areas for Risk Reduction

The spatial distribution of wildfire susceptibility classes provides important insights into the wildfire risk structure within Dajti National Park. The analysis indicates that a substantial portion of the park falls within the moderate and high wildfire susceptibility classes, which together represent the dominant wildfire risk categories across the landscape (**Fig. 9**). Although very high susceptibility zones occupy a relatively small proportion of the total park area, they form spatially coherent clusters that represent critical hotspots for wildfire prevention and management interventions. These areas are typically located near transportation corridors, recreational facilities, and settlement boundaries where human activities increase the probability of wildfire ignition. In contrast, low susceptibility areas are limited in spatial extent and are generally associated with zones characterized by lower vegetation density or reduced accessibility. These areas exhibit comparatively lower wildfire risk due to less favorable conditions for ignition and fire spread.

The final wildfire susceptibility map therefore provides a robust spatial framework for identifying priority areas for wildfire risk reduction and management planning. Very high-risk zones located near infrastructure and recreational areas represent critical locations where fuel management, monitoring programs, and access control measures should be prioritized. Furthermore, the presence of extensive high susceptibility zones forming continuous spatial belts across the landscape suggests that wildfire prevention strategies should also consider broader landscape-level processes rather than focusing exclusively on isolated hotspots.

Moderate risk areas also warrant attention, as they may transition into higher susceptibility classes under extreme climatic conditions such as prolonged drought or heat waves. Overall, the results highlight the importance of spatially explicit wildfire risk mapping in supporting evidence-based wildfire prevention strategies and sustainable management of protected mountain landscapes.

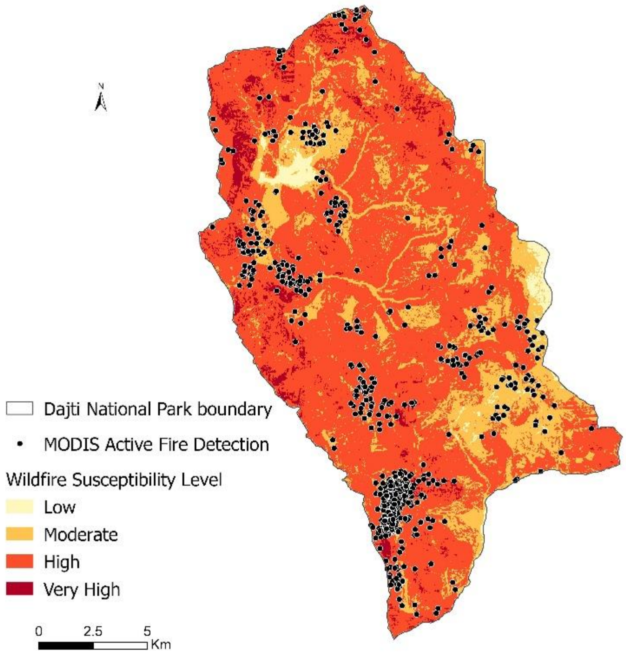

Fig. 9. Spatial validation of the wildfire susceptibility model through overlay analysis of historical fire detections and predicted wildfire risk classes in Dajti National Park. Historical fire occurrences (MODIS active fire detections, 2001–2023) are superimposed on the wildfire susceptibility map to assess the spatial correspondence between observed fire events and modeled risk zones.

4. DISCUSSION

4.1. Spatial Patterns of Wildfire Susceptibility

The wildfire susceptibility assessment conducted for Dajti National Park reveals a spatial configuration that reflects the combined influence of environmental and anthropogenic drivers typical of Mediterranean mountainous landscapes. The predominance of moderate and high susceptibility classes across large portions of the park indicates that wildfire risk is not restricted to isolated hotspots but rather represents a landscape-scale phenomenon shaped by multiple interacting factors.

Topographic conditions play an important role in shaping the observed spatial patterns of susceptibility. Areas characterized by steeper slopes are systematically associated with higher wildfire risk levels. Steep terrain promotes faster fire propagation through increased flame tilt and enhanced pre-heating of fuels, while simultaneously limiting accessibility for fire suppression operations. These relationships have been widely documented in wildfire behavior studies and are particularly relevant in mountainous protected areas where complex terrain influences both ignition dynamics and fire spread (Chuvieco & Salas, 1996; Sharples, 2009).

Vegetation-related variables also contribute significantly to the spatial distribution of wildfire susceptibility. Areas with high vegetation density, as represented by NDVI, correspond to zones with greater fuel availability and biomass accumulation, which can increase potential fire intensity once ignition occurs. At the same time, LULC characteristics influence ignition susceptibility. In the present study, grassland and shrubland areas exhibited higher susceptibility levels due to the presence of fine and highly flammable fuels, while forest areas were associated with moderate susceptibility levels. This distinction reflects the fact that fine fuels generally ignite more easily and promote rapid fire spread, whereas forest fuels may support higher fire intensity but may require stronger ignition conditions (Pausas & Keeley, 2009; Silva et al., 2019). The resulting spatial pattern therefore reflects the interaction between fuel availability, terrain characteristics, and accessibility, which together determine wildfire susceptibility across the landscape.

4.2. Anthropogenic Influence and the Wildland–Urban Interface

Anthropogenic factors represent a key driver of wildfire susceptibility in the study area. The spatial analysis demonstrates that areas located in close proximity to roads and buildings tend to exhibit higher wildfire susceptibility levels. This pattern reflects the strong influence of human activity on wildfire ignition in Mediterranean environments, where the majority of fires are caused by accidental or intentional human actions (Moreira et al., 2011).

Dajti National Park is situated immediately adjacent to the metropolitan area of Tirana and therefore represents a pronounced wildland–urban interface (WUI) environment. The presence of recreational facilities, tourism infrastructure, and transportation corridors increases human presence within the park, particularly during the summer season when climatic conditions are also most favorable for wildfire ignition and spread. Under such circumstances, wildfire risk is shaped not only by environmental factors but also by patterns of land use, accessibility, and human behavior. The results of the susceptibility analysis highlight the need for wildfire prevention strategies that integrate ecological management measures with spatial planning and public awareness initiatives, particularly in protected areas experiencing increasing recreational pressure.

4.3. Implications for Disaster Risk Reduction and Protected Area Management

From a disaster risk reduction perspective, the spatial delineation of wildfire susceptibility zones provides a valuable framework for prioritizing prevention and mitigation measures within Dajti National Park. Areas classified as high and very high susceptibility, particularly those where dense vegetation, steep slopes, and proximity to infrastructure overlap, represent priority zones for wildfire risk management. In these areas, targeted interventions such as fuel management, vegetation thinning, improved monitoring systems, and early detection measures could significantly reduce wildfire risk. The spatial identification of such zones allows management authorities to allocate resources more efficiently and to focus preventive actions where they are most needed.

At the same time, the widespread presence of moderate susceptibility zones suggests that wildfire risk management should adopt a broader landscape perspective. Moderate-risk areas may become highly susceptible under extreme climatic conditions such as prolonged drought or heat waves. Therefore, preventive strategies should address landscape-level fuel continuity and connectivity rather than focusing exclusively on localized hotspots.In this context, GIS-based wildfire susceptibility mapping provides a practical decision-support tool for integrating wildfire risk considerations into protected area management and spatial planning processes.

4.4. Methodological Considerations, Limitations and Future Research

The GIS-based MCA framework applied in this study provides a transparent and reproducible approach for wildfire susceptibility assessment in data-limited contexts. The integration of environmental and anthropogenic variables within a weighted overlay model allows the identification of spatial patterns of wildfire risk even where detailed fire occurrence datasets are limited.

One methodological limitation concerns the use of literature-based weighting for the susceptibility factors rather than deriving weights through statistical calibration. Although such approaches are widely applied in wildfire susceptibility studies (Malczewski, 2006; Pourghasemi et al., 2016), they may introduce a degree of subjectivity in the relative influence assigned to individual variables. Nevertheless, the comparison between the wildfire susceptibility map and historical fire occurrences derived from MODIS active fire detections demonstrates a strong spatial agreement between predicted risk zones and observed wildfire events. The majority of recorded fires occurred within the moderate and high susceptibility classes, supporting the predictive capability of the model.

Future research could further improve the accuracy of wildfire susceptibility assessments by incorporating higher-resolution vegetation data, longer-term fire occurrence datasets, and dynamic climatic indicators that capture seasonal variations in fuel moisture and fire weather conditions. Such developments would allow more detailed statistical calibration and enable the development of dynamic wildfire risk models capable of supporting adaptive management strategies.

5. CONCLUSIONS

This study applied a GIS-based MCA framework to assess wildfire susceptibility in Dajti National Park, a protected mountainous landscape located at the wildland–urban interface of the Tirana metropolitan region. By integrating topographic, vegetation, climatic, and anthropogenic factors within a weighted overlay model, the analysis produced a spatially explicit wildfire susceptibility map that reveals significant spatial variability in wildfire risk across the park.

The results indicate that moderate and high wildfire susceptibility zones dominate the park landscape, demonstrating that wildfire hazard represents a structurally embedded environmental risk rather than a localized phenomenon. High and very high susceptibility zones are primarily associated with the combined presence of steep terrain, dense vegetation cover, and proximity to roads and settlements. These findings highlight the importance of both environmental conditions and human accessibility in shaping wildfire risk patterns within protected areas located near urban centers.

The validation of the susceptibility model using historical wildfire detections further confirms the reliability of the proposed methodological approach. The majority of recorded wildfire events occur within areas classified as moderate and high susceptibility, demonstrating strong spatial correspondence between modeled risk zones and observed fire activity.

From a disaster risk reduction perspective, the study demonstrates the value of GIS-based wildfire susceptibility mapping as a decision-support tool for prevention-oriented wildfire management.

The identification of spatial risk gradients provides a practical basis for prioritizing intervention areas and supporting more efficient allocation of resources for fuel management, monitoring, and access control.

Although the analysis relies partly on literature-based weighting due to data limitations, the transparency and reproducibility of the adopted methodology make it particularly suitable for data-scarce environments such as many protected areas in Southeastern Europe. The proposed framework therefore provides a useful basis for supporting wildfire risk awareness, improving spatial planning, and guiding sustainable management strategies in wildfire-prone protected landscapes.

REFERENCES

Abatzoglou, J.T., & Williams, A.P., 2016. Impact of anthropogenic climate change on wildfire across western US forests. Proceedings of the National Academy of Sciences, 113(42), 11770–11775. https://doi.org/10.1073/pnas.1607171113

Bowman, D.M.J.S., Balch, J.K., Artaxo, P., Bond, W.J., Carlson, J.M., Cochrane, M.A., D'Antonio, C.M., DeFries, R.S., Doyle, J.C., Harrison, S.P., Johnston, F.H., Keeley, J.E., Krawchuk, M.A., Kull, C.A., Marston, J.B., Moritz, M.A., Prentice, I.C., Roos, C.I., Scott, A.C., Swetnam, T.W., van der Werf, G.R., & Pyne, S.J., 2009. Fire in the Earth system. Science, 324(5926), 481–484. https://doi.org/10.1126/science.1163886

Catry, F.X., Rego, F.C., Bação, F., & Moreira, F., 2010. Modeling and mapping wildfire ignition risk in Portugal. International Journal of Wildland Fire, 19(7), 902–917. https://doi.org/10.1071/WF07123

Chuvieco, E., & Salas, J., 1996. Mapping the spatial distribution of forest fire danger using GIS. International Journal of Geographical Information Systems, 10(3), 333–345. https://doi.org/10.1080/02693799608902170

Chuvieco, E., Cocero, D., Riaño, D., Martin, P., Martínez-Vega, J., de la Riva, J., & Pérez, F., 2004. Combining NDVI and surface temperature for the estimation of live fuel moisture content in forest fire danger rating. Remote Sensing of Environment, 92(3), 322–331. https://doi.org/10.1016/j.rse.2004.01.019

Chuvieco, E., Aguado, I., Yebra, M., Nieto, H., Salas, J., Martín, M.P., Vilar, L., Martínez, J., Martín, S., Ibarra, P., de la Riva, J., Baeza, J., Rodríguez, F., Molina, J.R., Herrera, M.A., & Zamora, R., 2010. Development of a framework for fire risk assessment using remote sensing and geographic information system technologies. Ecological Modelling, 221(1), 46–58. https://doi.org/10.1016/j.ecolmodel.2008.11.017

Chuvieco, E., Pettinari, M.L., Lizundia-Loiola, J., Storm, T., & Padilla, M., 2021. Integrated fire danger assessment. International Journal of Applied Earth Observation and Geoinformation, 98, 102299. https://doi.org/10.1016/j.jag.2021.102299

Feizizadeh, B., Blaschke, T., Nazmfar, H., & Rezaei Moghaddam, M.H., 2014. Landslide susceptibility mapping using GIS-based multicriteria decision analysis. Environmental Earth Sciences, 73(11), 6599–6616. https://doi.org/10.1007/s12665-014-3798-8

Hersbach, H., Bell, B., Berrisford, P., Hirahara, S., Horányi, A., Muñoz-Sabater, J., Nicolas, J., Peubey, C., Radu, R., Schepers, D., Simmons, A., Soccorsi, M., Dee, D., & Thépaut, J.N., 2020. The ERA5 global reanalysis. Quarterly Journal of the Royal Meteorological Society, 146(730), 1999–2049. https://doi.org/10.1002/qj.3803

Jaiswal, R.K., Mukherjee, S., Raju, K.D., & Saxena, R., 2002. Forest fire risk zone mapping from satellite imagery and GIS. International Journal of Applied Earth Observation and Geoinformation, 4(1), 1–10. https://doi.org/10.1016/S0303-2434(02)00006-5

Jolly, W.M., Cochrane, M.A., Freeborn, P.H., Holden, Z.A., Brown, T.J., Williamson, G.J., & Bowman, D.M.J.S., 2015. Climate-induced variations in global wildfire danger from 1979 to 2013. Nature Communications, 6, 7537. https://doi.org/10.1038/ncomms8537

Li, J., & Heap, A.D., 2014. Spatial interpolation methods applied in the environmental sciences: A review. Environmental Modelling & Software, 53, 173–189. https://doi.org/10.1016/j.envsoft.2013.12.008

Malczewski, J., 2006. GIS-based multicriteria decision analysis: A survey of the literature. International Journal of Geographical Information Science, 20(7), 703–726. https://doi.org/10.1080/13658810600661508

Moreira, F., Viedma, O., Arianoutsou, M., Curt, T., Koutsias, N., Rigolot, E., Barbati, A., Corona, P., Vaz, P., Xanthopoulos, G., Mouillot, F., & Bilgili, E., 2011. Landscape–wildfire interactions in southern Europe: Implications for landscape management. Journal of Environmental Management, 92(10), 2389–2402. https://doi.org/10.1016/j.jenvman.2011.06.028

Pausas, J.G., & Keeley, J.E., 2009. A burning story: The role of fire in the history of life. BioScience, 59(7), 593–601. https://doi.org/10.1525/bio.2009.59.7.10

Pourghasemi, H.R., Gayen, A., Panagos, P., Rezaie, F., & Blaschke, T., 2016. Multi-model forest fire susceptibility mapping. Remote Sensing, 8(6), 465. https://doi.org/10.3390/rs8060465

San-Miguel-Ayanz, J., Durrant, T., Boca, R., Libertà, G., Branco, A., de Rigo, D., & Ferrari, D., 2021. Forest Fires in Europe, Middle East and North Africa 2020. Publications Office of the European Union. https://data.europa.eu/doi/10.2760/511620

Sharples, J.J., 2009. An overview of mountain meteorological effects relevant to fire behaviour and bushfire risk. International Journal of Wildland Fire, 18(7), 737–754. https://doi.org/10.1071/WF08041

Vilar, L., Woolford, D.G., Martell, D.L., & Martín, M.P., 2010. A model for predicting human-caused wildfire occurrence in the region of Madrid, Spain. International Journal of Wildland Fire, 19(3), 325–337. https://doi.org/10.1071/WF08184

Wulder, M.A., Roy, D.P., Radeloff, V.C., Loveland, T.R., Anderson, M.C., Johnson, D.M., Healey, S.P., Zhu, Z., Scambos, T.A., & others, 2019. Fifty years of Landsat science and impacts. Remote Sensing of Environment, 225, 127–147. https://doi.org/10.1016/j.rse.2019.02.015

HYDROCHEMICAL CHARACTERIZATION AND INTEGRATED WATER QUALITY ASSESSMENT OF TRANSBOUNDARY KARST SPRINGS IN THE ALBANIAN ALPS (ALBANIA–MONTENEGRO)

Arben PAMBUKU [1], Entela VAKO [2], Sherif LUSHAJ [3], Rrapo ORMENI [1], Anita BERBERI [1], Dhori DAPI [4], Stela GUXO [5]& Ergest NAKO [5]*

DOI: 10.21163/GT_2026.213.03

ABSTRACT

This study investigates the hydrochemical characteristics and water quality of transboundary karst springs located in the Albanian Alps along the Albania‑Montenegro border. Eleven representative springs were sampled and analyzed for 26 physical, chemical, and trace-element parameters during two sampling campaigns conducted in November 2024 (high-flow conditions) and June 2025 (dry season period). The investigated springs are associated with carbonate formations of Triassic, Jurassic, and Cretaceous age, forming highly karstified aquifers characterized by high permeability and rapid groundwater circulation. The hydrochemical composition of the springs was evaluated using major ion analysis, hydrochemical diagrams, and two widely applied water quality indices: the Water Quality Index (WQI) and the Heavy Metal Pollution Index (HPI). Spring discharges range from less than 1 l/s to several tens of liters per second, reflecting the heterogeneity of the karst aquifer systems. Results indicate that most springs are dominated by calcium‑bicarbonate hydrochemical facies typical of carbonate aquifers. The calculated WQI values classify the majority of the springs as having excellent to good water quality for drinking purposes, while HPI values indicate minimal heavy metal contamination. The high-water quality observed in the study area is primarily related to the dominance of carbonate aquifers, limited anthropogenic pressure, and the progressive depopulation of rural mountainous areas. However, increasing tourism activity highlights the need for sustainable groundwater management, particularly in a transboundary context. The findings provide valuable baseline data and contribute to improved understanding, monitoring, and joint management of transboundary groundwater resources in the Albanian Alps within the broader Dinaric karst region.

Keywords: *Karst hydrogeology; Transboundary aquifer; Groundwater quality; WQI; HPI; Cemi/Cijevna basin; Monitoring network.*

1. INTRODUCTION

The protection and sustainable management of groundwater resources in karst environments represent a major challenge, particularly in transboundary regions where water systems extend across national borders (Ford & Williams, 2007; White & White, 1989). Albanian Alps, part of the Dinaric karst, one of the most extensive karst systems in Europe, are characterized by highly permeable carbonate formations, complex underground drainage networks and strong interactions between surface and groundwater (DIKTAS Project, 2015; Stevanović et al., 2016).

In this context, the Cem (Cijevna) River basin constitutes a typical transboundary karst system shared between Albania and Montenegro. The basin is dominated by Mesozoic carbonate formations,

[1]*Unit of Geoscience and Geoengineering, Academy of Sciences of Albania, Tirana, *Corresponding author urtesi2001@yahoo.com (AP), rrapo55@yahoo.com (RO), anriberberi@gmail.com (AB)*
[2]*Department of Hydrology, Institute of Geoscience, Polytechnic University of Tirana, Albania, entelavako@gmail.com (EV)*
[3] *POLIS University, Tirana, Albania, sheriflushaj@universitetipolis.edu.al (SL)*
[4]*Ministry of Infrastructure and Energy, Tirana, Albania, doridapi@gmail.com (DD)*
[5]*Freelance expert, Tirana, Albania, ergest.nako@gmail.com (EN), stela.guxo@gmail.com (SG)*

mainly limestones and dolomites, which form highly karstified aquifers with rapid groundwater circulation and high infiltration capacity (Domenico & Schwartz, 1998; Ford & Williams, 2007). These characteristics make the system particularly vulnerable to environmental pressures, but also highly important as a freshwater resource (Chaudhari et al., 2024).

Despite the recognized hydrogeological importance of the basin, previous studies have mainly focused on hydrology, basin management and environmental assessment, while detailed hydrochemical investigations of karst springs remain limited. In particular, there is a lack of comprehensive studies that combine physico-chemical analysis, heavy metal assessment and quantitative evaluation of water quality using integrated indices.

At the same time, the study area has undergone significant socio-economic changes during the last decades. Rural depopulation has led to a substantial decrease in traditional agricultural activities and livestock pressure, which may have contributed to the preservation of groundwater quality. Conversely, the rapid growth of tourism in the Albanian Alps introduces new potential pressures on fragile karst water systems, highlighting the need for systematic monitoring and assessment.

This study aims to evaluate the hydrochemical characteristics and water quality of karst springs located in the transboundary Cem/Cijevna basin along the Albania‑Montenegro border. A total of 11 representative springs were analyzed for 26 physical, chemical and trace element parameters. Water quality was assessed using the Water Quality Index (WQI) and the Heavy Metal Pollution Index (HPI), while hydrochemical processes were interpreted through major ion analysis and hydrogeological context (Shanmugasundharam et al., 2023).

The results of this study provide new insights into the functioning of transboundary karst aquifers and contribute to the scientific basis for sustainable groundwater management in the Dinaric region.

2. STUDY AREA

The study area is located in the northern part of Albania, within the Albanian Alps (Prokletije Mountains), and forms part of the transboundary Cemi/Cijevna River basin shared between Albania and Montenegro. The investigated sector corresponds to the upstream mountainous portion of the basin, where a series of karst springs emerge and represent key groundwater discharge points.

The basin is characterized by rugged mountainous terrain with strong altitudinal contrasts and deeply incised valleys. The hydrographic network is dominated by the Cemi/Cijevna River and its tributaries, which originate in the Albanian territory and flow towards Montenegro, where they join the Morača River system. The geomorphology of the area is closely controlled by tectonic structures and intensive karst processes that have shaped the landscape. From a geological perspective, the study area is dominated by Mesozoic carbonate formations, mainly limestones and dolomites of Triassic, Jurassic and Cretaceous age. These formations are strongly fractured and exhibit a high degree of karstification. As a result, the aquifer system is characterized by very high permeability, allowing rapid infiltration and groundwater circulation through fissures, conduits and karst channels.

Karstification is particularly well developed along river valleys and structural zones, where dissolution processes have created an interconnected network of underground flow paths. In these conditions, infiltration rates are very high and a significant proportion of precipitation contributes directly to groundwater recharge. Surface runoff is therefore limited, while subsurface flow dominates the hydrological regime.

All investigated springs are associated with carbonate aquifers and emerge either directly from exposed limestone formations or from zones with a very thin eluvial cover. Most springs are characterized by direct discharge from karstified limestone, indicating minimal natural protection from surface contamination. Only a limited number of springs show a partial cover of unconsolidated deposits, which may locally influence infiltration processes. The springs are mainly located along valley bottoms, structural contacts and zones where the piezometric surface intersects the topography (**Fig. 1**). Their discharge varies significantly, ranging from very small local springs used by rural communities to larger karst springs with higher and higher discharge. This variability reflects the heterogeneity of the karst aquifer system and the complexity of groundwater flow paths.

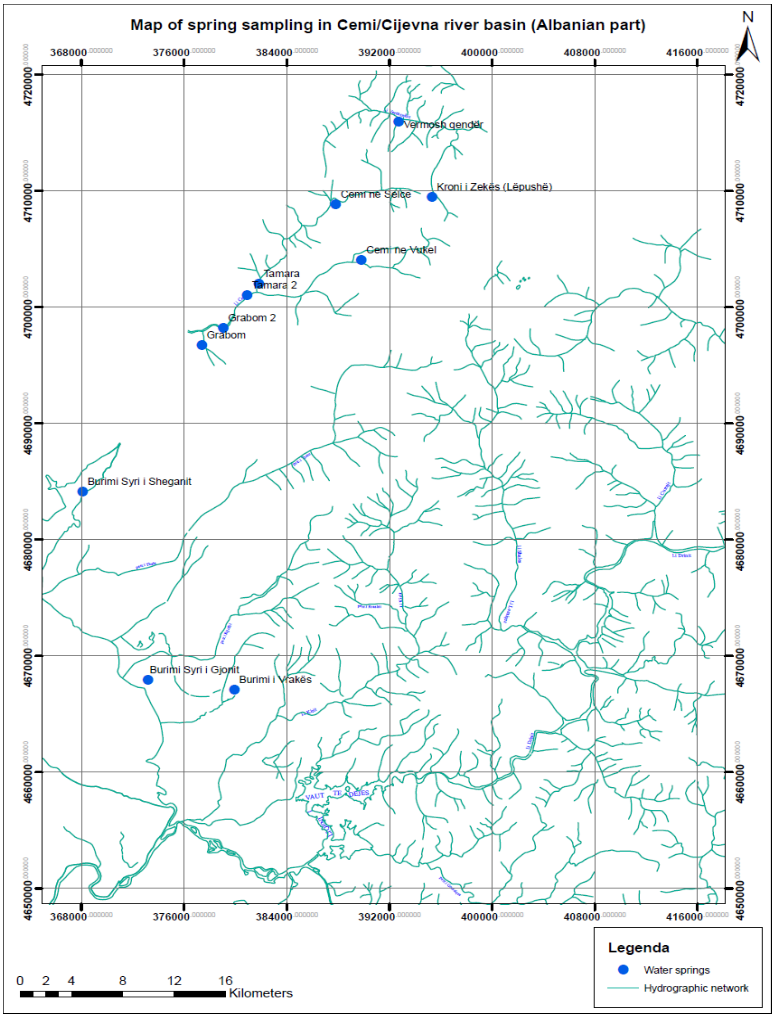

Fig. 1. The map of spring sampling - Cemi/Cijevna river basin catchment.

An important characteristic of the study area is the relatively low level of anthropogenic pressure. During the last 10–15 years, many rural settlements in the Albanian Alps have been partially or completely abandoned, leading to a decrease in agricultural activities and livestock pressure. This has likely contributed to the preservation of groundwater quality. However, in recent years the region has experienced a noticeable increase in tourism, which may introduce new environmental pressures, particularly in sensitive karst environments.

The hydrogeological system of the Cem/Cijevna basin is therefore controlled by the interaction of highly karstified carbonate formations, tectonic structures and climatic conditions. This results in a dynamic groundwater system characterized by rapid recharge, short residence times and strong connectivity between surface and groundwater, which has important implications for both water quality and resource management in this transboundary basin. The hydrogeological behavior of the study area is strongly controlled by karstified carbonate formations, which allow rapid infiltration and complex subsurface flow paths. In such environments, groundwater divides rarely coincide with surface watershed boundaries. In the Cemi/Cijevna basin, the spatial distribution of springs suggests a hydrogeological system extending beyond the topographic catchment. This interpretation is consistent with regional tectonic structures controlling groundwater flow.

Field observations indicate the possibility of localized river water losses, particularly along the Tamarë-Grabom segment. However, this hypothesis remains unconfirmed due to the lack of tracer tests and continuous monitoring data. Given the transboundary nature of the system, such interpretations must be approached with caution.

The proposed monitoring network represents a critical step toward reducing hydrogeological uncertainty. It includes monitoring wells, hydrological stations, and isotopic measurements, enabling a better understanding of groundwater flow dynamics and potential hydraulic connections between Albania and Montenegro. In addition, recent socio-economic changes, including rural depopulation and increasing tourism, may influence future water use and quality, highlighting the need for sustainable management strategies. The spatial distribution of sampling points covers the extended basin, including springs with varying discharge rates and elevations. The geological setting is dominated by kastic limestone and dolomite, which strongly influence groundwater chemistry through dissolution processes.

3. DATA AND METHODS

3.1. Sampling design and timeframe

Groundwater samples were collected during two distinct field campaigns: (i) November 2024, representing high-flow conditions in springs hydraulically connected to high-altitude recharge zones of the Albanian Alps, and (ii) June 2025, representing dry-season conditions. Three springs (Syri i Sheganit, Syri i Gjonit, and Vraka spring) were sampled during the November 2024 campaign, while the remaining springs were sampled in June 2025. These two campaigns capture contrasting hydrological conditions (low-flow vs. dry season), providing a representative snapshot of the hydrochemical variability of the investigated karst systems. Although continuous seasonal monitoring was not conducted, the selected periods allow for a preliminary assessment of hydrochemical stability and variability.

Sampling locations were selected to represent the main transboundary karst systems along the Albania–Montenegro border, taking into account geological structure, discharge variability, and accessibility, while also ensuring that samples reflect natural hydrochemical conditions.

All samples were collected directly at spring outlets, avoiding areas potentially affected by surface contamination such as livestock shelters, tourist paths, or surface runoff accumulation zones. The sampling network includes both high-discharge karst springs and smaller local springs that are directly used by rural communities and livestock. Although some springs exhibit relatively low discharge, they were intentionally included due to their socio-economic importance as local drinking water sources.

3.2. Standard analytical procedures

All samples were analyzed at the ALPHA Studio laboratory following standard analytical procedures. Quality assurance and quality control (QA/QC) measures included calibration using certified reference standards, duplicate analyses, and ionic balance error verification to ensure analytical reliability.

All concentrations were initially expressed in mg/l and subsequently converted into meq/l and meq%. These conversions are presented in the respective **Tables 1-3** and are essential for hydrochemical interpretation. Hydrochemical analysis included:

Major ions: Ca^{2+}, Mg^{2+}, Na^{+}, K^{+}, HCO_3^{-}, SO_4^{2-}, Cl^{-}

Heavy metals: Fe, Mn, Pb, As, Cr (VI), Co.

This approach ensures that the obtained data reflect the intrinsic hydrochemical characteristics of the karst aquifer system rather than localized external impacts.

Table 1.

Physical and general parameters.

Category	Parameter	Unit
Physical parameters	pH	–
	Electrical conductivity (EC)	µS/cm
	Total dissolved solids (TDS)	mg/l
	Dissolved oxygen (DO)	mg/l
	Organic matter	mg/l
Major cations	Calcium (Ca^{2+})	mg/l
	Magnesium (Mg^{2+})	mg/l
	Sodium (Na^{+})	mg/l
	Potassium (K^{+})	mg/l
Major anions	Bicarbonate (HCO_3^{-})	mg/l
	Sulfate (SO_4^{2-})	mg/l
	Chloride (Cl^{-})	mg/l
	Nitrate (NO_3^{-})	mg/l
	Nitrite (NO_2^{-})	mg/l
	Ammonium (NH_4^{+})	mg/l
	Phosphate (PO_4^{3-})	mg/l
	Fluoride (F^{-})	mg/l
Hydrochemical parameters	Total hardness	mg/l as $CaCO_3$
	Total mineralization	mg/l
Trace elements (heavy metals)	Iron (Fe)	µg/l
	Manganese (Mn)	µg/l
	Lead (Pb)	µg/l

Table 2.

Springs and analyses expressed in meq/l.

Sample	Ca meqL	Mg_ meqL	Na+K meqL	HCO3 meqL	SO4 meqL	Cl meqL
1. Grabom	1.99	0.98	0.15	2.86	0.07	0.2
2. Grabom 2	2.39	0.69	0.12	2.45	0.00	0.08
3. Tamara	2.79	0.39	0.14	2.54	0.00	0.06
4. Tamara 2	2.54	0.88	0.12	2.45	0.01	0.15
5. Vermosh Q.	2.29	1.67	0.20	2.70	0.13	0.11
6. Kroni i Zekës	1.59	0.79	0.11	2.45	0.05	0.09
7. Cemi Selcë	1.99	0.49	0.10	1.96	0.00	0.11
8. Cemi Vukël	2.09	0.29	0.09	1.96	0.00	0.08
9. Vrakë	1.99	0.19	0.10	1.76	0.02	0.13
10. Syri i Sheganit	1.99	0.59	0.11	2.13	0.00	0.15
11. Syri i Gjonit	1.79	0.593	0.09	1.83	0.02	0.13

Table 3.

Physico-chemical characteristics.

Sample	Ca mg/l	Mg mg/l	Na mg/l	K mg/l	HCO_3 mg/l	SO4 mg/l	Cl mg/l
1. Grabom	40	12.0	3.51	0.15	175	3.62	7.09
2. Grabom 2	48	8.40	2.66	0.27	150	0.38	2.84
3. Tamara	56	4.80	3.13	0.26	155	0.31	2.13
4. Tamara 2	51	10.80	2.87	0.18	150	0.50	5.67
5. Vermosh Q.	46	20.40	4.06	0.93	165	6.31	3.97
6. Kroni i Zekës	32	9.60	2.49	0.18	150	2.50	3.54
7. Cemi Selcë	40	6.00	2.47	0.05	120	0.44	4.25
8. Cemi Vukël	42	3.60	2.14	0.04	120	0.37	2.84
9. Vrakë	40	2.40	2.15	0.38	108	1.30	4.96
10. Syri i Sheganit	40	7.20	2.34	0.52	130	0.20	5.67
11. Syri i Gjonit	36	7.20	1.95	0.42	112	1.20	4.96

4. RESULTS

4.1. The physico-chemical characteristics

The physico-chemical characteristics of the investigated springs show a consistent hydrochemical behavior typical of groundwater circulating within carbonate karst systems.

The measured pH values range between 7.3 and 7.5, indicating neutral to slightly alkaline conditions. This reflects a well-buffered hydrochemical system controlled by carbonate equilibria, particularly the interaction between dissolved carbon dioxide and carbonate minerals. Such conditions are characteristic of groundwater circulating in limestone and dolomite formations (**Fig. 2a**).

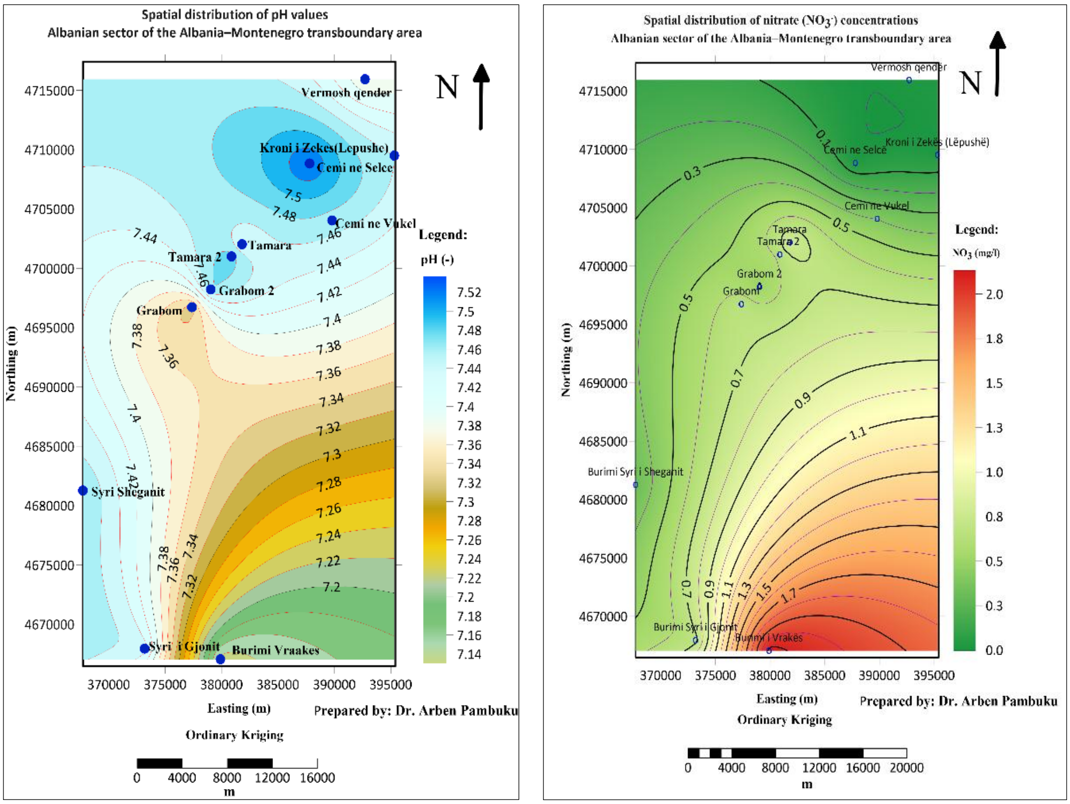

a b

Fig. 2. Spatial distribution of:

(a) groundwater pH values in the Albanian Alps (Albania–Montenegro transboundary area), interpolated using the Ordinary Kriging method based on point measurements from groundwater sources (WGS 1984 / UTM Zone 34N), indicating predominantly neutral to slightly alkaline conditions controlled by lithological and hydrogeological settings;

(b) nitrate (NO_3^-) concentrations in groundwater across the same area and projection, derived from measured values using the same interpolation approach, showing generally low levels and suggesting limited anthropogenic impact and good groundwater quality.

Electrical conductivity values generally range from approximately 250 to 300 µS/cm, while total dissolved solids (TDS) vary between about 120 and 200 mg/l. These relatively low values indicate limited mineralization and confirm that the investigated waters belong to fresh groundwater systems. The low mineralization is consistent with rapid groundwater circulation and limited residence time within the aquifer. Dissolved oxygen concentrations are relatively high, typically between 9 and 10 mg/l, suggesting active recharge conditions and rapid infiltration processes. This is a typical feature of karst systems, were water infiltrates quickly through fractures and conduits, maintaining high oxygen levels.

Nutrient concentrations (NO_3^-, NO_2^-, NH_4^+ and PO_4^{3-}) are generally very low across all sampling points (**Tab. 1-3**). This indicates the absence of significant anthropogenic contamination sources such as agriculture or wastewater infiltration, and reflects the relatively preserved environmental conditions of the study area. The concentration of NO^3-N (**Fig. 2b**), commonly derived from agricultural runoff and human activities, serves as a significant indicator of nutrient pollution, which can result in eutrophication (Dewata et al., 2025).

4.2. The hydrochemical diagrams and interpretation

The hydrochemical characterization of groundwater was performed using three complementary diagrams: the Piper diagram (**Fig. 3**) as the primary classification tool, the Schoeller diagram (**Fig. 4**) for comparative analysis of major ions, and the Chadha diagram (**Fig. 5**) for validation of hydrochemical facies.

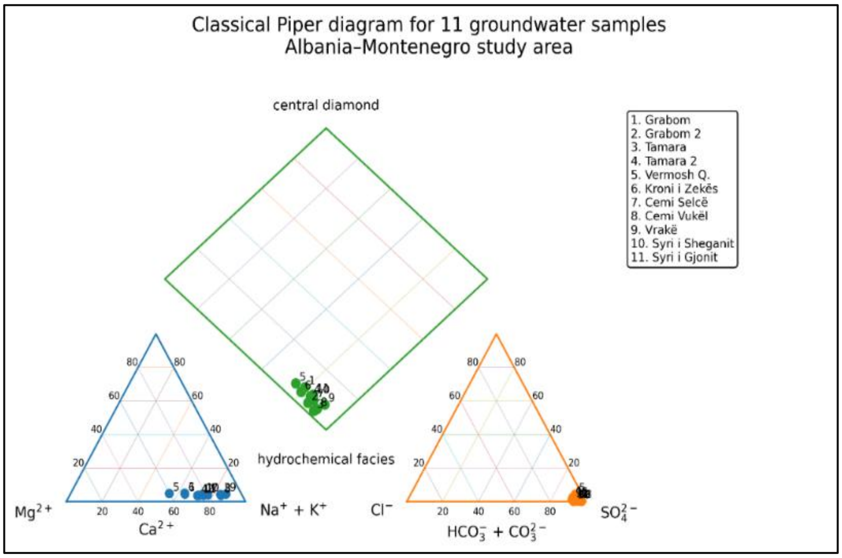

Fig. 3. Hydrochemical characterization based on the Piper diagram.

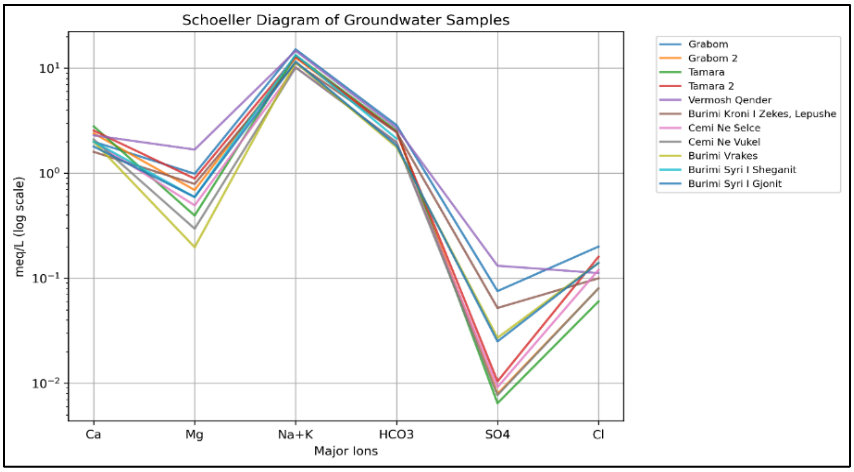

Fig. 4. Hydrochemical characterization based on the Schoeller Diagram.

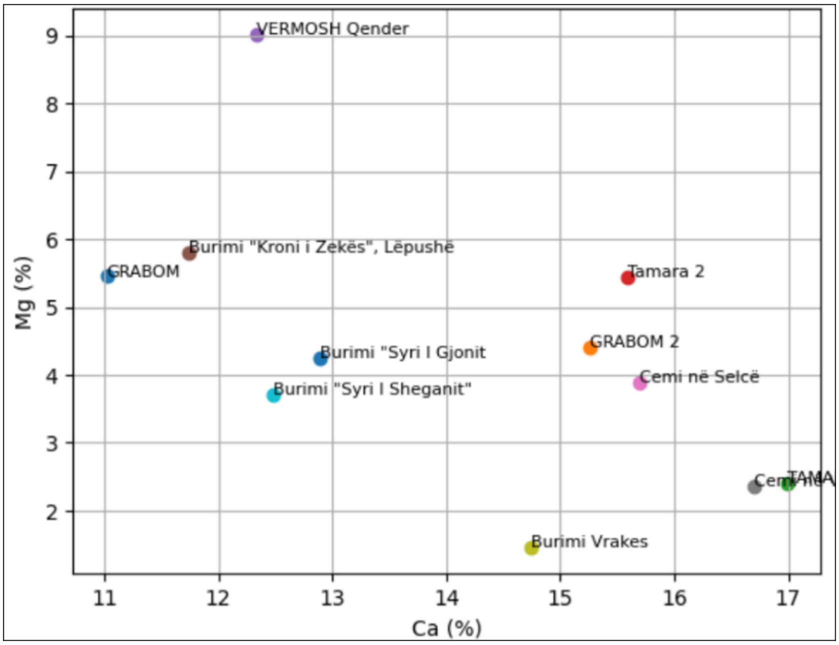

Fig. 5. Chadha diagram – validation.

These diagrams are complementary and together provide a robust interpretation of hydrochemical processes. The hydrochemical signature observed in the Piper diagram is consistent with the geological context of the Albania‑Montenegro border region, which is largely dominated by carbonate formations. Similar hydrochemical patterns have been reported in recent studies of karst aquifers, where carbonate dissolution dominates groundwater chemistry (Gu et al., 2021), (Zhang et al., 2023).

The prevalence of Ca^{2+}, Mg^{2+}, and HCO_3^- ions indicates intensive water–rock interaction, dissolution of calcite ($CaCO_3$) and dolomite ($CaMg(CO_3)_2$) (Appelo & Postma, 2004; Drever, 1997). This hydrochemical signature is typical for groundwater circulating in carbonate aquifers and reflects equilibrium processes between CO_2, water and carbonate minerals (Hem, 1985; Plummer et al., 1978). This suggests that groundwater circulation occurs mainly through karstic and carbonate aquifers, with relatively short to moderate residence times. The Piper diagram (**Fig. 3**) is widely used as a standard tool for hydrochemical classification of groundwater ("A Graphic Procedure in the Geochemical Interpretation of Water-analyses," 1944) and confirms that all samples fall within the Ca–HCO_3 facies.

To further interpret the hydrochemical characteristics of the groundwater system, Scholler and Chadha diagrams were employed to classify the water types and identify dominant geochemical processes. The hydrochemical characteristics of the investigated groundwater samples were evaluated using a combined Schoeller semi-logarithmic diagram, which allows a comparative visualization of major ion concentrations expressed in milliequivalents per liter (meq/l). The Schoeller diagram provides a comparative representation of major ion concentrations and is particularly useful for identifying similarities and differences between groundwater samples (Schoeller, 1965).

The dominance of bicarbonate ions over sulfate and chloride confirms that groundwater chemistry is mainly controlled by carbonate dissolution processes rather than evaporation or anthropogenic inputs (Appelo & Postma, 2004; Gibbs, 1970).

In particular, the concentrations of $Na^+ + K^+$ exhibit the highest values among the cations, followed by Ca^{2+} and Mg^{2+}. This distribution indicates a significant contribution from both carbonate rock dissolution and possible silicate weathering processes.

Among the anions, bicarbonate (HCO_3^-) clearly dominates over sulfate (SO_4^{2-}) and chloride (Cl^-), confirming that the groundwater is primarily controlled by carbonate equilibrium reactions. The relatively low concentrations of sulfate suggest a negligible influence of evaporitic formations such as gypsum or anhydrite, while the moderate chloride levels indicate limited anthropogenic impact and minimal influence from saline intrusion or wastewater sources.

The overall hydrochemical facies of the groundwater can therefore be classified predominantly as Ca‑Na‑HCO_3 type, with a tendency towards Na‑HCO_3 facies in some samples. This variability reflects differences in residence time, water‑rock interaction intensity, and local geological heterogeneity within the study area.

Furthermore, the relatively narrow spread of the Schoeller curves (**Fig. 4**) suggests a certain degree of hydrochemical homogeneity among the samples, although subtle variations in magnesium and chloride concentrations indicate localized geochemical processes. These differences may be attributed to variations in lithology, permeability, and recharge conditions across the investigated zones.

The absence of significant sulfate and chloride enrichment, combined with the dominance of bicarbonate ions, indicates that the groundwater is largely of natural origin and has not been substantially affected by anthropogenic contamination. This is consistent with the hydrogeological setting of the area, which is characterized by carbonate formations and active recharge conditions.

Overall, the Schoeller diagram proves to be an effective tool for identifying the hydrochemical signature of the groundwater system and supports the interpretation of a predominantly carbonate-controlled aquifer with minor contributions from other geochemical processes.

The Chadha diagram (**Fig. 5**), derived from the differences between major cations and anions, provides a simplified yet powerful classification of hydrochemical facies.

All samples plot in the upper-right quadrant, which corresponds to waters dominated by:

alkali metals ($Na^+ + K^+$) over alkaline earths ($Ca^{2+} + Mg^{2+}$)

weak acids (HCO_3^-) over strong acids ($Cl^- + SO_4^{2-}$)

This confirms that the groundwater belongs predominantly to the Na‑HCO_3 type, reflecting advanced stages of geochemical evolution.

4.3. Relationship between discharge and water chemistry

The analyzed springs exhibit a wide range of discharge values, reflecting the heterogeneity of the karst aquifer system. Larger springs tend to show more stable physico-chemical characteristics, while smaller springs display slightly higher variability. These characteristics confirm that the investigated springs represent high-quality karst groundwater systems with minimal anthropogenic impact, controlled primarily by natural geological processes.

A general trend can be observed in which springs with higher discharge tend to exhibit lower mineralization, as indicated by lower TDS and EC values. This behavior is typical for karst systems, where high-discharge springs are often associated with rapid groundwater circulation and shorter residence times. In contrast, smaller springs may be influenced by localized hydrogeological conditions, leading to slightly higher variability in chemical composition (**Tab. 4**).

The measured pH values range between 7.3 and 7.5, indicating neutral to slightly alkaline conditions. This reflects a well-buffered hydrochemical system controlled by carbonate equilibria, particularly the interaction between dissolved carbon dioxide and carbonate minerals. Such conditions are characteristic of groundwater circulating in limestone and dolomite formations.

Electrical conductivity values generally range from approximately 250 to 300 µS/cm, while total dissolved solids (TDS) vary between about 120 and 200 mg/l. These relatively low values indicate limited mineralization and confirm that the investigated waters belong to fresh groundwater systems. The low mineralization is consistent with rapid groundwater circulation and limited residence time within the aquifer.

Dissolved oxygen concentrations are relatively high, typically between 9 and 10 mg/l, suggesting active recharge conditions and rapid infiltration processes. This is a typical feature of karst systems, where water infiltrates quickly through fractures and conduits, maintaining high oxygen levels.

Nutrient concentrations (NO_3^-, NO_2^-, NH_4^+ and PO_4^{3-}) are generally very low across all sampling points. This indicates the absence of significant anthropogenic contamination sources such as agriculture or wastewater infiltration, and reflects the relatively preserved environmental conditions of the study area.

Table 4.

Summary of physico-chemical parameters of the investigated springs and interpretation.

Parameter	Min	Max	Average (approx.)	Interpretation
pH	7.3	7.5	~7.4	Neutral–slightly alkaline
EC (µS/cm)	250	300	~275	Low mineralization
TDS (mg/l)	120	200	~160	Fresh groundwater
DO (mg/l)	9.0	10.0	~9.5	Well oxygenated
NO_3^- (mg/l)	very low	very low	–	No agricultural impact
PO_4^{3-} (mg/l)	very low	very low	–	Minimal contamination

Major ions and hydrochemical facies. The chemical composition of the analyzed springs is dominated by calcium (Ca^{2+}) among cations and bicarbonate (HCO_3^-) among anions. Magnesium (Mg^{2+}) is present in secondary concentrations, while sodium (Na^+) and potassium (K^+) are found in relatively low amounts.

Among anions, bicarbonate clearly dominates, whereas sulfate (SO_4^{2-}) and chloride (Cl^-) occur in significantly lower concentrations. This ionic composition reflects the dissolution of carbonate rocks as the main geochemical process controlling groundwater chemistry (**Tab. 5**).

Table 5.

Generalized major ion composition, their importance and geology influence.

Ion group	Dominant ions	Relative importance	Hydrogeochemical significance
Cations	Ca^{2+}	High	Carbonate dissolution
	Mg^{2+}	Moderate	Dolomite contribution
	Na^+, K^+	Low	Minor influence
Anions	HCO_3^-	Very high	Carbonate equilibrium
	SO_4^{2-}	Low	Limited sulfate sources
	Cl^-	Low	Minimal external inputs

Based on the relative distribution of major ions, all investigated springs can be classified within the Ca–HCO_3 hydrochemical facies, which is typical of groundwater circulating in carbonate aquifers. This hydrochemical signature indicates that the dominant geochemical processes are related to carbonate weathering, particularly the dissolution of calcite and dolomite under the influence of carbon dioxide-rich water

*Heavy metals***.** The concentrations of trace elements (Fe, Mn, Pb, Cr VI, Co and As) are generally very low in all analyzed samples. Most measured values are below or close to detection limits and remain well within international drinking water standards (**Tab. 6**). Low concentrations of trace elements are commonly associated with natural geogenic background levels in carbonate aquifers (Adimalla et al., 2022).

Iron (Fe) and manganese (Mn) are present in low concentrations, consistent with natural geogenic background levels in carbonate environments. Toxic elements such as lead (Pb), arsenic (As) and chromium (Cr VI) show very low concentrations, indicating the absence of significant contamination sources.

This distribution suggests that groundwater quality is not affected by industrial, agricultural or urban pollution, and that the hydrochemical composition is primarily controlled by natural geological processes.

Table 6.

Summary of heavy metal concentrations.

Metal	Observed level	Standard comparison	Interpretation
Fe	very low	below limits	Natural background
Mn	very low	below limits	Geogenic origin
Pb	very low	below limits	No contamination
As	very low	below limits	No contamination
Cr (VI)	very low	below limits	No contamination
Co	very low	below limits	Minimal presence

The analyzed springs exhibit a wide range of discharge values, reflecting the heterogeneity of the karst aquifer system. Larger springs tend to show more stable physico-chemical characteristics, while smaller springs display slightly higher variability.

A general trend can be observed in which springs with higher discharge tend to exhibit lower mineralization, as indicated by lower TDS and EC values. This behavior is typical for karst systems, where high-discharge springs are often associated with rapid groundwater circulation and shorter residence times. In contrast, smaller springs may be influenced by localized hydrogeological conditions, leading to slightly higher variability in chemical composition.

4.4. Water quality indices

The Water Quality Index (WQI) is widely applied as an integrated tool for assessing the suitability of groundwater for drinking purposes, as it combines multiple physico-chemical parameters into a single representative value(Shanmugasundharam et al., 2023; Vasanthavigar et al., 2010). This approach facilitates a comprehensive evaluation of water quality and allows for easier comparison across different sampling locations. The classification of water quality in this study follows internationally recognized standards, particularly those established by the European Commission (2020), ensuring consistency and reliability in the interpretation of results. (European Commission, 2020).

4.4.1. Overall Water Quality (WQI)

The WQI approach applied in this study is widely used in recent hydrogeochemical research for integrated groundwater quality assessment (Li et al., 2013; Shanmugasundharam et al., 2023).

The Water Quality Index (WQI) was applied to evaluate the overall suitability of the investigated spring waters for drinking purposes (**Tab. 7-8**). The index integrates multiple physico-chemical parameters into a single value, allowing a comprehensive assessment of water quality.

Based on the calculated WQI values, all investigated springs fall within the categories of excellent to good water quality, indicating that the water is generally suitable for human consumption without significant treatment. The low WQI values are mainly controlled by: low TDS concentrations, stable pH conditions, very low nutrient content and absence of significant contamination

The WQI was calculated using the weighted arithmetic index method:

$$WQI = \frac{\sum(W_i \times Q_i)}{\sum W_i} \quad (1)$$

where:

W_i is the weight assigned to each parameter

Q_i is the quality rating of each parameter

The quality rating Qi was calculated as:

$$Q_i = \frac{(C_i - C_{ideal})}{(S_i - C_{ideal})} \times 100 \quad (2)$$

where:

C_i is the measured concentration
S_i is the standard permissible value
C_{ideal} is the ideal value (usually 0, except for pH and DO)

The classification of water quality based on WQI values is as follows:

Table 7.
The classification of water quality based on WQI values

WQI	Water quality
< 50	Excellent
50–100	Good
100–200	Poor
200–300	Very poor
> 300	Unsuitable for drinking

Table 8.
WQI classification of the investigated springs.

Spring	WQI (approx.)	Class	Water quality
Grabom	25–35	< 50	Excellent
Grabom 2	30–40	< 50	Excellent
Tamara	35–45	< 50	Excellent
Tamara 2	40–50	50 (limit)	Excellent–Good
Vermosh center	30–40	< 50	Excellent
Kroni i Zekës	35–45	< 50	Excellent
Cemi – Selcë	40–55	50–100	Good
Cemi – Vukël	35–50	< 50	Excellent
Syri i Sheganit	25–35	< 50	Excellent
Burimi i Vrakës	30–45	< 50	Excellent
Syri i Gjonit	30–45	< 50	Excellent

The low WQI values are mainly controlled by: low TDS concentrations, stable pH conditions, very low nutrient content and absence of significant contamination. The predominance of excellent WQI values reflects minimal anthropogenic pressure, efficient natural filtration processes, rapid groundwater circulation typical of karst systems. The slightly higher values observed in some springs may be related to local hydrogeological variability and minor influence of surface conditions.

4.4.2. Heavy Metal Pollution (HPI)

The Heavy Metal Pollution Index (HPI) was used to assess the overall impact of trace elements on water quality. The HPI was calculated using the expression:

$$HPI = \frac{\sum(W_i \times Q_i)}{\sum W_i} \quad (3)$$

where:
W_i is the unit weight of each metal
Q_i is the sub-index of each metal

$$Q_i = \frac{(M_i - I_i)}{(S_i - I_i)} \times 100 \quad (4)$$

where:
M_i is the measured concentration
S_i is the standard permissible value
I_i is the ideal value (usually 0)

Interpreted HPI classification is shown at the **Table 9**.

Table 9.
HPI values for the investigated springs.

Spring	HPI (approx.)	Category	Interpretation
Grabom	10–20	< 50	Low contamination
Grabom 2	15–25	< 50	Low contamination
Tamara	20–30	< 50	Low contamination
Tamara 2	20–35	< 50	Low contamination
Vermosh center	10–25	< 50	Low contamination
Kroni i Zekës	15–30	< 50	Low contamination
Cemi – Selcë	25–40	< 50	Low contamination
Cemi – Vukël	20–35	< 50	Low contamination
Syri i Sheganit	10–20	< 50	Low contamination
Burimi i Vrakës	15–25	< 50	Low contamination
Syri i Gjonit	15–25	< 50	Low contamination

Table 10.
The HPI classification.

HPI	Interpretation
< 50	Low contamination
50–100	Moderate contamination
> 100	High contamination

The Heavy Metal Pollution Index (HPI) (**Tab. 9-10**) was calculated to evaluate the potential impact of trace elements on water quality. The obtained HPI values are consistently low across all sampling points, remaining well below the critical threshold of 100 (**Fig. 6a and 6b**).

The very low concentrations of heavy metals indicate the absence of significant anthropogenic contamination and reflect natural geogenic background levels (Edmunds & Smedley, 2000; Papazotos, 2021) also: absence of heavy metal pollution, dominance of natural geochemical background levels and lack of industrial or urban contamination sources. This is particularly important given the vulnerability of karst systems, which are typically highly sensitive to contamination due to rapid infiltration and limited natural filtration. The hydrochemical composition of the investigated springs is predominantly characterized by calcium‑bicarbonate facies. Spring discharge values vary significantly, reflecting the heterogeneity of the karst system and differences in recharge conditions.

The analyzed physico-chemical parameters indicate generally stable hydrochemical conditions across the sampled springs, with no significant anomalies observed in major ion composition or trace elements. The relatively low mineralization values (TDS generally below 200 mg/l) indicate short groundwater residence times and rapid circulation within the karst system. This is consistent with the highly fractured and karstified nature of the Mesozoic carbonate formations, which allow fast infiltration and limited water‑rock interaction time. The observed hydrochemical composition reflects typical karst geochemical processes, including carbonate weathering and minor contributions from silicate dissolution (Drever, 1997; Stumm, 1967).

The relatively low mineralization indicates short residence times and rapid groundwater circulation, which are characteristic features of karst aquifers (Freeze & Cherry, 1979; Zhang et al., 2023). The dominance of bicarbonate ions, combined with low sulfate and chloride concentrations, suggests that the hydrochemical evolution of groundwater is primarily controlled by natural geochemical processes rather than external inputs such as evaporation, anthropogenic contamination or interaction with evaporitic formations. Furthermore, the relatively uniform hydrochemical composition across all sampling points indicates a high degree of hydrogeological connectivity within the karst aquifer system. This suggests that groundwater flow paths are well developed and interconnected, allowing mixing and homogenization of water chemistry.

The Piper diagram (**Fig. 3**) shows that all samples fall within: $Ca\text{-}HCO_3$, $Ca\text{-}Mg\text{-}HCO_3$ facies.

The Schoeller diagram (**Fig. 4**) confirms: consistent ion distribution and dominance of Ca and HCO_3. The Chadha diagram (**Fig. 5**) provides further validation of the same classification.

Heavy metal concentrations (**Table 7**) are very low and within drinking water standards, indicating no significant anthropogenic impact.

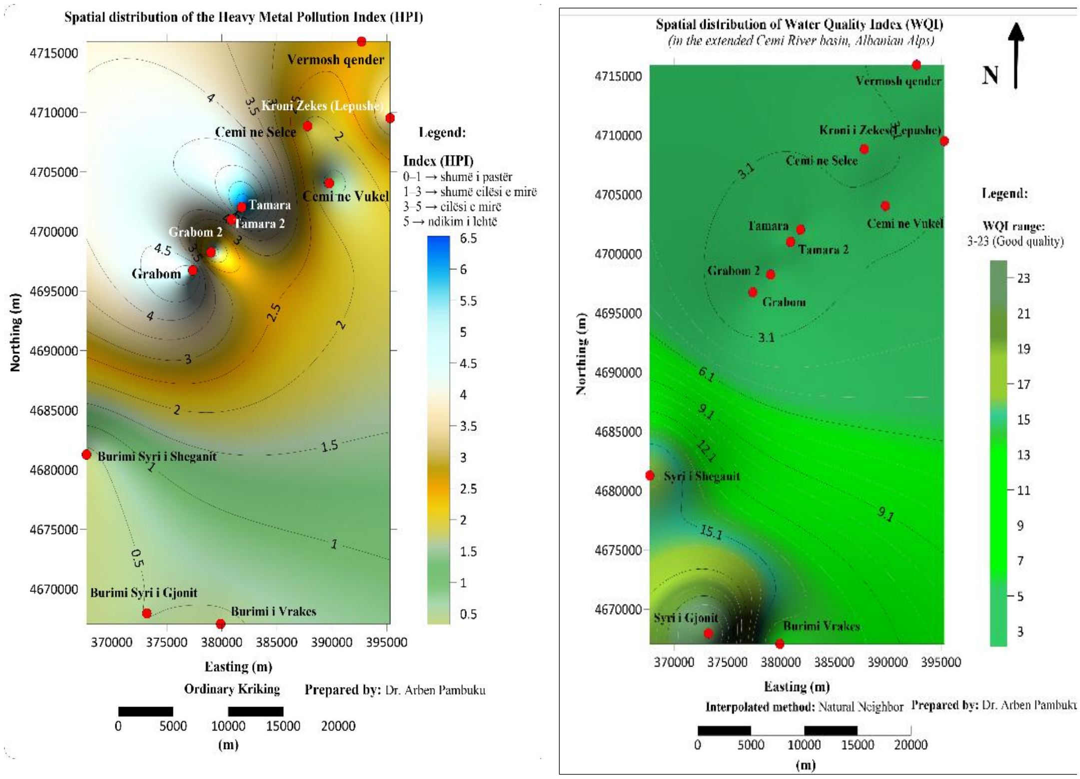

a b

Fig. 6. Spatial distribution of:

a) the Heavy Metal Pollution Index (HPI) in groundwater of the study area, derived using the Ordinary Kriging interpolation method. The index integrates the concentrations of Fe, Mn, Cr(VI), Pb, and Co to assess the overall impact of heavy metals on water quality. Lower values (0–1) indicate excellent quality, moderate values (1–3) reflect good to acceptable conditions, while higher values (>3) suggest increasing levels of contamination. The spatial pattern reveals localized zones of elevated HPI influenced by geological and hydrogeochemical factors, with generally low to moderate contamination across the study area.

b) the Water Quality Index (WQI) in the Cem River basin, Albanian Alps. The index was computed based on selected physicochemical parameters and standard guideline values. Spatial interpolation was carried out using Natural Neighbor, highlighting variations in groundwater quality, from good (green) to poor (red) conditions

5. DISCUSSION

This study provides the first integrated assessment of groundwater quality and quantity in the Albanian Alps, establishing a baseline for future hydrogeological investigations in this Albanian transboundary karst region. The findings contribute to a broader understanding of groundwater systems shared between Albania and Montenegro, where scientific data have historically been limited.

The dominance of Ca‑HCO_3 hydrochemical facies reflects the strong influence of carbonate lithology (limestone and dolomite) and confirms that groundwater chemistry is primarily controlled by carbonate dissolution processes. This is characteristic of highly karstified aquifers with rapid groundwater circulation and limited water‑rock interaction time.

Similar hydrochemical patterns have been widely reported in karst systems of the Dinaric Alps and other Mediterranean regions, where carbonate aquifers dominate and groundwater chemistry is largely governed by natural geogenic processes. This consistency supports the reliability of the obtained results and confirms that the investigated springs behave as typical karst groundwater systems.

The generally low concentrations of heavy metals and stable physicochemical parameters indicate minimal anthropogenic impact in the study area. This can be attributed to low population density, absence of industrial activities, and relatively preserved natural conditions. However, increasing tourism activity may represent a potential future risk, particularly through diffuse pollution and inadequate wastewater management.

From a transboundary perspective, the investigated karst aquifers represent interconnected groundwater systems that extend across national boundaries. Due to the high permeability and conduit-dominated flow in karst environments, groundwater flow paths are not constrained by political borders. This highlights the necessity for coordinated monitoring strategies and joint management approaches between Albania and Montenegro.

A limitation of the present study is the absence of continuous temporal monitoring, which restricts a comprehensive assessment of seasonal variability. However, the inclusion of two contrasting hydrological periods (high-flow and dry season) provides a useful initial insight into hydrochemical conditions. To address this limitation, a comprehensive and modern monitoring system has been proposed for the extended Cemi/Cijevna River basin, including multi-season sampling and tracer-based investigations aimed at improving the understanding of groundwater flow dynamics and transboundary connectivity.

The use of multiple graphical methods is justified by their complementary roles: the Piper diagram is primarily used for hydrochemical classification, the Schoeller diagram allows detailed comparison of ionic concentrations, and the Chadha diagram serves as a validation tool. The strong agreement between these diagrams significantly increases the reliability and robustness of the hydrochemical interpretation. Although small deviations are observed in some samples, these likely reflect minor local processes such as ion exchange or silicate weathering. However, these processes do not significantly alter the overall hydrochemical facies, which remains consistently dominated by carbonate dissolution mechanisms. The relatively low total dissolved solids (TDS < 200 mg/l), combined with high dissolved oxygen concentrations, indicate short groundwater residence times and rapid circulation within a highly karstified system. These characteristics reflect an active recharge regime and strong hydraulic connectivity, typical of karst aquifers.

Water quality assessment based on the Water Quality Index (WQI) demonstrates that most samples fall within the excellent to good categories. This confirms that groundwater is suitable for drinking purposes with minimal treatment. In parallel, the Heavy Metal Pollution Index (HPI) values indicate very low levels of heavy metal contamination, confirming the absence of significant anthropogenic pollution sources.

The spatial distribution of hydrochemical parameters (**Fig. 2**) supports the interpretation of a hydraulically connected system with relatively homogeneous hydrochemical behavior. This spatial coherence suggests that groundwater flow paths are well integrated within the karst system. Similar findings have been reported in recent studies, which indicate that groundwater quality in karst environments is primarily controlled by lithology, residence time, and recharge conditions (Adimalla et al., 2022; Li et al., 2013).

The transboundary monitoring network presented in **Fig. 7** (Cem/Cijevna River basin) further highlights the importance of integrated hydrogeological assessment. The map includes existing and proposed monitoring stations in both Albania and Montenegro, such as groundwater wells, hydrological stations, sampling points, and isotopic pluviometers. This network is designed to support the evaluation of surface water–groundwater interactions and to improve understanding of the karst aquifer system within the DIKTAS II framework (DIKTAS Project, 2015).

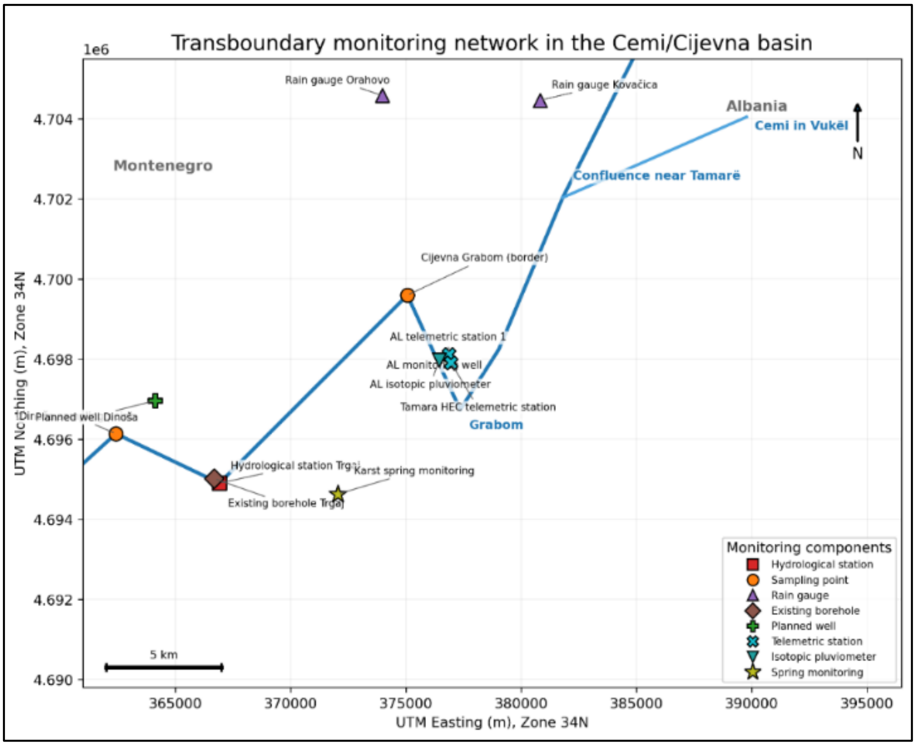

Fig. 7. Transboundary monitoring network in the Cemi/Cijevna River basins.

Despite the currently high groundwater quality, karst systems are inherently vulnerable. Rapid infiltration processes, thin soil cover, and limited natural filtration capacity make them particularly sensitive to contamination. Therefore, continuous monitoring is essential. An effective monitoring network should include all major springs, strategic locations along river systems, and seasonal sampling campaigns to capture temporal variability.

The observed limited anthropogenic impact is closely related to reduced agricultural activity and rural depopulation. However, increasing tourism development represents an emerging environmental pressure that may pose risks to groundwater quality in the future.

Overall, the results demonstrate that groundwater in the Cem/Cijevna basin is dominated by Ca‑HCO_3 facies, controlled by carbonate dissolution processes, characterized by low mineralization, and exhibits excellent water quality with minimal pollution influence. The strong agreement between analytical data, hydrochemical diagrams, and quality indices confirms the robustness of the results and highlights the importance of this aquifer as a high-quality water resource that requires careful protection and sustainable management.

6. CONCLUSIONS

The present study provides a comprehensive hydrochemical characterization and water quality assessment of transboundary karst springs in the Albanian Alps. The results demonstrate that groundwater is predominantly characterized by Ca‑ HCO_3 facies, controlled by carbonate dissolution processes within highly karstified aquifers.

The applied water quality indices (WQI and HPI) indicate that groundwater quality is generally excellent to good and suitable for drinking purposes, with minimal evidence of heavy metal contamination. These findings reflect limited anthropogenic pressure and relatively preserved natural conditions in the study area.

The hydrochemical consistency observed across the investigated springs suggests strong hydraulic connectivity and well-developed karst flow systems. However, the intrinsic vulnerability of karst aquifers, combined with increasing tourism activity, highlights the need for careful management and protection of groundwater resources.

From a transboundary perspective, the results emphasize the importance of coordinated monitoring and joint management strategies between Albania and Montenegro. The proposed monitoring framework for the Cemi/Cijevna basin provides a basis for future research and supports the sustainable management of shared groundwater resources.

Overall, this study contributes valuable baseline data for a relatively understudied karst region and supports the development of integrated approaches for transboundary groundwater assessment and protection.

ACKNOWLEDGEMENTS

The authors gratefully acknowledge the financial support provided by the National Agency for Scientific Research and Innovation (NASRI) through the project entitled “Quantitative and qualitative assessment of natural water resources in the transboundary areas of Albania with Montenegro, Kosovo, and North Macedonia.” Additional support from the Academy of Sciences of Albania is also sincerely appreciated.

The authors further express their gratitude to all project team members for their valuable contributions and collaboration. Special thanks are extended to the ALPHA Studio laboratory for the high quality of the analytical work, as well as for their professionalism, reliability, and continuous support throughout the study.

REFERENCES

A graphic procedure in the geochemical interpretation of water-analyses. (1944). *Eos, Transactions American Geophysical Union*, *25*(6), 914–928. https://doi.org/10.1029/TR025i006p00914

Adimalla, N., Manne, R., Zhang, Y., Xu, P., & Qian, H. (2022). Evaluation of groundwater quality and its suitability for drinking purposes in semi-arid region of Southern India: An application of GIS. *Geocarto International*, *37*(25), 10843–10854. https://doi.org/10.1080/10106049.2022.2040603

Appelo, C. A. J., & Postma, D. (2004). *Geochemistry, Groundwater and Pollution* (C. A. J. Appelo & D. Postma, Eds.; 0 ed.). CRC Press. https://doi.org/10.1201/9781439833544

Chaudhari, M. P., George, A., Sanyal, M., & Shrivastav, P. S. (2024). Hydrochemistry and groundwater quality assessment of Gujarat, India: A compendious review. *Physics and Chemistry of the Earth, Parts A/B/C*, *135*, 103635. https://doi.org/10.1016/j.pce.2024.103635

Dewata, I., Barlian, E., Syah, N., Umar, I., Heldi, Yuniarti, E., Putra, A., Yulius, Ramdhan, M., Candra, O., Sari, S. M., Suciandica, M., Yuzandi, I., & Fachrin, R. D. (2025). INTEGRATION OF WATER QUALITY ASSESSMENT AND WASTE MANAGEMENT SYSTEMS: A STRATEGIC APPROACH TOWARDS A SUSTAINABLE GREEN CAMPUS IN THE UI GREENMETRIC FRAMEWORK. *Geographia Technica*, *20*(1/2025), 143–160. https://doi.org/10.21163/GT_2025.201.11

DIKTAS Project. (2015). *Dinaric Karst Aquifer System Atlas*. https://iwlearn.net/documents/2824?utm_source

Domenico, P. A., & Schwartz, F. W. (1998). *Physical and chemical hydrogeology* (2nd ed). Wiley.

Drever, J. I. (1997). *The geochemistry of natural waters: Surfaces and groundwater environments* (3. ed). Prentice Hall.

Edmunds, W. M., & Smedley, P. L. (2000). Residence time indicators in groundwater: The East Midlands Triassic sandstone aquifer. *Applied Geochemistry*, *15*(6), 737–752. https://doi.org/10.1016/S0883-2927(99)00079-7

European Commission. (2020). *Directive (EU) 2020/2184 of the European Parliament and of the Council of 16 December 2020 on the quality of water intended for human consumption (recast). Official Journal of the European Union, L435, 1–62.* https://eur-lex.europa.eu/legal-content/EN/TXT/?uri=CELEX:32020L2184

Ford, D. C., & Williams, P. (2007). *Karst hydrogeology and geomorphology*. John Wiley & sons.

Freeze, R. A., & Cherry, J. A. (1979). *Groundwater*. Prentice-Hall.

Gibbs, R. J. (1970). Mechanisms Controlling World Water Chemistry. *Science*, *170*(3962), 1088–1090. https://doi.org/10.1126/science.170.3962.1088

Gu, Z., Zhang, Y., & Fan, H. (2021). Mapping inter- and intra-annual dynamics in water surface area of the Tonle Sap Lake with Landsat time-series and water level data. *Journal of Hydrology*, *601*, 126644. https://doi.org/10.1016/j.jhydrol.2021.126644

Hem, J. D. (1985). *Study and interpretation of the chemical characteristics of natural water* (3rd ed). U.S. Geological Survey.

Li, P., Wu, J., & Qian, H. (2013). Assessment of groundwater quality for irrigation purposes and identification of hydrogeochemical evolution mechanisms in Pengyang County, China. *Environmental Earth Sciences*, *69*(7), 2211–2225. https://doi.org/10.1007/s12665-012-2049-5

Papazotos, P. (2021). Potentially toxic elements in groundwater: A hotspot research topic in environmental science and pollution research. *Environmental Science and Pollution Research*, *28*(35), 47825–47837. https://doi.org/10.1007/s11356-021-15533-7

Plummer, L. N., Wigley, T. M. L., & Parkhurst, D. L. (1978). The kinetics of calcite dissolution in CO 2 -water systems at 5 degrees to 60 degrees C and 0.0 to 1.0 atm CO 2. *American Journal of Science*, *278*(2), 179–216. https://doi.org/10.2475/ajs.278.2.179

Schoeller, H. (1965). *Methods and techniques of groundwater investigation and development*. UNESCO.

Shanmugasundharam, A., Akhina, S. N., Adhithya, R. P., Singh, D. S. H., & Krishnakumar, S. (2023). Water quality index (WQI), multivariate statistical and GIS for assessment of surface water quality of Karamana river estuary, west coast of India. *Total Environment Research Themes*, *6*, 100031. https://doi.org/10.1016/j.totert.2023.100031

Stevanović, Z., Krešić, N., & Kukuricwith, N. (Eds.). (2016). *Karst without boundaries* (First Edition). CRC Press/Balkema. International conference Karst without Boundaries.

Stumm, W. (Ed.). (1967). *Equilibrium Concepts in Natural Water Systems* (Vol. 67). AMERICAN CHEMICAL SOCIETY. https://doi.org/10.1021/ba-1967-0067

Vasanthavigar, M., Srinivasamoorthy, K., Vijayaragavan, K., Rajiv Ganthi, R., Chidambaram, S., Anandhan, P., Manivannan, R., & Vasudevan, S. (2010). Application of water quality index for groundwater quality assessment: Thirumanimuttar sub-basin, Tamilnadu, India. *Environmental Monitoring and Assessment*, *171*(1–4), 595–609. https://doi.org/10.1007/s10661-009-1302-1

White, W. B., & White, E. L. (Eds.). (1989). *Karst hydrology: Concepts from the Mammoth Cave area*. Springer Science+Business Media, LLC.

Zhang, T., Wang, P., He, J., Liu, D., Wang, M., Wang, M., & Xia, S. (2023). Hydrochemical Characteristics, Water Quality, and Evolution of Groundwater in Northeast China. *Water*, *15*(14), 2669. https://doi.org/10.3390/w15142669

Geographia Technica, Vol. 21, Issue 3, 2026, pp 51 to 69

COMPARATIVE ASSESSMENT OF WATER QUALITY AND TROPHIC LEVEL INDICES IN SUMBERKIMA COASTAL WATERS, BULELENG, PROVINCE OF BALI, INDONESIA

Iis TRIYULIANTI [1*], Eghbert Elvan AMPOU [2], Dessy BERLIANTY [3], Yoke Hany RESTIANGSIH [3] & Vivi Eka INDRAYANI [4]

DOI: 10.21163/GT_2026.213.04

ABSTRACT

The assessment of water quality in this study utilized the Water Quality Index (WQI) and Trophic State Indexes (TSI and TRIX) values as crucial components of information required for managing aquatic resources. The primary aim of this study was to compare the evaluation of water quality in the coastal waters of Sumberkima, Buleleng, Province of Bali, using the performance of WQI, TSI, and TRIX values. The WQI, TSI, and TRIX values were derived from measurements of dissolved oxygen (DO), nutrient levels, and chlorophyll-a (ChA), pH, temperature, salinity, and turbidity. Water samples were collected from the surface waters at 37 physical stations and 18 chemical and biological stations. The WQI ranged from 80.00 to 96.60 with mean value was 89.44 ± 3.66 revealed the water quality was good to excellent. The TSI and TRIX values for assessing trophic level in marine coastal waters of Sumberkima ranged from 12.76 – 65.13 with mean value was 30.73 ± 13.96 (TSI) and (4.41 ± 0.69) for TRIX values across all monitoring stations. The comparative indices of trophic level revealed that the coastal waters of Sumberkima were categorized as oligotrophic, mesotrophic, and eutrophic according to TSI values, while TRIX had four (4) classes of trophic level. Furthermore, TRIX values showed a stronger correlation with WQI (R^2= 0.3418) than TSI (R^2 = 0.006). The findings of this study suggest that the TRIX value possesses a more comprehensive and strong trophic classification to characterize water quality. This study addresses a critical research gap in the identification of trophic levels by integrating physical, chemical, and biological assessments of water quality parameters.

Keywords: *Water quality index (WQI); Trophic state index (TSI); Trophic index (TRIX); Sumberkima coastal waters; Spatial analysis.*

1. INTRODUCTION

The coastal waters of Sumberkima Village are an area in the northern waters of Bali Province, which has a unique landscape and supports diverse marine life that expands from west to east and has been utilized by the community for various fishery activities, catch and farming, and ecotourism (Ampou et al., 2023; Irawan et al., 2023; Nurjayanti et al., 2023). According to Rodrigues-Filho et al. (2023), coastal waters are dynamic ecosystems that play an essential role in maintaining biodiversity, creating resources, and driving economic activity. However, these ecosystems are increasingly threatened by human activities, including pollution from land-based sources, agricultural runoff, and industrial discharge, all of which may dramatically affect water quality and ecological balance (Sahavacharin et al., 2022).

[1*]*Research Center for Deep Sea, National Research and Innovation Agency (BRIN), Jakarta, Indonesia; Corresponding author iist001@brin.go.id (IT)*
[2]*Reseach Center for Biota Systems, National Research and Innovation Agency (BRIN), Bogor-West Java, Indonesia; eghb001@brin.go.id (EEA)*
[3]*Research Center for Oceanology, National Research and Innovation Agency (BRIN), Jakarta, Indonesia; dess011@brin.go.id (DB); yoke002@brin.go.id (YHR)*
[4]*Lombok Marine Aquaculture Center, Ministry of Marine and Fisheries of the Republic of Indonesia, Lombok, Indonesia; vivi.indrayani@kkp.go.id (VEI).*

Human stressors in coastal areas lead to a decline in water quality and biodiversity, the destruction of essential ecosystems, and a general deterioration in the residents' quality of life (Herrera-Silveira & Morales-Ojeda, 2009).

The water quality information is required because the effectiveness of marine aquaculture is strongly linked to the quality of the water used at the aquaculture site (Boyd et al., 2017). The increased use of marine space and coastal areas has provided ecological pressure that will decrease the health of the aquatic environment (Chen & Chen, 2007; Drira et al., 2017; Neumann et al., 2017). The increasing environmental degradation caused by development highlights the critical need for initial ecological assessments to determine baseline conditions, facilitating sustainable development (Reyers & Selig, 2020). The changes in water quality conditions resulting from space utilization include physical, chemical, and nutritional factors, which may adversely affect the development of cultured organisms or lead to mortality, eventually resulting in diminished output (Reid et al., 2019). The preservation of water quality and the evaluation of trophic status are critical for ensuring the sustainability of these valuable resources and the livelihoods that depend upon them (Triyulianti et al., 2021).

Evaluations are used to determine suitable management strategies and evaluate their effectiveness over time. An index that provides a simple screening tool to categorize different water bodies based on their trophic condition would be valuable. Evaluations are crucial for assessing the health of aquatic ecosystems and informing suitable conservation strategies, including disaster mitigation in urban settings (Gandaseca, 2011; Yusuf et al., 2025). Nevertheless, more comprehensive studies into water quality are required in coastal areas, where the levels of contaminants (ecological pressure) are frequently higher than those of the open sea.

A simple index could be derived from frequently measured metrics or effectively identify water bodies that are likely to be problematic or non-problematic in terms of eutrophication (O'Boyle et al., 2013). Consequently, water quality indices and risk evaluation can be used to analyze water quality in Sumberkima, a coastal area in northern Bali, and detect possible human and ecological health risks. Water quality indices offer a useful method for assessing the overall water quality by integrating various parameters into a single value. Water quality evaluations are useful in identifying and evaluating the possible hazards that pollutants pose to human and ecological health (Shaaban, 2022; Zotou et al., 2018).

The water quality index (WQI) is the most useful technique for analyzing and controlling water quality information (Radfard et al., 2019; Yousefi et al., 2019). The WQI is widely used to evaluate water quality due to its effortless form compared to physical-processed or hydrological models (Benaissa et al., 2022, 2023; Yan et al., 2022). The WQI is an effective method for evaluating the overall water quality by integrating various parameters into a single score. The scores describe the results of the risk assessments to assist in the identification and evaluation of potential risks that waste products may pose to human and ecosystem health (Shaaban, 2022; Zotou et al., 2018). Therefore, analyzing and evaluating the coastal water quality in Sumberkima coastal waters is important for managing the marine environment and enhancing water quality. Trophic State Index (TSI) and Trophic Index (TRIX) were determined with a comprehensive method that integrates ChA, DO saturation, nitrogen, and phosphorus to provide a holistic assessment of marine water productivity and marine health (Peng, 2015; Triyulianti et al., 2021).

Dissolved oxygen is a basic component of aquatic organisms, and its existence regulates several biological and chemical processes. Oxygen dissolved in the water column is a product of biological processes that directly affect aquatic life, especially aerobic respiration, growth, and reproduction (Diaz & Breitburg, 2009). In addition, nutrients in the form of inorganic nitrogen and phosphorus compounds act as vital nutrients for marine flora and fauna. Nitrogen and phosphorus enrichment is the principal eutrophication catalyst in numerous coastal habitats (Howarth & Marino, 2006).

This research represents an essential to environmental monitoring, aimed at collecting primary data that could be used to develop scientific knowledge. The main objectives of this study are (1) to evaluate the characteristics of hydro-oceanographic and water quality conditions of coastal waters in Sumberkima, Buleleng, Bali Province, Indonesia and (2) to identify and evaluate the WQI and the

Trophic State level in coastal waters of Sumberkima Village, Buleleng, Bali using TSI and TRIX indices. The water quality indicates the water enrichment level, which subsequently increases the water productivity. These indices have an efficient approach to assessing the overall water quality by integrating many parameters into a single score. The findings of this research are intended to inform the selection of marine biogeochemistry and physical oceanography parameters specifically designed to determine the productivity of tropical marine ecosystems.

2. STUDY AREA

The research was conducted on the coastal waters of Sumberkima Village, which is located at 8°S latitude and 114°E longitude (**Fig. 1**). The research location is Sumberkima Coastal Waters, Gerokgak Subdistrict, Buleleng Regency, Bali Province. The coastal waters of Sumberkima form a bay that is quite sheltered by Gili Putih sand dunes, specifically at the east site. Data collection was undertaken in April 2021.

The water quality parameters were measured at 37 stations scattered from west to east (**Fig. 1**). The station grouping is based on the coastal waters used. The selected station points are representatives of the existing land use activities in coastal waters, such as intensive marine aquaculture (fish enlargement activities in floating net cages) with its surrounding landscape as well as the all along seaside hatchery farms in the west site (St. 1, 2, 3, 4, 5, 7, 8, 9, 10, 11, 13, 15, 20, 21, 22, 31, 34, 35, 36, 37), attractive destinations of coastal tourism (coral reefs, seagrass and mangroves) and Pegametan Bay in the east site (St. 6, 12,14, 16, 17, 18, 19, 23, 24, 25, 26, 27, 28, 29, 30, 32, 33) as mentioned in corresponding table. The sampling locations represent spatial differences in the ecological characteristics of study site and documented a limited number of water quality parameters. The water quality measurement at 37 stations used the Water Quality Checker (WQC) for in situ measurement at the surface layer consisting of sea surface temperature (SST), sea surface salinity (SSS), surface current (SC), turbidity, and pH.

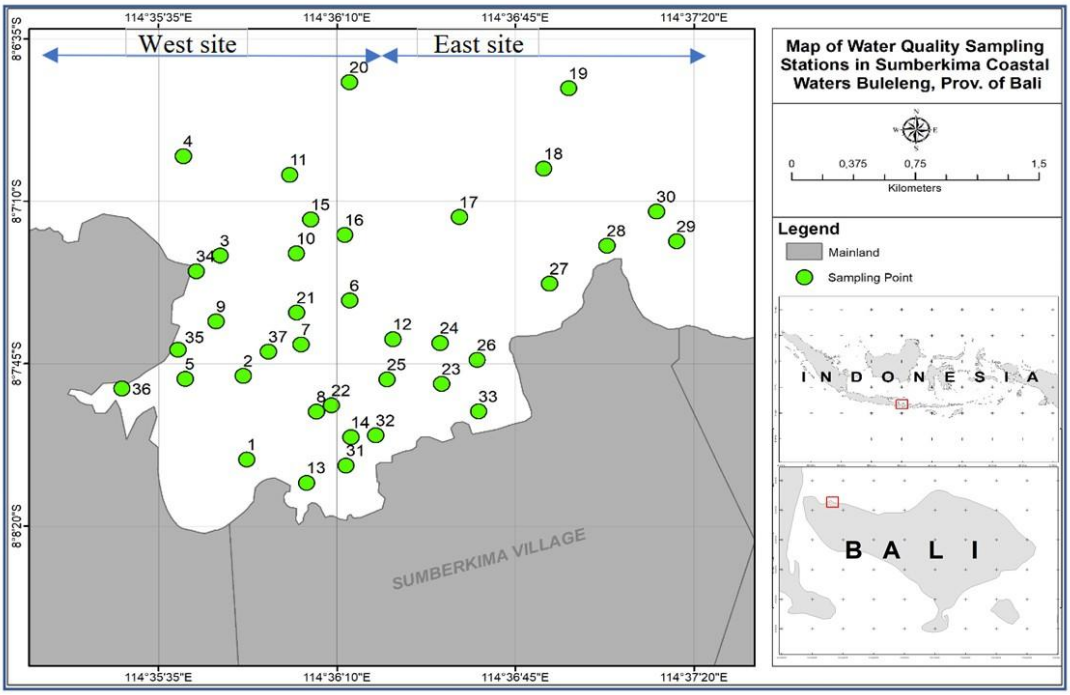

Fig. 1. Research stations (green dots with number) in the Sumberkima Coastal Waters, Indonesia.

3. DATA AND METHODS

3.1. Sampling method and water quality parameters

Water samples were taken using a Van Dorn water sampler to measure the concentration of Dissolved Oxygen (DO), Nutrients (Nitrate, Nitrite, Ammonia, Phosphate) and Chlorophyll-a (ChA) at 18 stations. The selected stations represented the west site (St. 1, 2, 3, 4, 5, 7, 8, 9, 10, 11 and 15) and the east site (St. 6, 12, 14, 16, 17, and 18). The water sample was placed in a bottle and transferred to the Laboratory of Water Quality in the Institute for Marine Research and Observation (IMRO) in Perancak, Bali Province.

Water samples were collected from the surface layer at the depth of between 0 – 25 m. The analytical detection limit (DL) of total phosphorus (TP), was around 0.001 mg/L. For statistical and trophic index estimates, concentrations below the detection limit were written as <DL and thought of as half of the detection limit.

3.2. Comparative index of water quality and trophic level

The Water Quality Index (WQI) is a widely used index for the comprehensive assessment of marine ecosystems. It has emerged as a widely utilized instrument for assessing water quality owing to its straightforward structure, which is in contrast to physical-processed or hydrological models. This index has been applied to evaluate surface water quality conditions. In this study, the WQI was measured using data derived from three water quality parameters: turbidity, TP, and DO. The WQI was calculated using the normalized values of three or more variables as follows (Pesce & Wunderlin, 2000):

$$WQI = \frac{(C_{v1} + C_{v2} + C_{v3} \ldots C_{vn})}{n} \tag{1}$$

where C_v is the normalized value relative to a given water quality critical variable in the detailed system and is the number of variables involved in the calculation.

The WQI represents a mathematical integration of normalized water quality measurements through arithmetic weighting. The normalizations and weightings vary according to the specific water usages (Pesce & Wunderlin, 2000; Xu et al., 2024). **Table 1** shows the normalizing factors for the WQI index calculation for this research. The quality classification was based on the ranges of WQI values and their respective conditions could be found in **Table 2**, where WQI ≤ 25 is very bad, 26 ≤ 50 is bad, 51 ≤ WQI ≤ 70 is regular, 71 ≤ WQI ≤ 90 is good, and 91 ≤ WQI ≤ 100 is rated as excellent (Pesce & Wunderlin, 2000; Xu et al., 2024).

Table 1.

Normalizing factors for the WQI calculation (Pesce & Wunderlin, 2000).

	100	**90**	**80**	**70**	**60**	**50**	**40**	**30**	**20**	**10**	**0**
DO (µg/L)	≥ 7.5	≥7.0	≥6.5	≥6.0	≥5.0	≥4.0	≥3.5	≥2.0	≥	≥1.0	<1.0
TP (µg/L)	<0.05	<0.05	<0.05	<0.1	<0.1	<0.15	<0.15	<0.2	<0.2	<0.3	<0.3
Turb. (NTU)	<5	<10	<15	<20	<25	<30	<40	<60	<80	≤100	>100

Table 2.
Classification of Trophic State Index (TSI) (Klippel et al., 2020), Trophic Index (TRIX), and Water Quality Index (Pesce & Wunderlin, 2000; Vollenweider et al., 1998).

TSI	TRIX	WQI	Condition
Low (Oligotrophic) <30 30-40	≤ 4 Oligotrophic	Bad (≤ 50)	Scarsely productive coastal waters Good water transparency – Absence of anomalous water colors – Absence of oxygen under saturation in the bottom waters
Moderate (Mesotrophic) 40–50	4 < 5 Mesotrophyc	Regular (51 - 70)	Moderately productive waters – Occasionally water turbidity – Occasionally anomalous water colors – Occasionally bottom waters hypoxia episodes
High (Eutrophic) 50–60 60–70	5 < TRIX < 6 Mesotrophic to Eutrophic	Good (71 - 90)	Very productive waters (High productivity) – Low water transparency – Frequently anomalous waters colors – Hypoxia and occasionally anoxia episodes in the bottom layers – Suffering of the benthic communities
Very high (hypertrophic) 70–80 > 80	6 < TRIX < 10 Eutrophic	Excellent (91 - 100)	Strongly productive waters – High water turbidity – Diffuse and persistent anomaly in the water colors – Diffuse and persistent hypoxia/anoxia episodes in the bottom waters – High mortality rate of benthic organisms – Alteration of the benthic communities and strong decrease of the biodiversity

The data obtained through measurements of water quality parameters can be used to evaluate trophic status. The trophic status of bodies of water is an essential metric of aquatic ecosystem health, revealing the degree of nutrient enrichment and primary production, significantly affecting the composition and dynamics of aquatic ecosystems (Vollenweider et al., 1998). The TRIX method has been widely used to assess the eutrophic state of marine bodies (Smith et al., 1999; Stramma et al., 2008). TRIX has been developed to determine the trophic status of coastal waters through the measurement of aquatic chemistry (Pavluk & bij de Vaate, 2017).

The TRIX index is defined as a linear combination of logarithms values of 4 parameters related to eutrophication: ChA concentration in μg/L, concentration of nitrate, nitrite, ammonia (DIN), and total phosphorus (TP) in μg/L, and percent oxygen saturation deviation (aD%O) (Seisdedo et al., 2014). The results of 4 parameters measurements for applying the TRIX index (DIN, TP, aD%O, and ChA) in the study location provided an overview of the conditions of the surface water trophic level. The trophic status is determined using the TRIX index with the following formula:

$$TRIX = \frac{\log_{10}(ChA \times |\Delta DO| \times DIN \times TP) + k}{m} \quad (2)$$

$$\Delta DO = \left|\frac{DO_{observation} - DO_{saturation}}{DO_{saturation}}\right| = aD\%\text{O} \quad (3)$$

where, ChA is the concentration of chlorophyll-a (μg/L), aD %O is the concentration of oxygen as the absolute percentage deviation of oxygen saturation (100%), DIN is Dissolved Inorganic Nitrogen (μg/L) and TP is Total Phosphorus (μg/L). The coefficients k and m are 1.5 and 1.2, respectively.

TRIX index values have a scale of 0-10 that can be categorized into 4 categories or 4 levels (**Table 2**). The higher the TRIX index value (maximum 10) is, the higher the eutrophication rate of its waters (high water productivity). The TRIX index value shows the category tropic level (Pavluk & bij de Vaate, 2017), with the category assessment range in **Table 2**. Eutrophication triggers the occurrence of anoxia (Seisdedo et al., 2014). The higher the intensity or density of anthropogenic activities allows the region to experience an excessive increase in trophic status (Saygu et al., 2023).

The Trophic State Index (TSI) evaluates ecosystem health by evaluating current biological productivity levels (Klippel et al., 2020) (**Table 2**). The TSI values were determined based on the interconnected variables TP ($TSI_{(TP)}$), DIN ($TSI_{(DIN)}$), and total chlorophyll-a ($TSI_{(ChA)}$). The equation applied to compute TSI is as follows:

$$TSI_{(ChA)} = 9.81 * \ln_{(ChA)} \quad + \ 30.6 \left(\frac{\mu g}{l}\right) \tag{4}$$

$$TSI_{(TP)} = 14.42 * \ln_{(TP)} \quad + \ 4.15 \left(\frac{\mu g}{l}\right) \tag{5}$$

$$TSI_{(DIN)} = 54.4 * 14.43 * \ln_{(DIN)} \left(\frac{\mu g}{l}\right) \tag{6}$$

$$Average\,TSI \ = \ \overline{TSI_{(ChA)} + TSI_{(TP)} + TSI_{(DIN)}} \tag{7}$$

3.3. Data analysis

The water quality parameter measurements were evaluated spatially and presented in a horizontal description. Statistical analyses were performed to assess relationship between WQI, TSI, and TRIX. Pearson correlation coefficients were computed between WQI and TSI; WQI and TRIX. Data are presented as mean ± standard error of the mean (SE).

4. RESULTS

4.1.Water quality parameters

The measurable surface temperature (SST) distribution at the research site in April 2021 showed an average SST value (28.79 ± 0.26 °C) in the range of 28–29.4 °C (**Fig. 2a** and **Table 3**) with the distribution values of SST at the west site stations were 28.53 – 28.50 ºC and 28 – 29.20 ºC on the east site station. The distribution of these values characterizes the surface water temperatures of coastal waters in Indonesia in accordance with environmental quality standards. The average SST at the east site of our research area is warmer than that at the west site (**Table 3**). The research locations with the highest average SST values were close to the mainland (**Fig. 2a**).

The spatial distribution of Sea Surface Salinity (SSS) values was 31.2 – 31.9 and 31.72 ± 0.19 PSU (**Table 3**) as an average value of SSS (**Fig. 2b**), the distribution values at the west site stations were 31.50 – 31.90 PSU and 31.20 – 31.90 PSU at the east site. A marginal rise in salinity was observed in the nearshore waters in the eastern stations (St. 17, St. 18, St. 28, and St. 27), in contrast to the more oceanic waters at the northwest endpoint of each transect and the southern transects, as opposed to the eastern transects.

The SSS values of the southern transects or stations (St. 1, St. 13, St. 31, St. 14, St. 32, and St. 33) increased with distance from the coastline (**Fig. 2b**). Measurements of SST and SSS on the western and eastern sides show maximum average values that are inversely related between the two parameters. The strongest Surface Current (SC) values in April 2021 varied from 0 to 0.5 m s-1 (**Table 3**). The mean SC values at the west site were higher than those at the east site, indicating that the SC is an environmental variable that influences the productivity levels in coastal marine ecosystems. The spatial distribution of the DIN measurement results (**Fig. 3a**) in the form of nitrates (NO_3), nitrites (NO_2), and ammonia (NH_4) provides a description of the nutrient content or concentration at the research site in April 2021.

Table 3.

Statistic summary of water quality parameters collected from surface waters (0 – 25 m) in Sumberkima coastal waters, Buleleng, Bali (for N/P the values were mumtiplied by 10).

West Site Stations	SST (°C)	SSS (PSU)	SC (m/s)	*DO (µg/L)	*DIN (µg/L)	*TP (µg/L)	aD%O (%)	*ChA (µg/L)	N/P .10	pH	Turb. (NTU)
Mean	28.80	31.76	0.2	6263	35	1.2	97.72	0.15	6.7	7.95	0.82
Median	28.80	31.80	0.2	6123	32	0.5	90.71	0.11	6.6	7.96	0.01
SD	0.12	0.11	0.13	230	9	2.3	2.81	0.12	2.7	0.20	2.5
Min	28.53	31.50	0.1	5754	22	0.0005	85.32	0.05	2.8	7.55	0.01
Max	28.90	31.90	0.5	6942	55	799	95.36	0.34	11	8.24	0.30
East Site Stations	**SST (°C)**	**SSS (PSU)**	**SC (m/s)**	***DO (µg/L)**	***DIN (µg/L)**	***TP (µg/L)**	**aD%O (%)**	***ChA (µg/L)**	**N/P**	**pH**	**Turb. (NTU)**
Mean	29.01	31.15	0.12	6538	71	0.5	97.72	0.33	2.7	7.76	0.01
Median	28.97	31.77	0.1	6519	51	0.5	97.75	0.27	94	7.78	0.01
SD	0.40	0.28	0.08	480	53	0.5	6.80	0.24	13	0.21	0.00
Min	28.00	31.20	0.01	5995	38	0.5	88.98	0.07	5.9	7.51	0.01
Max	29.20	31.90	0.2	7163	176	0.5	106.31	0.78	35	7.99	0.01

** the values of DO, DIN, TP and ChA were multiplied .10^3*

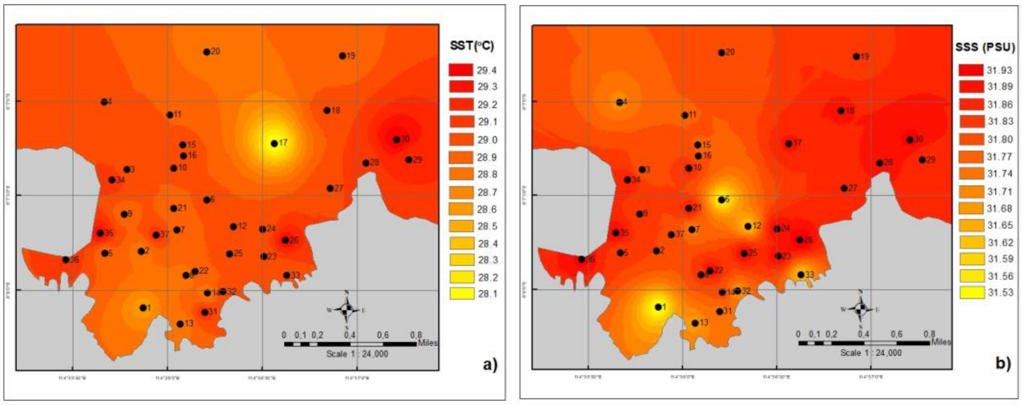

Fig. 2. Spatial distribution of (a) sea surface temperature (SST) and (b) sea surface salinity (SSS).

The spatial distribution of DIN values of the coastal waters of Sumberkima ranges from 22.2 to 176 µg/L, as depicted in **Fig. 3a**. with the average of DIN value was 38.3 ± 11.9 µg/L. The highest DIN concentration was found at St. 17, located in the middle area of the study, and the lowest concentration was found in St. 1. The measurement stations identified as having DIN concentration values below the mean value (38.3 ± 11.9 µg/L) are close to the mainland. The spatially distributed pattern of DIN concentrations revealed an increase in values from stations near the shore to those in the open sea.

The range of TP concentration values obtained in the west site stations was 0.5 – 8 µg/L, with an average value was 1.2 ± 2.3 µg/L (**Table 3**) and the distribution values illustrated in **Fig.3b**. The research location exhibited a restricted phosphate concentration (**Fig. 3b**). The TP measurement results at the study site indicated limited phosphate presence, almost under detection limit (1 µg/L).

According to the information provided in **Table 3** and **Fig. 3b**, the N/P ratio is the comparison of DIN with TP values, indicating that the availability of nutrients for algal growth was higher than 16. This finding indicates that the coastal waters of Sumberkima exhibited a phosphorus-limited state during this season (**Fig. 3b**) considering the N/P ratios. In this study, the phosphate concentrations in the coastal waters of Sumberkima are often very close to the analytical detection limit.

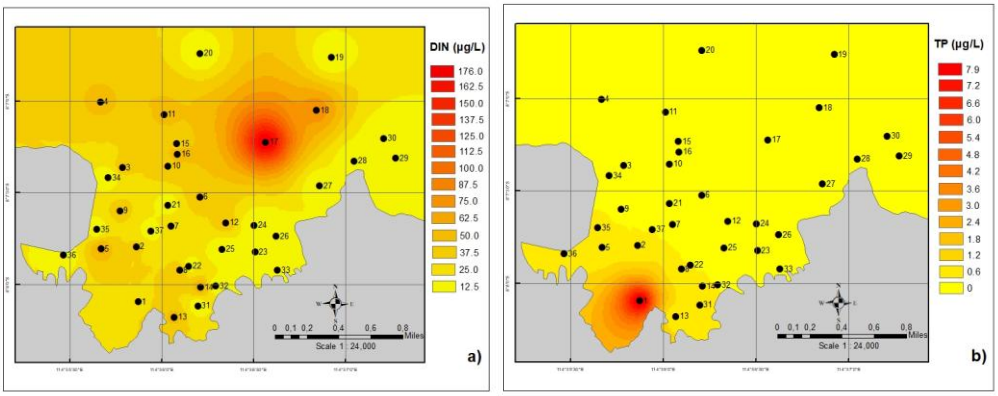

Fig. 3. Spatial distribution of (a) dissolved inorganic nitrogen (DIN) and (b) total phosphate (TP).

The measurable dissolved oxygen concentration (DO) at the study site (**Fig. 4a**) was above the standard quality threshold of ≥ 5000 µg/L (**Table 3**). The DO range at the research area was 5754 – 7163 µg/L, with the average value of DO for all station was 6243 ± 366 µg/L (**Table 3** and **Fig. 3a**), where the mean values were higher at the east site (6537 ± 480 µg/L) than at the west site (6263 ± 299 µg/L. Measurement and spatial analysis results of DO and ChA in the Sumberkima coastal waters are shown in **Figs. 4a** and **4b**, respectively. The ChA concentrations ranged from 182 to 135 µg/L, with the highest values found in the seagrass area (East site), with measurements at station St. 17 (789 µg/L) and St. 18 (450 µg/L). Station 17 had the highest concentrations of DIN, DO, and ChA, as illustrated in **Fig. 3a** (DIN), **Fig. 4a** (DO), and **Fig. 4b** (ChA).

The pH values ranged from 7.51 to 8.24, with an average of 7.95 ± 0.20 in the west site and 7.76 ± 0.21 in the east site. The stations recorded pH values above 8.0 (St. 14, 31, 13, 18, 22, 6, 7, 2, 21, 37, 5, 36, 35, 9, 34, 3, 4, 11, 20, 15, 16, and 10). The pH values were found ≥ 8 located on study area that was close to the main island (**Table 4**). The turbidity is another measurement with a range of values of 0.0-8.30 NTU with an average was 0.74 ± 2.45 NTU. The results from sampling stations at the east site were lower than those recorded at the west site (**Table 4**).

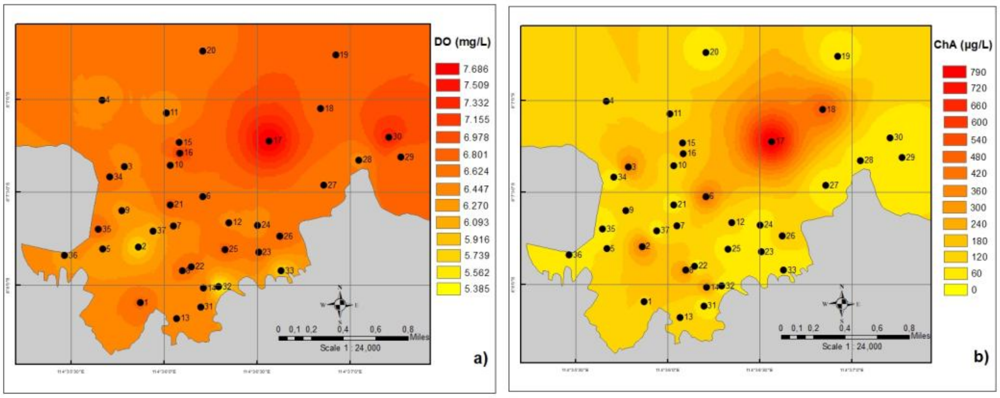

Fig. 4. Spatial Distribution of Dissolved Oxygen (DO) (a) and Chlorophyll-a (ChA).

4.2.Water quality indexes

4.2.1. Water quality index (WQI)

The WQI values in the coastal waters of Sumberkima, Buleleng, Bali Province, have a mean value of 87.88 ± 3.08 in the west station and 91 ± 3.25 (**Table 4** and **Fig. 5**), with values ranging from 80 to 97. The WQI values distribution indicated that the coastal waters quality of Sumberkima could be classified were in Good and Excellent. The water quality of Sumberkima coastal waters indicates that the condition of waters was varied in two classes (Good to Excellent) (**Table 4** and **Fig. 5**).

The comparison of the two groups of study area performed at the West site has the average value was 87.88 ± 3.08 lower than East site (91 ± 3.25). The WQI classification for assessing the water quality at stations WS 18 and WS 17 (**Fig. 5** and **Fig**. **6a**) in the East Site indicates excellent conditions, while other stations are categorized as having been in good condition. **Fig. 6a** shows the spatial distribution of WQI values, indicating that station WS18, situated in the East site, has the highest WQI value (97) characterized with the highest DO (6.94 mg/L) and the TRIX index value (6.44).

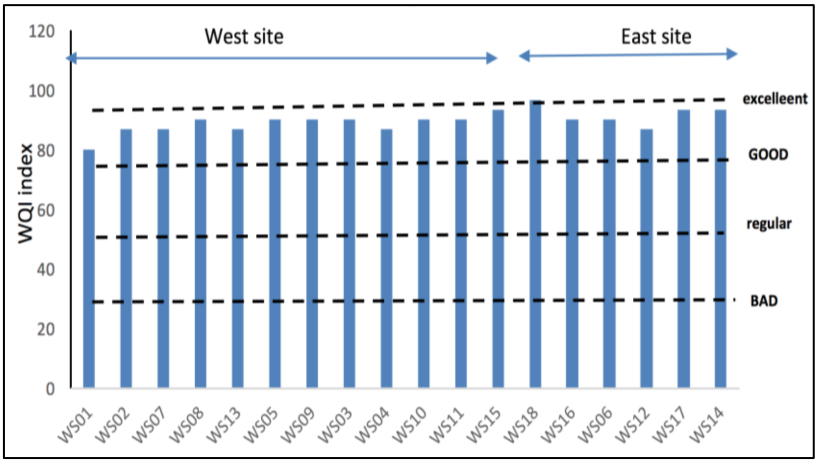

Fig. 5. Water Quality Index (WQI) in Water Sampling (WS) stations in Sumberkima coastal waters, Buleleng, Bali Province, in April 2021

4.2.2. Trophic index (TRIX) and trophic state index (TSI)

The outcomes of the calculation of the four parameters for trophic status evaluation using the TRIX index application are detectable in the distribution at the observation, as shown in **Fig. 6**. The TRIX values ranged from 3.22 to 6.50, with a mean of 4.41 ± 0.69 and the distribution values of TRIX approximates normality. The TRIX index value was found to have a range value indicates the trophic state were in the Oligotrophic, Mesotrophic, Mesotrophic to Eutrophic and Eutrophic type. The trophic condition of those TRIX values indicated that the waters were very productive (high productivity) with low water transparency into frequently anomalous waters colors and hypoxia and occasionally anoxia episodes in the bottom layers (**Table 3** and **Fig. 6b**.).

The average TRIX value in the study area was 4.41 ± 0.69 which may be characterized by the Mesotrophic to Eutrophic of the water productivity level or trophic level. The productivity level is characterized by moderately productive waters with occasionally anomalous water color. Hypoxia and occasionally anoxia episodes could also be found in the bottom layers, indicating the suffering of the benthic communities. The result of counting the TRIX algorithm also illustrates the distribution classes of marine productivity in study area.

The western site had range TRIX values were 3.22 into 6.50 means all those areas were in Oligotrophic, Mesotrophic, Mesotrophic to Eutrophic and Eutrophic condition (**Table 4**, **Fig. 6**) and the east site stations have two (2 classes) condition of trophic state were Mesotrophic and Mesotrophic to Eutrophic. The highest score of TSI found in the west site (St. 17) characterized by the highest of the DIN, ChA, and DO concentrations. Water quality assessment from the result of TSI algorithm revealed that the study areas have three classes of trophic level based on Nutrients and Chlorophyll-a concentration were Oligotrophic, Mesotrophic and Eutrophic (**Table 4** and **Fig. 6**).

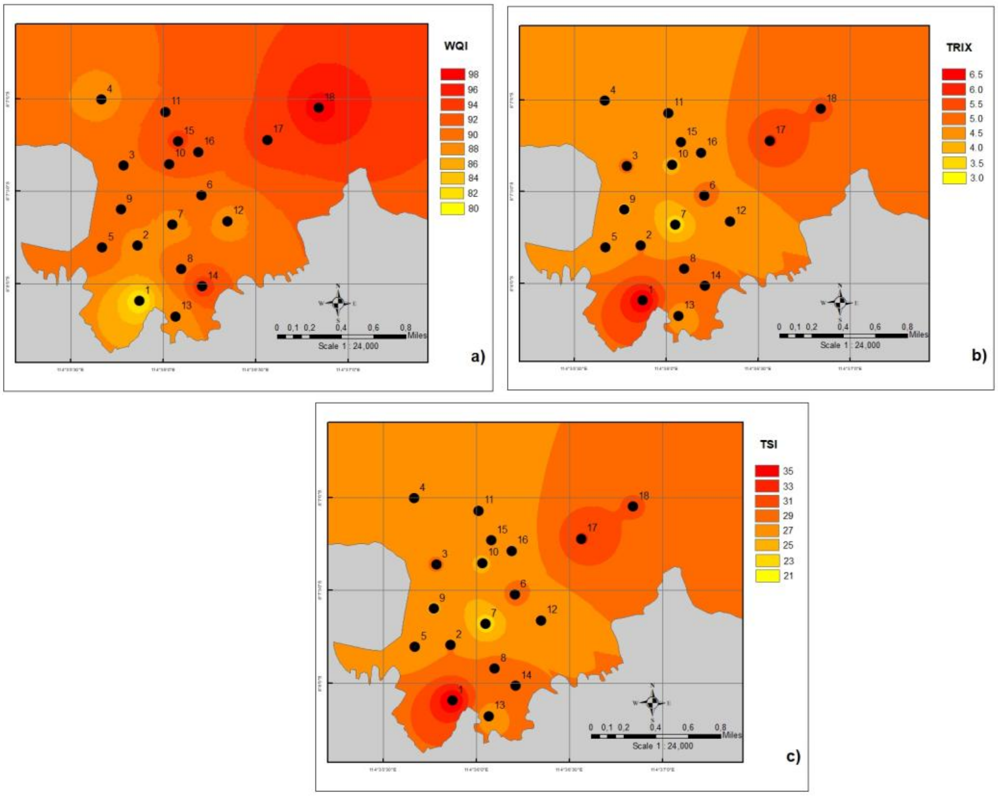

Fig. 6. Spatial distribution of WQI, TRIX, and TSI in Sumberkima coastal waters

The findings suggest that the TRIX score provides a more comprehensive and strong trophic classification to characterize water quality. The level of productivity has three classes (Oligotrophic, Mesotrophic and Eutrophic) for all stations along the West side into the East side, which illustrated the condition of the waters in **Fig. 6c**.

4.2.3. Comparison of the water quality indices

However, the evaluation of water quality is a crucial step in conserving and effectively managing coastal and marine water resources, which are constantly under threat from human-induced physical and chemical pressures (such as water over-exploitation and pollution), climate change, and uncertainty. The results of the comparative analysis using regression analysis between WQI with TRIX and TSI depicted in **Fig. 7**.

Linear regression analysis showed that WQI scores were more strongly correlated with TRIX than with TSI. Specifically, the coefficient of determination (R^2) value of TRIX with WQI shows a higher value ($R^2 = 0.3418$) than TSI ($R^2 = 0.006$). This value indicates a stronger correlation between WQI and TRIX than with TSI. The linear regression equation obtained shows a negative correlation with TRIX and a positive correlation with TSI. The negative correlation with TRIX ($y = -0.0683x + 11.934$) a potential inverse relationship with trophic status.

However, the group classification of trophic level in TSI indicated the classification of trophic levels is more widespread which has three (3) classes. The results highlight the fact that, although neither index accurately reflects the nutrient-based WQI classification, the TRIX values provide a more accurate approximation and may therefore be a more appropriate method for water quality assessment in this context.

Table 4.
Distribution of Water Quality Parameters with the Water Quality Index (WQI) and the Trophic State Index (TSI and TRIX).

Para-meter	SST (°C)	SSS (PSU)	Turb. (NTU)	pH	ChlA (µg/L)	DO (µg/L)	DIN (µg/L	TP (µg/L)	WQI	TRIX	TSI	Condi-tio/ State (Ave.)
QS*	**28-30**	**33-34**	**< 5**	**7–8.5**		**> 5000**	**308**	**15**				
West Site												
St.1	28.53	31.50	0.00	7.78	119	6338	22	8	80	6.50	57	
St.2	28.70	31.80	0.00	7.55	339	6992	176	0.5	93	4.52	65	
St.7	28.70	31.80	0.30	8.03	119	5996	28	0.5	87	3.22	30	
St.8	28.70	31.90	0.07	7.55	307	5936	27	0.5	87	4.64	19	
St.13	28.70	31.80	0.00	7.89	110	6439	40	0.5	90	4.26	34	**Oligo**
St.5	28.70	31.67	8.53	8.22	59	6036	41	0.5	87	4.15	25	**-tro-**
St.9	28.70	31.80	0.00	7.99	59	6600	55	0.5	93	3.96	38	**phic**
St.3	28.80	31.80	0.00	8.15	335	6278	55	0.5	90	4.56	23	**into**
St.4	28.80	31.80	0.00	8.24	110	6117	33	0.5	90	4.25	16	**Eu-**
St.10	28.90	31.77	0.00	8.13	51	6130	31	0.5	90	3.87	32	**Tro-**
St.11	28.90	31.70	0.00	8.14	59	5755	42	0.5	87	4.03	25	**phic**
St.15	28.90	31.83	0.03	8.04	162	6177	30	0.5	90	4.33	13	
Mean	**28.8**	**31.72**	**0.50**	**7.91**	**153**	**6263**	**35**	**1.18**	**87.8**	**4.36**	**31**	
SD	**0.26**	**0.19**	**2.0**	**0.23**	**111**	**299**	**9**	**2.3**	**3.66**	**0.82**	**16**	
Para-meter	**SST (°C)**	**SSS (PSU)**	**Turb. (NTU)**	**pH**	**ChlA (µg/L)**	**DO (µg/L)**	**DIN (µg/L**	**TP (µg/L)**	**WQI**	**TRIX**	**TSI**	**Condi-tio/ State**
QS*	**28-30**	**33-34**	**< 5**	**7–8.5**		**> 5000**	**308**	**0.015**				
East Site												
St.18	28.53	31.77	0.00	7.87	450	7163	70	0.5	90	5.02	19	**Oligo**
St.16	28.90	31.77	0.00	7.87	163	6036	47	0.5	93	4.46	24	**-tro-**
St.6	28.9	31.77	0.00	7.74	391	6439	40	0.5	97	4.72	46	**phic**
St.12	28.97	31.87	0.00	7.67	76	5596	38	0.5	90	4.09	31	**into**
St.17	29.0	31.77	0.00	7.51	789	6992	176	0.5	90	5.55	37	**Eu-**
St.14	29.1	31.2	0.00	7.90	272	6600	55	0.5	87	4.72	20	**Tro-**
Mean	**29.01**	**31.61**	**0.00**	**7.77**	**358**	**6537**	**71**	**0.5**	**91**	**4.70**	**29**	**phic**
SD	**0.12**	**0.28**	**0.00**	**0.16**	**252**	**480**	**53**	**0.00**	**3.44**	**0.58**	**11**	

**QS as Water Quality Standard for biota and marine culture based on the Environment Quality Standard No.51 2004 Republic of Indonesia*

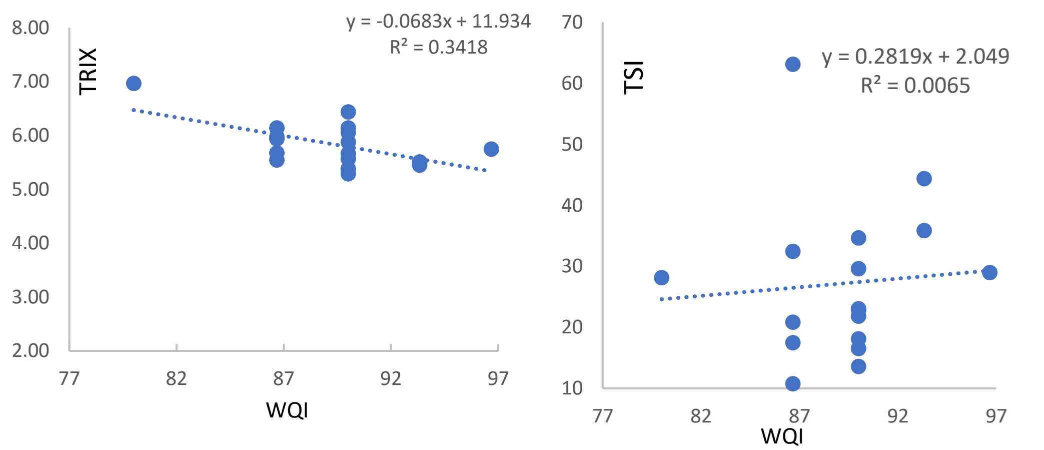

Fig. 7. Linear regression analysis of the WQI, TRIX, and TSI in the Sumberkima coastal waters. The scatterplots represent the linear regression and coefficient of determination (R^2) for each index, pointing out the direction and strength of the connections.

Fig. 8 shows a comparison of the trophic status distribution at water quality measuring stations. Approximately 50 percent of water quality monitoring stations are in good condition, predominantly classified as mesotrophic. The results indicate that water quality varies from good to excellent classes (WQI), which are related to the trophic levels of oligotrophic and mesotrophic environments (**Fig. 8**). However, there are a significant difference in TSI and others scores groups (WQI and TRIX), suggesting higher response to variations in chlorophyll-a and nutrient levels, emphasizing its fundamental function in assessing eutrophication dynamics.

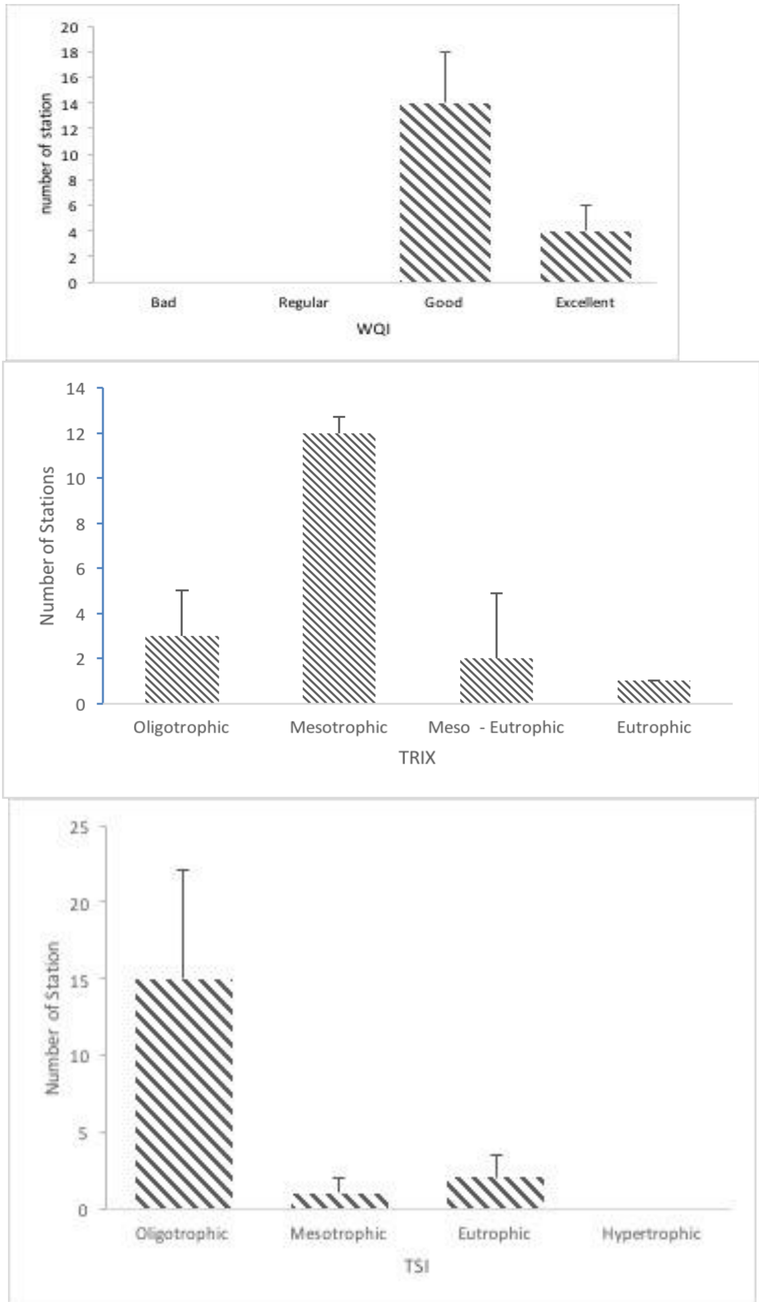

Fig. 8. Comparison of the trophic status distribution of WQI, TRIX, and TSI at water quality measuring stations.

5. DISCUSSION

5.1. Evaluation of the water quality

The sea surface water in the research area had the range values (**Table 4**) were naturally warmer due to exposure to the sun throughout the day. Nevertheless, as the wind blew, a mixing process transpired and a mixed layer was formed within the surface layer (0 m) to a depth where the temperature was uniformly still measured (Wyrtki, 1961). The SST was affected by weather conditions, whereby factors such as precipitation, evaporation rate, atmospheric humidity, air temperature, wind velocity, and solar intensity contributed to variations in SST (Tukenmez & Altiok, 2022). The mixed layer in the study areas reached temperatures of up to 28°C, Ariadji et al. (2024) also found the average of SST conducted in March 2021 was 28.6 °C. This result also aligns closely with the study by Khalishah et al., (2022) which is stated that the northern region of Bali has a surface temperature of around 27-30°C. The distribution changes of SST in marine environments are affected by solar radiation exposure (temperature of atmosphere), currents, regional season (Bradshaw & Holzapfel, 2008). Water temperature is critical to evaluating water quality and analyzing aquatic habitats. It significantly affects several chemical and biological processes and influences the dispersal of marine creatures (Ustaoğlu & Aydın, 2020).

The salinity variations are influenced by many causes, including geomorphological and topographical formations that may create disparities in salt solubility and ion ratios. The findings indicate that evaporation rates and the residence duration of coastal waters are the primary variables affecting salinity throughout the measurement period due to all the measurements were taken from 9 am to noon. Geng & Boufadel (2017) observed that evaporation significantly raised the pore water salinity, exceeding 85 g/L inside the superficial layer, which is approximately 10 cm under the sea surface. The analysis of SST and SSS values from the depth 5 – 25 m revealed that the water body was thoroughly mixed with significant vertical density gradients throughout the sample period.

Previous study by Khalishah et al., (2023) and Ilahude & Gordon (1996) found that the northern waters of Bali are predominantly influenced by water masses from the Java Sea which have the surface currents with the characteristics of the Indonesian monsoon current. The Indonesian monsoon current crosses from the China Sea into Java, extending to the Flores Sea and Banda Sea.The highest SC mean value found in the west site (0.2 ± 0.13 m/s) of the sampling stations is influenced by the movement of the monsoon winds and tidal energy. The surface currents in Bali's northern and southern waterways move from west to east (Siswanto & Suratno, 2010) and conversely, the southeast monsoon (May to October), the currents move from east to west, resulting in a dynamic marine environment.

The research area revealed a limited phosphate content, with almost the TP measurement result at the study field beings nearly below the detection limit (1 μg/L). The highest concentration was found in the west site (St.01). A previous study in Sumberkima coastal waters found that the primary source of organic matter input in marine waters, particularly in Pegametan Bay, comes from fish culture feed. The feed consists of nitrogen and phosphorus, which solubilise in water and are utilised by the cultured organisms (Ariadji et al., 2024; Mok et al., 2021). Marine organisms require nutrients to survive, and previous research has shown a positive correlation between the health of aquatic ecosystems and phosphorus and nitrogen levels (Abo-El-Khair et al., 2016). Physical and biological processes may influence the regulation of TP and DIN levels in the study areas due to the present study revealed that elevations in TP and DIN were found by decreasing in salinity, indicating the role of sewage effluents in providing N and P compounds to coastal saline ecosystems (Mahmoud et al., 2020).

According to Ahmad et al. (2017), fishing activities might contribute to the concentrations of nutrients, which is evident from Ariadji et al. (2024) found that the concentrations of NO_2 are less than the other forms of nitrogen (NO_3 and NH_3). The instability can be ascribed to its capacity to oxidated become nitrate or reduction to ammonia through chemical reactions and biological bacteria (Canfield et al., 2010; Ward, 2008). The salinity, water temperature, and dissolved oxygen are the most important factors influencing nutrient patterns in coastal regions (Pesce & Wunderlin, 2000). The ratio of Nitrogen and Phosphate is a crucial ecological parameter influencing primary production and eutrophication (Abdelmongy & El-Moselhy, 2015). The average N/P ratios in the study area was higher than 16, phytoplankton growth may be limited by phosphorus or acts as the limiting factor (Redfield et al., 1963). The fluctuation of the N/P ratios may be described to the diverse discharges entering the research region. N-limited aquatic systems exhibit N/P molar ratios above 5, whereas P-deficient aquatic systems also display N/P molar ratios above 5 (Abo-El-Khair et al., 2016b).

Oxygen compounds are those directly associated with carbon through photosynthesis and respiration processes (Oschlies et al., 2018; Stramma et al., 2008). The presence or profile of oxygen concentrations in the aquatic ecosystem area mirrors the concentration and profile of nutrient distribution as mentioned by (Diaz & Breitburg, 2009). Oceanic fronts are areas characterized by intensified surface gradients in physicochemical characteristics between adjacent water masses (Belkin & Cornillon, 2005; Belkin & O'Reilly, 2009). The observation results (**Fig. 4a**) indicate that the area surrounding station 03 has a seagrass cover percentage of 80.63%, whereas the areas around stations 17 and 18 exhibit a higher coverage of 84.22%.

The minimum and maximum DO concentrations recorded were 5755 and 7163 µg/L, respectively (**Fig. 4a**). The highest ChA concentration (7890 µg/L) was found in stations 17, which is in the East site. The similarity trend values of ChA with DO concentration exhibited correlate with those obtained at this site (**Fig. 9**). This finding suggests that DO and ChA could be used as indicators of the scale of photosynthetic aquatic organisms, as previously demonstrated by Mashoreng et al. (2019). As shown by linear regression (**Fig. 9**), the correlation between DIN, DO, and ChA suggests that these parameters are required during photosynthesis in addition to absorbed atmospheric carbon dioxide (CO_2) and oxygen (O_2) production. The weak relation between ChA and DIN (R^2 were 0.26 and 0.07) suggested that DIN availability in the primary productive process is significantly limited. However, the majority of sea surface waters are low in inorganic nitrogen, phosphorus, iron and/or silica; nutrients that limit primary generation in the ocean (Bristow et al., 2017).

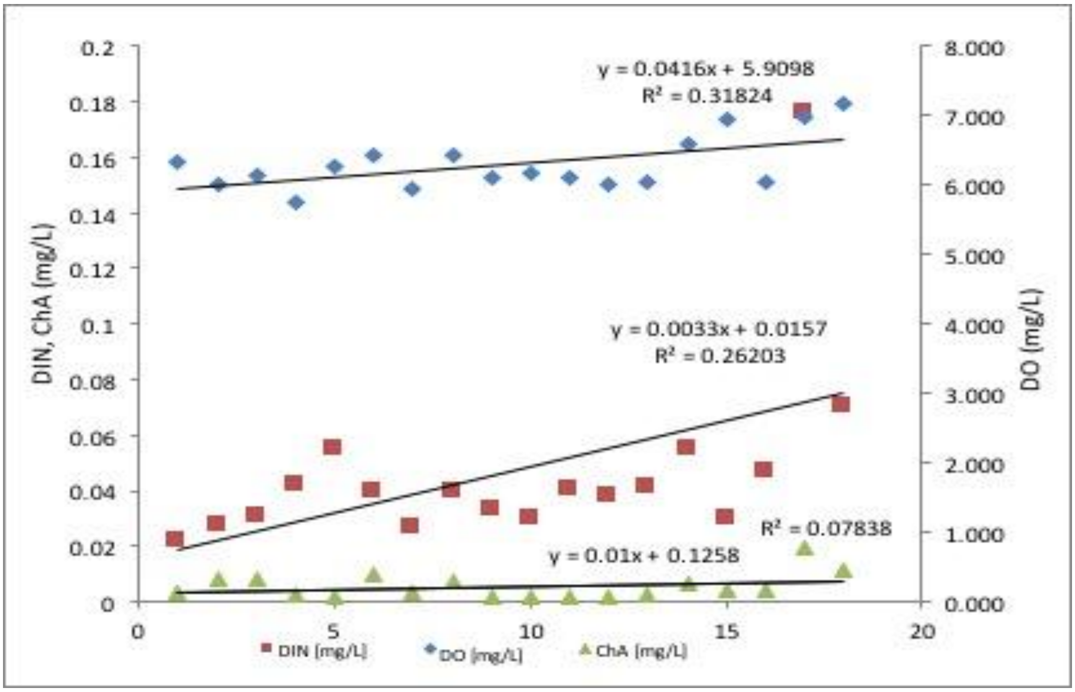

Fig. 9. Linear regression analysis of DO, TN and ChA Values at the 18 Stations of Study Areas

5.2. Comparison of water quality indices

A comparative evaluation of the efficacy of WQI, TRIX, and TSI for evaluating water quality in tropical coastal ecosystems reveals significant differences. The TRIX exhibits a significant negative relationship with WQI (R^2 = 0.34, $p < 0.01$), suggesting that the trophic state index significantly impact overall water quality, hence establishing TRIX as a reliable indicator of ecosystem degradation as evidenced by WQI. Increasing TRIX values, signifying enhanced nutrient enrichment and phytoplankton biomass, correlate with diminished WQI scores, indicating declining physic-chemical water quality. This pattern is found over the studied data range, suggesting that eutrophication significantly affects regional water quality.

The trophic status was calculated and assessed from four water quality parameters, namely DIN, TP, % DO, and ChA obtained an index value for all stations indicating the condition of the waters is at Mesotrophic up to Eutrophic level (Pesce & Wunderlin, 2000; Vollenweider et al., 1998). The TRIX index value also shows that the research location as a typical ecosystem of tropical coastal areas as expressed by (Welsh, 2000).

The linear regression between TSI and WQI (**Fig. 7**) indicated a negligible association between TSI and WQI (R^2 = 0.006) shows that fluctuations in trophic status occur independently of alterations in overall water quality, underscoring the restricted responsiveness of WQI to eutrophication-related phenomena. We analyzed the spatial distribution of the WQI, TRIX, and TSI indices (**Fig. 6a**, **Fig. 6b**, **Fig. 6c**) and discovered a value distribution pattern of those indices in which the study area with the highest WQI value coincides with lower TRIX and TSI values.

The distribution of TSI index values across all 18 sampling stations was oligotrophic to eutrophic (**Fig. 6c**). The average TSI index value at the west side research location (31±16) and stations on the east side was 29.4 ± 11, indicating mesotrophic conditions.

The highest trophic level (eutrophic) was discovered at station 17, which is located on the east side. This is attributed to the high levels of organic and inorganic waste in the region caused by increased land use, economic growth, and rapid urbanization. These findings are comparable with those of Abdel-Hamid (2017), who identified several important terrestrial and marine activities that contribute to eutrophication.

WQI integrates several physical and chemical properties to describe comprehensive water quality, whereas TRIX focuses on nutrient enrichment and phytoplankton response, making it more sensitive to eutrophication processes. A positive relationship was found between elevated productivity and persistently higher nutrient consumption levels in the studied area, suggesting that these levels transcend those of the realistic scenario (Giovanardi & Vollenweider, 2004).

According to Primpas & Karydis (2011), TRIX is useful for quantifying environmental quality due to it's has several advantages: (a) it produces a single number, (b) it is a multimetric index that includes four variables related to eutrophication, and (c) the environmental variables involved can be measured directly on a regular basis. Evaluating trophic status is crucial for determining the health of coastal aquatic ecosystems. By analysing nutrient concentrations and trophic interactions, researchers and policymakers can comprehend the ecological condition of coastal marine ecosystems (Bricker et al., 1999).

In April 2021, the water quality of coastal waters in Sumberkima, Buleleng, Bali Province, typically revealed that the results of measurements are still within the range of Standard Quality (SQ) criteria for marine biota and marine culture (Kementerian Lingkungan Hidup, 2004), excepts for nutrients as mentioned in **Table 4**. The results of the previous study found the condition of environmental degradation of marine culture in the north Bali coastal waters district has not occurred yet, but continuously efforts to control and anticipate it should be done as to achieve integrated marinculture Soto (2009). Soto (2009) proposed that integrated mariculture provides a mitigation strategy for the surplus nutrients and organic matter produced by intense aquaculture practices, especially in marine environments.

6. CONCLUSION

This study highlights that WQI, TRIX, and TSI provide complementary but distinct insights into water quality situations. The significant negative correlation between TRIX and WQI indicates that eutrophication is a principal factor in a decline of water quality in the studied area. The lack of a significant correlation between TSI and WQI suggests that fluctuations in trophic status may occur independently of alterations in overall water quality.

Comparing these indicators with nutrient concentration measurements in Sumberkima coastal waters, Bali Province offers a more comprehensive understanding of the determinants influencing water quality and presents a more complete overview of the condition of coastal aquatic ecosystems. Among the assessed indices, the WQI and TRIX indices exhibit a more robust significant correlation than the TSI. TRIX and TSI offer a more precise representation of trophic conditions affected by nutrients. The TRIX index demonstrates increased sensitivity in categorizing ecosystems as oligotrophic, mesotrophic, mesotrophic to Eutrophic and Eutrophic. These findings strengthen its potential as a dependable biomarker for identifying modest trophic changes in nutrient-dense environments.

The findings of this study represent conditions from an a single sampling time (April 2021) and should be regarded as a temporal snapshot. Additional multi-seasonal measurements are necessary to fully comprehend the seasonal variability in the research area. One of the future challenge in this research is to ensure data quality and consistency collecting, particularly under changing environmental circumstances. Adaptive sampling techniques may be necessary due to the potential for findings to be impacted by external influences, such as seasonal variations or unpredictable disruptions. Moreover, restricted access to advanced tools and processing resources can affect comprehensive research. Addressing these problems requires careful analysis, ongoing oversight, and cooperation with field specialists. This study may get more accurate and significant results by using advanced technology and enhancing procedures.

ACKNOWLEDGEMENTS

The authors are grateful to the Ministry of Marine Affairs and Fisheries for providing financial support for the study through APBN 2021. This paper as part of the research activities with the title 'Utilisation of Satellite Data, Observation, and Modelling for Coastal Areas' in 2021 in Sumberkima Village, Gerokgak District, Buleleng Regency and Perancak Mangrove, Jembrana Regency, Bali Province.

REFERENCES

Abdel-Hamid, E. (2017). Assessment of Some Water Quality Characteristics and Bacterial Contamination in Water, Sediments and Some Fish species of El-Manzala Lake. *Egyptian Journal for Aquaculture*, *7*(1), 55–75. https://doi.org/10.21608/eja.2019.31473

Abdelmongy, A. S. & El-Moselhy, K. M. (2015). Seasonal Variations of the Physical and Chemical Properties of Seawater at the Northern Red Sea, Egypt. *Journal of Ocean and Coastal Sciences*, *2*(1). https://doi.org/10.15764/OCS.2015.01001

Abo-El-Khair, E. M., Fattah, L. M. A., Abdel-Halim, A. M., Abd-Elnaby, M. A., Fahmy, M. A., Ahdy, H. H., Hemeilly, A., El-Soud, A. A. & Shreadah, M. A. (2016). Assessment of the Hydrochemical Characteristics of the Suez Gulf Coastal Waters during 2011-2013. *Journal of Environmental Protection*, *07*(11), 1497–1521. https://doi.org/10.4236/jep.2016.711126

Ahmad, I., Babitha Rani, A. M., Verma, A. K. & Maqsood, M. (2017). Biofloc technology: an emerging avenue in aquatic animal healthcare and nutrition. *Aquaculture International*, *25*(3), 1215–1226. https://doi.org/10.1007/s10499-016-0108-8

Ampou, E. E., Triyulianti, I., Pradisty, N. A., Widagti, N., Swastana, I. G. A. & Mariasa, I. P. M. (2023). Sea bunnies as a potential marine ecotourism in sumberkima, Buleleng Regency, Bali. *E3S Web of Conferences*, *442*, 01006. https://doi.org/10.1051/e3sconf/202344201006

Ariadji, Z. A., Suantika, G. & Aditiawati, P. (2024). Trophic state assessment of marine ecosystems used for floating net cage aquaculture: a case study in Pegametan Bay, North Bali, Indonesia. *Aquaculture International*, *32*(5), 6611–6647. https://doi.org/10.1007/s10499-024-01481-9

Belkin, I. M. & Cornillon, P. C. (2005). Bering Sea Thermal Fronts from PathFinder Data Seasonal and Interannual Variability. http://www.po.gso.uri.edu/~belkin/index.html.

Belkin, I. M. & O'Reilly, J. E. (2009). An algorithm for oceanic front detection in chlorophyll and SST satellite imagery. *Journal of Marine Systems*, *78*(3), 319–326. https://doi.org/10.1016/J.JMARSYS.2008.11.018

Benaissa, C., Bouhmadi, B., Rossi, A., Benaissa, C., Bouhmadi, B. & Rossi, A. (2023). An assessment of the physicochemical, bacteriological quality of groundwater and the water quality index (WQI) used GIS in Ghis Nekor, Northern Morocco://creativecommons.org/licenses/by/4.0/). *Scientific African*, *20*, 1623. https://doi.org/10.1016/j.sciaf.2023.e01623

Benaissa, C., Bouhmadi, B., Rossi, A., El Hammoudani, Y. & Dimane, F. (2022). Assessment of Water Quality Using Water Quality Index – Case Study of Bakoya Aquifer, Al Hoceima, Northern Morocco. *Ecological Engineering & Environmental Technology*, *23*(4), 31–44. https://doi.org/10.12912/27197050/149495

Boyd, P. W., Ellwood, M. J., Tagliabue, A. & Twining, B. S. (2017). Biotic and abiotic retention, recycling and remineralization of metals in the ocean. *Nature Geoscience*, *10*(3), 167–173. https://doi.org/10.1038/ngeo2876

Bradshaw, W. E. & Holzapfel, C. M. (2008). Genetic response to rapid climate change: it's seasonal timing that matters. *Molecular Ecology*, *17*(1), 157–166. https://doi.org/10.1111/J.1365-294X.2007.03509.X

Bricker, S. B., Clement, C. G., Pirhalla, D. E., Orlando, S. P. & Farrow, D. R. G. (1999). National Estuarine Eutrophication Assessment: Effects of Nutrient Enrichment in the Nation's Estuaries. http://spo.nos.noaa.gov

Bristow, L. A., Mohr, W., Ahmerkamp, S. & Kuypers, M. M. M. (2017). Nutrients that limit growth in the ocean. *Current Biology*, *27*(11), R474–R478. https://doi.org/10.1016/J.CUB.2017.03.030

Canfield, D. E., Glazer, A. N. & Falkowski, P. G. (2010). The Evolution and Future of Earth's Nitrogen Cycle. *Science*, *330*(6001), 192–196. https://doi.org/10.1126/science.1186120

Chen, B. & Chen, G. Q. (2007). Modified ecological footprint accounting and analysis based on embodiedexergy-a case study of the Chinese society 1981-2001. *Ecological Economics*, *61*(2–3), 355–376. https://doi.org/10.1016/j.ecolecon.2006.03.009

Diaz, R. J. & Breitburg, D. L. (2009). Chapter 1 The Hypoxic Environment. *Fish Physiology*, *27*(C), 1–23. https://doi.org/10.1016/S1546-5098(08)00001-0

Drira, Z., Chaari, D., Hamza, A., Hassen, M. B., Pagano, M. & Ayadi, H. (2017). Diazotrophic cyanobacteria signatures and their relationship to hydrographic conditions in the Gulf of Gabes, Tunisia. *Journal of the Marine Biological Association of the United Kingdom*, *97*(1), 69–80. https://doi.org/10.1017/S0025315415002210

Gandaseca. (2011). Status of Water Quality Based on the Physico-Chemical Assessment on River Water at Wildlife Sanctuary Sibuti Mangrove Forest, Miri Sarawak. *American Journal of Environmental Sciences*, *7*(3), 269–275. https://doi.org/10.3844/ajessp.2011.269.275

Geng, X. & Boufadel, M. C. (2017). The influence of evaporation and rainfall on supratidal groundwater dynamics and salinity structure in a sandy beach. *Water Resources Research*, *53*(7), 6218–6238. https://doi.org/10.1002/2016WR020344

Giovanardi, F. & Vollenweider, R. A. (2004). Trophic conditions of marine coastal waters: experience in applying the Trophic Index TRIX to two areas of the Adriatic and Tyrrhenian seas. *J. Limnol*, *63*(2), 199–218.

Herrera-Silveira, J. A. & Morales-Ojeda, S. M. (2009). Evaluation of the health status of a coastal ecosystem in southeast Mexico: Assessment of water quality, phytoplankton and submerged aquatic vegetation. *Marine Pollution Bulletin*, *59*(1–3), 72–86. https://doi.org/10.1016/J.MARPOLBUL.2008.11.017

Howarth, R. W. & Marino, R. (2006). Nitrogen as the limiting nutrient for eutrophication in coastal marine ecosystems: Evolving views over three decades. *Limnology and Oceanography*, *51*(1part2), 364–376. https://doi.org/10.4319/LO.2006.51.1_PART_2.0364

Ilahude, G. and A. Gordon. (1996). Thermocline Stratification within the Indonesian Seas. J. Geophysical Resources : Oceans, 101(C5), 12401-12409

Irawan, L. Y., Kamal, M. F. M., Devy, M. M. R., Prasetyo, W. E., Lelitawati, M. & Sumarmi. (2023). Using physical parameters for tourism potential mapping: Study case of beach tourism destination in Gajahrejo, Malang. *IOP Conference Series: Earth and Environmental Science*, *1190*(1), 012014. https://doi.org/10.1088/1755-1315/1190/1/012014

Khalishah P.V., Naulita Y, and Hernawan U. (2023). Characteristic of North Pacific Water Masses in The Bali Sea. IOP Conference Series : earth and EnvironmentalScience. 1251.012039

Kementerian Lingkungan Hidup. (2004). Water quality standard for biota and marine culture based on Environment Quality Standard No. 51 2004 Republic Indonesia. moz-extension://3ec545ad-74a2-47d6-ae3a-1b212aae675f/enhanced-reader.html?openApp&pdf=https%3A%2F%2Fppkl.menlhk.go.id%2Fwebsite%2Ffilebox%2F824%2F191009100640Keputusan%2520MENLH%2520Nomor%252051%2520tahun%25202004%2520%2520tentang%2520Baku%2520Mutu%2520Air%2520Laut.pdf

Klippel, G., Macêdo, R. L. & Branco, C. W. C. (2020). Comparison of different trophic state indices applied to tropical reservoirs. *Lakes & Reservoirs: Research & Management*, *25*(2), 214–229. https://doi.org/10.1111/LRE.12320

Mahmoud, M. G., El-Khir, E. A., Ebeid, M. H., Mohamed, L. A., Fahmy, M. A. & Shaban, K. S. (2020). An Assessment on the Coastal Seawater Quality of the Gulf of Suez, Egypt. *Journal of Environmental Protection*, *11*(01), 34–47. https://doi.org/10.4236/jep.2020.111004

Mashoreng, S., Alprianti, S., Samad, W., Isyrini, R. & Inaku, D. F. (2019). SERAPAN KARBON LAMUN Thalassia hemprichii PADA BEBERAPA KEDALAMAN. *Jurnal Ilmu Kelautan SPERMONDE*. https://doi.org/10.20956/JIKS.V5I1.7031

Mok, J.-S., Choi, A., Kim, B., An, S.-U., Lee, W.-C., Kim, H. C., Kim, J., Yoon, C. & Hyun, J.-H. (2021). Phosphorus Dynamics Associated With Organic Carbon Mineralization by Reduction of Sulfate and Iron in Sediment Exposed to Fish Farming. *Frontiers in Marine Science*, *8*. https://doi.org/10.3389/fmars.2021.645449

Neumann, K., Fahmy, A. G., Müller-Scheeßel, N. & Schmidt, M. (2017). Taxonomic, ecological and palaeoecological significance of leaf phytoliths in West African grasses. *Quaternary International*, *434*, 15–32. https://doi.org/10.1016/j.quaint.2015.11.039

Nurjayanti, Hatta, M. & Tuwo, A. (2023). Evaluating Coastal Area Suitability and Ecological Carrying Capacity in Topejawa Village, South Sulawesi. *IOP Conference Series: Earth and Environmental Science*, *1272*(1), 012034. https://doi.org/10.1088/1755-1315/1272/1/012034

O'Boyle, S., McDermott, G., Noklegaard, T. & Wilkes, R. (2013). A Simple Index of Trophic Status in Estuaries and Coastal Bays Based on Measurements of pH and Dissolved Oxygen. *Estuaries and Coasts*, *36*(1), 158–173. https://doi.org/10.1007/S12237-012-9553-4

Oschlies, A., Brandt, P., Stramma, L. & Schmidtko, S. (2018). Drivers and mechanisms of ocean deoxygenation. *Nature Geoscience*, *11*(7), 467–473. https://doi.org/10.1038/s41561-018-0152-2

Pavluk, T. & bij de Vaate, A. (2017). Trophic Index and Efficiency. *Encyclopedia of Ecology: Volume 1-4, Second Edition*, *1*, 495–502. https://doi.org/10.1016/B978-0-12-409548-9.00608-4

Peng, S. (2015). The nutrient, total petroleum hydrocarbon and heavy metal contents in the seawater of Bohai Bay, China: Temporal–spatial variations, sources, pollution statuses, and ecological risks. *Marine Pollution Bulletin*, *95*(1), 445–451. https://doi.org/10.1016/J.MARPOLBUL.2015.03.032

Primpas, I. & Karydis, M. (2011). Scaling the trophic index (TRIX) in oligotrophic marine environments. *Environmental Monitoring and Assessment*, *178*(1–4), 257–269. https://doi.org/10.1007/s10661-010-1687-x

Radfard, M., Gholizadeh, A., Azhdarpoor, A., Badeenezhad, A., Mohammadi, A. A., Yousefi, M., Azhdarpoor, A. & Mohammadi, A. A. (2019). *Health risk assessment to fluoride and nitrate in drinking water of rural residents living in the Bardaskan city, arid region, southeastern Iran*. https://doi.org/10.5004/dwt.2019.23651

Redfield, C., Ketchum, B. H. & Richards, F. a. (1963). The influence of organisms on the composition of sea water. *The Sea*, *2*, 26–77.

Reid, G. K., Gurney-Smith, H. J., Marcogliese, D. J., Knowler, D., Benfey, T., Garber, A. F., Forster, I., Chopin, T., Brewer-Dalton, K., Moccia, R. D., Flaherty, M., Smith, C. T. & De Silva, S. (2019). Climate change and aquaculture: Considering biological response and resources. *Aquaculture Environment Interactions*, *11*, 569–602. https://doi.org/10.3354/AEI00332

Reyers, B. & Selig, E. R. (2020). Global targets that reveal the social–ecological interdependencies of sustainable development. *Nature Ecology & Evolution*, *4*(8), 1011–1019. https://doi.org/10.1038/s41559-020-1230-6

Rodrigues-Filho, J. L., Macêdo, R. L., Sarmento, H., Pimenta, V. R. A., Alonso, C., Teixeira, C. R., Pagliosa, P. R., Netto, S. A., Santos, N. C. L., Daura-Jorge, F. G., Rocha, O., Horta, P., Branco, J. O., Sartor, R., Muller, J. & Cionek, V. M. (2023). From ecological functions to ecosystem services: linking coastal lagoons biodiversity with human well-being. *Hydrobiologia*, *850*(12–13), 2611–2653. https://doi.org/10.1007/s10750-023-05171-0

Sahavacharin, A., Sompongchaiyakul, P. & Thaitakoo, D. (2022). The effects of land-based change on coastal ecosystems. *Landscape and Ecological Engineering*, *18*(3), 351–366. https://doi.org/10.1007/s11355-022-00505-x

Saygu, İ., Akoglu, E., Gül, G., Bedikoğlu, D. & Demirel, N. (2023). Fisheries impact on the Sea of Marmara ecosystem structure and functioning during the last three decades. *Frontiers in Marine Science*, *9*. https://doi.org/10.3389/fmars.2022.1076399

Seisdedo, M., Moreira, A. R., Comas, A. A. & Arencibia, G. (2014). Analysis of tools for trophic status assessment of water in Cienfuegos bay, Cuba. *Pan-American Journal of Aquatic Sciences*, *9*(2), 103–111.

Shaaban, N. A. (2022). Water quality and trophic status of Lake Mariut in Egypt and its drainage water after 8-year diversion. *Environmental Monitoring and Assessment*, *194*(6), 392-. https://doi.org/10.1007/S10661-022-10009-8/TABLES/7

Siswanto, & Suratno. (2010). Seasonal pattern of wind induced upwelling over Java-Bali sea waters and surrounding area. *International Journal of Remote Sensing and Earth Sciences*, *5*(1). https://doi.org/10.30536/J.IJRESES.2008.V5.A1228

Soto, Doris. (2009). *Integrated mariculture : a global review*. Food and Agriculture Organization of the United Nations.

Stramma, L., Johnson, G. C., Sprintall, J. & Mohrholz, V. (2008). Expanding oxygen-minimum zones in the tropical oceans. *Science*, *320*(5876), 655–658. https://doi.org/10.1126/science.1153847

Triyulianti, I., Ampou, E. E., Widagti, N. & Swastana, I. G. A. (2021). Penilaian Status Trofik Ekosistem Terumbu Karang dan Lamun di Perairan Selat Lembeh dengan Aplikasi Indeks TRIX (Trophic Level Assessment of Coastal and Seagrass Ecosystem in Lembeh Strait Waters using TRIX Indices Application). *Journal of Fisheries and Marine Research*, (Vol. 5 No. 2), 426–435. https://jfmr.ub.ac.id/index.php/jfmr/article/view/566/276

Tukenmez, E. & Altiok, H. (2022). Long-Term Variations of Air Temperature, SST, Surface Atmospheric Pressure, Surface Salinity and Wind Speed in the Aegean Sea. *Mediterranean Marine Science*, *23*(3), 668–684. https://doi.org/10.12681/MMS.25770

Ustaoğlu, F. & Aydın, H. (2020). Health risk assessment of dissolved heavy metals in surface water in a subtropical rivers basin system of Giresun (North-eastern Turkey). *Desalination and Water Treatment*, *194*, 222–234. https://doi.org/10.5004/dwt.2020.25900

Vollenweider, R. A., Giovanardi, F.., Montanari, G. & Rinaldi, A. (1998). Characterization of the trophic conditions of marine coastal waters with special reference to the NW Adriatic Sea: proposal for a trophic scale, turbidity and generalized water quality index. Environmetrics, Wiley Online Library. https://onlinelibrary.wiley.com/doi/epdf/10.1002/%28SICI%291099-095X%28199805/06%299%3A3%3C329%3A%3AAID-ENV308%3E3.0.CO%3B2-9

Ward, B. B. (2008). Nitrification in Marine Systems. In *Nitrogen in the Marine Environment* (pp. 199–261). Elsevier. https://doi.org/10.1016/B978-0-12-372522-6.00005-0

Welsh, D. T. (2000). Nitrogen fixation in seagrass meadows: Regulation, plant–bacteria interactions and significance to primary productivity. *Ecology Letters*, *3*(1), 58–71. https://doi.org/10.1046/J.1461-0248.2000.00111.X

Wyrtki, K. (1961). *NAGA REPORT Volume 2 Scientific Results*.

Xu, J., Mo, Y., Zhu, S., Wu, J., Jin, G., Wang, Y. G., Ji, Q. & Li, L. (2024). Assessing and predicting water quality index with key water parameters by machine learning models in coastal cities, China. *Heliyon*, *10*(13). https://doi.org/10.1016/j.heliyon.2024.e33695

Yan, T., Shen, S. L. & Zhou, A. (2022). Indices and models of surface water quality assessment: Review and perspectives. *Environmental Pollution (Barking, Essex : 1987)*, *308*. https://doi.org/10.1016/J.ENVPOL.2022.119611

Yousefi, M., Ghalehaskar, S., Asghari, F. B., Ghaderpoury, A., Dehghani, M. H., Ghaderpoori, M. & Mohammadi, A. A. (2019). Distribution of fluoride contamination in drinking water resources and health risk assessment using geographic information system, northwest Iran. *Regulatory Toxicology and Pharmacology: RTP*, *107*. https://doi.org/10.1016/J.YRTPH.2019.104408

Yusuf, Y. B. M., Karlinasari, L., Alinda Fitriany, M., Panuju, D. R. & Jati, R. (2025). Identifying coastal area resilience through ecological integration and disaster risk approaches case study: north jakarta, indonesia. *IOP Conference Series: Earth and Environmental Science*, *1557*(1), 012019. https://doi.org/10.1088/1755-1315/1557/1/012019

Zotou, I., Tsihrintzis, V. A. & Gikas, G. D. (2018). Comparative Assessment of Various Water Quality Indices (WQIs) in Polyphytos Reservoir-Aliakmon River, Greece. *Proceedings 2018, Vol. 2, 2*(11), 611. https://doi.org/10.3390/PROCEEDINGS2110611

Geographia Technica, Vol. 21, Issue 3, 2026, pp 70 to 86

INTEGRATING LANDSAT-8, EMAG2V3, AND GGMPLUS GRAVITY DATA FOR GEOTHERMAL PROSPECT ZONATION AT DORMANT VOLCANO (CASE: MOUNT PUSUK BUHIT, NORTH SUMATRA, INDONESIA)

Rina Dwi INDRIANA[1], Ihya Qothrunnada RAHMANI[1]*, Agus SETYAWAN[1]*, Ahmad Ali MUCKHAROM[1] & Richard LEWERISSA[2]

DOI: 10.21163/GT_2026.213.05

ABSTRACT

Indonesia has an estimated 23,591.75 MWe of geothermal potential, but exploration is costly and time-consuming. One of the islands in Indonesia, namely Sumatra, has 104 geothermal prospects, including the Simbolon–Samosir area, where Mount Pusuk Buhit has 150 MWe of inferred resources. This study uses satellite imaging to map surface and subsurface features at Mount Pusuk Buhit. Landsat-8 imagery is processed to create visualisations, while GGMPlus gravity data are analysed to map the land's structure. The NDVI calculation results are -0.51 to 0.87. The NDVI at the hot spring is lower than its surroundings, at -0.51 to 0.17. The research area has an LST of 19.72°C to 36.04°C. LST maps reveal localised heat anomalies on the flanks and foothills of Pusuk Buhit, some coinciding with known geothermal manifestations. Low NDVI values in these areas indicate reduced vegetation cover. Negative gravity anomalies are interpreted as fractured or fluid-influenced low-density zones, and positive anomalies indicate dense volcanic or intrusive bodies that may act as structural boundaries. Integrated LST and gravity overlay identifies four prospect zones. High LST coinciding with negative gravity is the most favourable for upflow. The Curie Depth Point values are generally around 28 to 31 km, which correlates well with heat flow values of around 48 to 50 mW/m². The results demonstrate the effectiveness and cost-effectiveness of combining Landsat-8 thermal, EMAG2V3, and GGMPlus gravity anomalies in assessing geothermal potential in volcanic terrains. The workflow can be used for other geothermal prospects in Indonesia.

Keywords: *Landsat-8, EMAG2V3, GGMPlus, geothermal, dormant, volcano, Pusuk Buhit.*

1. INTRODUCTION

Indonesia is located along a volcanic arc with abundant geothermal potential. Indonesia's estimated geothermal potential currently stands at 23,591.75 MWe, while its realised utilisation is only around 5%. In Sumatra, there are 104 geothermal prospects, including Mount Pusuk Buhit in Samosir Regency. The Simbolon–Samosir Geothermal Project working area, which is part of the Pusuk Buhit system, is estimated to have an indicated geothermal potential of approximately 150 MWe. Geothermal systems in volcanic regions are often difficult to map because of vegetation cover, weathering, and significant topographic variation. Mount Pusuk Buhit is a type-C volcano. Although no eruption has been recorded, the area is characterised by fumaroles and other signs of subsurface heat and fluid circulation. Such "dormant" systems are difficult to investigate because surface manifestations may be weak, while the subsurface structures that control permeability and fluid migration are hard to identify. Therefore, techniques capable of mapping both surface thermal manifestations and inferring subsurface structures would be highly useful.

[1]*Universitas Diponegoro, Department of Physics, Faculty of Science and Mathematics, 50275, Semarang, Indonesia; rinadwiindriana@lecturer.undip.ac.id (RDI), ihyaqothrunnada@alumni.undip.ac.id (IQR), agussetyawan@fisika.fsm.undip.ac.id (AS), alimuckharom@students.undip.ac.id (AAM).*

[2]*Universitas Papua, Department of Physics, Faculty of Mathematics and Natural Sciences, 98314, Manokwari, Papua Barat, Indonesia; r.lewerissa@unipa.ac.id (RL).*

**Corresponding authors: ihyaqothrunnada@alumni.undip.ac.id, agussetyawan@fisika.fsm.undip.ac.id*

Geothermal exploration requires substantial resources, is time-consuming, and is often constrained operationally. Field mapping and sampling are hindered by steep topography, settlements, and weather conditions, all of which may increase uncertainty in geothermal identification. Satellite-based approaches can provide broad, efficient coverage, enabling geothermal target screening. Remote sensing has been used to highlight anomalous zones for further investigation in Indonesia and other volcanic regions (Bian et al., 2024; Weldeyohannes et al., 2022). Among the available satellite options, Landsat-8 OLI/TIRS has been widely used in preliminary geothermal studies through the analysis of surface thermal anomalies that may indicate the presence of geothermal resources (Azis et al., 2022). Various studies have demonstrated the effectiveness of Landsat-8 imagery for mapping land surface temperature in volcanic environments with geothermal resources (Saraswati et al., 2019).

In addition to thermal information, geological structural factors also play an important role in geothermal systems. Faults and fractures act as migration pathways for geothermal fluids from the reservoir to the surface (Grant & Bixley, 2011). In this study, we used Fault Fracture Density (FFD) analysis, which has been widely applied to delineate permeable zones (Ahmadi & Pekkan, 2021; Hutauruk et al., 2024). The integration of LST and FFD analyses is commonly treated as a unified interpretive framework and has been widely applied in geothermal exploration in various areas, both in active volcanic environments and non-volcanic geothermal systems (Alqahtani et al., 2023; Rabuffi et al., 2025; Rafiq et al., 2025).

To complement this geothermal potential analysis, we also used the gravity method based on the satellite-derived Global Gravity Model Plus (GGMPlus) dataset from Hirt et al., (2013). The gravity method can serve as a complementary tool for identifying subsurface structures, such as fractures, that act as pathways for ascending hot fluids. Gravity methods are widely used in geological investigations because they are sensitive to variations in rock density (Blakely, 1995; Telford et al., 1990). For example, gravity anomaly analysis has been proven to provide important information for detecting geothermal areas at Mount Ungaran and in other geothermal regions (Pratiwi et al., 2026; Setyawan et al., 2015, 2021, 2024). More recently, (Pratiwi et al., 2026) also successfully delineated structures controlling hydrothermal activity in the Arjuno–Welirang volcanic area. Therefore, the gravity method is highly suitable for the analysis conducted in this study.

Many regions worldwide (Indriana, 2019; Pramudya et al., 2025; Prihatini et al., 2025) have achieved successful results using this approach (Azis et al., 2022; Setyawan et al., 2015). However, validation data are still needed to assess whether the approach used in this study is effective. The next method we selected was the magnetic method, which is sensitive to the response of subsurface heat sources. We used Emag2v3 data from Meyer et al., (2017), which were analysed to estimate Curie depth. Several studies have also shown that Curie Point Depth (CPD) can be used to derive thermal gradients and heat flow based on the Curie temperature of magnetite (Demarco et al., 2021; Kassa et al., 2022; Kongpet & Kanjanapayont, 2024; Mono et al., 2018). A previous study by Muckharom et al., (2026) reported that the magnetic method is effective for estimating heat flow in several areas of Sumatra using Curie-depth analysis.

Based on these considerations, this study integrates several methods to assess geothermal potential in the Pusuk Buhit area, namely LST, FFD, gravity, and magnetic methods. The objective of this study is to identify geothermal potential in the Pusuk Buhit area in a more comprehensive manner. The originality of this study lies in the integrated use of geophysical and remote sensing methods. Its main novelty is the focus on the Pusuk Buhit area, which is still at an early exploration stage and therefore requires multiple types of data to support geothermal development. In addition, the novelty of this study lies in integrating geothermal and structural parameters, particularly through the application of the magnetic method to assess the regional-scale heat source, while hot fluids generally migrate through subsurface rock fractures or accumulate in reservoirs. The presence of these fractures and reservoirs is then identified using gravity and FFD methods, while surface thermal manifestations are analysed using the LST method. The study thus provides a more robust framework for reducing uncertainty in preliminary geothermal targeting, especially in dormant volcanic systems where surface manifestations are limited or ambiguous.

2. STUDY AREA

This study focuses on the Mount Pusuk Buhit geothermal zone, Samosir Regency (North Sumatra), which is part of the Simbolon Samosir Geothermal Working Area and is characterized by volcanic geomorphology with documented geothermal surface manifestations. Simbolon Samosir Geothermal area position 2°33’15.62” S - 2°38’34.39” S and 98°36’1,89 E - 98°41’22.65” E, the elevation height 904 - 2157 m (**Fig. 1**). Mt. Pusuk Buhit is classified as a dormant quaternary volcano. This research utilizes three satellite-compiled geophysical datasets: Landsat-8 OLI/TIRS, Global Gravity Model Plus (GGM+), and EMAG2-V3. Global Gravity Model Plus (GGMPlus) imagery to derive surface indicators (composite bands, NDVI, and land surface temperature). GGMPlus satellite gravity data to analyze subsurface density structure patterns at approximately ~200 m spatial resolution. EMAG2-V3 compiled magnetic anomaly data to estimate Curie Point Depth (CPD) and derive thermal proxies (geothermal gradient and heat flow) at a regional scale (Hirt et al., 2013; Meyer et al., 2017). Landsat-8 OLI/TIRS is downloaded from USGS, GGMPlus is free support from Curtin University, and EMAG2-V3 is free from ICGEM.

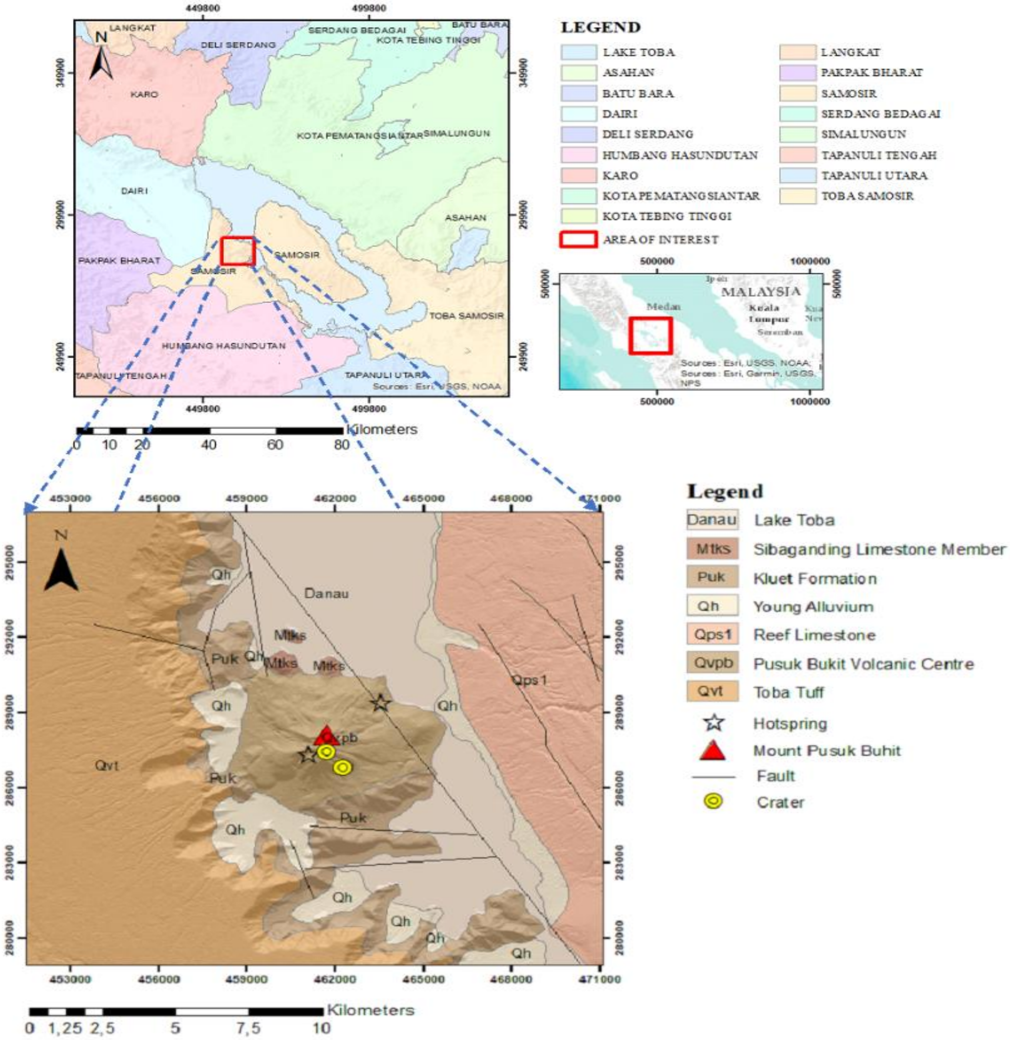

Fig. 1. The research area and geological map of Pusuk Buhit.

Based on the geological map on **Fig. 1**, The Sidikalang and (part of) Sinabang, Sumatra by Aldiss, (1983), the formations in the study area consist of the Toba Tuff Formation (Qvt) with rhyodacite tuff (partially cemented), the Pusuk Buhit Formation (Qvpb) with dacite and/or rhyolite rock types, the Kluet Formation (Puk) with metacuarzic sandstone, metaclastic, shale, and phyllite rock types, the Kualu Formation (Mtks) with sibaganding limestone: biocalcilutite, and the Alluvium Formation (Qh) with gravel, sand, mud, fan conglomerate, diatomaceous earth, and coral.

3. DATA AND METHODS

3.1. Landsat-8 preprocessing and surface parameter retrieval

3.1.1. Normalized Difference Vegetation Index (NDVI)

Vegetation cover was quantified using the Normalized Difference Vegetation Index (NDVI) to reduce land-cover bias in thermal interpretation and to support emissivity estimation in heterogeneous volcanic terrain. NDVI was calculated as equation (1).

$$\mathrm{NDVI} = \frac{\mathrm{NIR} - \mathrm{Red}}{\mathrm{NIR} + \mathrm{Red}} \tag{1}$$

In this respect, NIR and Red represent near-infrared reflectance and red reflectance, respectively. Typically, low NDVI values are associated with sparse vegetation, exposed soil, or altered surface materials, whereas higher NDVI values are associated with more vegetative surfaces (Alqahtani et al., 2023).

3.1.2. Thermal radiance and brightness temperatures (TIRS)

Thermal processing used Landsat-8 TIRS measurements, beginning with conversion from the thermal band digital number (DN) to spectral radiance was expressed as equation (2).

$$L_\lambda = M_L \cdot Q_{cal} + A_L \tag{2}$$

where L_λ is spectral radiance, M_L is the radiance multiplicative scaling factor, A_L is the radiance additive scaling factor, and Q_{cal} is the quantized calibrated pixel value (DN).

Brightness temperature was then computed as equation (3).

$$T_B = \frac{K_2}{\ln\left(\frac{K_1}{L_\lambda} + 1\right)} \tag{3}$$

where T_B is the at-sensor brightness temperature (K) and K_1, K_2 are band-specific thermal calibration constants.

This radiance-to-temperature step provides a physically consistent thermal measure before correcting for surface emissivity.

3.1.3. Land Surface Temperature (LST) and emissivity correction

Land Surface Temperature (LST) was derived from brightness temperature with emissivity correction to better represent true surface conditions. A commonly used form that is adapted to the emissivity shown in equation (4).

$$\text{LST} = \frac{T_B}{1 + \left(\frac{\lambda T_B}{\rho}\right)\ln(\varepsilon)} \tag{4}$$

where λ is the effective thermal wavelength, $\rho \approx 1.438 \times 10^{-2}$ m · K(with $\rho = h\,c/\sigma$), and $\varepsilon$is land surface emissivity.

Emissivity was estimated via an NDVI-based approach to account for mixed land-cover conditions. Vegetation proportion (PV) was calculated as equation (5).

$$PV = \left(\frac{\text{NDVI} - \text{NDVI}_{min}}{\text{NDVI}_{max} - \text{NDVI}_{min}}\right)^2 \tag{5}$$

and emissivity was approximated using equation (6).

$$\varepsilon = 0.004 \cdot PV + 0.986 \tag{6}$$

This NDVI-based emissivity estimation is widely used to reduce LST error associated with variable surface materials (soil, vegetation, water) and is particularly relevant in volcanic terrains where alteration and land cover vary over short distances (Alqahtani et al., 2023).

3.2. GGMPlus gravity processing

The gravity field data used for this research is provided by GGMplus, a high-resolution representation of the global gravity field with nominally 200 m resolution on land. GGMplus is based on satellite gravimetry observations (GRACE and GOCE), terrestrial gravimetry observations, airborne gravimetry, marine gravity observations from altimetry, and models of topographic mass (Hirt et al., 2013). These gravity disturbances are ideal for geological or geophysical studies at a regional and local level, particularly over areas with limited land-based gravimetry data. Gravity data are affected by the simultaneous action of latitude, topography, the Earth's rotation rate, and the subsurface mass distribution.

The geological information on subsurface density changes can be uncovered after a series of standard corrections for gravity are applied to the data. The free-air correction is due to the decrease in gravity from the topographical datum to the observation level, where there is no mass between the observation level and the topographical datum on the ground.

The Bouguer and Terrain correction affected of the attraction due to the mass between the observation level and the datum by simulating an infinitely extended horizontal bed of homogeneous rocks of 2.67 g/cm³ density for continental regions (Blakely, 1995). The Bouguer anomaly was calculated using equation (7).

$$\Delta g_{Bouguer} = g_{obs} - g_n + \delta gFA - \delta gB + \delta gT \tag{7}$$

where g_{obs} is the observed gravity, g_n is the normal gravity, δgFA is the free-air correction, δgB is the Bouguer correction, and δgT is the terrain correction.

The terrain correction is particularly important in regions with significant topographic relief and improves the accuracy of the Bouguer anomaly (Arifianto et al., 2025). Analysis of subsurface density variations using local anomaly data. Separation of local and regional anomalies using the upward continuation method. Further study to strengthen the vertical and horizontal subsurface identification rock density variation model created using a 2D inversion model.

3.2.1. Inverse model

Gravity Inversion modelling is a quantitative geophysical method aiming to recover the subsurface pattern of density contrast responsible for a set of observed gravity anomalies, formulated as a solution of a regularised inverse problem. The inversion formula was calculated using equation (8).

$$\mathbf{d}=\mathbf{Gm} \tag{8}$$

where **d** is the vector of observed gravity anomalies at measurement locations, **m** is the model parameter vector (density contrasts in discretized cells), and **G** is the sensitivity matrix that relates the influence of each model cell on each observation.

The entries of **G** are computed from Newton's law of gravitation for the chosen cell geometry (e.g., prisms, tetrahedra). Inversion solves for **m** by minimizing an objective function and is calculated using equation (9).

$$\phi(\mathbf{m})=\|\mathbf{W}_{d}(\mathbf{d}_{obs}-\mathbf{G}_{m})\|^2+\lambda^2\|\mathbf{W}_{m}(\mathbf{m}-\mathbf{m}_{ref})\|^2 \tag{9}$$

where $\mathbf{d}_{\text{obs}}$ are observed data, $\mathbf{W}_d$ is the data weighting matrix accounting for measurement uncertainties, $\mathbf{W}_m$ is a regularization operator enforcing smoothness or focusing constraints, $\mathbf{m}_{\text{ref}}$ is a reference model, and λ is the regularization parameter balancing data misfit and model complexity (Blakely, 1995; Y. Li & Oldenburg, 1996).

3.3. Curie Point Depth (CPD)

Regional magnetic anomaly data were obtained from the EMAG2-V3 global compilation (2 arc-min grid at ~ 4 km altitude), which integrates satellite, marine, airborne, and shipborne magnetic surveys and applies kriging-based interpolation to improve consistency across heterogeneous survey tracks (Meyer et al., 2017). In CPD analysis, the grid was projected into overlapping sub-areas to support local spectral estimation. The CPD was estimated using the 2D spectral method applied to each windowed magnetic anomaly subset. The radially averaged power spectrum was computed from the 2D Fourier transform, and linear segments of ln[P(k)] versus wavenumber k were fitted to estimate depths of the magnetized layer following established formulations (C. F. Li et al., 2017). Z is the depth (vertical distance) from the Earth's surface to a magnetic source, measured positive downward, typically expressed in kilometers (km). The depth to the top of the magnetic source (Zt) was estimated from the high-wavenumber slope (s_(high)) and the centroid (Z_0) from the low-wavenumber slope (s_(low)) using the following relationship. That calculated using equation (10).

$$\ln P(k) = lnC - 2kZ \tag{10}$$

The depth to the bottom of the magnetized layer (Zb), interpreted as CPD, was then obtained using the relation proposed in the centroid method (Okubo & Matsunaga, 1994).

$$\mathrm{Z}_b = 2\mathrm{Z}_0 - \mathrm{Z}_\mathrm{t} \tag{11}$$

3.3.1. Geothermal gradient and heat flow from CPD

Assuming the Curie temperature (Tc) of dominant magnetic minerals is ~580°C, the geothermal gradient (G) can be approximated from the Curie isotherm depth as equation (12).

$$\frac{dT}{dZ} = \frac{\theta}{Z} = \frac{580°\mathrm{C}}{Z_b} \tag{12}$$

where T is the mean surface temperature (or a reference near-surface temperature), and Z_b is CPD (Kongpet & Kanjanapayont, 2024; Maden et al., 2009).

Geothermal heat flow (Q) was then estimated using Fourier's law in equation (13).

$$Q = \lambda \frac{dT}{dZ} = \lambda \left(\frac{580°C}{Z_b}\right) \tag{13}$$

where λ is the thermal conductivity of the crustal column (Saada, 2016). Spatial patterns of CPD, geothermal gradient, and heat flow were mapped and later integrated with the surface thermal and gravity-derived structural indicators.

The complete research flowchart is presented in **Fig. 2**.

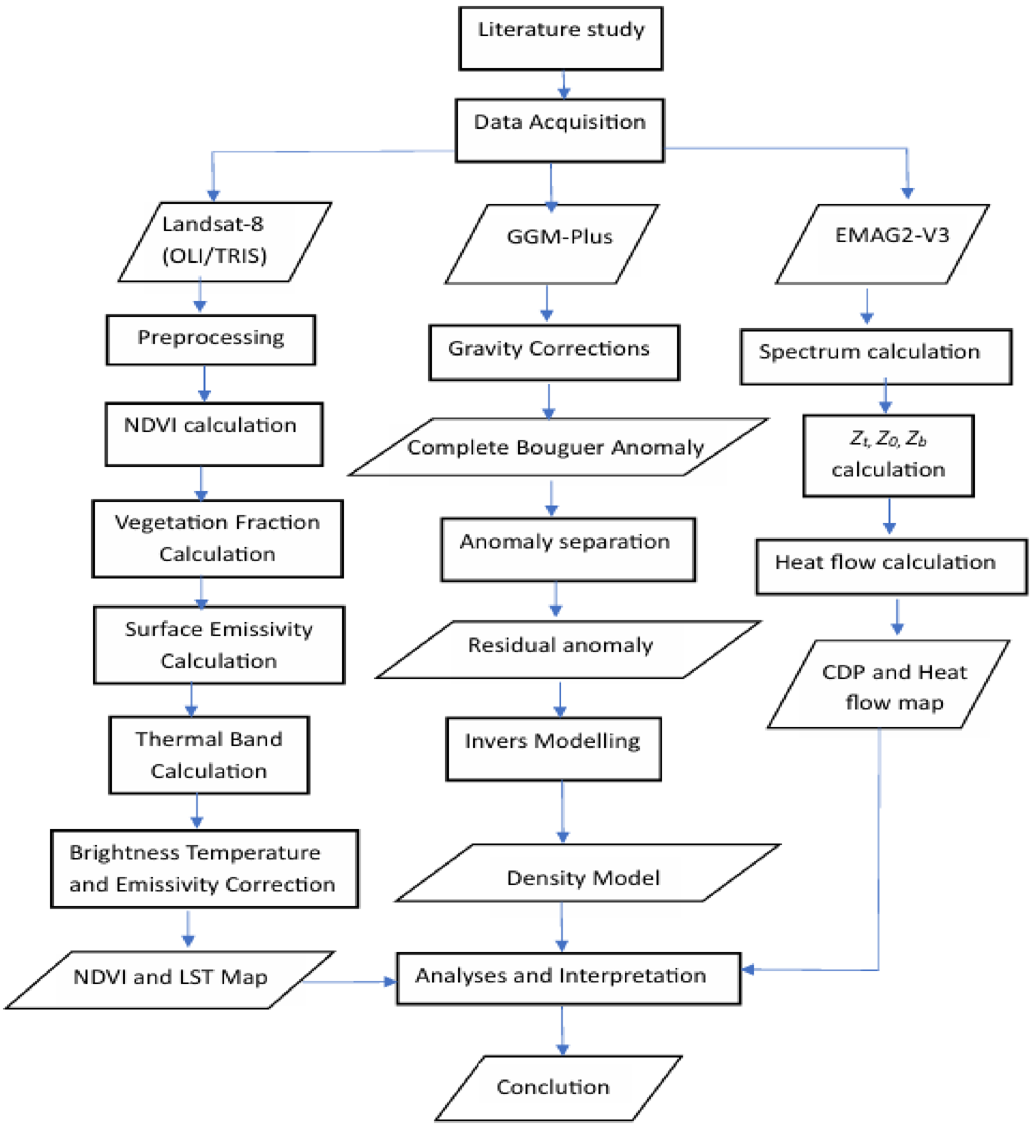

Fig. 2. The research flowchart.

4. RESULTS

4.1. NDVI and LST

The Landsat 8 composite band provides a first glance at heterogeneity, where it is possible to distinguish geomorphological differences based on volcanic cones, flow units, and potential alteration areas at Mount Pusuk Buhit. The geomorphological differences are important as geothermal surface features in volcanic environments are known to be concentrated around areas that are characterised by alterations, exposed ground, and unique geomorphological features that indicate permeability. In this study, the composite imagery is used to contextualise the spatial distribution of subsequent thermal indicators by delineating surface units where thermal behaviour is expected to differ due to material properties and land cover. NDVI mapping shows in **Fig. 3a**, a clear spatial variation in vegetation density across the Pusuk Buhit.

The NDVI calculation results are -0.51 to 0.87. The NDVI at the hot spring is lower than its surroundings, at -0.51 to 0.17. The northeastern hot spring has a high anomaly pattern flanking the fault line. Other areas with low NDVI include Lake Toba and residential areas. Mount Pusuk Buhit has relatively well-maintained vegetation density. NDVI assists in the identification of areas that are sparsely vegetated but could be geothermally significant because the heat anomaly is easier to detect where the surface energy contrast caused by vegetation is low. Areas that have high NDVI values suggest that the vegetation is dense and could potentially obscure the surface heat through the processes of evapotranspiration and shading. In view of the above, the heat anomaly needs to be assessed in the context of vegetation. As already stated, the NDVI-heat anomaly is consistent with other research that suggests that vegetation indices show positive associations with geothermal-related heat anomalies where surface heat is high in areas that have less vegetation (Alqahtani et al., 2023; Azis et al., 2022; Chan & Chan, 2023).

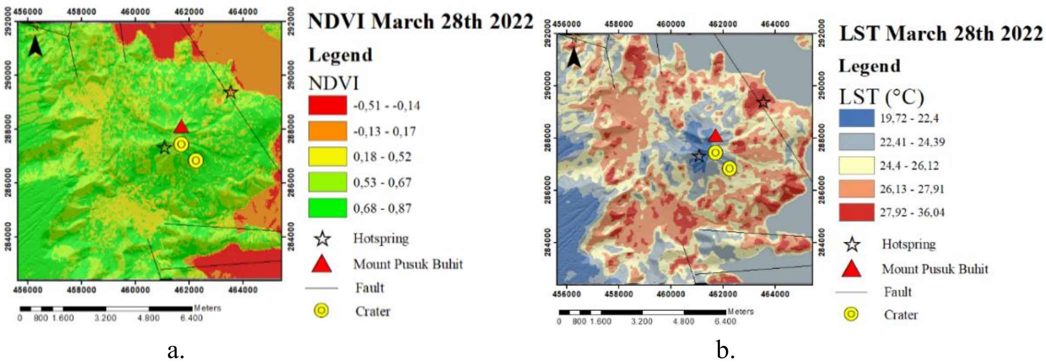

Fig. 3. Spatial distribution derived from Landsat-8 TIRS across the study area a) NDVI values highlighting areas of low vegetation density associated with altered or thermally affected zones, b) Land Surface Temperature (LST) showing the distribution of surface thermal anomalies

The entire research area has an LST of 19.720°C to 36.04°C. The peak area of Mount Pusuk Buhit has a low LST compared to its surroundings. There are 2 hot springs, on the west side of the crater and on the northeast of the crater. Hot spring in the northeast are in a fault area that trends southeast - northwest. The LST values at hot springs are different, ranging from 22.41°C to 24.39°C. Emissivity-corrected LST mapping reveals that localized thermal anomalies are largely confined along the flanks of Mount Pusuk Buhit (**Fig. 3b**). The hotspots are not continuous but rather localized, implying focused permeability pathways for near-surface geothermal activity. LST anomalies indicate increased flow of heat in the vicinity of near-surface fluids moving upward or heat flow from underlying hotter regions. This finding is consistent with research that associates Landsat thermal anomalies with geothermal phenomena, such as hot springs and fumaroles. In previous research carried out in Taiwan and Indonesia, it has been known that satellite thermal anomalies tend to coincide with geothermal activity, thereby making Landsat a thermal anomaly mapping tool employed for the investigation of geothermal potential (Chan & Chan, 2023; Muhajir et al., 2023). In Pusuk Buhit, Landsat-8 thermal anomaly regions are identified as potential domains of geothermal manifestation to be verified by additional subsurface factors.

4.2. CBA and Residual Anomaly

The GGMplus data used is the gravity disturbance, which is then corrected to CBA. Bouguer and Terrain corrections use an average density of 2.67 g/cc. CBA is obtained in the range of -86.6 mGal to -74.5 mGal. High anomalies (-81 mGal to 74.5 mGal) cover Mount Pusuk Buhit, while low anomalies (-86.6 mGal to 83 mGal) are in the Pusuk Buhit peak area. The distribution of CBA values is mapped as shown in **Fig. 4a**. In the processed GGMPlus gravity anomaly map, there are identifiable regions with positive and negative values. The negative regions point to regions of lower density, which may include regions with fractures or hydrothermal zones associated with geothermal resources. The positive regions may point to regions with higher density associated with competent volcanic rocks.

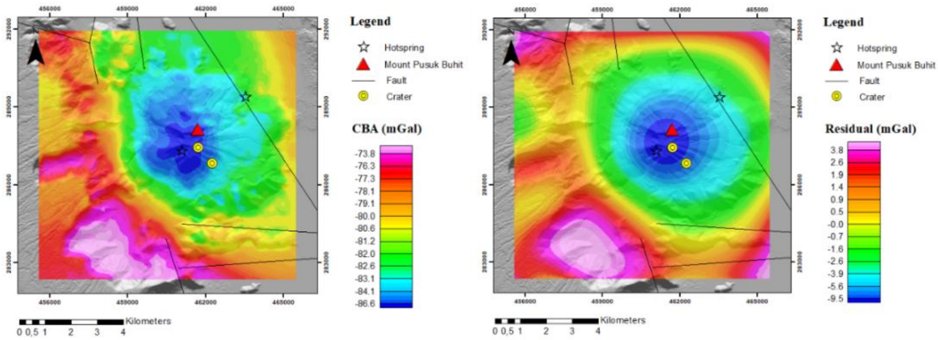

a. b.

Fig. 4. a) Bouguer gravity anomaly map and b) residual anomaly map beneath Mount Pusuk Buhit derived from GGMPlus

Further analysis was conducted to separate local and regional anomalies using the upward continuation method. Upward continuation is an effective approach to minimize high-frequency noise and focus interpretation on regional gravity trends relevant to geothermal systems (Muhajir et al., 2023). By obtaining regional values, local/residual anomaly values can be obtained.

Fig. 4b shows a map of the distribution of residual anomaly values ranging from -9.5 mGal to 3.8 mGal. The geothermal area is situated in a low to moderate anomaly zone, characterized by blue to green colors (-9.5 mGal to -2.6 mGal). This matches the conventional structural interpretation of geothermal data, where positive values are associated with magmatic intrusions and/or structural highs, and negative values are associated with fractured and altered areas where geothermal fluids might be present (Alqahtani et al., 2023). In this context, the gravity map of the Pusuk Buhit area serves as an indicator of the underlying structural characteristics, assisting in determining whether the thermal anomalies are of geothermal origin or of a transient nature.

4.3. Density Modeling

Subsurface modeling of the Pusuk Buhit area based on residual anomaly data, as shown in **Fig. 5.** Inverse modeling was performed on the B-B' traverse with an SN direction crossing the central formation of Pusuk Buhit (Qvpb), the Kluet formation (Puk), faults, and hot spring manifestations.

The rock density beneath the B-B' line ranges from 1.97 g/cc to 2.96 g/cc. The geothermal area has a density of 2.3 g/cc to 2.65 g/cc and is associated with a low-density zone in the south. There is a medium to low-density zone to the south, the position of which coincides with the previously mapped geological structure (fault).

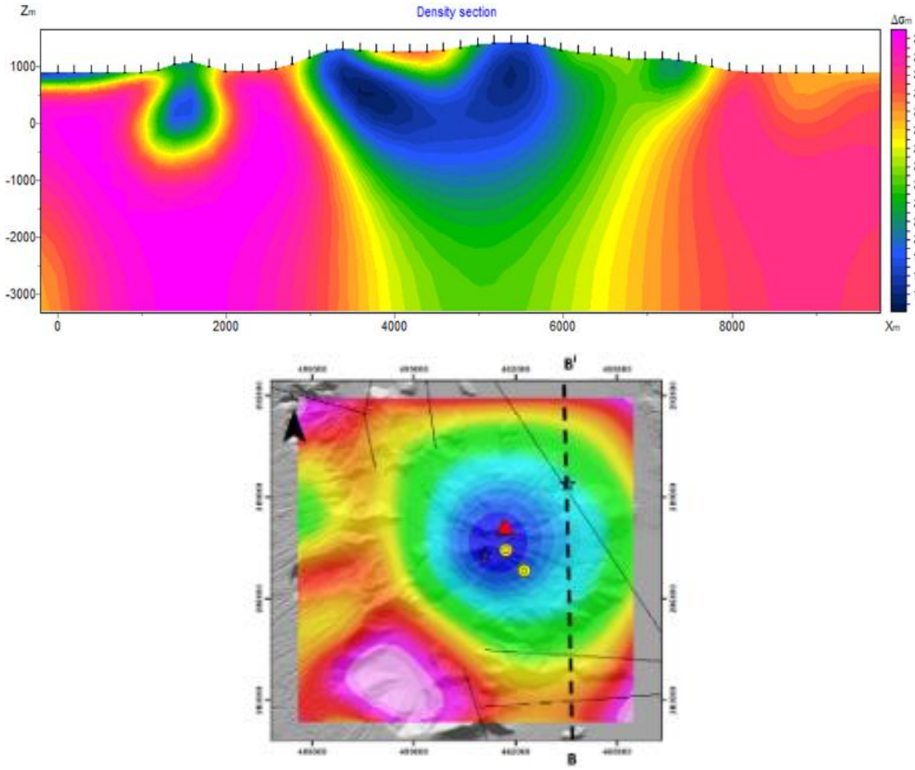

Fig. 5. Subsurface density model Pusuk Buhit area (line 463261,592 m E).

4.4. Fault and Fracture Density (FFD) Analysis

A map showing the spatial distribution of fracture linear density values is presented in **Fig. 6**.

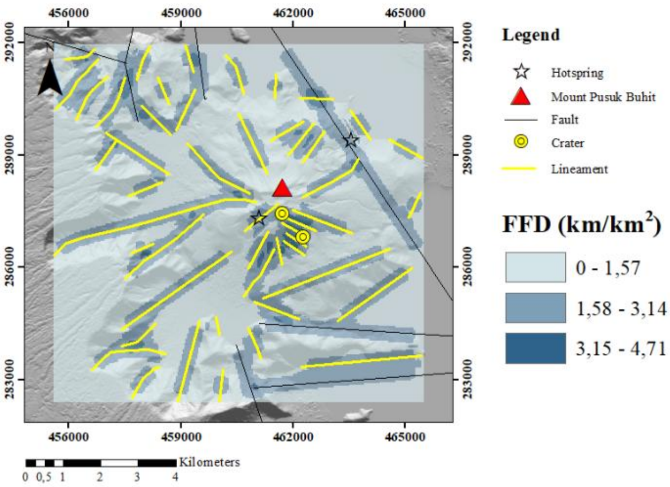

Fig. 6. Fracture Density (FFD) Pusuk Buhit.

High density values, ranging from 3.15 to 4.71 / km, are evident along the mountain peaks, while low to medium density values range from 0 to 1.57 /km and from 1.58 to 4.14 /km, respectively. Hot water manifestations pass through faults in areas with medium fracture density. High-density values are found on Mount Pusuk Buhit, which is related to the deformation of the volcano/past volcanic activity of Mount Pusuk Buhit, resulting in the formation of many faults and fractures.

Mount Pusuk Buhit is a recharge area in the geothermal system, serving as an entry point for rainwater to fill the permeable zone in the geothermal system. The lack of hot springs in the summit area and the presence of the hot springs on the northeastern slope of the mountain can be explained on the basis of geological structure. The area of manifestation of the hot spring, as indicated in the map, is located in the junction zone of the fracture system and the fault. This suggests that the structure is likely the path of hydrothermal fluid rising from below the surface. Additionally, this reinforces the assumption that Mount Pusuk Buhit still exhibits geothermal activity, even though it is currently inactive.

4.5. Curie Point Depth (CPD) and Heat Flow (HF)

Fig. 7, the trend of Curie Depth Point (CPD) data to surface heat flow values at the Pusuk Buhit geothermal area shows a distinct inverse trend, where areas with shallower Curie depths relate to areas of relatively high surface heat flow. The Curie Depth Point values are generally around 28 to 31 km, which correlates well with heat flow values of around 48 to 50 mW/m², which show a moderate heat flow regime. This trend correlates well with the theory of conductive heat flow, where the heat flow values increase as the Curie depth values decrease.

In the absence of very shallow Curie depths (<15 km), as would be expected in an actively magmatic geothermal environment, a moderately low heat flow as determined from the CPD data suggests a deep thermal source and not a magma chamber. This suggests that Mount Pusuk Buhit is a dormant (Type-C) volcanic environment in which there is little manifestation at the surface and which is controlled more by regional processes than magmatic intrusions.

The relationship between Curie Depth Point (CPD) and heat flow observed in this study is consistent with recent spectral analyses applied to aeromagnetic data, which demonstrate that shallower Curie depths correspond to higher geothermal gradients and increased surface heat flow (Ejiga et al., 2022). Specifically, several regional studies have shown that mapping CPD provides an indirect but reliable approach for estimating the thermal regime of the crust, including geothermal gradient and heat flow distribution (Boumehdi et al., 2025; Muckharom et al., 2026). The determined CPD and heat flow values provide a basis for understanding the thermal structure of crustal segments and support the interpretation of subsurface heat transfer processes in geothermal contexts.

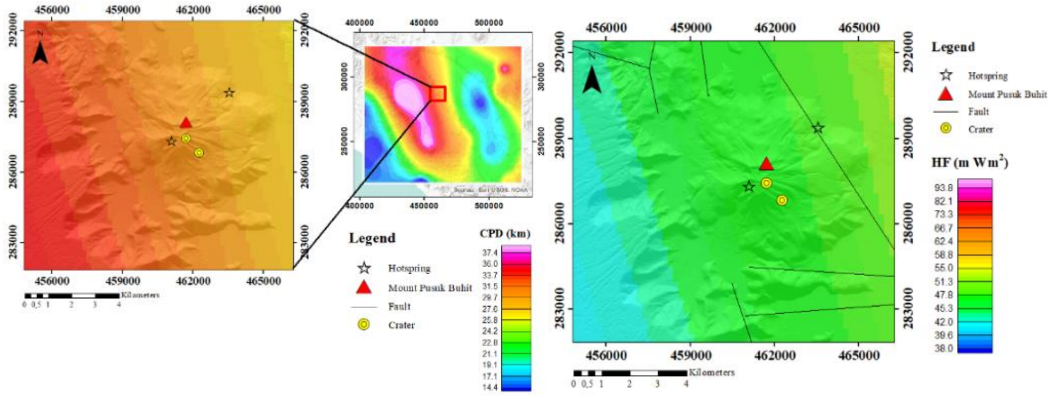

Fig. 7. Integrated interpretation of surface and subsurface results

Integration analysis was performed by overlaying LST, NDVI, CPD, CBA, residual gravity anomaly, and subsurface density model profiles on the line 463261.592 m East. This line passes through two fault zones (east-southwest and east-northwest faults) and geothermal manifestations. The analysis presented in **Fig. 8** shows a consistent spatial association between surface heat signals, subsurface heat signals, and subsurface density structures. The north-south cross-section in the figure demonstrates the integrated response of surface thermal anomalies, gravity anomalies, subsurface density patterns, and estimates of Curie Point Depth (CPD)-Heat Flow (HF), which distinguish two major sections: the crater area (grid points 23-30) and the manifestation area (grid points 35-42).

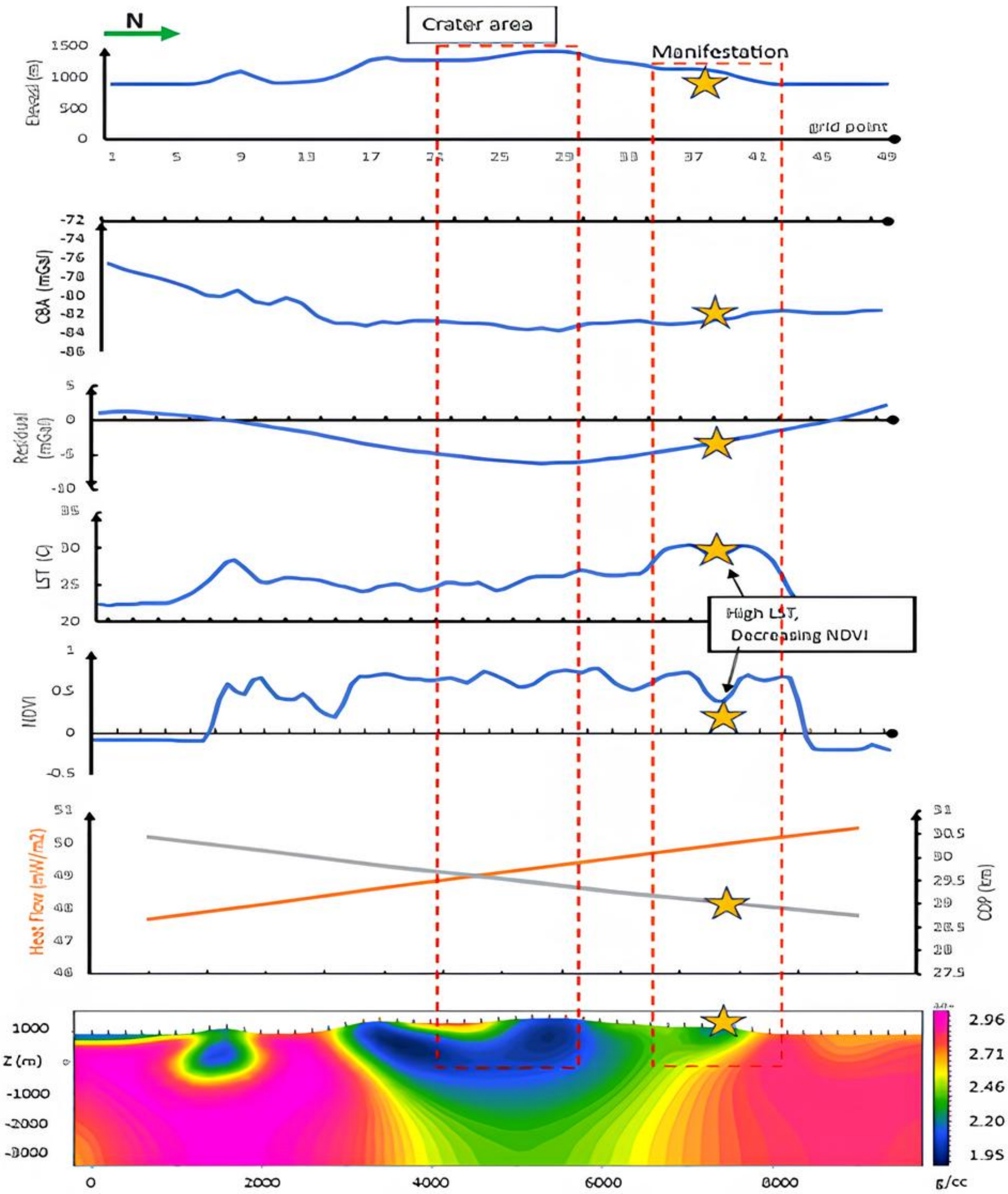

Fig. 8. Integrated map overlaying LST anomalies and gravity anomaly patterns to delineate prospective geothermal zones at Mount Pusuk Buhit.

In terms of morphological characteristics, the crater area is found within the area of relatively higher topography, while the manifestations are found downslope following the major topographic ridge, suggesting that the surface expressions of geothermal activity are not controlled by topography alone but are dominated by subsurface patterns and structural pathways that channel heat and fluid migration. The Complete Bouguer Anomaly (CBA) is characterized by a regional decrease from the northern part of the area toward the central part of the section, followed by a trend of flattening. Significantly, there is a slight modification of the trend of the CBA near the manifestation area, which suggests a change of the regional density domain, perhaps from lower-density volcanic-altered rocks to a more competent and higher-density block, or the influence of a major structural boundary. This is also reflected by the residual gravity anomaly, which is more responsive to shallow-to-intermediate crustal density contrasts, as the residuals progressively become more negative toward the central part and then reverse, becoming progressively more positive (less negative, approaching zero) at the manifestation area. This is generally expected for a local density contrast or a sharp lateral density transition across a lithologic contact or fault boundary. In geothermal areas, this kind of residual gravity anomaly is generally interpreted as a structurally damaged and fractured area of higher permeability, which acts as a structurally controlled conduit for the upward migration of hydrothermal fluids and heat.

The strongest surface thermal anomaly is captured in the Land Surface Temperature (LST) curve, which shows a clear, localized LST maxima in the manifestation area (around 300°C - 32°C). The sharpness of the LST maxima and the fact that it does not correlate straightforwardly with topography argue for a localized, geothermal heat leakage feature, rather than a strictly atmospheric and topographic feature. Most importantly, the LST maxima are associated with a simultaneous decrease in NDVI for the same area, such that the high LST and decreasing NDVI feature together offer a reliable proxy for the presence of non-atmospheric, high-temperature conditions, indicative of stressed and possibly altered biologic and surface conditions in response to the presence of subsurface heat and hydrothermal fluids.

At depth, the density cross-sectional profile further emphasizes the structural control, in which the crater area is positioned over a relatively large, lower-density area possibly indicative of unconsolidated volcanic materials, pervasive alteration, and a possibly fractured and porous area, and in which the manifestation area shows a sharp density gradient, from lower to higher density, indicative of a block boundary and large fault/contact, which may act to channel fluids upwards. This suggests that surface manifestations are preferentially found not necessarily over the center of the density-low area, but over its edge, where the density and structural contrasts are largest, and where permeability contrasts may act to channel and concentrate the release of hydrothermal fluids.

These multiparameter measurements are mutually consistent within the CPD-HF panel, which indicates an inverse correlation between Curie depth and heat flow. The data point corresponding to the manifestation zone is distinguished by its relatively shallower CPD (29 km) and its higher HF (48-50 mW/m^2) value than the other profiles on the transect, which suggests an elevated upper-to-middle-crustal thermal regime and an increased geothermal gradient below the manifestation zone. While the CPD measurements are generally in the moderate to deep range and do not suggest an abnormally shallow Curie depth as would be expected for shallow, magmatically active geothermal systems (CPD < 15 km), the spatial coincidence of the elevated HF, the LST peak, the low NDVI, the residual gravity transition, and the sharp density boundary strongly suggests the presence of a deep-seated regional heat source underlying the Pusuk Buhit system as a dormant volcanic geothermal system, and the surface expression is due to the structurally focused flow of heat and fluid. In this model, the crater area is dominantly a morphologic and/or alteration-recharge area, while the manifestation zone is the discharge area, which develops where the structural permeability is maximal, as indicated by the gravity and density contrasts, and is the location where the subsurface thermal anomaly is optimally manifested on the surface through the LST and the corresponding NDVI reduction. These integration findings are consistent with previous studies that validate the combined approach of thermal remote sensing and gravity to delineate geothermal prospect zones.

In various prospects, including case studies in Indonesia, thermal anomalies from Landsat/ASTER are reported to correlate with gravity anomalies indicating subsurface reservoirs, thereby increasing confidence in integrated surface and subsurface screening (Muhajir et al., 2023; Weldeyohannes et al., 2022). The comprehensive analysis is characterized by surface indicators (LST anomalies, reduced vegetation through NDVI, shallow CPD compared to the surrounding area, alignment and position of manifestations) supported by subsurface structural evidence (gravity-based density contrasts and indications of fracture domains). This approach is consistent with commonly used criteria for defining more reliable geothermal prospect zones (Bian et al., 2024; Chen et al., 2021).

5. DISCUSSIONS

Compared with geothermal systems in similar volcanic environments, such as Taiwan and the Ethiopian Rift (Chan & Chan, 2023; Weldeyohannes et al., 2022), the Pusuk Buhit system exhibits a comparable pattern. Surface thermal anomalies are spatially associated with structure-controlled permeability zones, rather than directly overlying the primary heat source. In contrast to active volcanic systems, which typically have a shallow Curie Point Depth (CPD) (<15 km), the deeper CPD values in the Pusuk Buhit area (28–31 km) suggest that the geothermal system is controlled more by regional conductive heat flow than by shallow magmatic intrusions, which are characteristic of dormant volcanic systems.

Gravity data strengthen the geological validation of the surface thermal model. Negative gravity anomalies may indicate low-density zones associated with fractures, hydrothermal alteration, and/or fluids. In contrast, positive anomalies reflect high-density rocks, such as intrusive or compacted volcanic rocks that could act as heat sources or fluid barriers. These patterns are also observed in other volcanic environments, where positive anomalies are linked to heat sources and negative anomalies to fracture zones or hydrothermal systems (Alqahtani et al., 2023; Pratiwi et al., 2026).

Furthermore, the presence of LST anomalies above the gravity structure strengthens the evidence that the geothermal system at Mount Pusuk Buhit is controlled by geological structures. Areas with high LST values indicate heat flow to the surface through fractures and faults, which can also be identified through structural patterns derived from gravity anomalies and remote sensing (Muhajir et al., 2023; Rabuffi et al., 2025). The integration of Landsat-8 thermal imagery and the gravity satellite GGMPlus has been shown to improve exploration capabilities by linking surface temperature variations with subsurface structural patterns associated with geothermal systems (Muhajir et al., 2023; Weldeyohannes et al., 2022).

The Landsat-8 and GGMPlus integration approach provides key advantages for early-stage exploration. It lowers costs, reduces risks, and efficiently covers large areas (Bian et al., 2024; Muhajir et al., 2023). The best target zones are where LST anomalies—unusual surface heat—align with gravity-derived structures that indicate subsurface density changes. These areas meet two main geothermal criteria: available heat and pathways for fluid flow, such as faults or fractures. This integration approach identifies these features by combining surface thermal indicators with subsurface density variations (Putri et al., 2021).

In this context, the Curie Point Depth (CPD) derived from magnetic data reveals regional variations in thermal conductivity. However, it does not directly map local upflow zones controlled by fault permeability. Therefore, the difference between the surface hotspot and the shallowest CPD does not necessarily lower geothermal prospectivity. Instead, it shows that the geothermal system at Mount Pusuk Buhit is interpreted as structure-controlled, with local effects on regional thermal trends. Also, interpreting the link between surface features and CPD needs caution, since the EMAG2-V3 model shows different scales that better reflect regional features. The CPD is best for outlining a regional thermal framework. For prospect mapping, higher-resolution data (such as structural mapping, geochemistry, resistivity (e.g., MT), and multi-temporal LST–NDVI analysis) are needed.

6. CONCLUSIONS

This study confirms that the integration of Landsat 8 surface thermal anomalies with GGMPlus gravity data provides a reliable and cost-effective approach for preliminary geothermal exploration at Mount Pusuk Buhit. The NDVI calculation results are -0.51 to 0.87. The NDVI at the hot spring is lower than its surroundings, at -0.51 to 0.17. The research area has an LST of 19.72°C to 36.04°C. The spatial coincidence of high LST anomalies with negative gravity values indicates that geothermal heat and fluids are preferentially channeled through low-density subsurface zones associated with fractures, altered rocks, and fault-controlled permeability, while positive gravity anomalies reflect denser volcanic or intrusive bodies that may act as heat sources or structural barriers. The strong correspondence between LST anomalies and gravity-defined structural corridors supports a structurally controlled geothermal system rather than a shallow magmatic heat source, with low NDVI–high LST areas further suggesting surface thermal stress or hydrothermal alteration. The Curie Depth Point values are generally around 28 to 31 km, which correlates well with heat flow values of around 48 to 50 mW/m^2. Although Curie Point Depth (CPD) derived from magnetic data effectively constrains the regional thermal regime, it does not resolve localized hydrothermal upflow, indicating that the lack of coincidence between surface hotspots and shallow CPD does not preclude geothermal prospectivity.

This study shows that integrating Landsat 8 thermal data with GGMPlus gravity data provides an effective and low-cost framework for preliminary geothermal exploration at Mount Pusuk Buhit. Its main scientific contribution lies in demonstrating that geothermal surface manifestations are spatially associated with gravity-defined low-density structural zones, highlighting the dominant role of fault- and fracture-controlled permeability in the geothermal system. In addition, the study clarifies that Curie Point Depth reflects the regional thermal structure rather than localized hydrothermal upflow. These findings support the use of integrated thermal and gravity analysis as a transferable prefeasibility tool for geothermal exploration in complex volcanic settings.

ACKNOWLEDGEMENT

We acknowledge the use of Landsat data provided by the United States Geological Survey (USGS), GGMPlus gravity data were freely provided by Curtin University, the EMAG2-V3 magnetic model was obtained free of charge from the International Centre for Global Earth Models (ICGEM). The authors acknowledge the use of AI-based tools for assistance with language polishing and manuscript organization. The tools did not influence the scientific content, and all responsibility for the manuscript rests with the authors.

REFERENCES

Ahmadi, H., & Pekkan, E. (2021). Fault-based geological lineaments extraction using remote sensing and gis—a review. *Geosciences (Switzerland)*, *11*(5). https://doi.org/10.3390/geosciences11050183

Aldiss, D. T. (1983). *Geologic map of the Sidikalang quadrangle, Sumatra 1:250,000*.

Alqahtani, F., Aboud, E., Ehsan, M., Naseer, Z., Abdulfarraj, M., Abdelwahed, M. F., & El-Masry, N. (2023). Geothermal Exploration Using Remote Sensing, Surface Temperature, and Geophysical Data in Lunayyir Volcanic Field, Saudi Arabia. *Sustainability (Switzerland)*, *15*(9). https://doi.org/10.3390/su15097645

Arifianto, I., Nishijima, J., & Wibowo, R. C. (2025). Maetec: An Optimized Matlab-Based Approach For Accurate And Efficient Terrain Correction In Complete Bouguer Anomaly. *Rudarsko-Geološko-Naftni Zbornik*, *40*(5), 43–56. https://doi.org/10.17794/rgn.2025.5.4

Azis, B. N. L., Sariningtyas, G. C., Ardiansyah, W., Wulandari, S., & Muhammad Azis Albar. (2022). Identification of Geothermal Manifestation With Integration of Geomagnetic Data and Landsat-8 Satellite Imaging in Umbul Temple - Telomoyo, Central Java. *PIT IAGI 51st 2022* .

Bian, Y., Ni, Y., Guo, Y., Wen, J., Chen, J., Chen, L., & Yang, Y. (2024). Urban Geothermal Resource Potential Mapping Using Data-Driven Models—A Case Study of Zhuhai City. *Sustainability (Switzerland)*, *16*(17). https://doi.org/10.3390/su16177501

Blakely, R. J. (1995). *Potential Theory in Gravity and Magnetic Applications*. Cambridge University Press, Cambridge Core.

Boumehdi, M., Hahou, Y., Amrouch, K., Berkat, N. E., Carneiro, J., Correia, A., & Sadki, O. (2025). New assessment of geothermal resources in Morocco: Evaluation of the curie point depth method using magnetic data for geothermal gradient and heat flow estimation. *Scientific African*, *28*. https://doi.org/10.1016/j.sciaf.2025.e02726

Chan, H.-P., & Chan, Y.-C. (2023). Thermal pattern at kueishantao (KST) volcano of Taiwan from satellite-observed temperatures and its implication. *Environmental Research Communications*. https://doi.org/https://doi.org/10.1088/2515-7620/ace760

Chen, W., Tenzer, R., Xu, X., Wang, S., & Wang, B. (2021). Moho Depth Estimation Beneath Tibet From Satellite Gravity Data Based on a Condensation Approach. *Earth and Space Science*, *8*(6).

Demarco, N., Prezzi, C., & Bettucci, S. (2021). Review of Curie point depth determination through different spectral methods applied to magnetic data. *Geophysical Journal International*, *224*(1), 17–39. https://doi.org/10.1093/gji/ggaa361/5881306

Ejiga, E. G., Yusoff, I. Bin, el Hidayah, N., & Kumar, R. (2022). Geothermal energy assessment through the Curie point depth, geothermal gradient, and heat flow around the Akiri hot spring region in Central Nigeria. *Environmental Earth Sciences*, *81*(4).

Grant, M. A., & Bixley, P. F. (2011). *Geothermal reservoir engineering* (2nd ed.). Academic Press.

Hirt, C., Claessens, S., Fecher, T., Kuhn, M., Pail, R., & Rexer, M. (2013). New ultrahigh-resolution picture of Earth's gravity field. *Geophysical Research Letters*, *40*(16), 4279–4283. https://doi.org/10.1002/grl.50838

Hutauruk, S. A. Y., Sabrian, P. G., Putri, R. I., Saepuloh, A., & Shoedarto, R. M. (2024). Identification of geothermal pathways by fault fracture density (ffd) and gravity methods in Karangan sub-district, East Kutai district, East Kalimantan province. *IOP Conference Series: Earth and Environmental Science*, *1373*(1). https://doi.org/10.1088/1755-1315/1373/1/012031

Indriana, R. D. (2019). Distribution of subsurface anomalies in the Muria Peninsula and depth analysis with euler deconvolution. *International Journal of Physical Sciences and Engineering*, *3*(3), 21–30. https://doi.org/10.29332/ijpse.v3n3.355

Kassa, M., Alemu, A., & Muluneh, A. (2022). Determination of Conrad and Curie point depth relationship with the variations in lithospheric structure, geothermal gradient and heat flow beneath the central main Ethiopian rift. *Heliyon*, *8*(11). https://doi.org/10.1016/j.heliyon.2022.e11735

Kongpet, P., & Kanjanapayont, P. (2024). Curie point depth from airborne magnetic data analysis for geothermal exploration in southern Thailand. *Journal of Asian Earth Sciences*, *261*. https://doi.org/10.1016/j.jseaes.2023.105984

Li, C. F., Lu, Y., & Wang, J. (2017). A global reference model of Curie-point depths based on EMAG2. *Scientific Reports*, *7*. https://doi.org/10.1038/srep45129

Li, Y., & Oldenburg, D. W. (1996). 3-D inversion of magnetic data. *Geophysics*, *61*(2), 394–408. https://doi.org/10.1190/1.1443968

Maden, N., Gelisli, K., Eyuboglu, Y., & Bektas, O. (2009). Determination of tectonic and crustal structure of the eastern pontide orogenic belt (NE Turkey) using gravity and magnetic data. *Pure and Applied Geophysics*, *166*(12), 1987–2006. https://doi.org/10.1007/s00024-009-0529-7

Meyer, B., Chulliat, A., & Saltus, R. (2017). Derivation and Error Analysis of the Earth Magnetic Anomaly Grid at 2 arc min Resolution Version 3 (EMAG2v3). *Geochemistry, Geophysics, Geosystems*, *18*(12), 4522–4537. https://doi.org/10.1002/2017GC007280

Mono, J. A., Ndougsa-Mbarga, T., Tarek, Y., Ngoh, J. D., & Owono Amougou, O. U. I. (2018). Estimation of Curie-point depths, geothermal gradients and near-surface heat flow from spectral analysis of aeromagnetic data in the Loum – Minta area (Centre-East Cameroon). *Egyptian Journal of Petroleum*, *27*(4), 1291–1299. https://doi.org/10.1016/j.ejpe.2018.07.002

Muckharom, A. A., Setyawan, A., Rahmani, I. Q., Dwi Indriana, R., & Martha, A. A. (2026). Geothermal Resource Assessment On Sumatra Island: Estimating Thermal Gradient And Heat Flow Based On Aeromagnetic Data Via Curie Point Analysis. *Journal of Applied Science and Engineering*, *31*, 26031017. https://doi.org/10.6180/jase.202608_31.017

Muhajir, M. A., Seminar, K. B., & Nelwan, L. O. (2023). Detecting thermal anomalies in lahendong geothermal prospect using ASTER TIR and Landsat 8. *Jurnal Pengelolaan Sumberdaya Alam Dan Lingkungan*, *13*(3), 494–503. https://doi.org/10.29244/jpsl.13.3.494-503

Okubo, Y., & Matsunaga, T. (1994). Curie point depth in northeast Japan and its correlation with regional thermal structure and seismicity. *Journal of Geophysical Research*, *99*(B11). https://doi.org/10.1029/94jb01336

Pramudya, A. N., Indriana], R. D., M Sabri, L. O., & Pahlevi, A. M. (2025). Gravity Data Decomposition through Upward Continuation and Wavelet Transform, Case Study at Muria Peninsula, Java Island, Indonesia. *International Journal of Research and Review*, *12*(3), 128–136. https://doi.org/10.52403/ijrr.20250318

Pratiwi, R. N. J., Martha, A. A., Hartono, H., Wijayanti, R., Muckharom, A. A., Kinanti, A. S. A., & Ngaeni, N. P. N. (2026). Identification of Subsurface Geological Structures of the Arjuno-Welirang Geothermal Potential Area Using the Gravity Method. *Malaysian Journal of Fundamental and Applied Sciences*, *22*(1), 90–101. https://doi.org/10.11113/mjfas.v22n1.4573

Prihatini, A., Indriana, R. D., Setyawan, A., & Fahmi, M. (2025). Seismotectonic Characteristics of the Cugenang Fault, Cianjur, West Java, Based on a-Value, b-Value, Seismic Moment and Satellite Gravity (Earthquake Data of 2008-2023). *Sains Malaysiana*, *54*(8), 1889–1900. https://doi.org/10.17576/jsm-2025-5408-02

Putri, D. R., Ismail, N., Idroes, R., Rizal, S., Nur, S., & Nanda, M. (2021). Analysis of Land Surface Temperature (LST) in Bur Ni Geureudong Geothermal Field, Aceh, Indonesia Using Landsat 8 OLI / TIRS Images. *Chiang Mai University Journal of Natural Sciences*, *20*(4), 1–13. https://doi.org/10.12982/CMUJNS.2021.084

Rabuffi, F., Musacchio, M., Silvestri, M., Cianfarra, P., Salvini, F., & Buongiorno, M. F. (2025). Integrating satellite remote sensing and proximal data to investigate the role of brittle tectonics in the distribution of geothermal surface manifestations. Insights from the Parco Naturalistico delle Biancane - Larderello geothermal field (Southern Tuscany, Italy). *Geothermics*, *132*. https://doi.org/10.1016/j.geothermics.2025.103428

Rafiq, J., Abu-Mahfouz, I. S., Chavanidis, K., Arrofi, D., & Soupios, P. (2025). Spatial distribution of structural lineaments in the Al-Lith geothermal field, western Saudi Arabia: Remote sensing and aeromagnetic data analysis. *Journal of Asian Earth Sciences: X*, *13*. https://doi.org/10.1016/j.jaesx.2025.100191

Saada, S. A. (2016). Curie point depth and heat flow from spectral analysis of aeromagnetic data over the northern part of Western Desert, Egypt. *Journal of Applied Geophysics*, *134*, 100–111. https://doi.org/10.1016/j.jappgeo.2016.09.003

Saraswati, G. P., Prasetyo, Y., & Sukmono, A. (2019). Analisis Estimasi Energi Panas Bumi Dan Rekomendasi Lokasi Pembangkit Listrik Tenaga Panas Bumi Menggunakan Citra Landsat 8 (Studi Kasus : Kawasan Gunung Ungaran, Jawa Tengah). *Jurnal Geodesi Undip Januari*, *8*(1), 170–179. https://doi.org/https://doi.org/10.14710/jgundip.2019.22554

Setyawan, A., Khusna, L. M., Suseno, J. E., Rina, D. I., Yulianto, T., & Aribowo, Y. (2021). Detecting hot spring manifestations based on gravity data satellite on mountain Lawu. *Journal of Physics: Conference Series*, *1943*(1). https://doi.org/10.1088/1742-6596/1943/1/012034

Setyawan, A., Nadhila, M. F., Suseno, J. E., & Indriana, R. D. (2024). 2d Sparse Inversion Gravity Method For Subsurface Interpretation By Simpeg: A Case Study Of Ungaran Volcano. *Journal of Southwest Jiaotong University*, *59*(3). https://doi.org/10.35741/issn.0258-2724.59.3.36

Setyawan, A., Yudianto, H., Nishijima, J., & Hakim, S. (2015). Horizontal Gradient Analysis for Gravity and Magnetic Data Beneath Gedongsongo Geothermal Manifestations, Ungaran, Indonesia. *Proceedings World Geothermal Congress*, 19–25.

Telford, W., Geldart, L., & Sheriff, R. (1990). *Geofisika Terapan* (2nd ed.). Cambridge University Press.

Weldeyohannes, T. T., Hailu, B. T., Muluneh, A. A., & Kidane, T. (2022). Detection of geothermal anomalies in the Northern Lake Abaya geothermal field, Main Ethiopian Rift. *Journal of Volcanology and Geothermal Research*, *430*. https://doi.org/10.1016/j.jvolgeores.2022.107638

MONITORING RESERVOIR WATER LEVEL AND SURFACE AREA DYNAMICS USING SATELLITE ALTIMETRY AND OPTICAL IMAGERY: TSALKA RESERVOIR, GEORGIA

Nika TKESHELASHVILI [1*]**, *Tamar PAPACHASHVILI*** [1] ***& Giorgi BREGVADZE*** [2]

DOI: 10.21163/GT_ GT_2026.213.06

ABSTRACT

Monitoring of inland water body dynamics is essential for understanding hydrological variability and supporting sustainable management of freshwater resources, especially in regions with limited hydrometric observations. This study evaluates the potential of integrated use of Sentinel-3 radar altimeter data and PlanetScope optical imagery for monitoring surface water area and level parameters of the Tsalka (Khrami) Reservoir in Georgia over the period 2017–2024. Water level time series were derived from Sentinel-3 SRAL data, while reservoir surface area was extracted from PlanetScope imagery. Validation against in situ measurements demonstrates high accuracy of radar altimeter (Bias = 0.097 m, RMSE = 0.192 m, r = 0.997, NSE = 0.993). The results reveal pronounced seasonal and interannual variability of Tsalka Reservoir, with water levels ranging from 1498.86 m to 1508.42 m and surface area from 5.69 km² to 24.54 km². The study confirms that the combined use of altimetry and high-resolution optical data provides a reliable and cost-effective framework for hydrometric monitoring of medium size inland water bodies.

Keywords: *Hydrometric monitoring; Radar altimetry; Optical remote sensing; Tsalka Reservoir.*

1. INTRODUCTION

Effective monitoring of water levels, volumes, and surface area dynamics of freshwater lakes and reservoirs is a fundamental component of sustainable water resources management. It is essential for hydropower plant (HPP) operation, the proper functioning of drinking water and irrigation systems, and for assessing natural and societal risks associated with hydrological processes under ongoing climate change (Wang et al., 2025; Woolway et al., 2020). These issues are aligned with the United Nations Sustainable Development Goals 6, 13, and partially with Goal 14.

Monitoring of inland water resources has traditionally relied on in situ hydrological stations. Data collected from these stations are used to characterize the magnitude of variability and the spatio-temporal dynamics of both quantitative and qualitative parameters of specific water bodies. However, this approach is associated with several limitations, including the sparse distribution of hydrological stations due to high operational costs and the lack of a unified monitoring network. In addition, access to such data is often restricted, and heterogeneity in data types may introduce interoperability challenges (Luo et al., 2022; Chen et al., 2022).

----

[1] *Georgian Technical University, Department of Engineering Geodesy & Geoinformatics, Tbilisi, Georgia.*
[*] *Corresponding author tkeshelashvili.nika@gtu.ge, t.papachashvili@gtu.ge*
[2] *Ivane Javakhishvili Tbilisi State University, Department of Geography, Tbilisi, Georgia, giorgi.bregvadze@tsu.ge*

Georgia is relatively rich in water resources, with more than 26,000 rivers and over 1,350 lakes and reservoirs, including small glacial lakes. Nevertheless, the absence of a unified national water monitoring network remains a significant challenge. In recent years, monitoring conditions have improved for river systems; however, no hydrometric parameters are systematically observed by state institutions for lakes and reservoirs.

In cases where reservoirs are operated by hydroelectric power companies, water level monitoring is conducted by private operators, but such data are generally not accessible to the scientific community, relevant governmental agencies, or the public. For a large proportion of lakes and reservoirs, hydrometric data are entirely lacking, which substantially limits the assessment of freshwater resources, the advancement of scientific research, and effective water resources management. This limitation, in turn, constrains the development of multiple economic sectors dependent on these resources. Consequently, long-term changes in key quantitative indicators of water resources since the collapse of the Soviet Union and the subsequent independence of Georgia remain largely unknown, particularly in the context of ongoing, accelerated environmental and climate changes driven by both anthropogenic and natural factors.

To address these challenges facing the country, it is necessary to develop alternative approaches for water resource monitoring based on modern technologies. In recent years, advances in satellite remote sensing, in particular radar-based systems, have created new opportunities for monitoring the dynamics of inland water bodies with high temporal resolution and extensive spatial coverage. (Kossieris et al., 2024; An et al., 2022). Originally developed for oceanography, radar altimetry is now widely applied to lakes, rivers, and reservoirs, offering continuous observations largely independent of weather conditions and cloud cover (Jamali et al., 2025). Modern missions operating in synthetic aperture radar (SAR) mode, such as Sentinel-3, provide improved spatial resolution and accuracy compared to earlier low-resolution altimeters (Tang et al., 2023; Bazzi et al., 2025). At the same time, optical remote sensing techniques have demonstrated considerable potential for reconstructing long-term lake surface variability and analyzing changes in water extent, even in cases where image availability is limited (Haidu et al., 2024; El Orfi et al., 2025).

A number of recent studies have demonstrated the effectiveness of integrating satellite altimetry and optical remote sensing for inland water monitoring in different environmental settings (Zeng et al., 2023). Nevertheless, despite the increasing use of Sentinel-3 altimetry and PlanetScope imagery independently, studies combining these datasets for integrated assessment of reservoir water level and surface area dynamics remain relatively limited, particularly for small and medium reservoirs located in mountainous regions with complex shoreline morphology and sparse hydrological observations. In contrast, the present study is specifically oriented toward a medium-sized mountainous reservoir located in a region characterized by the absence of a unified inland water monitoring network and limited accessibility of in situ hydrometric data. The scientific contribution of this work therefore lies not only in the application of multi-sensor remote sensing techniques, but also in the adaptation and evaluation of an integrated methodological framework under conditions of strong seasonal shoreline variability, complex surrounding topography, and restricted ground-based observations. In addition, the study represents first long-term satellite-based assessments of reservoir water level and surface area dynamics in Georgia.

Therefore, the aim of this study is to evaluate the potential of integrated use of data from the European Space Agency's Sentinel-3 mission, with high spatial resolution PlanetScope optical imagery provided by Planet Labs, for the seasonal and multi-year monitoring of surface area and level fluctuations of the largest artificial reservoir in Georgia, the Tsalka (Khrami) Reservoir. Tsalka Reservoir, located in the Tsalka Municipality, southern Georgia, represents one of the most significant freshwater resources in the country. Its water is utilized for hydropower generation by three hydroelectric power plants, as well as for agricultural irrigation and fisheries. The primary inflow to the reservoir is provided by the Ktsia–Khrami river system, a transboundary river shared between Georgia and Azerbaijan. In addition, the study seeks to evaluate applicability of proposed methods for the monitoring of other lakes and reservoirs in Georgia within the coverage of these and similar remote sensing missions.

2. STUDY AREA AND DATASETS

2.1. Study area

The Tsalka (Khrami) Reservoir (**Fig. 1**) is located in southern Georgia, within the Kvemo Kartli region, in the central part of the Tsalka volcanic plateau, approximately 100 km southwest of the capital, Tbilisi. The reservoir was constructed in 1946 on the Ktsia–Khrami river system and, with a design surface area of approximately 33 km^2, represents the largest artificial water body in Georgia.

The Tsalka Reservoir is a channel-type reservoir. The steepness of its coastal slopes' ranges from 5° to 90°, reflecting highly variable shoreline morphology. The reservoir has a length of approximately 14.5 km, an average width of 2.4 km, and a maximum width of 3.5 km. Its average depth is 9.3 m, with a maximum depth reaching 25.0 m (Iordanishvili et al., 2023). The reservoir constitutes the central component of the Khrami Hydropower Cascade, supplying water to three hydroelectric power plants. In addition, it is used for irrigation and fisheries, highlighting its importance as a multifunctional freshwater resource at the national scale.

The hydrological regime of the reservoir is primarily controlled by inflows from the Khrami River and its tributaries, supplemented by atmospheric precipitation, snowmelt, and groundwater contributions. The reservoir exhibits pronounced seasonal variability, with water levels typically increasing during spring and early summer in response to snowmelt and elevated river discharge. In contrast, declining water levels are observed during autumn and winter, partly due to regulated outflows associated with hydropower generation.

The climatic conditions of the reservoir area are characterized by cold winters and mild summers. According to ERA5-Land data, the average annual air temperature at 2 m above the surface during the study period (2017–2024) ranges from 6.2 °C to 7.18 °C. Based on GPM data, the average annual precipitation varies between 591.32 mm and 842.14 mm.

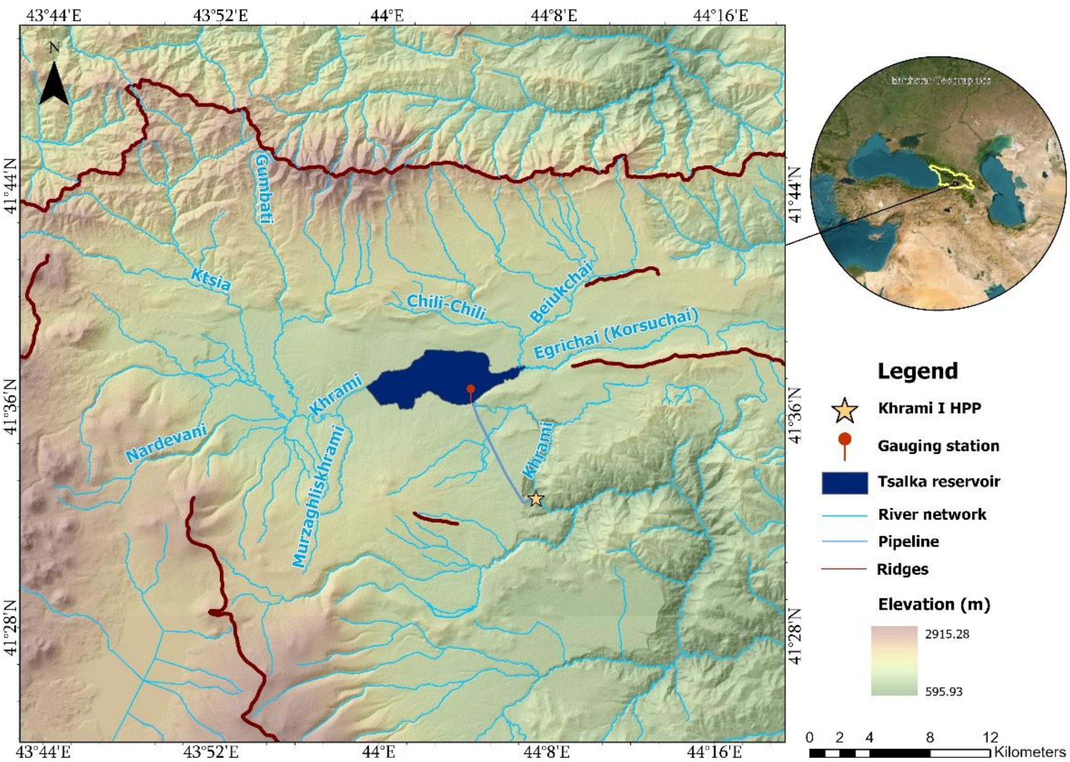

Fig. 1. Study area.

It should be noted that for the characterization of climatic parameters of the study area ERA5-Land and GPM datasets were used because no in situ meteorological observations was available. Although climatic characteristics of the region are discussed in Soviet-era literature, more recent datasets were preferred due to ongoing climate change and the necessity of representing contemporary climatic conditions during the study period. Both ERA5-Land and GPM products are widely used in recent climatological and hydrological studies because of their continuous temporal coverage and suitability for regions with complex topography and sparse observation networks (Dalla Torre et al., 2024; Jawad et al., 2024). The area surrounding the Tsalka Reservoir is sparsely populated. The landscape is predominantly composed of agricultural land and pastures, with steppe-type landscapes prevailing throughout the region. As noted above, under conditions of ongoing climate change and a sparse hydrological monitoring network, the use of satellite altimetry can significantly fill the data gaps. The hydrometric characteristics of the Tsalka Reservoir provide favorable conditions for testing this approach and for its potential integration into a national inland water monitoring system in Georgia.

2.2. Datasets

2.2.1. Sentinel-3 altimetry data

Sentinel-3 is a polar-orbiting, sun-synchronous Earth observation mission (98.6° inclination) developed as part of the European Space Agency's Copernicus Programme, designed to monitor ocean and land topography, land ice, inland waters, and key climate parameters. The first satellite, Sentinel-3A, was launched on 16 February 2016, followed by Sentinel-3B on 25 April 2018, while Sentinel-3C is scheduled for launch in 2026 (https://www.esa.int). The satellites operate at an orbital altitude of approximately 814.5 km, with a 27-day repeat cycle corresponding to 385 orbits per cycle. The Sentinel-3 platform carries three primary instruments: the Synthetic Aperture Radar Altimeter (SRAL), the Ocean and Land Colour Instrument (OLCI), and the Sea and Land Surface Temperature Radiometer (SLSTR). For the purposes of this study, data acquired from the SRAL instrument were used to derive reservoir surface heights. SRAL is a radar altimeter designed to measure surface elevations over oceans, ice sheets, rivers, and lakes. It operates as a dual-frequency sensor, utilizing Ku and C bands. The Ku band (≈13.57 GHz) provides the primary ranging measurements, while the C band (≈5.41 GHz) is used to correct for ionospheric delays. After SAR processing, the along-track spatial resolution of the sensor is approximately 300 m.

Sentinel-3 data used in this study were obtained from the French Centre for Ocean and Hydrosphere Topography (CTOH - https://www.legos.omp.eu/ctoh/) (requested and accessed on 21 May 2025). For the Tsalka Reservoir, measurements from track 526 were used for the period January 2017 to December 2024. However, at the time of the data acquisition, measurements for three months in 2024 (May–July) were not available; therefore, the analysis was performed excluding these data.

2.2.2. PlanetScope Imagery

The optical imagery used in this study was obtained under the Education and Research Program license of Planet Labs PBC. During the study period, the PS-2 four-band surface reflectance product was used for extraction of the monthly water-covered area of the Tsalka Reservoir. The imagery has a spatial resolution of 3 m and a radiometric resolution of 12 bits. The Dove/PS-2 satellites are equipped with four spectral bands covering the blue (455–515 nm), green (500–590 nm), red (590–670 nm), and near-infrared (780–860 nm) regions of the electromagnetic spectrum. This product is geometrically and atmospherically corrected.

PlanetScope's revisit time of approximately 1 day is particularly advantageous for this type of analysis. Its high temporal resolution enables the acquisition of multispectral imagery of the reservoir closely matching the Sentinel-3 altimetry measurement dates, thereby allowing accurate extraction of the water-covered area. In recent years, PlanetScope imagery has also been successfully applied in

Georgia and the Greater Caucasus region for glacier and proglacial lake mapping, highlighting its suitability for monitoring cryospheric and inland water environments (Tielidze et al., 2025a; Tielidze et al., 2025b).

2.2.3. In situ measurements

As noted, hydrometric parameters are not systematically monitored by relevant state institutions for lakes and reservoirs in Georgia. The Tsalka Reservoir forms part of the infrastructure of the Khrami Hydropower Cascade. In situ daily water level data for the period 2017–2024 were provided by JSC "KHRAMHESI I", the operating company of the Khrami I Hydropower Plant. The data were obtained from a single hydrological station equipped with an automatic level gauge and referenced to mean sea level.

3. METHODS

3.1. Satellite altimetry processing and water level time series extraction

Satellite radar altimeters measure surface elevation by determining the two-way travel time of a microwave pulse between the satellite and the reflecting surface. During propagation through the atmosphere, the radar signal is affected by several atmospheric and geophysical factors, requiring the application of corresponding corrections to obtain accurate surface elevations. Taking these effects into account, the orthometric height (h) of the water surface can be expressed as (Eq. (1)):

$$h = H - R_0 - \Delta R_{corr} - N \tag{1}$$

where, H is the satellite altitude above the reference ellipsoid, R_0 - the measured range at nadir (i.e., the distance between the satellite center and the reflecting surface), ΔR_{corr} represents the sum of applied corrections, and N denotes the geoid undulation. The corrections applied to the H and R have been the focus of several studies in the literature (Frappart et al., 2017).

The total correction term ΔR_{corr} accounts for atmospheric propagation delays and other geophysical effects (Crétaux et al., 2017) (Eq. (2)):

$$\Delta R_{corr} = \Delta R_{iono} + \Delta R_{dry} + \Delta R_{wet} + \Delta R_{solid} + \Delta R_{pole} \tag{2}$$

These components correspond, respectively, to ionospheric delay, dry tropospheric delay, wet tropospheric delay, and solid Earth and pole tide corrections. The application of these corrections is essential, as atmospheric refraction alters the propagation speed of the radar signal, leading to biases in surface height estimation. Tropospheric and ionospheric effects are particularly significant over inland water bodies; therefore, their accurate modeling is important. (Fernandes et al., 2014).

All parameters required for surface elevation retrieval are provided in the Level-2 GDR product provided by CTOH, including the geophysical corrections described above. It should be noted that the Level-2 GDR dataset includes multiple retracking algorithms (ICE-1, Ocean, and Seaice). In this study, the ICE-1 retracker was used, which is based on the Offset Center of Gravity (OCOG) technique. The altimetry data are provided in NetCDF (.nc) format and were processed and analyzed using the Panoply and ALTiS software tools. As previously mentioned, only a single Sentinel-3 ground track (Track 526) intersects the Tsalka Reservoir (**Fig. 2**).

For the construction of the reservoir water level time series, the initial step involved defining a virtual station at the intersection of the satellite ground track and the water surface. The maximum extent of the reservoir during the study period was delineated from a corresponding PlanetScope image and digitized in ArcGIS Pro.

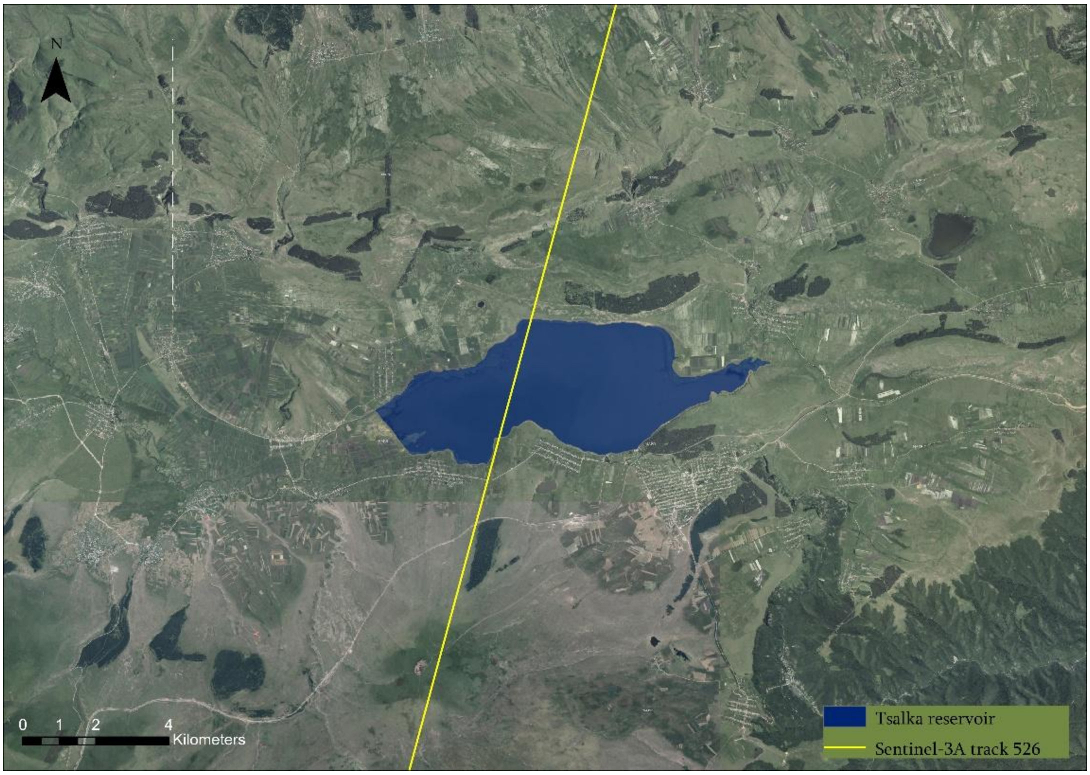

Fig. 2. Sentinel-3A track 526 over Tsalka Reservoir (superimposed on 2016-2017 orthomosaic provided by the National Agency of Public Registry of Georgia)

The resulting polygon was used to define the virtual station, which was subsequently imported into the ALTiS software to extract water level time series. Due to pronounced seasonal variations in the water-covered area of the Tsalka Reservoir, the extracted time series were manually adjusted on a date-specific basis, and altimeter footprints falling outside the water extent were removed. Following this filtering procedure, several altimeter footprints (up to a maximum of 12) remained within the virtual station for each measurement date.

Assuming hydrostatic equilibrium, the free surface of the reservoir represents an equipotential surface and is therefore approximately horizontal under normal conditions, particularly over such a limited spatial extent. Consequently, individual elevation measurements obtained for a given date are expected to be consistent. In practice, however, outliers may occur due to waveform contamination, mixed land–water echoes near the shoreline, surface roughness variations, and retracking inaccuracies. To ensure the reliability of the water level estimates, an outlier detection and removal procedure was applied to each measurement set.

First, the median value ($\tilde{h}$) of the measurements within the virtual station was calculated for each satellite pass. The individual measurements (h), were then compared with the median, and the residuals (r) were computed as the difference between them (Eq. (3)):

$$r = h - \tilde{h} \tag{3}$$

In applying this method, it is necessary to define a tolerance threshold (T) for the residuals. Measurements for which the absolute residual ($|r|$) exceeds T, are classified as outliers and excluded from further analysis. In this study, T was tested within the range of 0.3–0.7 m, and a value of 0.5 m was selected as optimal. The filtering procedure was applied iteratively, resulting in a consistent cluster of measurements with reduced influence of extreme deviations. After outlier removal, the reservoir water level time series was derived by computing the median of the remaining valid measurements.

The surface elevations derived from the Sentinel-3 radar altimeter are referenced to the WGS84 ellipsoid. To obtain water levels relative to mean sea level, a geoid correction was applied. Geoid undulation values (N) were obtained from the EGM2008-5 global geoid model and subtracted from the ellipsoidal heights. As a result, a time series of orthometric water surface elevations was derived. This transformation is essential for the direct comparison of altimetry-derived results with in situ measurements and for subsequent hydrological analyses.

3.2. Water-covered area extraction

The seasonal and interannual variability of the Tsalka Reservoir surface area was analyzed using PlanetScope surface reflectance imagery for 93 months of the study period. The selection of PlanetScope data is justified by its high spatial resolution (3 m), which enables detailed delineation of the fragmented shoreline. In addition, the high revisit frequency of PlanetScope satellites allows the acquisition of scenes closely matching the Sentinel-3 altimetry measurement dates. For each Sentinel-3 observation month, images were selected within a ±5-day time window to map the water-covered area and minimize temporal discrepancies between water level and surface area estimates.

The Normalized Difference Water Index (NDWI), originally proposed by McFeeters (1996), was used to delineate the water surface of the reservoir. This index is defined as the normalized difference between the green and near-infrared (NIR) spectral bands of multispectral imagery, enhancing the detection of open water bodies. For each PlanetScope image, NDWI was calculated as Eq. (4):

$$NDWI = \frac{Green - NIR}{Green + NIR} \tag{4}$$

For PlanetScope imagery, green corresponds to band 2 and NIR corresponds to band 4. After NDWI computation, a threshold-based classification was applied to separate water from non-water pixels. In general, pixels with positive NDWI values are associated with open water, while negative or low NDWI values correspond to surrounding non-water surfaces. Because spectral conditions varied slightly among acquisition dates, the classification threshold was adjusted individually for each PlanetScope scene. Pixels with NDWI values above the selected thresholds were classified as water, and all remaining pixels were classified as non-water. Derived rasters were vectorized into polygon features. This approach is consistent with previous studies that have applied spectral indices to delineate surface water from optical imagery, including PlanetScope data, and remains an effective method, particularly in the context of high-frequency observations and efficient data processing (Alcaras et al., 2022; Van et al., 2025).

However, this approach is valid under ice-free conditions. During periods when the reservoir is partially covered by ice or snow, automatic spectral separation of water and non-water surfaces becomes less reliable, as frozen water surfaces and snow cover in adjacent areas alter the spectral characteristics of the reservoir. In such cases, the automatically derived water masks were visually inspected and manually refined to obtain shoreline boundaries that more accurately represent the true water extent observed in the imagery (Cheng et al., 2023; Wang et al., 2020). Manual delineation procedures have also been applied in recent studies conducted in the Georgian Caucasus using PlanetScope imagery for mapping proglacial lakes and monitoring glacier changes (Tielidze et al., 2025a). The automated computation of NDWI for the PlanetScope time series was performed in a Python programming environment using Jupyter Notebook. As a result of the above procedures, monthly surface area values were derived for the Tsalka Reservoir, with acquisition dates closely matching the Sentinel-3 measurements.

3.3. Construction of the stage-area curve

The relationship between water level and water-covered area in the Tsalka Reservoir was established using paired observations of water level and surface area derived for the study period, as described in the preceding subsections.

To obtain a continuous functional representation of the relationship between water level and water-covered area, a nonlinear regression model was fitted to the observed data. A four-parameter logistic (4PL) function was employed, as it effectively captures the sigmoidal response characteristic of reservoirs, where the surface area increases slowly at low water levels, more rapidly at intermediate levels, and gradually approaches quasi-asymptotic behavior at higher levels. The model is expressed as Eq. (5):

$$A(L) = A_{min} + \frac{A_{max} - A_{min}}{1 + \exp[-k(L - L_0)]} \tag{5}$$

where, $A(L)$ represents the reservoir surface area at water level L, A_{min} and A_{max} denote the lower and upper asymptotic limits of the surface area estimated by the model, respectively, k is the growth rate (steepness) of the curve, and L_0 is the inflection point corresponding to the water level at which the rate of area increase is maximal.

Model parameters were estimated using nonlinear least-squares optimization (Eq. (6)), minimizing the sum of squared residuals:

$$S = \sum_{i-1}^{N} [A_i - A(L_i)]^2 \tag{6}$$

where, L_i represents the water level and A_i is the corresponding surface area for observation i.

The fitted function provides a smooth approximation of the discrete observations and enables the estimation of water-covered area for any water level within the observed range. It should be noted that the dataset does not encompass the full range of possible reservoir storage conditions. Accordingly, the asymptotic parameters A_{min} and A_{max} should not be interpreted as the absolute minimum and maximum extents of inundation, but rather as model parameters describing the empirical relationship within the range of water level values considered in this study.

3.4. Quantitative validation of altimetry data accuracy

To quantitatively assess the accuracy of the water level time series derived from the Sentinel-3 radar altimeter, the results were validated against daily in situ observations provided by JSC "KHRAMHESI I" for the corresponding measurement dates.

The systematic deviation between the two datasets was quantified using the mean bias error (Bias), defined as Eq. (7):

$$Bias = \frac{1}{n} \sum_{i=1}^{n} (A_i - G_i) \tag{7}$$

where, A_i represents the water level derived from the radar altimeter and G_i denotes the corresponding in situ measurement. Ideally, the resulting value should be close to zero.

To quantify the magnitude of the absolute discrepancy, the root mean square error (RMSE) was used, calculated as follows (Eq. (8)):

$$RMSE = \sqrt{\frac{1}{n} \sum_{i=1}^{n} (A_i - G_i)^2} \tag{8}$$

The strength of the linear relationship between altimetry-derived and in situ water levels was quantified using the Pearson correlation coefficient (Eq. (9)):

$$r = \frac{\sum_{i=1}^{n}(A_i - \bar{A})(G_i - \bar{G})}{\sqrt{\sum_{i=1}^{n}(A_i - \bar{A})^2}\sqrt{\sum_{i=1}^{n}(G_i - \bar{G})^2}} \tag{9}$$

where, $\bar{A}$ and $\bar{G}$ represent the mean values of the altimetry-derived and in situ water level series, respectively. This coefficient quantifies the degree to which the radar altimeter captures the variability of water level fluctuations observed in the gauge data. Values close to 1 indicate a strong correspondence in temporal dynamics.

In addition, the Nash–Sutcliffe efficiency coefficient (NSE) (Nash & Sutcliffe, 1970) was used to evaluate the agreement between altimetry-derived and in situ measurements (Eq. (10)):

$$NSE = 1 - \frac{\sum_{i=1}^{n}(A_i - G_i)^2}{\sum_{i=1}^{n}(G_i - \bar{G})^2} \tag{10}$$

NSE quantifies how well altimetry-derived values reproduce the variability observed in ground-based measurements. An NSE value of 1 indicates perfect agreement, a value of 0 suggests that the model performs no better than the mean of the observations, and negative values indicate unsatisfactory predictive performance.

3.5. NDWI extracted surface area uncertainty assessment

Because no independent reference datasets describing reservoir surface area were available for the study area, uncertainty associated with the extracted water-covered areas was estimated using a shoreline displacement approach. Considering the 3 m spatial resolution of PlanetScope imagery, ±3 m and ±6 m buffer scenarios were applied to the minimum and maximum reservoir extents observed during the study period.

For each case, surface area uncertainty (U_A) was calculated as half of the difference between the outward buffered ($A_{outward}$) and inward buffered (A_{inward}) polygon areas according to Eq. (11):

$$U_A = \frac{A_{outward} - A_{inward}}{2} \tag{11}$$

Relative uncertainty ($U_A(\%)$) was additionally calculated using Eq. (12):

$$U_A(\%) = \frac{U_A}{A} \times 100 \tag{12}$$

where A is the NDWI mapped reservoir area (km^2).

4. RESULTS

4.1. Validation of Sentinel-3A water levels

Altimeter–derived water level measurements were compared with hydrological station observations over the 93 months of the study period. The validation metrics indicate a small systematic offset and low discrepancies between the two datasets, with Bias = 0.097 m, RMSE = 0.192 m, Pearson's r = 0.997, and NSE = 0.993. In addition to the monthly comparison, the data were aggregated to an annual scale and evaluated using the same indicators. At this temporal resolution, Bias remained nearly unchanged (0.099 m), while RMSE decreased to 0.114 m, indicating that a portion of the differences observed in the monthly series is associated with short-term fluctuations rather than persistent deviations.

The scatter plot of monthly observations (**Fig. 3**) shows that, across the full range of water levels, most points cluster closely around the 1:1 reference line. Larger deviations are observed at lower water levels, likely due to mixed land–water returns recorded by the altimeter under low-stage conditions. The overall positive bias indicates that satellite-derived water levels are, on average, slightly higher than the corresponding station measurements. However, this deviation is small relative to the total water level range of nearly 10 m observed during the study period and does not significantly affect the characterization of seasonal dynamics.

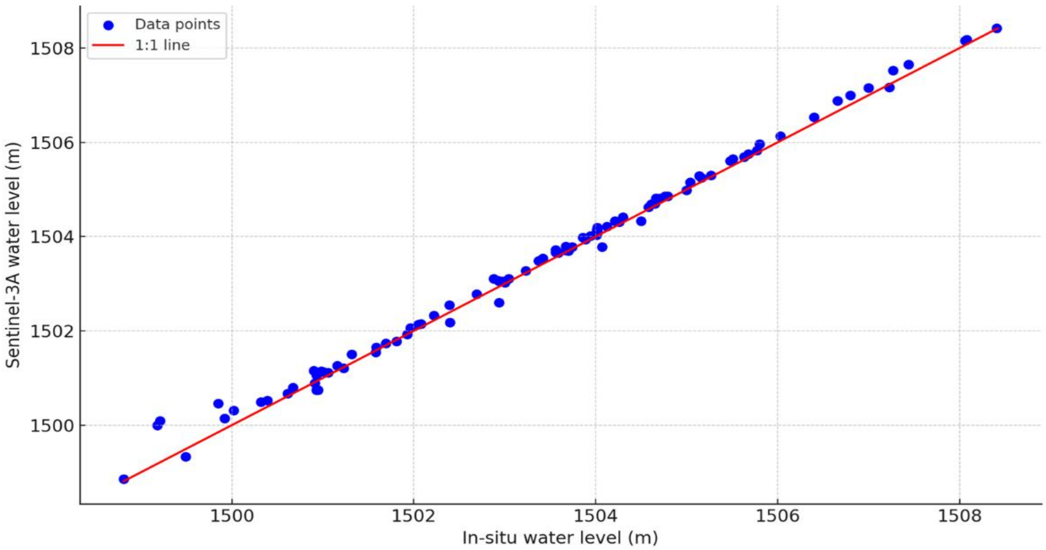

Fig. 3. Sentinel-3A altimetry vs in situ measurements monthly scatter plot.

Analysis of water level variations in the Tsalka Reservoir (**Fig. 4**), based on hydrological station and radar altimeter data, shows that both datasets follow the same sequence of water level increase and decrease. Differences between the curves are most evident during periods of rapid change, particularly during the reservoir filling phase in spring and the recession phase in autumn. The RMSE between Sentinel-3 and in situ water levels was used as an estimate of water level uncertainty. Therefore, the uncertainty of altimetry-derived water levels was considered to be approximately ±0.192 m.

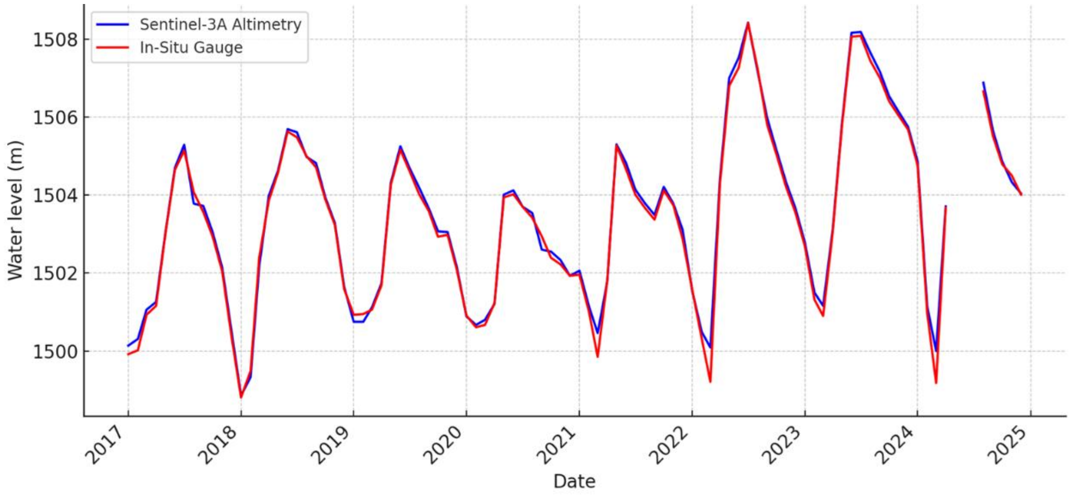

Fig. 4. Superposition of water levels from Sentinel-3A with in situ measurements.

4.2. Seasonal and interannual variability of reservoir water levels

The results indicate that the Tsalka Reservoir exhibits a pronounced seasonal cycle and significant interannual variability (**Fig. 5**). Throughout the study period, the lowest water levels were generally observed from mid-winter to early spring, typically between January and April. A rapid increase begins in mid-spring, with maximum levels reached between June and August. Following the peak, water levels gradually decline during autumn and early winter.

From 2017 to 2019, interannual fluctuations were relatively moderate, with summer maxima slightly exceeding 1505 m and winter minima generally ranging between 1499 and 1500 m. The overall minimum of the study period was recorded in 2018, reaching 1498.86 m. In 2020, a reduced amplitude was observed, with water levels remaining within approximately 1501–1504 m.

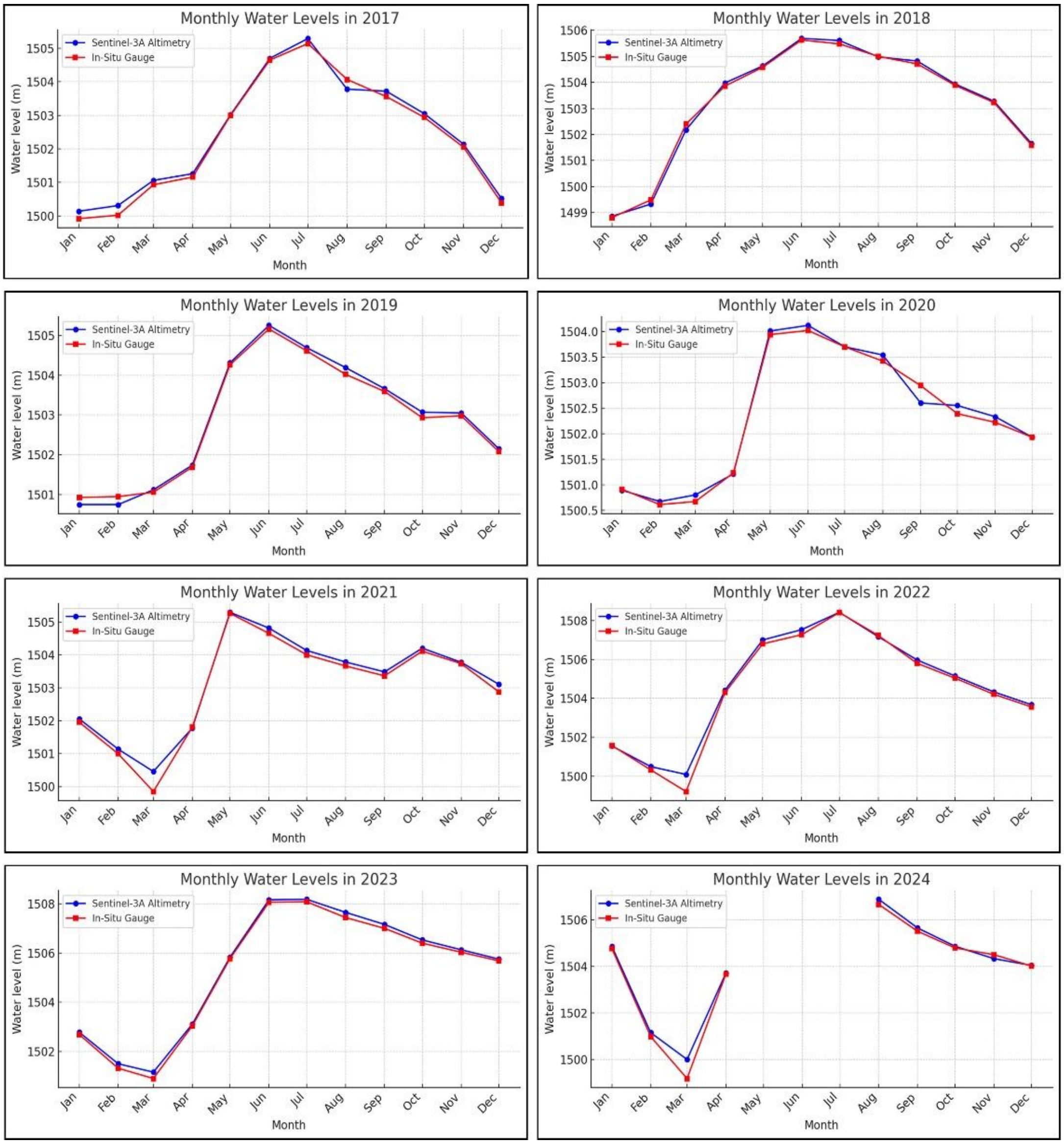

Fig. 5. Annual water level variations in Tsalka Reservoir from 2017 to 2024 – superposition of Sentinel-3A altimetry with in situ measurements.

Despite relatively weak seasonal variability, rapid filling events occurred in late spring in both 2020 and 2021. The largest fluctuations were recorded in 2022, when water levels declined to one of the lowest values of the study period and subsequently increased rapidly to the overall maximum (1508.42 m). Elevated water levels were also observed in 2023; however, in this case, the hydrograph indicates that these conditions were sustained over a longer period. As noted, altimetry data for 2024 are incomplete, with no observations available for May–July; nevertheless, the available monthly measurements and gauging station data indicate a seasonal pattern comparable to previous years.

The boxplot grouped by calendar month (**Fig. 6**) summarizes the annual cycle of the Tsalka Reservoir for the period 2017–2024.

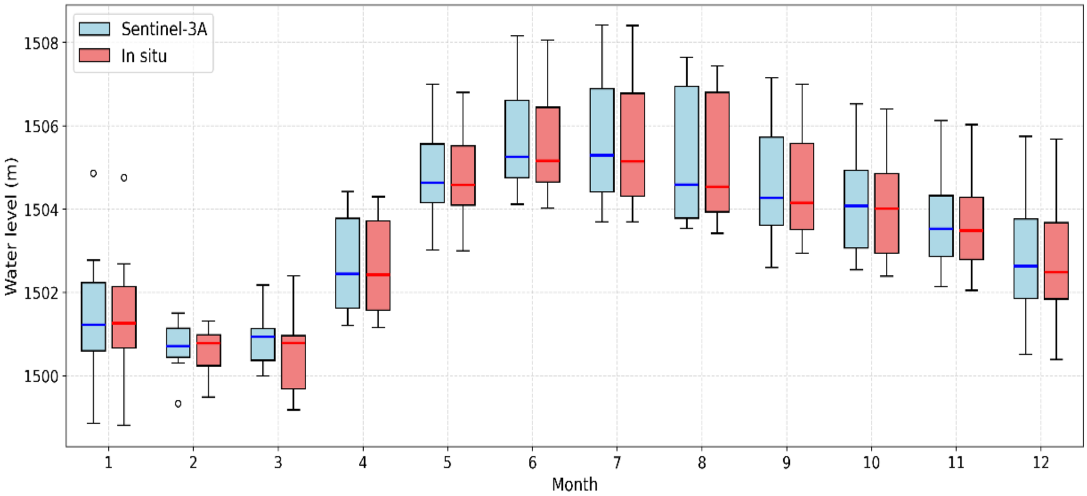

Fig. 6. Monthly water level variations from 2017 to 2024 – Sentinel-3A and in situ measurements.

February and March exhibit the lowest median values and include the minimum water levels in the dataset. From April onward, the distribution increases rapidly, reflecting the onset of reservoir filling. The highest median levels are observed in June and July. These months, together with August, display relatively high variability, as they encompass both moderate conditions and extreme high-water levels recorded in 2022 and 2023. From August to November, median values gradually decline, corresponding to the recession phase. The boxplot also highlights the asymmetry of the reservoir regime. The rise from minimum to maximum water levels occurs over a relatively short period (approximately three to four months), whereas the subsequent decline extends over a longer duration.

4.3. Variability of water-covered area and stage-area relationship

The wide range of water level fluctuations in the Tsalka Reservoir results in pronounced variations in water-covered area. **Fig. 7** illustrates the contrast between the minimum and maximum extents of inundation observed during the study period.

In January 2018, the area covered by water was 5.69 km², mainly confined to the deepest central part of the basin. By July 2022, at peak water levels, the area had increased to 24.54 km², representing more than a fourfold expansion. Spatial analysis of surface area variability indicates that even small changes in water level within certain ranges result in substantial horizontal shifts of the shoreline. The expansion of the reservoir area occurs primarily across the relatively shallow western and northern sectors. In contrast, the southern shoreline is characterized by rocky and steeper terrain, and therefore contributes minimally to the overall increase in surface area. At low water levels, the shoreline becomes fragmented, and the reservoir is divided into several disconnected sections. In the northern part, where water persists under these conditions, small lakes existed prior to reservoir construction. As the water level rises, these sectors reconnect and form a continuous water surface.

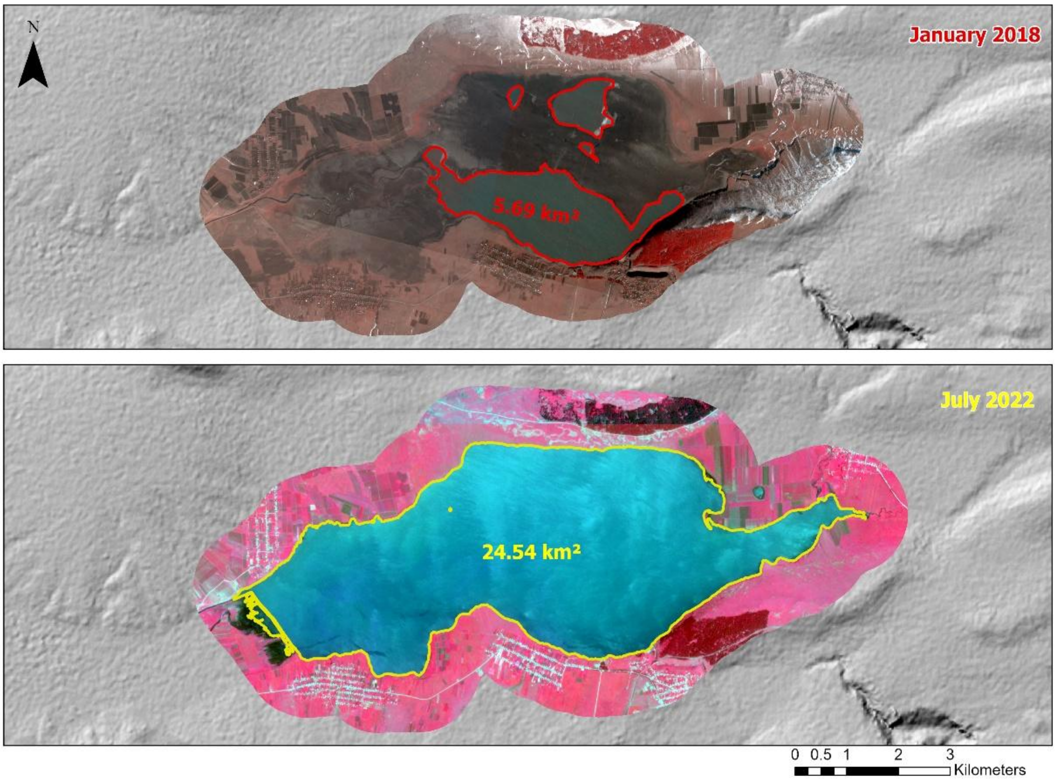

Fig. 7. Minimum and maximum reservoir extent observed during the study period (PlanetScope false color composites).

According to the Surface area uncertainty assessment results, under the ±3 m scenario, uncertainty was estimated as 0.06 km² for the minimum reservoir extent and 0.09 km² for the maximum extent, corresponding to 1.05% and 0.36% of the mapped area, respectively. Under the more conservative ±6 m scenario, uncertainty increased to 0.12 km² and 0.19 km², corresponding to 2.10% and 0.77%, respectively. The results indicate that relative uncertainty is considerably higher during low-water conditions, where shoreline fragmentation and narrow inundated zones increase sensitivity to shoreline displacement. Conversely, uncertainty decreases during high water stages due to the formation of a more continuous water surface and the reduced proportional influence of shoreline variability on the total mapped area.

The potential impact of temporal mismatch between Sentinel-3 and PlanetScope observations was additionally quantified using in situ water level measurements corresponding to paired acquisition dates. The analysis demonstrated that the mean temporal offset was 1.53 days (maximum 5 days), while the mean corresponding water level difference was 0.063 m, with a median difference of 0.02 m and standard deviation of 0.14 m. These results indicate that short-term water level variations between paired observations were generally minor, suggesting that the adopted ±5-day pairing window introduced limited uncertainty into the derived stage–area relationship.

The relationship between water level and surface area is nonlinear and exhibits a sigmoidal pattern (**Fig. 8**). Although the fitted 4PL model adequately reproduces the overall nonlinear stage–area relationship, the distribution of observations is uneven across the full range of reservoir stages, with most measurements concentrated within intermediate water levels. As described in the Methods section, the presented curve is derived solely from observations within the study period and does not represent the full range of possible reservoir storage conditions. Slight deviations observed during low and high-water conditions may additionally reflect increased shoreline uncertainty, fragmented inundation geometry, and limited observation density near extreme reservoir stages.

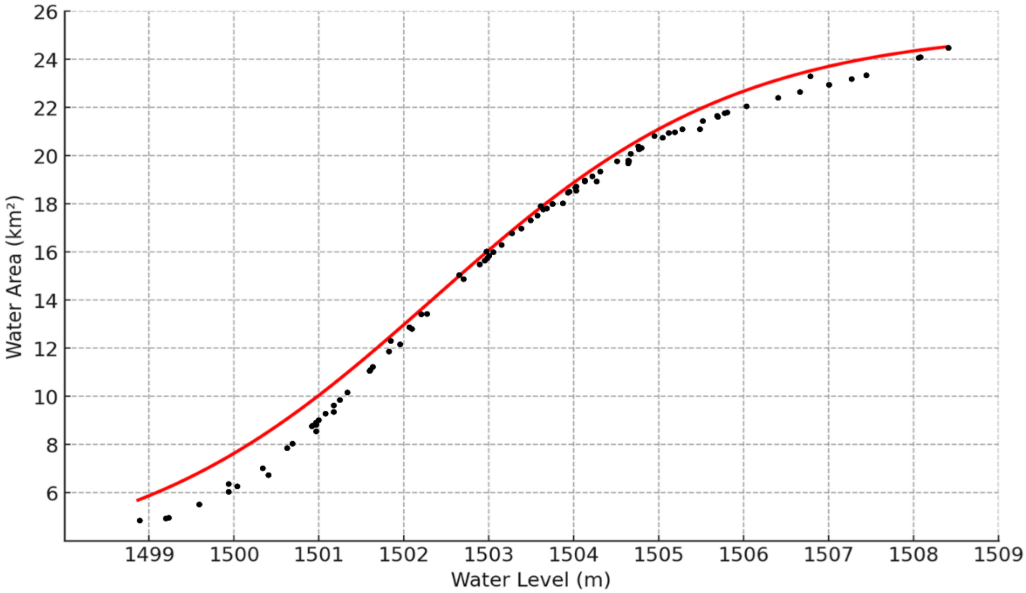

Fig. 8. Relationship between reservoir water level and water-covered area derived from Sentinel-3 altimetry and PlanetScope imagery during the 2017–2024 study period. Black points represent level–area pairs, while the red curve shows the fitted four-parameter logistic (4PL) stage–area relationship.

At low water levels, increases in stage result in relatively small changes in surface area, as the reservoir remains confined to the deeper central part of the basin. Within the intermediate range (approximately 1502–1505 m), the curve steepens, indicating rapid inundation of the shallow marginal zones. Above approximately 1506 m, the curve gradually flattens, indicating that further increases in water level continue to enlarge the reservoir extent, but at a reduced rate.

5. DISCUSSION

A comparison of Sentinel-3A SRAL water levels with in situ observations demonstrates that the radar altimeter captures the hydrodynamic behavior of the Tsalka Reservoir with high accuracy, even under complex topographic conditions of the study area. The obtained statistical metrics (RMSE = 0.192 m, Bias = 0.097 m, r = 0.997, NSE = 0.993) indicate that discrepancies between the two datasets are minor relative to the full range of observed water levels and do not influence the interpretation of seasonal and interannual dynamics. Similar performance of Sentinel-3 has been reported in recent studies, which show that, under favorable conditions, sub-decimeter to decimeter-level accuracy can be achieved for inland water bodies (Nielsen, Andersen, and Ranndal, 2020; Jiang et al., 2020; Xu et al., 2024).

The accuracy of the results depends strongly on the data processing methodology. As demonstrated by the obtained results, the methods applied in this study effectively reduced the influence of anomalous measurements on overall accuracy. In particular, the use of a dynamic virtual station, iterative outlier filtering, and median-based aggregation is well suited for reservoirs such as Tsalka, where seasonal shoreline migration increases the likelihood of mixed land–water returns. The sensitivity of radar altimetry to such conditions, including retracker performance and waveform heterogeneity, has been widely discussed in the context of applications related to inland water bodies (Taburet et al., 2020; Nielsen, Andersen, and Ranndal, 2020). For targets like the Tsalka Reservoir, where specular reflections from the water surface may be contaminated by signals from surrounding terrain, the use of the ICE-1 (OCOG-type) retracker remains an appropriate choice.

The water level dynamics identified in this study reflect a regulated reservoir system, characterized by a clear seasonal pattern and distinct interannual variability. Radar altimetry data effectively capture both gradual seasonal trends and more pronounced deviations. These findings indicate that, despite its 27-day repeat cycle, Sentinel-3 is capable of reliably representing the dynamics of a medium-sized reservoir, particularly when extended time series are considered.

The seasonal and interannual behavior of the reservoir generally corresponds to the climatic regime of the study area, where increased precipitation and rising air temperatures during spring and early summer likely contribute to enhanced inflow and reservoir filling. In contrast, declining water levels during late summer and autumn are consistent with reduced precipitation input. The minimum reservoir level and surface extent observed in January 2018 correspond to one of the lowest mean air temperatures recorded for the preceding October–December period (2.5 °C according to ERA5-Land 2 m temperature data), as well as one of the lowest cumulative precipitation totals for the same period (179.26 mm based on GPM data). Conversely, the maximum reservoir extent and water level observed in 2022 followed the highest cumulative March–June precipitation total during the study period (394.76 mm), while the mean air temperature for the same period reached 6.7 °C. However, the absence of reservoir operation records for the study period limits the ability to separate the effects of climatic forcing and operational regulation on the observed reservoir dynamics.

The integration of high spatial resolution PlanetScope optical imagery enabled detailed mapping of the reservoir shoreline dynamics. In addition, the short revisit interval of this satellite constellation reduced temporal discrepancies relative to the altimetry measurements. However, the limitations of optical data and applied methods for surface area extraction should also be acknowledged. Uncertainties in surface area estimates are primarily associated with threshold selection, mixed pixels along the shoreline, and seasonal snow and ice cover, which makes the spectral separation of water more challenging. The uncertainty assessment performed in this study indicates that the influence of shoreline displacement becomes proportionally more significant during low-water conditions, when fragmented shoreline increase the sensitivity of mapped surface area to positional inaccuracies. Conversely, uncertainty decreases during high-water stages due to the formation of a more continuous water surface.

From a broader perspective, the results of this study confirm the effectiveness of radar altimetry combined with high-resolution optical imagery, as well as the applied methodological framework, for monitoring inland water bodies in regions where in situ data are limited or unavailable. In the Georgian context, where systematic hydrological observations of lakes and reservoirs are largely absent, the approach presented in this study provides a viable alternative for estimating certain hydrometric parameters and reconstructing the dynamics of inland waters. However, reliance on a single satellite mission imposes constraints on both spatial and temporal coverage. In the future, the combined use of other altimetry missions, such as ICESat-2, CryoSat-2, Topex/Poseidon, ENVISAT, SWOT, Sentinel-6, etc., will enable monitoring of a larger number of water bodies, especially when it comes to small and morphologically complex systems (Kwanghee et al., 2024).

Despite the overall effectiveness of the proposed approach, several limitations should be acknowledged. As noted in previous sections, only a single Sentinel-3A ground track intersects the Tsalka Reservoir, which limits the spatial representativeness of the data and increases the sensitivity of altimetry measurements to local conditions along the track, potentially introducing errors. Nevertheless, previous studies have demonstrated that reliable water level retrievals can still be achieved using a single Sentinel-3A ground track. For example, Frappart et al. (2021) reported R^2 values exceeding 0.9 and RMSE values below 0.1 m for Lake Thun in Switzerland. The 27-day repeat cycle constrains the ability to capture short-term fluctuations associated with rapid reservoir filling (e.g., following intense precipitation events within the catchment) and drawdown (e.g., due to operational releases for hydropower generation). In addition, seasonal ice cover in certain years, as well as incomplete data for 2024, may introduce additional uncertainties in the analysis. These limitations emphasize the importance of multi-mission integration and, where possible, the incorporation of auxiliary data sources (e.g., meteorological observations and reservoir operation records).

6. CONCLUSIONS

In this study, surface area and level variations of the Tsalka (Khrami) Reservoir were assessed for the period 2017–2024 using Sentinel-3 radar altimetry and PlanetScope optical imagery. The accuracy of the altimetry-derived time series, obtained from the Level-2 GDR product, was validated against in situ hydrological station data. The resulting statistical metrics indicate a high level of agreement between satellite-based and ground observations, confirming the reliability of the data and methodology used in the study for monitoring medium-sized reservoirs, particularly in regions where in situ data are sparse or not regularly available.

Time series analysis of water levels shows a clear seasonal regime in the Tsalka Reservoir, characterized by rising water levels during the spring and summer period with peak levels typically reached in late summer. This phase is followed by a gradual decline throughout autumn and winter. During the study period, the maximum annual amplitude of water levels reached approximately 10 m, indicating the highly dynamic nature of the reservoir system.

The integration of high spatial and temporal resolution optical imagery enabled not only the assessment of water levels but also the analysis of associated shoreline dynamics. Although the design surface area of the Tsalka Reservoir exceeds 33 km², this limit was not reached during the 8-year study period, with a maximum observed area of 24.54 km². Despite this, the Tsalka Reservoir remains the largest artificial reservoir in the country even based on observed maximum water-covered extent. Notably, the difference between the maximum (2022) and minimum (2018) recorded areas is 18.85 km², indicating strong variability in reservoir extent.

Overall, the results demonstrate that Sentinel-3 altimetry provides sufficient accuracy for monitoring medium-sized inland water bodies, while high spatial and temporal resolution PlanetScope imagery is well suited for deriving surface area in support of altimetry observations. In the context of expanding spatial coverage and ongoing technological advances in current and forthcoming satellite altimetry missions, the approach presented in this study constitutes a cost-effective framework that can be effectively integrated into the development of a national inland water monitoring system in Georgia.

ACKNOWLEDGMENTS

The Authors are grateful to the JSC "KHRAMHESI I" for providing Tsalka Reservoir in situ water level observations.

REFERENCES

Alcaras, E., Amoroso, P.P., Figliomeni, F.G., Parente, C. and Prezioso, G. (2022) Accuracy evaluation of coastline extraction methods in remote sensing: a smart procedure for Sentinel-2 images, *The International Archives of the Photogrammetry, Remote Sensing and Spatial Information Sciences*, XLVIII-4/W3-2022, pp. 13–19. Available from: https://doi.org/10.5194/isprs-archives-XLVIII-4-W3-2022-13-2022

An, Z., Chen, P., Tang, F., Yang, X., Wang, R. and Wang, Z. (2022) Evaluating the performance of seven ongoing satellite altimetry missions for measuring inland water levels of the Great Lakes, *Sensors*, 22, 9718. Available from: https://doi.org/10.3390/s22249718

Bazzi, H., Baghdadi, N., Ngo, Y.-N., Normandin, C., Frappart, F. and Cazals, C. (2025) Assessing SWOT interferometric SAR altimetry for inland water monitoring: insights from Lake Léman, *Frontiers in Remote Sensing*, 6, 1572114. Available from: https://doi.org/10.3389/frsen.2025.1572114

Chen, J. and Duan, Z. (2022) Monitoring spatial-temporal variations of lake level in Western China using ICESat-1 and CryoSat-2 satellite altimetry, *Remote Sensing*, 14, 5709. Available from: https://doi.org/10.3390/rs14225709

Cheng, C., Zhang, F., Li, X., Tan, M.L., Kumar, P., Johnson, B.A., Shi, J., Zhao, Q. and Liu, C. (2023) Variations in water storage of Bosten Lake, China, over the last two decades based on multi-source satellite data, *Journal of Hydrology: Regional Studies*, 49, 101496. Available from: https://doi.org/10.1016/j.ejrh.2023.101496

Crétaux, J.-F., Nielsen, K., Frappart, F., Papa, F., Calmant, S. and Benveniste, J. (2017) Hydrological applications of satellite altimetry: rivers, lakes, man-made reservoirs, inundated areas, in Stammer, D. and Cazenave, A. (eds.) *Satellite altimetry over oceans and land surfaces*. Boca Raton, FL: CRC Press

Dalla Torre, D., Di Marco, N., Menapace, A., Avesani, D., Righetti, M. and Majone, B. (2024) Suitability of ERA5-Land reanalysis dataset for hydrological modelling in the Alpine region, *Journal of Hydrology: Regional Studies*, 52, 101718. Available from: https://doi.org/10.1016/j.ejrh.2024.101718

El Orfi, T., El Gachi, M., Lebaut, S. and Haidu, I. (2025) Monitoring the water surface dynamics of four Mediterranean mountain lakes in the Middle Atlas (Morocco) using Landsat imagery in a global change context, *Journal of Hydrology: Regional Studies*, 60, 102516. Available from: https://doi.org/10.1016/j.ejrh.2025.102516

Fernandes, M.J., Lázaro, C., Nunes, A.L. and Scharroo, R. (2014) Atmospheric corrections for altimetry studies over inland water, *Remote Sensing*, 6, pp. 4952–4997. Available from: https://doi.org/10.3390/rs6064952

Frappart, F., Blumstein, D., Cazenave, A., Ramillien, G., Birol, F., Morrow, R. and Rémy, F. (2017) Satellite altimetry: principles and applications in Earth sciences, in *Wiley Encyclopedia of Electrical and Electronics Engineering*. Hoboken, NJ: John Wiley & Sons, Inc., pp. 1–25. ISBN 047134608X

Frappart, F., Blarel, F., Fayad, I., Bergé-Nguyen, M., Crétaux, J.-F., Shu, S., Schregenberger, J. and Baghdadi, N. (2021) Evaluation of the performances of radar and lidar altimetry missions for water level retrievals in mountainous environment: the case of the Swiss lakes, *Remote Sensing*, 13(11), 2196. Available from: https://doi.org/10.3390/rs13112196

Haidu, I., El Orfi, T., Magyari-Sáska, Z., Lebaut, S. and El Gachi, M. (2024) Modeling the long-term variability in the surfaces of three lakes in Morocco with limited remote sensing image sources, *Remote Sensing*, 16(17), 3133. Available from: https://doi.org/10.3390/rs16173133

Han, K., Kim, S., Mehrotra, R. and Sharma, A. (2024) Enhanced water level monitoring for small and complex inland water bodies using multi-satellite remote sensing, *Environmental Modelling & Software*, 180, 106169. Available from: https://doi.org/10.1016/j.envsoft.2024.106169

Iordanishvili, K., Iordanishvili, I., Iremashvili, I. and Kandelaki, N. (2023) *Peculiarities of engineering-ecological problems of mountain and foothill reservoirs* (in Georgian). Tbilisi: Sachino Publishing House.

Jamali, S., Zaidi, A. and Ali, T. (2025) Integrating satellite altimetry and SAR technology for Manchar Lake water monitoring, *Discover Water*, 5, 114. Available from: https://doi.org/10.1007/s43832-025-00292-0

Jawad, M., Bhattacharya, B., Young, A. and van Andel, S.J. (2024) Evaluation of near real-time Global Precipitation Measurement (GPM) precipitation products for hydrological modelling and flood inundation mapping of sparsely gauged large transboundary basins—A case study of the Brahmaputra Basin, *Remote Sensing*, 16(10), 1756. Available from: https://doi.org/10.3390/rs16101756

Jiang, L., Nielsen, K., Dinardo, S., Andersen, O.B. and Bauer-Gottwein, P. (2020) Evaluation of Sentinel-3 SRAL SAR altimetry over Chinese rivers, *Remote Sensing of Environment*, 237, 111546. Available from: https://doi.org/10.1016/j.rse.2019.111546

Kossieris, S., Tsiakos, V., Tsimiklis, G. and Amditis, A. (2024) Inland water level monitoring from satellite observations: a scoping review of current advances and future opportunities, *Remote Sensing*, 16, 1181. Available from: https://doi.org/10.3390/rs16071181

Luo, S., Song, C., Ke, L., Zhan, P., Fan, C. and Liu, K. *et al.* (2022) Satellite laser altimetry reveals a net water mass gain in global lakes with spatial heterogeneity in the early 21st century, *Geophysical Research Letters*, 49, e2021GL096676. Available from: https://doi.org/10.1029/2021GL096676

McFeeters, S.K. (1996) The use of the normalized difference water index (NDWI) in the delineation of open water features, *International Journal of Remote Sensing*, 17(7), pp. 1425–1432. Available from: https://doi.org/10.1080/01431169608948714

Nash, J.E. and Sutcliffe, J.V. (1970) River flow forecasting through conceptual models part I — A discussion of principles, *Journal of Hydrology*, 10(3), pp. 282–290. Available from: https://doi.org/10.1016/0022-1694(70)90255-6

Nielsen, K., Andersen, O.B. and Ranndal, H. (2020) Validation of Sentinel-3A based lake level over US and Canada, *Remote Sensing*, 12, 2835. Available from: https://doi.org/10.3390/rs12172835

Taburet, N., Zawadzki, L., Vayre, M., Blumstein, D., Le Gac, S., Boy, F. *et al.* (2020) S3MPC: improvement on inland water tracking and water level monitoring from the OLTC onboard Sentinel-3 altimeters, *Remote Sensing*, 12, 3055. Available from: https://doi.org/10.3390/rs12183055

Tang, F., Chen, P., An, Z., Xiong, M., Chen, H. and Qiu, L. (2023) A dual-threshold algorithm for ice-covered lake water level retrieval using Sentinel-3 SAR altimetry waveforms, *Sensors*, 23, 9724. Available from: https://doi.org/10.3390/s23249724

Tielidze, L.G., Nadaraia, A., Kumladze, R.M., Cook, S.J., Lobjanidze, M., Liu, Q., Megrelidze, I., Mackintosh, A.N. and Imnadze, G. (2025) Post-Little Ice Age shrinkage of the Tsaneri–Nageba glacier system and recent proglacial lake evolution in the Georgian Caucasus, *Water*, 17(22), 3209. Available from: https://doi.org/10.3390/w17223209

Tielidze, L.G., Mackintosh, A.N., Gavashelishvili, A., Gadrani, L., Nadaraia, A. and Elashvili, M. (2025) Post-Little Ice Age equilibrium-line altitude and temperature changes in the Greater Caucasus based on small glaciers, *Remote Sensing*, 17(9), 1486. Available from: https://doi.org/10.3390/rs17091486

Van, L.N., Nguyen, G.V., Kim, Y., Do, M.T.T., Kwon, S., Lee, J. and Lee, G. (2025) Rapid urban flood detection using PlanetScope imagery and thresholding methods, *Water*, 17, 1005. Available from: https://doi.org/10.3390/w17071005

Wang, J. and Gao, Y. (2025) Monitoring long-term water storage of lakes and reservoirs in arid ungauged basin based on underwater topography derived from multi-source satellite data, *Science of the Total Environment*, 966, 178662. Available from: https://doi.org/10.1016/j.scitotenv.2025.178662

Wang, X., Guo, X., Yang, C., Liu, Q., Wei, J., Zhang, Y. *et al.* (2020) Glacial Lake inventory of high-mountain Asia in 1990 and 2018 derived from Landsat images, *Earth System Science Data*, 12, pp. 2169–2182. Available from: https://doi.org/10.5194/essd-12-2169-2020

Woolway, R.I., Kraemer, B.M., Lenters, J.D., Merchant, C.J., O'Reilly, C.M. and Sharma, S. (2020) Global Lake responses to climate change, *Nature Reviews Earth & Environment*, 1, pp. 388–403. Available from: https://doi.org/10.1038/s43017-020-0067-5

Xu, J., Xia, M., Ferreira, V.G., Wang, D. and Liu, C. (2024) Estimating and assessing monthly water level changes of reservoirs and lakes in Jiangsu Province using Sentinel-3 radar altimetry data, *Remote Sensing*, 16, 808. Available from: https://doi.org/10.3390/rs16050808

Zeng, F., Song, C., Cao, Z., Xue, K., Lu, S., Chen, T. and Liu, K. (2023) Monitoring inland water via Sentinel satellite constellation: a review and perspective, *ISPRS Journal of Photogrammetry and Remote Sensing*, 204, pp. 340–361. Available from: https://doi.org/10.1016/j.isprsjprs.2023.09.011

SPATIAL INTERPOLATION OF RAINFALL AT LAKE TOBA REGION WITH ORDINARY AND EXTERNAL DRIFT KRIGING

Nicholas ABISHA [1], *Sri NURDIATI* [2*], *Endar Hasafah NUGRAHANI* [3], *Mohamad Khoirun NAJIB* [2] & *Syukri Arif RAFHIDA* [2]

DOI: 10.21163/GT_2026.213.07

ABSTRACT

This study aims to interpolate rainfall in the Lake Toba region using ordinary kriging (OK) and external drift kriging (EDK) with elevation and distance-to-lake as drift variables. Rainfall data from 34 stations (2007-2017) were evaluated across three scenarios: (1) without imputation, (2) sparse data using only complete stations, and (3) all stations using k-nearest-neighbors imputation. Leave-one-out cross-validation revealed that in dense-data scenarios (1 and 3), OK and EDK produced similar accuracy, indicating that dense local observations override the need for auxiliary variables. However, in the sparse-data scenario (2), EDK with distance-to-lake significantly outperformed both OK and EDK with elevation. Geographically, this highlights that standard assumptions of orographic lift fail in the caldera due to complex rain shadows over Samosir Island. Instead, distance-to-lake serves as a reliable proxy for the localized lake-land breeze circulations that drive the basin's microclimate. Ultimately, this study demonstrates that spatial interpolation in complex, data-sparse regions must be grounded in variables that accurately reflect physical hydrometeorological realities.

Keywords: *Rainfall, Kriging, Lake Toba, Elevation, Distance-to-Lake.*

1. INTRODUCTION

Recent studies have reported a concerning decline and fluctuation in Lake Toba's water level, which has drawn increasing attention due to its implications for tourism and hydropower production (Irwandi et al., 2021). Falling water levels may disrupt cruise ship operations, while Irwandi et al. (2021) also noted a reduction in hydroelectric power generation affecting aluminium production at PT Inalum. These changes are likely driven by rising air temperatures and decreasing rainfall, as supported by multiple observations across the region.

Building on this, Irwandi et al. (2023) analyzed climate trends in the Lake Toba region using bias-corrected ERA5-Land data. The utility of ERA5 reanalysis data for characterizing extreme rainfall events has also been demonstrated in other parts of the Indonesian archipelago (Koesuma et al., 2025). The analysis found that 70\% of the area showed increasing rainfall trends, while the rest showed declines. However, further verification using in-situ station data is required to confirm the spatial distribution of these trends. Understanding this spatial variability is essential for assessing its linkage to lake hydrology and the ongoing water level decline.

----

[1] *Master's Program in Applied Mathematics, School of Data Science, Mathematics, and Informatics, IPB University, Bogor, Indonesia, abishanicholas@apps.ipb.ac.id (NA),*
[2] *Division of Computational Mathematics, School of Data Science, Mathematics, and Informatics, IPB University, Bogor, Indonesia.* [*] *Corresponding author nurdiati@apps.ipb.ac.id (SN), mkhoirun_najib@apps.ipb.ac.id (MKN), asrafhida@apps.ipb.ac.id (SAR)*
[3] *Division of Mathematical Economics, Finance, and Actuarial Science, School of Data Science, Mathematics, and Informatics, IPB University, Bogor, Indonesia, e_nugrahani@apps.ipb.ac.id (EHN),*

Spatial interpolation methods are frequently employed to estimate rainfall at ungauged locations. Common techniques include inverse distance weighting (IDW), ordinary kriging (OK), and external drift kriging (EDK), among others (Fung et al., 2022; Caloiero et al., 2021). Comprehensive reviews indicate that while geostatistical methods generally outperform deterministic techniques for monthly and annual rainfall, their relative success depends heavily on network density and the availability of secondary variables (Ly et al., 2013). Previous comparative studies show varying results regarding kriging performance. For example, Das & Islam (2021) found that kriging with external drift (KED) using longitude as a covariate significantly outperformed both OK and IDW in mapping annual average rainfall across Bangladesh. Conversely, Frazier et al. (2016) found that OK produced lower error statistics than multivariate methods for rainfall interpolation in the Hawaiian Islands, suggesting that added model complexity does not always guarantee improved accuracy. These findings underscore that the effectiveness of kriging methods depends not only on station density, but also on the suitability and spatial relevance of drift variables (Kyriakidis et al., 2001). Historically, elevation has been the most common auxiliary variable incorporated into multivariate geostatistical algorithms for rainfall interpolation, often yielding significant accuracy improvements in mountainous regions (Goovaerts, 2000).

A critical factor influencing kriging accuracy is the choice and fitting of the variogram model. The spherical variogram model remains widely used due to its suitability for isotropic spatial processes and ease of parameter estimation, as demonstrated in recent applications such as Somayasa et al. (2021) where it was employed to model spatial variability in agricultural land using weighted universal kriging. Empirical variograms are typically estimated using methods such as the Cressie-Hawkins estimator, and parameter fitting is often performed via weighted least squares (Pearse et al., 2024). The Cressie-Hawkins estimator remains a relevant and widely adopted approach for robust variogram estimation, as demonstrated by its implementation in recent geostatistical software such as SciKit-Gstat (Mälicke, 2022) and GstatSim (Mackie et al., 2023), which emphasize reproducibility and flexibility in modern Python-based spatial analysis workflows.

Beyond software adoption, recent literature also affirms the value of the Cressie-Hawkins estimator in applied geostatistics. Gutierrez-Lopez (2021) proposed a modification of the Cressie-Hawkins estimator (CH-GLo) by incorporating the fourth statistical moment, enhancing its performance for mapping extreme hydrological events. The modified estimator effectively reduced the impact of outliers in rainfall data during an extreme storm event in Queretaro, Mexico. Similarly, Mahdi et al. (2020) conducted comparative analyses of empirical variogram estimators including CH. While alternative models like VNN performed better in their groundwater case study, CH remained a robust and valid comparator, especially in small-sample contexts. In the domain of geochemical exploration, Nguyen (2020) employed the Cressie-Hawkins estimator to mitigate the influence of outliers in the spatial analysis of ore-forming elements. Their results demonstrated the estimator's utility in quantifying moderate spatial dependence in skewed geochemical datasets. Collectively, these applications demonstrate that the CH estimator remains a practical and theoretically grounded approach in diverse spatial modeling problems.

While previous geostatistical studies have evaluated kriging methods globally, there is a distinct lack of comparative research tailored to the unique topographical and microclimatic conditions of Indonesia's major caldera lakes. The novelty of this study lies in explicitly testing whether standard auxiliary variables like elevation—which are often successful in temperate or continental mountainous regions—remain effective in the equatorial, lake-driven microclimate of the Lake Toba basin, particularly when compared against a localized distance-to-water metric. This study aims to map the spatial distribution of rainfall across the Lake Toba region using and comparing OK and EDK methods, incorporating robust spherical variogram models estimated via the Cressie-Hawkins method. By filling this critical regional knowledge gap with a rigorously validated spatial rainfall model, this research provides the essential hydrometeorological baseline needed to investigate and mitigate Lake Toba's declining water levels.

2. MATERIALS AND METHODS

2.1. Study Area and Data

The study area is the Lake Toba region, Indonesia, covering a geographical grid 86 from 98.27◦E-99.32◦E longitude and 2.05◦N-3.05◦N latitude. The locations of the 34 meteorological stations used in this study are shown in **Fig. 1**. The primary data consisted of monthly rainfall (mm) time series from 34 stations, collected from January 1971 to December 2017, and obtained from the Indonesian Agency for Meteorology, Climatology, and Geophysics (BMKG). Two external variables were used for EDK: (1) Elevation (Elev), obtained from the public Open-Elevation API, depicting the caldera's physical terrain (**Fig. 1A**), and (2) Distance from the Lake (Dist), defined as the shortest distance from each station to the shoreline, calculated using GADM administrative area shapefiles, representing the proximity to the primary moisture source (**Fig. 1B**).

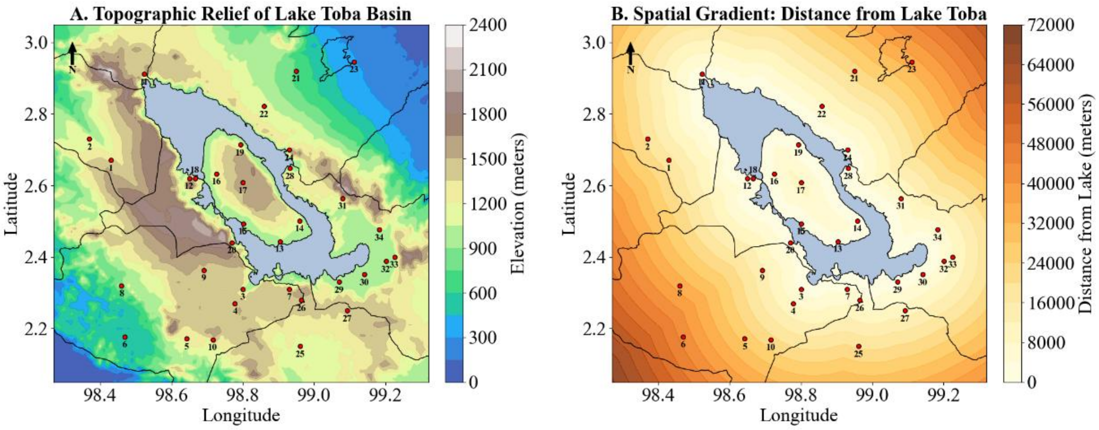

Fig. 1. Location of the 34 meteorological stations in the Lake Toba region. Panel (A) displays the topographic relief (elevation) of the basin, while Panel (B) illustrates the spatial gradient representing the shortest distance from each station to the lake shoreline.

2.2. K-Nearest Neighbors Imputation

Imputation is a class of procedures performed with the aim of estimating missing data values (Batista and Monard 2002). One imputation method that can be applied is k-nearest-neighbors (KNN). The KNN imputation method applies the concept of estimation based on the nearest neighbors. The KNN method works by predicting the value of a missing observation using information from the k nearest samples. The proximity between two points is calculated using a distance metric. The most commonly used metric is the Euclidean distance (Kuhn and Johnson 2013):

$$d(a,b) = \sqrt{\sum_{j=1}^{p} \left(x_{aj} - x_{bj}\right)^2}$$

This method was selected for its computational efficiency and its effectiveness in preserving the local spatial correlation structures of the rainfall data.

2.3. Empirical Variogram

The experimental variogram, or empirical variogram, is a function computed from the observed data $z(x_i), i = 1, 2, \dots$, to describe the spatial correlation before a theoretical model is fitted (Webster and Oliver 2007). The classical empirical variogram estimator, also known as the method of moments estimator, was introduced by Matheron (Cressie 1993; Webster and Oliver 2007). It is defined as:

$$\hat{\gamma}(h) = \frac{1}{2|N(h)|} \sum_{(i,j)\in N(h)} \left(z(x_i) - z(x_j)\right)^2,$$

where $N(h)$ is the set of all pairs of observation points (i, j) separated by a lag vector h.

While common, the Matheron estimator is known to be sensitive to outliers in the data (Cressie and Hawkins 1980; Oliver and Webster 2015). To address this, a more robust empirical variogram estimator was proposed by Cressie and Hawkins (1980), which is given by

$$\hat{\gamma}(h) = \frac{\left(\frac{1}{|N(h)|}\sum_{(i,j)\in N(h)} \left|z(x_i) - z(x_j)^{0.5}\right|\right)^4}{2\left(0.457 + \frac{0.494}{|N(h)|} + \frac{0.045}{|N(h)|^2}\right)}.$$

In this study, the empirical variogram was modeled by applying this robust Cressie-Hawkins estimator (Cressie 1985; Al-Mofleh et al. 2016; Mohebzadeh 2018).

2.4. Theoretical Variogram

A theoretical variogram is a model obtained by fitting a mathematical function to the experimental (empirical) variogram (Webster and Oliver 2007). One form of a theoretical variogram is the spherical model, which is given by:

$$\gamma(h;\theta) = f(x) = \begin{cases} c_0 + c\left[\frac{3h}{2a} - \frac{1}{2}\left(\frac{h}{a}\right)^3\right], & 0 \le h < a \\ c_0 + c, & h \ge a \end{cases},$$

where $\theta = (c_0, c, a)$. The spherical variogram function is designed to be bounded above.

This is because bounded semivariance is more commonly encountered in geostatistics (Cressie 1985; Webster and Oliver 2007). The parameters θ are defined as follows:

- Total Sill $(c_0 + c)$: The maximum value of the semivariance.
- Range (a): The value of h at which the theoretical variogram reaches the total sill.
- Nugget Effect (c_0): The component of the total sill representing the semivariance at lag 0, often interpreted as micro-scale variation.
- Partial Sill (c): The other component of the total sill, representing the spatially correlated portion of the variance.

A robust method for fitting the spherical theoretical variogram, according to Cressie (1985) as cited in Al-Mofleh (2016), is the Weighted Least Squares (WLS) method. This method applies the weights:

$$w_i = \frac{|N(h_i)|}{\gamma(h_i;\theta)^2}, \quad i = 1,2,\dots,n,$$

where $|N(h_i)|$ denotes the number of pairs represented by the lag h_i, and $\gamma(h_i;\theta)$ is the value of the theoretical semivariance at lag h_i.

2.5. Ordinary Kriging

Ordinary Kriging (OK) is a geostatistical estimation method that predicts the value of a random variable, Z, at an unobserved point, x_0, using a weighted linear combination of sample points $z(x_1),\dots,z(x_n)$ (Webster and Oliver 2007). The OK estimator is:

$$\hat{Z}(x_0) = \sum_{i=1}^{n} \lambda_i z(x_i),$$

where λ_i are the weights assigned to each observation.

The weights are the solutions to the system of equations $A\lambda = b$, where A is the covariance matrix between all observations, b is the covariance vector between all observations and the target location, and λ is the weight vector.

2.6. External Drift Kriging

The Ordinary Kriging method assumes that the mean of the process is stationary (constant). However, some spatial processes contain a trend, also known as a drift, where the expected value is not stationary (Webster and Oliver 2007). When the trend is a function of K external variables, $y_1, y_2, \dots, y_K$, which are known at all locations, the model is modified to incorporate these auxiliary predictors (Hengl et al., 2003):

$$Z(x) = \sum_{k=0}^{K} \beta_k y_k(x) + \varepsilon(x),$$

where β_k are unknown coefficients.

This process is known as Kriging with External Drift or External Drift Kriging (EDK). The EDK estimator is:

$$\hat{Z}_{KED}(x_0) = \sum_{i=1}^{n} \lambda_i^{KED} z(x_i).$$

The weights λ_i^{KED} are solved using the extended matrices: $\lambda^{KED} = \{\lambda_1^{KED}, \dots, \lambda_n^{KED}, \varphi_0, \dots, \varphi_p\}^{\mathsf{T}}$, where λ^{KED} is the vector of solved weights and φ_p are the Lagrange multipliers.

3. EXPERIMENTAL DESIGN

The analysis was performed using data from the 2007--2017 period. To assess the impact of missing data (NaN values) on interpolation accuracy, three distinct data-handling scenarios were designed:

- Scenario 1 (S1): All 34 stations were used. Missing values (288 cells, 6.41% of data) were left as NaN, with the risk of bias from an unbalanced dataset.
- Scenario 2 (S2): The dataset was reduced to only the 15 stations that had complete data records for the entire period. This ensures minimal bias but reduces spatial coverage.
- Scenario 3 (S3): All 34 stations were used. The 288 missing values were imputed using KNN method, balancing data completeness and spatial coverage.

For Scenario 3, a Monte-Carlo simulation (50 iterations) was performed to determine the optimal imputation hyperparameters. This simulation, which involved randomly masking known values, found that $K = 16$ neighbors with distance-based weighting yielded the lowest RMSE. Finally, for all three scenarios, the 11-year monthly time-series data was aggregated into four quarterly averages to minimize seasonal variance: Jan-Mar (JFM), Apr-Jun (AMJ), Jul-Sep (JAS), and Oct-Dec (OND).

The kriging interpolation was implemented using the Python GSTools library. The interpolation was performed on a 100×100 grid covering the study area. The full experimental plan involved 36 unique interpolation models:

- 12 Ordinary Kriging (OK) models (4 quarters × 3 scenarios).
- 24 External Drift Kriging (EDK) models (4 quarters × 3 scenarios × 2 drift variables [Elev and Dist]).

Model accuracy was evaluated using Leave-One-Out Cross-Validation (LOOCV). In this study, for each iteration ($i = 1, \dots, n$), a single station (x_i) was removed from the dataset. The remaining $n - 1$ stations were used to re-calculate the variogram parameters and perform kriging to predict the value at x_i. This process was repeated for all n stations. The resulting prediction errors ($e_i = \hat{z}(x_i) - z(x_i)$) were compiled, and RMSE, MAE, and MAPE were calculated to compare model performance.

4. RESULTS AND DISCUSSIONS

4.1. Data Validation, Drift Selection, and Variogram Modeling

The analysis began with an exploratory data analysis to validate the three data-handling scenarios. As shown in **Table 1**, a comparison of Scenario 1 (original data) and Scenario 3 (imputed data) reveals that their descriptive statistics are highly comparable.

Table 1.

Mean and standard deviation of rainfall data across all scenarios and partitions.

Scenario		Mean (mm)				Std. Dev. (mm)			
		JFM	AMJ	JAS	OND	JFM	AMJ	JAS	OND
S1	No imp.	172.034	174.171	152.627	247.280	46.311	50.837	41.322	58.152
S2	$n = 15$	173.196	174.585	151.693	250.506	49.090	42.064	29.317	44.889
S3	Imputed	172.778	173.132	154.041	244.665	46.417	49.671	40.997	54.535

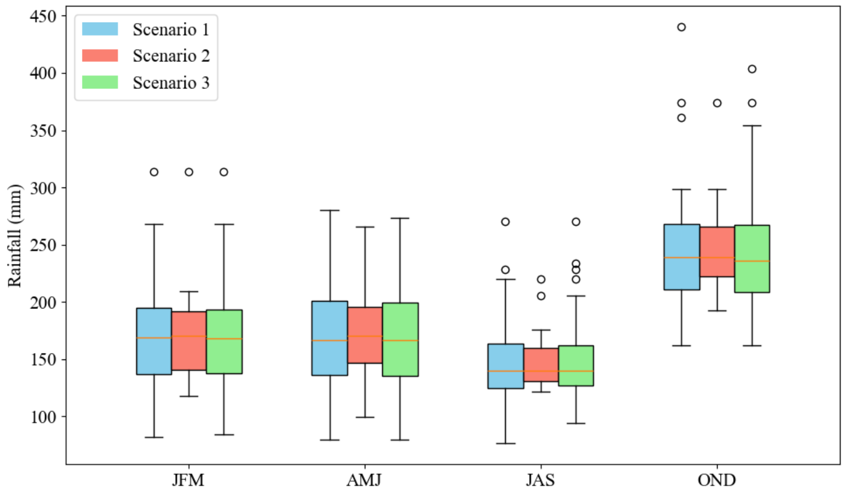

Fig. 2. Boxplot of rainfall in all partitions across all scenarios.

The minor differences in mean and standard deviation (e.g., S1 OND Mean 247.28 mm vs. S3 OND Mean 244.67 mm) are the expected result of including the 6.41% of imputed data points. This lack of significant statistical distortion validates the S3 dataset as a complete and reliable representation of the original data. Conversely, Scenario 2 (reduced stations) showed notable deviations, such as a significantly lower variance in the JAS quarter (std. dev. 29.32 mm), confirming it as a biased sample.

Beyond central tendency, the data's distribution (**Fig. 2**) revealed the presence of significant outliers in all datasets except for AMJ in all scenarios. Shapiro-Wilk normality tests (**Table 2**) confirmed that for both S1 and S3, the driest (JAS) and wettest (OND) quarters were non-normally distributed ($p < 0.05$). This is a critical finding, as standard variogram estimators (like Matheron's) are highly sensitive to such extreme values in the data. Therefore, the data's non-normality and outliers justify the use of the robust Cressie-Hawkins estimator for variogram modeling.

Table 2.
Shapiro-Wilk normality test results across all scenarios and partitions.

Scenario		Quarter	W Statistic	p-value	Decision
S1	**No imp.**	**JFM**	0.9534	0.1548	Normal
		AMJ	0.9614	0.2678	Normal
		JAS	0.9164	0.0128	Not normal
		OND	0.8901	0.0025	Not normal
S2	$n = 15$	**JFM**	0.8557	0.0209	Not normal
		AMJ	0.9675	0.8197	Normal
		JAS	0.8585	0.0230	Not normal
		OND	0.8818	0.0505	Normal
S3	**Imputed**	**JFM**	0.9538	0.1592	Normal
		AMJ	0.9631	0.2980	Normal
		JAS	0.8958	0.0036	Not normal
		OND	0.9144	0.0113	Not normal

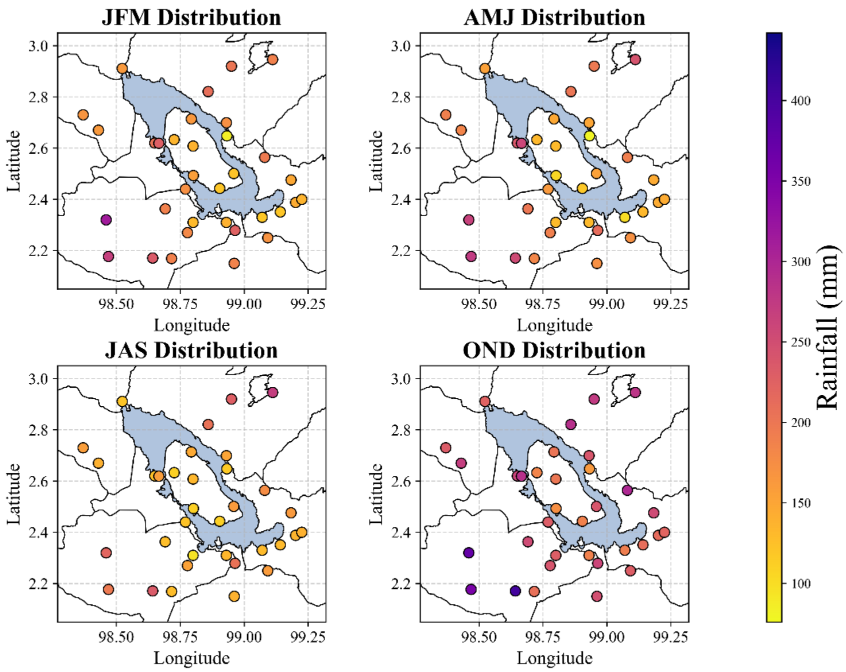

Fig. 3. Exploratory spatial distribution of observed seasonal rainfall across the Lake Toba basin for the JFM, AMJ, JAS, and OND quarters.

In addition to examining the statistical distribution, an exploratory spatial data analysis (ESDA) was conducted to visualize the raw seasonal precipitation patterns across the basin. As illustrated in **Fig. 3**, the observed rainfall data exhibits clear spatial heterogeneity. Throughout the year, higher precipitation volumes are consistently concentrated in the southwestern and northeastern regions of the outer basin. In contrast, a distinct dry zone persists over Samosir Island and the central caldera, particularly evident during the drier JAS quarter. This preliminary spatial mapping visually corroborates the complex microclimatic dynamics of the region, highlighting the need to carefully select and incorporate physical geographical variables into the interpolation model.

To evaluate potential drift variables for EDK, a Pearson correlation analysis was performed (**Table 3**). The analysis revealed that elevation (Elev) has a weak and mostly non-significant correlation with rainfall. In stark contrast, the distance from the lake (Dist) exhibited a strong, statistically significant positive correlation with rainfall across all quarters and scenarios ($r > 0.59$, $p < 0.01$). This confirms that Dist is a highly relevant and promising auxiliary variable, while Elev is expected to perform poorly.

Finally, spherical variogram models were fitted (**Table 4**). The fitted parameters for S1 and S3 were highly comparable, further demonstrating that the KNN imputation successfully preserved the underlying spatial correlation structure. In contrast, S2 (reduced stations) produced markedly different parameters, including a nugget effect of zero for most seasons. This suggests the sparse data led to an over-simplified model, unlike the more realistic micro-scale variability (noise) captured in S1 and S3.

Table 3.

Pearson correlation coefficients (r) and p-values for drift variables against quarterly rainfall.

Drift var.	Quarter	S1		S2		S3	
		r	p-value	r	p-value	r	p-value
Elev	JFM	-0.08	0.636	-0.02	0.940	-0.10	0.576
	AMJ	-0.11	0.541	0.17	0.554	-0.12	0.482
	JAS	-0.40	0.020	-0.22	0.427	-0.39	0.024
	OND	-0.19	0.271	-0.07	0.802	-0.20	0.245
Dist	JFM	0.65	0.000	0.75	0.001	0.66	0.000
	AMJ	0.70	0.000	0.65	0.009	0.68	0.000
	JAS	0.66	0.000	0.59	0.019	0.68	0.000
	OND	0.68	0.000	0.77	0.001	0.69	0.000

To show the variogram visually, the plot for the S3 models was shown (**Fig. 4**). The plot shows a clear spatial dependence structure that provided a reliable basis for interpolation. However, a clear full sill is not visible in the empirical plots. This is likely because the spatial extent of the study area (approx. 1.05 degrees) is comparable to the fitted spatial correlation range (0.75–1.00 degrees), meaning the maximum lag distance is insufficient to capture the full decorrelation. Additionally, outliers appear at greater distances. This is why weighted least squares was chosen for theoretical variogram fitting, it reduces the effect of these outliers at greater distances. These outliers may also show that the CH estimator has its limits.

Table 4.

Parameters of the fitted spherical variogram model.

Scenario		Parameter	JFM	AMJ	JAS	OND
S1	No imp.	Range (deg)	0.91	0.75	1.00	1.00
		Total Sill (mm^2)	3044.3	3667.86	2573.82	4590.05
		Nugget (mm^2)	592.58	400.59	195.93	645.97
S2	$n = 15$	Range (deg)	0.87	0.87	0.87	0.87
		Total Sill (mm^2)	4306.53	3595.28	1359.12	6019.41
		Nugget (mm^2)	0.00	0.00	183.08	0.00
S3	Imputed	Range (deg)	0.92	1.00	1.00	1.00
		Total Sill (mm^2)	3174.820	4076.37	2531.76	4224.46
		Nugget (mm^2)	460.27	665.67	167.23	719.72

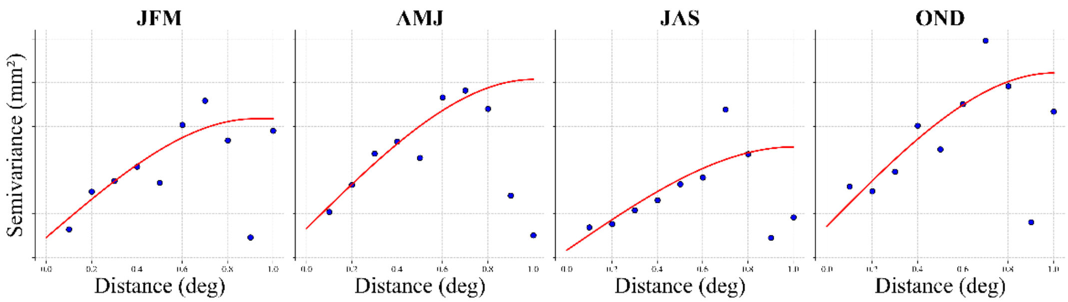

Fig. 4. Visual representation of the fitted theoretical variogram models in Scenario 3.

4.2. Kriging Performance and Spatial Interpolation

The 36 kriging models were evaluated using Leave-One-Out Cross-Validation (LOOCV), with results presented in **Table 5** (for OK) and **Table 6** (for EDK). Kriging was performed on untransformed data, as preliminary tests with log, square-root, and Box-Cox transformations did not improve evaluation metrics.

Table 5.

LOOCV evaluation metrics for Ordinary Kriging (OK).

Scenario		Quarter	RMSE	MAE	MAPE (%)
S1	**No imp.**	**JFM**	36.9534	26.6975	16.8347
		AMJ	35.5512	28.8207	18.8534
		JAS	34.9528	27.8754	19.2172
		OND	50.1285	34.9198	14.3593
S2	$n = 15$	**JFM**	45.4856	35.0459	19.2639
		AMJ	39.0001	31.7394	18.5105
		JAS	32.9532	25.1486	15.8229
		OND	41.1272	29.1662	10.819
S3	**Imputed**	**JFM**	35.4235	26.3160	16.3979
		AMJ	35.5623	29.4276	19.1713
		JAS	34.4482	27.7322	18.3211
		OND	45.6477	32.9888	13.7802

The validation metrics reveal two critical findings. First, for the dense-data scenarios (S1 and S3), the performance of OK and EDK was nearly identical. In S3, for example, the OND (wettest quarter) RMSE for OK was 45.65 mm, while EDK-Elev was 46.06 mm and EDK-Dist was 45.39 mm. These differences are negligible, which leads to a significant conclusion: with a sufficiently dense station network, the added complexity of EDK provides no tangible benefit. The kriging estimate is dominated by the wealth of nearby observations, rendering the influence of the auxiliary drift variable, whether strongly correlated or not, statistically insignificant.

The central finding of this study emerged from the sparse-data Scenario (S2). Here, the EDK-Dist model was the undisputed best-performing model, particularly in the JAS (RMSE 23.39) and OND (RMSE 26.97) quarters. This shift in performance aligns with findings by Camera et al. (2014), who observed that the ranking of interpolation techniques is directly dependent on observation density. They noted that higher station density leads to greater stability in method ranking, whereas sparse networks often necessitate specific techniques that can better capture spatial variability. This contrast is evident in our results: while dense scenarios showed little difference between methods, the sparse scenario (S2) revealed a stark divergence between the successful EDK-Dist and the poor-performing S2-OK (OND RMSE 26.97) and S2-EDK-Elev (OND RMSE 50.42).

Table 6.

LOOCV evaluation metrics for External Drift Kriging (EDK).

Scenario		Drift	Quarter	RMSE	MAE	MAPE (%)
S1	No imp.	Elev	JFM	35.8549	26.7138	16.6096
			AMJ	34.5249	27.0139	16.9901
			JAS	35.1094	27.5594	18.8782
			OND	50.5462	34.8214	14.2939
		Dist	JFM	36.3958	27.7241	17.3533
			AMJ	34.2258	27.6334	18.2767
			JAS	33.5745	26.3913	18.2241
			OND	50.4825	35.7599	14.5359
S2	$n = 15$	Elev	JFM	59.2182	41.8769	22.4403
			AMJ	49.171	38.2899	21.7479
			JAS	37.242	29.5129	18.6888
			OND	50.4235	34.2488	12.7015
		Dist	JFM	42.7698	31.7958	17.8031
			AMJ	37.1501	28.1417	16.3599
			JAS	23.3909	18.3329	11.5188
			OND	26.965	20.6127	7.694
S3	Imputed	Elev	JFM	34.6249	26.1632	16.1201
			AMJ	35.2068	28.0403	17.7584
			JAS	34.5546	27.397	17.9709
			OND	46.0575	33.0014	13.7706
		Dist	JFM	35.2718	27.5913	17.0083
			AMJ	34.0632	27.9627	18.4094
			JAS	33.1907	26.129	17.3101
			OND	45.3904	33.5958	13.9203

The failure of the EDK-Elevation model to outperform Ordinary Kriging is consistent with geostatistical theory; while Goovaerts (2000) demonstrated that external drift variables can significantly reduce error, this is contingent on a strong correlation. Similarly, Wagner et al. (2012) found that in monsoon-driven mountainous regions, elevation may show no significant correlation with rainfall. They demonstrated that variables representing the distance from a moisture source or orographic barrier (such as the Western Ghats escarpment) can be far superior predictors than local elevation. In our study, the 'Dist' variable, reflecting the lake's influence, acted as a powerful guide for the interpolation precisely because the observation data was too sparse to capture the pattern on its own.

The superior performance of the EDK-Dist model in the sparse-data scenario is deeply rooted in the physical microclimatology of the Lake Toba caldera. As a massive inland water body covering over 1,100 square kilometers, Lake Toba acts as the primary local moisture source for the immediate surrounding basin. The thermal contrast between the lake surface and the surrounding landmass generates strong, localized diurnal lake-land breeze circulations. Moisture evaporated from the lake is transported inland by these breezes, resulting in a precipitation gradient that is heavily dependent on proximity to the shoreline. In a sparse observation network where macro-scale synoptic weather patterns are under-sampled, this distance-to-lake variable effectively captures the dominant microclimatic driver of regional rainfall, providing a highly reliable spatial guide for the interpolation algorithm.

Conversely, the failure of elevation to improve interpolation accuracy is a direct result of the caldera's complex topography and resulting rain shadow effects. While geostatistical theory often assumes a positive linear correlation between elevation and rainfall due to orographic lift, the Lake Toba basin is characterized by exceptionally steep caldera walls and the central presence of Samosir Island.

Prevailing regional winds deposit the majority of their moisture on the windward slopes of the outer basin. By the time air masses descend into the caldera or cross over Samosir Island, they have lost significant moisture, creating localized rain shadows. Consequently, high-elevation stations on leeward slopes may record significantly lower rainfall than lower-elevation stations on windward slopes. Because a simple elevation variable cannot distinguish between windward and leeward positioning, its correlation with rainfall breaks down, rendering it an ineffective auxiliary drift variable for this specific geographical context.

The resulting interpolation maps (**Fig. 5** and **Fig. 6**) visually confirm these statistical findings. The OK maps (**Fig. 5**) show a consistent spatial trend with lower rainfall concentrated around Samosir Island. The EDK maps (**Fig. 6**) using 'Dist' reinforce this same trend but with a smoother, more regular pattern, which the validation metrics in **Table 6** proved to be a more accurate representation. The EDK-Elev maps, in contrast, appear coarser and less refined, reflecting the irrelevant spatial pattern of the elevation data.

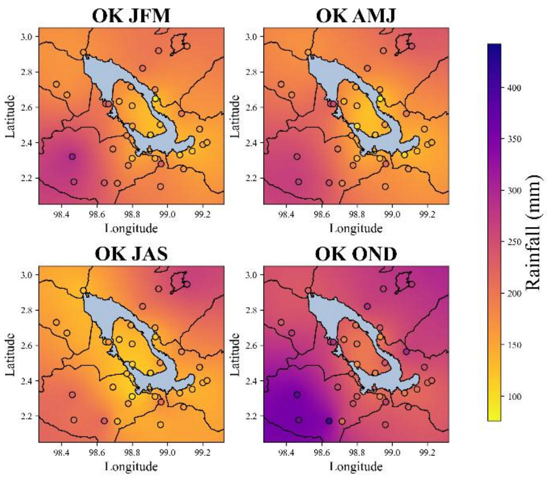

Fig. 5. Interpolated rainfall maps using ordinary kriging for Scenario 3.

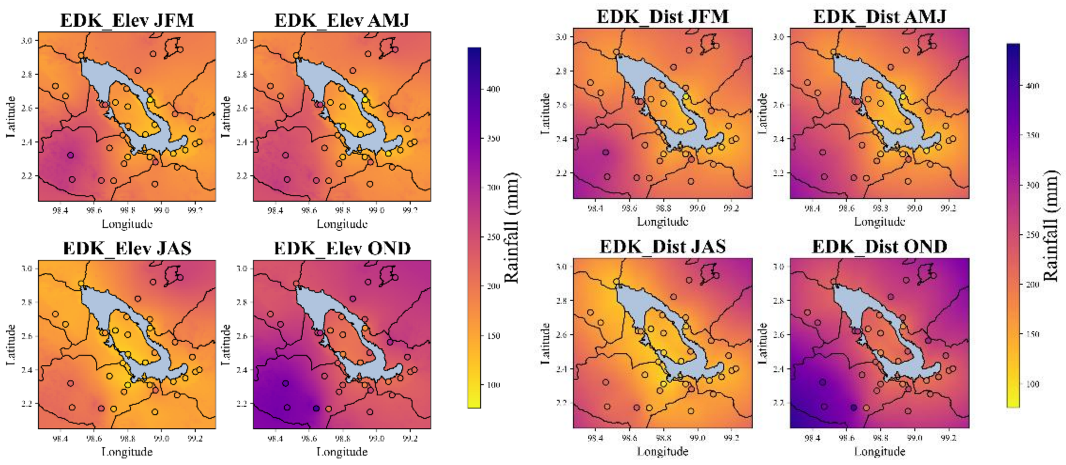

Fig. 6. Interpolated rainfall maps using external drift kriging for Scenario 3 with Elev (left) and Dist (right).

5. CONCLUSION

This study evaluated the spatial interpolation of rainfall in the Lake Toba region by comparing Ordinary Kriging (OK) and External Drift Kriging (EDK) across varied data-handling scenarios. Geographically, the spatial mapping confirmed a consistent precipitation pattern characterized by higher rainfall concentrations in the southwest and northeast, contrasting with a distinct dry zone over Samosir Island and the central caldera. Statistically, the application of k-nearest-neighbors (KNN) imputation proved highly robust, preserving the dataset's underlying spatial correlation structure without introducing the bias inherent in discarding incomplete station records.

The central finding of this research demonstrates that the mathematical effectiveness of interpolation models is deeply governed by the physical geography of the study area. In scenarios with a dense observation network, the abundance of local data points dominates the estimation, rendering the added complexity of EDK largely unnecessary. However, in data-sparse regions, accurate interpolation requires integrating the physical drivers of the local microclimate.

The stark contrast in EDK performance between the two auxiliary variables highlights this geographical dependency. The failure of the elevation variable (EDK-Elev) illustrates that standard assumptions of orographic lift do not uniformly apply in complex terrain; the steep caldera walls and Samosir Island create localized rain shadows that disrupt linear elevation-rainfall correlations. Conversely, the dramatic success of the distance-to-lake variable (EDK-Dist) mathematically confirms Lake Toba's role as the dominant moisture source driving the region's microclimate. By functioning as a proxy for localized lake-land breeze circulations, the distance variable successfully guided the interpolation where raw data was insufficient. Ultimately, this study concludes that spatial interpolation in complex topographical basins cannot rely on statistical optimization alone; it must be grounded in variables that accurately reflect the physical and climatic realities of the landscape.

REFERENCES

Al-Mofleh, H., Daniels, J., & Mckean, J. (2016). Robust variogram fitting using non-linear rank-based estimators. *International Journal of Mathematical, Computational, Physical, Electrical and Computer Engineering*, *10*(2), 68–77. https://www.researchgate.net/publication/299098198

Batista, G. E. A. P. A., & Monard, M. C. (2002). A study of k-nearest neighbour as an imputation method. *Soft Computing Systems: Design, Management and Applications*.

Caloiero, T., Pellicone, G., Modica, G., & Guagliardi, I. (2021). Comparative analysis of different spatial interpolation methods applied to monthly rainfall as support for landscape management. *Applied Sciences (Switzerland)*, *11*(20). https://doi.org/10.3390/app11209566

Camera, C., Bruggeman, A., Hadjinicolaou, P., Pashiardis, S., & Lange, M. A. (2014). Evaluation of interpolation techniques for the creation of gridded daily precipitation (1 × 1 km2); Cyprus, 1980–2010. *Journal of Geophysical Research*, *119*(2), 693–712. https://doi.org/10.1002/2013JD020611

Cressie, N. (1985). Fitting variogram models by weighted least squares. *Mathematical Geology*, *17*(5). https://doi.org/10.1007/BF01032109

Cressie, N. A. C. (1993). *Statistics for Spatial Data* (Revised Edition). John Wiley & Sons.

Cressie, N., & Hawkins, D. M. (1980). Robust estimation of the variogram: I. *Mathematical Geology*, *12*(2), 115–125.

Das, S., & Islam, A. R. M. T. (2021). Assessment of mapping of annual average rainfall in a tropical country like Bangladesh: remotely sensed output vs. kriging estimate. *Theoretical and Applied Climatology*, *146*(1–2), 111–123. https://doi.org/10.1007/s00704-021-03729-3

Frazier, A. G., Giambelluca, T. W., Diaz, H. F., & Needham, H. L. (2016). Comparison of geostatistical approaches to spatially interpolate month-year rainfall for the Hawaiian Islands. *International Journal of Climatology*, *36*(3), 1459–1470. https://doi.org/10.1002/joc.4437

Fung, K. F., Chew, K. S., Huang, Y. F., Ahmed, A. N., Teo, F. Y., Ng, J. L., & Elshafie, A. (2022). Evaluation of spatial interpolation methods and spatiotemporal modeling of rainfall distribution in Peninsular Malaysia. *Ain Shams Engineering Journal*, *13*(2). https://doi.org/10.1016/j.asej.2021.09.001

Goovaerts, P. (2000). *Geostatistical approaches for incorporating elevation into the spatial interpolation of rainfall*. www.elsevier.com/locate/jhydrol

Gutierrez-Lopez, A. (2021). A Robust Gaussian variogram estimator for cartography of hydrological extreme events. *Natural Hazards*, *107*(2), 1469–1488. https://doi.org/10.1007/s11069-021-04641-9

Hengl, T., Heuvelink, G. B. M., & Stein, A. (2003). *Comparison of kriging with external drift and regression-kriging* *. http://www.itc.nl/library/Academic

Irwandi, H., Rosid, M. S., & Mart, T. (2021). The effects of ENSO, climate change and human activities on the water level of Lake Toba, Indonesia: a critical literature review. In *Geoscience Letters* (Vol. 8, Issue 1). Springer Science and Business Media Deutschland GmbH. https://doi.org/10.1186/s40562-021-00191-x

Irwandi, H., Rosid, M. S., & Mart, T. (2023). Effects of Climate change on temperature and precipitation in the Lake Toba region, Indonesia, based on ERA5-land data with quantile mapping bias correction. *Scientific Reports*, *13*(1). https://doi.org/10.1038/s41598-023-29592-y

Koesuma, S., Faqih, A., Hendri, H., Listyarini, J., Kusuma, D. A., Hanggara, A. Z., & Gernowo, R. (2025). Analysis of extreme rainfall of tropical cyclone using solar radiation management and ERA5 data in eastern part of Indonesia. *Geographia Technica*, *20*(1), 298–312. https://doi.org/10.21163/GT_2025.201.20

Kuhn, M., & Johnson, K. (2013). *Applied Predictive Modeling* (1st ed.). Springer.

Kyriakidis, P. C., Kim, J., & Miller, N. L. (2001). Geostatistical mapping of precipitation from rain gauge data using atmospheric and terrain characteristics. *Journal of Applied Meteorology and Climatology*, *40*(1), 1855–1877.

Ly, S., Charles, C., & Degré, A. (2013). Different methods for spatial interpolation of rainfall data for operational hydrology and hydrological modeling at watershed scale. A review. In *Biotechnol. Agron. Soc. Environ* (Vol. 17, Issue 2).

Mackie, E. J., Field, M., Wang, L., Yin, Z., Schoedl, N., Hibbs, M., & Zhang, A. (2023). GStatSim V1.0: a Python package for geostatistical interpolation and conditional simulation. *Geoscientific Model Development*, *16*(13), 3765–3783. https://doi.org/10.5194/gmd-16-3765-2023

Mahdi, E., Abuzaid, A. H., & Atta, A. M. A. (2020). Empirical variogram for achieving the best valid variogram. *Communications for Statistical Applications and Methods*, *27*(5), 547–568. https://doi.org/10.29220/CSAM.2020.27.5.547

Mälicke, M. (2022). SciKit-GStat 1.0: A SciPy-flavored geostatistical variogram estimation toolbox written in Python. *Geoscientific Model Development*, *15*(6), 2505–2532. https://doi.org/10.5194/gmd-15-2505-2022

Mohebzadeh, H. (2018). *Comparison of Methods for Fitting the Theoretical Variogram to the Experimental Variogram for Estimation of Depth to Groundwater and its Temporal and Spatial Variations*. https://doi.org/10.5829/idosi.aejaes.2018.64.76

Nguyen, T. T. (2020). Analysis of Spatial Dependence of Ore-Forming Elements Using Geostatistics and Moran Correlogram. *Asian Review of Environmental and Earth Sciences*, *7*(1), 47–54. https://doi.org/10.20448/journal.506.2020.71.47.54

Oliver, M. A., & Webster, R. (2015). *Basic Steps in Geostatistics: The Variogram and Kriging*. Springer. http://www.springer.com/series/10183

Pearse, A. R., Cressie, N., & Gunawan, D. (2024). *Optimal prediction of positive-valued spatial processes: asymmetric power-divergence loss*.

Somayasa, W., Sutiari, D. K., & Sutisna, W. (2021). Optimal prediction in isotropic spatial process under spherical type variogram model with application to corn plant data. *Journal of Physics: Conference Series*, *1940*(1), 012003. https://doi.org/10.1088/1742-6596/1940/1/012003

Wagner, P. D., Fiener, P., Wilken, F., Kumar, S., & Schneider, K. (2012). Comparison and evaluation of spatial interpolation schemes for daily rainfall in data scarce regions. *Journal of Hydrology*, *464–465*, 388–400. https://doi.org/10.1016/j.jhydrol.2012.07.026

Webster, R., & Oliver, M. A. (2007). *Geostatistics for Environmental Scientists Second Edition* (S. Senn, M. Scott, & V. Barnett, Eds.; 2nd ed.). John Wiley & Sons Ltd.

MULTI-TEMPORAL SATELLITE ANALYSIS OF MORPHODYNAMIC CHANGE IN THE PERANCAK SANDSPIT, BALI, INDONESIA

Adzkia Noerma ARIFA[1,*], *Bayu MUNANDAR*[2,3] *& Amir Yarkhasy YULIARDI*[4]

DOI: 10.21163/GT_2026.213.08

ABSTRACT

Perancak Sandspit, located in Jembrana Regency, is one of the coastal landforms on the southwest coast of Bali, Indonesia. It is a large hook-shaped sandspit that experienced morphodynamic change between January 2024 and January 2025. The results reveal three periods of sandspit shortening and one period of sandspit elongation. During the first period, January to March 2024, and the third period, July to September 2024, the sandspit experienced shortening at a rate of about 0.3 meters/day. The second period, April to June 2024, was the only period of sandspit elongation with a rate of 0.59 meters/day. Although the sandspit elongated, its width remained unchanged from the first period at 150 meters. Conversely, in the fourth period, October 2024 to January 2025, the sandspit shrank significantly at a rate of 1.16 meters/day, with a concurrent decrease in width. In addition, in the first and fourth periods, changes in the direction of the distal end of the Perancak sandspit were observed, which were pushed toward the east-northeast. The result indicates that the longshore sediment transport rate during the elongation phase is around 104,000 m^3/year. Although the Perancak sandspit exhibits fluctuations in morphology and geometry, its overall characteristics in January 2025 remained similar to those observed in January 2024. It indicates recurring morphological and geometric variations of the Perancak sandspit.

Keywords*: Sandspit; Morphodynamic change; Multi-temporal; Longshore sediment transport rate; Bali.*

1. INTRODUCTION

Sandspit is one of the coastal landforms in the form of narrow and elongated sediment deposits. It is dominantly formed by longshore currents. The proximal part of the sandspit was always connected to the mainland, and the distal part often curves following the dominant wave direction. Sandspits were found on irregular shorelines where sediment availability and wave energy allowed the smoothing of the coastline by maintaining the direction of longshore currents and moving toward the coastal re-entrants or bay (Orford, 2006).

Morphological and geometrical changes of sandspits were best observed in a plan view perspective. Many studies have examined the dynamics of sandspits through field observations, analytical solutions, numerical and physical modeling, as well as satellite imagery analysis (Duy et al., 2023). Among these methods, satellite imagery analysis was the most widely used (Lawson et al., 2021).

[1] *Department of Marine Science, Faculty of Fisheries and Marine Science, Universitas Diponegoro, Indonesia. *Corresponding author: adzkia@lecturer.undip.ac.id (ANA).*
[2] *Department of Oceanography, Faculty of Fisheries and Marine Science, Universitas Diponegoro, Indonesia, bymunandar@gmail.com (BM).*
[3] *Study Program of Fisheries and Marine Technology and Business, Faculty of Fisheries and Marine Science, Universitas Diponegoro, Indonesia.*
[4] *Department of Marine Science, Faculty of Fisheries and Marine Science, Universitas Jendral Soedirman, Indonesia, amiryarkhasy@gmail.com (AYY).*

The length and width of a sandspit were the functions of the availability of sediments and net longshore-directed wave-generated transport. In general, the dominant sediment found in its deposits was fine sediments such as sand, but gravel-dominated spits could also be found if the main component of the sediment availability on the coast was also dominated by gravel. On the other hand, mud-dominated sandspits were unlikely to form because the spits were formed by the breaking wave activity (Orford, 2006).

Moreover, the formation of a sandspit on the coast generated a backspit lee with low-energy currents, such as tides and small waves, and the deposition of fine sediments in the form of tidal banks and salt marshes. The morphological and geometrical changes of sandspits would affect the river flow patterns and the sedimentation systems at the estuary. These conditions have impacted the coastal ecosystems and fishermen's navigation access, the coastal land use, and escalated the flood risk in the downstream areas.

Bali, Indonesia, including the Jembrana Regency, has shown a diversity of coastal dynamics due to the natural and anthropogenic processes. The Perancak Village is located on the southwest coast of Bali and directly borders the Bali Strait (**Fig 1**). The Bali Strait is a narrow passage that lies between Java and Bali, linking the Java Sea on the northern side and the Indian Ocean on the southern side. The bathymetry of the Bali Strait is characterized by a shallow area in the middle section, but becomes steeper in the southern part and is exposed directly to the Indian Ocean (Berlianty and Yanagi, 2015).

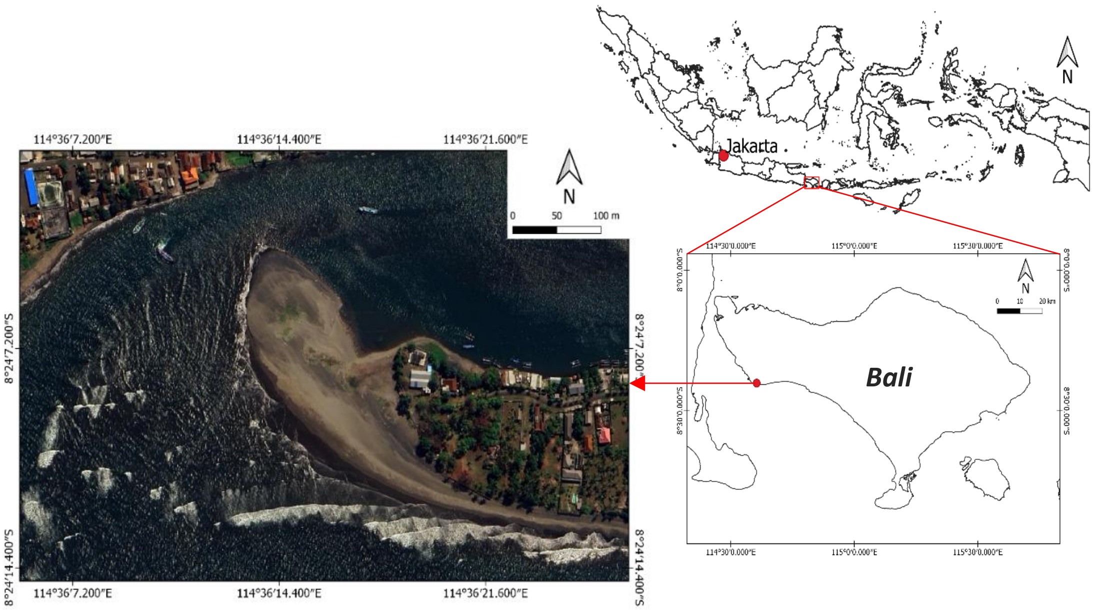

Fig. 1. Location of Bali in Indonesia (**right**) and the Perancak sandspit on the southwest coast of Bali (**left**).

The majority of its people worked as fishermen and farmers. The area also features other attractions, including turtle conservation sites and mangrove forests. In Perancak Village, a sandspit over 100 meters wide extends at the mouth of the Perancak estuary. As well as the Perancak beach, which consisted of medium sand on the bottom sediment (Paluphi et al., 2020), the Perancak sandspit was also constructed by fine sediment, such as sand. The anchoring area for fishing boats and the main tourist spot are located on the backspit.

Although multi-temporal satellite imagery analysis has been widely applied in coastal studies, its integration with sediment transport quantification to investigate the sandspit dynamics remains limited, particularly in the Perancak area. Due to the numerous strategic activities in the area, the sandspit dynamics here will affect local community livelihoods and existing tourism activities. Therefore, this study focuses on the morphological and geometrical changes of the sandspit found in Perancak, Jembrana, Bali, Indonesia.

2. MATERIALS AND METHODS

2.1. Satellite Image Analysis and Geometric Characteristics

The methodology employed in our study is depicted in **Fig 2**. The approach used in our study was satellite imagery analysis for the period of January 2024 to January 2025. First, the Sentinel-2 images were collected to observe the morphological and geometrical changes of the Perancak sandspit. These images were obtained from the Copernicus Data Space Ecosystem (**Table 1**). Second, the water line was distinguished from the sand using the modified normalized difference water index (MNDWI) at a resolution of 20 meters.

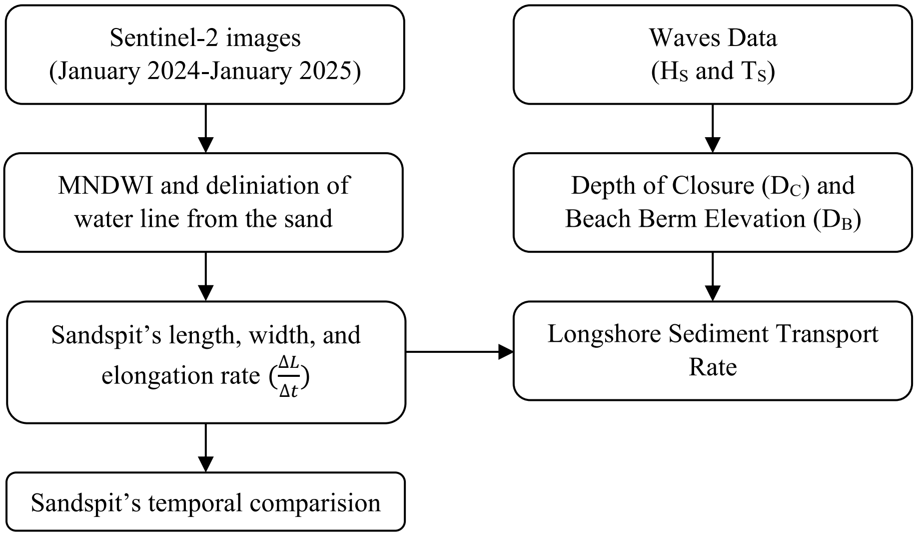

Fig. 2. Flow diagram for the research procedure.

Table 1.
An overview of Sentinel-2 data used in this study.

Date (dd/mm/yyyy)	Sensor	Resolution	Data Source
30/01/2024	Multispectral Instrument	10 m and 20 m	Sentinel-2
29/02/2024			
30/03/2024			
29/04/2024			
29/05/2024			
28/06/2024			
23/07/2024			
22/08/2024			
21/09/2024			
26/10/2024			
20/11/2024			
14/01/2025			

MNDWI was adopted because it was more suitable to improve the water information and can extract the water bodies more accurately than NDWI (Xu, 2006 and Du et al., 2016). The MNDWI from Sentinel-2 images was obtained through raster calculation using the following formula:

$$MNDWI = \frac{X_{green} - X_{SWIR}}{X_{green} + X_{SWIR}} \tag{1}$$

where X_{green} is the green band or Band 3 and X_{SWIR} is the short-wave infrared band or Band 11 of Sentinel-2.

Third, the length (L) and width (W) components were calculated based on the sandspit geometry. The length (L) component was drawn from the proximal point to the distal point of the sandspit. Meanwhile, the width (W) component was drawn transversely from the spit-platform geometry at the hook section.

2.2. Wave Data, Depth of Closure, and Beach Berm Elevation

The data used in this study include the wave data in the area of the Bali Strait (**Fig 3**), emphasizing the temporal change of the sandspit. The wave reanalysis data are from WAVERYS product (https://data.marine.copernicus.eu/product/GLOBAL_MULTIYEAR_WAV_001_032). The wave data were used for the calculation of the depth of closure (D_C) and the beam elevation (D_B). The depth of closure (D_C) and the beam elevation (D_B) were calculated using empirical calculations.

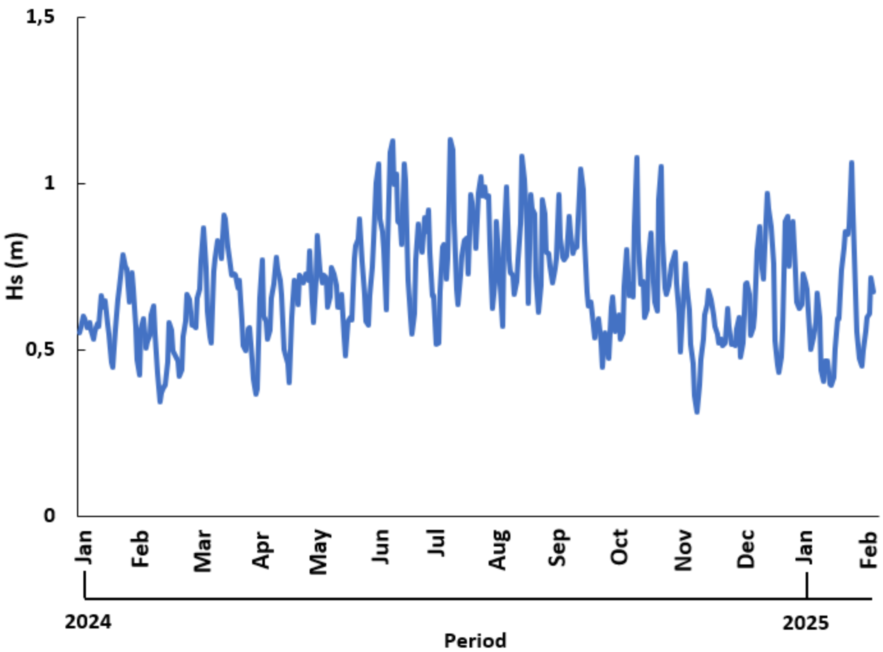

Fig. 3. The significant wave height between January 2024 and January 2025.

Two crucial factors for estimating the longshore sediment transport rate are the depth of closure (D_C) and the beam elevation (D_B). The depth of closure refers to the maximum offshore depth at which cross-shore sediment transport is negligible under normal wave and tide conditions (Durkin, Seenath & Knaapen, 2025). The depth of closure (D_C) was calculated using the equation proposed by Hallermeier (1978,1981) as follows:

$$D_C = 2.28H_{se} - 68.5\left(\frac{H_{se}^2}{gT_{se}^2}\right) \tag{2}$$

where Hse and Tse are the significant wave height and wave period of the extreme wave condition that is expected 12 h per year (Hallermeier, 1978) and g is the acceleration caused by gravity.

Hallermeier defined another equation of depth of closure based on the relationship between *Hse* and the annual mean of significant wave height as:

$$D_C = 2\overline{H}_s + 11\sigma_s \tag{3}$$

where σ_S is the standard deviation of the significant wave height.

In addition, the beach berm is a natural form of beach profile created by onshore sediment transport due to waves in the swash zone (Zhu et al., 2022). The beam elevation is the vertical distance from the crest of the berm to the specific datum, usually the mean sea level. An empirical equation relating the depth of closure to the berm elevation was defined by Uda (1997, as cited in Lawson et al., 2021 and Duy et al., 2023) and is represented as follows:

$$D_B = 0.32 \times D_C \tag{4}$$

2.3. Longshore Sediment Transport Estimation Model and Sandspit Growth Rate

The longshore sediment transport rate (LSTR) was estimated in this study using a straightforward mathematical calculation based on the methodology of Lawson et al. (2021). A schematic diagram of the model is shown below:

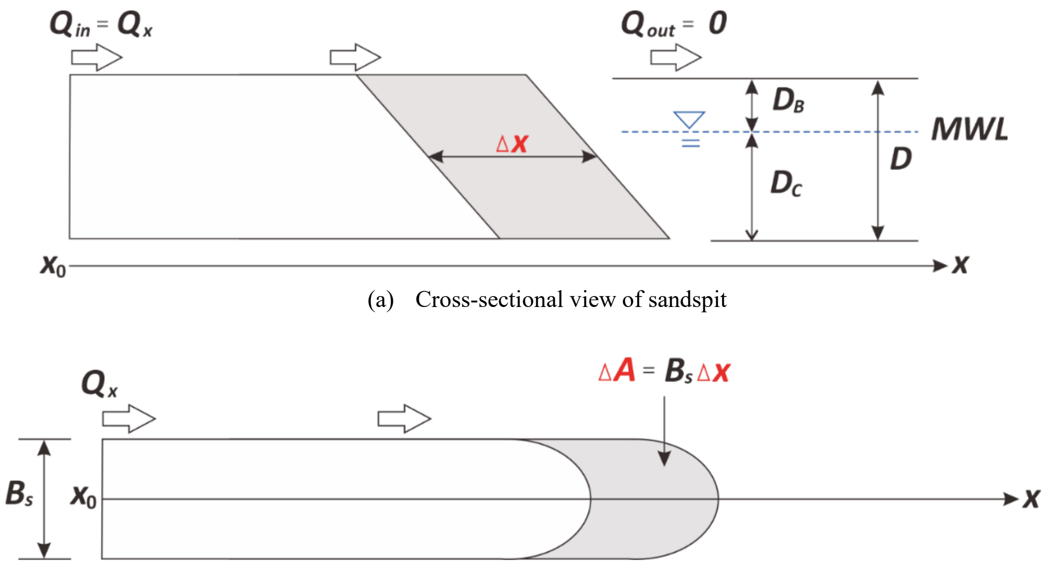

(a) Cross-sectional view of sandspit

(b) Plan view of sandspit

Fig. 4. Redrawn from Lawson et al. (2021), this schematic representation of the sandspit development process shows (a) a cross-sectional view and (b) a plan view.

According to the Lawson et al. (2021) model, the gradient in longshore sediment transport Q_{in} = Q_x is thought to contribute to the sandspit's elongation directly, while the sandspit's width (B_S) remains constant throughout its growth and there is no sediment loss at its tip (Q_{out} = 0). The assumption of Q_{out} = 0 is used to obtain the first-order approximation of longshore sediment transport by simplifying the sediment budget and neglecting sediment losses at the tip. Moreover, the depth of closure (D_C) plus the berm elevation (D_B) adds up to the depth of active sediment (D). Given the above assumption, the LSTR can be calculated as follows:

$$Q_{in} = \bar{Q}_x = D \times \frac{\Delta A}{\Delta t} \tag{5}$$

where D is the depth of active sediment motion, calculated as $D_C + D_B$, and ΔA/Δt represents the sandspit area changes over a given time period. ΔA/Δt can be substituted by:

$$\frac{\Delta A}{\Delta t} = B_S \times \frac{\Delta L}{\Delta t} \tag{6}$$

where B_S refers to the width of the sandspit, which is considered constant over the elongation period, and ΔL/Δt is the elongation rate of the sandspit, which was determined from the image analysis.

Thus, the LSTR can be determined as:

$$Q_{in} = Q_x = (D_B + D_C) \times B_S \times \frac{\Delta L}{\Delta t} \tag{7}$$

Studies by Udo, Ranasinghe & Takeda (2020), and Razak & Khan (2020) have addressed the constraints of using Equation (2). By contrasting the outcomes of field surveys of wave conditions with wave data obtained from the models, these limitations were found. The cumulative error of our estimations reflects the ±20% error tolerance we imposed on our depth of closure calculations due to these limitations.

The temporal variation of the length change (ΔL/Δt) and width change ($\Delta B_S/\Delta t$) were calculated using linear regression. Furthermore, we used a straightforward mathematical formula proposed by Duc Anh et al. (2020a) to predict the rate of sandspit growth in the elongation period as a function of the LSTR and sandspit width.

The hypothesis assumes that the sandspit width will remain constant during the elongation phase. The LSTR calculation in this study follows a similar assumption. This assumption leads to the following expression for the sandspit growth rate as follows:

$$R_S = \frac{Q_x}{(D_C + D_B)} \times \frac{1}{B_S} \tag{8}$$

where Q_x is the LSTR, D_C is the depth of closure, D_B is the berm elevation, and B_S is the sandspit width.

3. RESULTS AND DISCUSSION

3.1. Temporal Variation of Sandspit Geometry

3.1.1 Sandspit Length

Sandspits are attached to the land at one end and are longer than they are wide (Huggett, 2007). Based on research by Weidman and Ebert (1993), morphological changes in sandspits occurred cyclically and the periodic systems improved our understanding of inlet genesis and beach-barrier or sandspit evolution. Therefore, analyzing the temporal shoreline changes of the Perancak sandspit is important to understand the morphological dynamics. Changes in the shoreline of the Perancak sandspit are shown in **Fig 5**. It was shown that there were several periods of shortening and elongation from January 2024 to January 2025. Furthermore, we divided the morphological and geometrical timeframes into four periods (**Fig 6**). In this case, the elongation and shortening events were used to distinguish the periods.

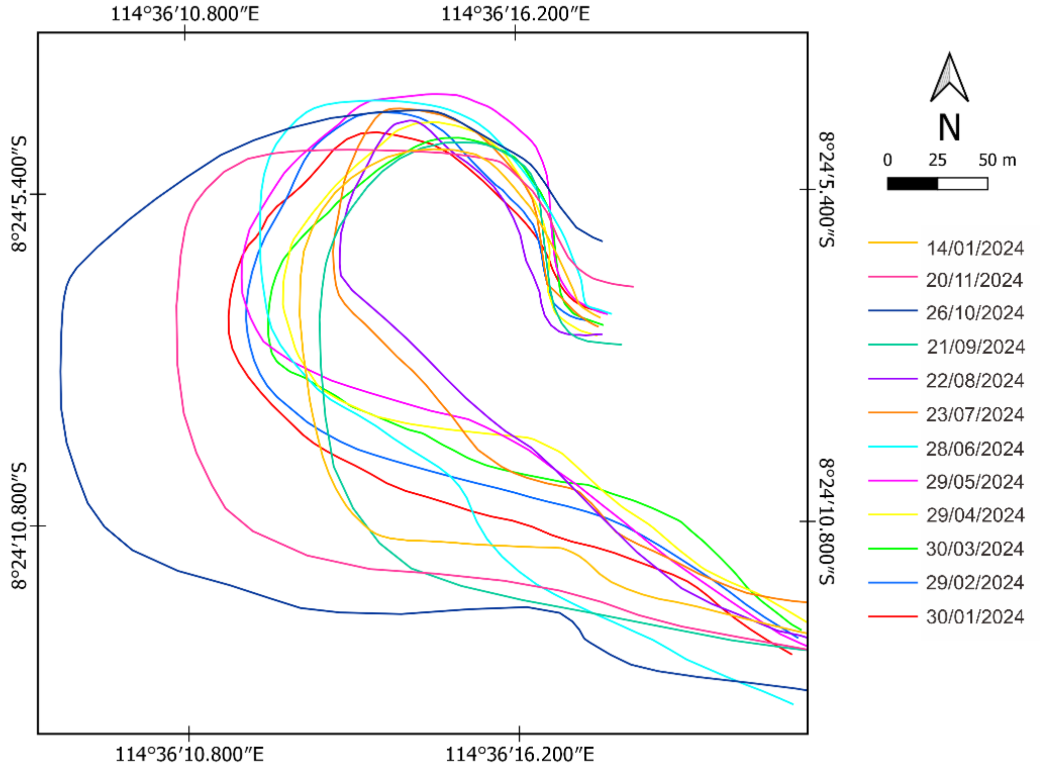

Fig. 5. Temporal variation of the Perancak sandspit's shoreline.

In the first period, January to March 2024, the sandspit experienced a gradual reduction in length or shortening. The rate of reduction was 0.33 meters/day. During the second period, April to June 2024, the sandspit experienced elongation and uninterrupted growth. The growth rate of the Perancak sandspit in this period was 0.59 m/day. Meanwhile, afterwards, a shortening was observed in July, indicating the end of Perancak sandspit growth in the second period.

In the third period, July to September 2024, a gradual reduction in the length occurred, similarly to the first period, with a rate of 0.36 meters/day. This period ended with significant sandspit growth until October 2024, with an increase of about 105.57 meters. This growth rate was 3.11 meters/day. In the fourth period, October 2024 to January 2025, a significant reduction in the length of the Perancak sandspit occurred with a rate of 1.16 meters/day.

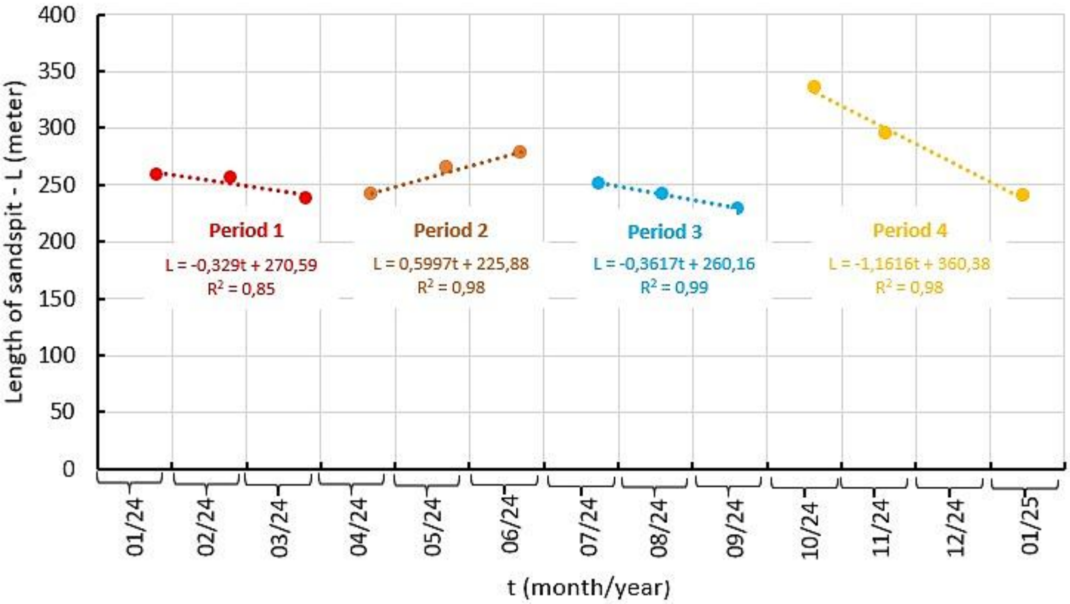

Fig. 6. Elongation and shortening of the Perancak sandspit from January 2024 to January 2025.

The sandspit dynamics are strongly linked to the sediment budget on the coast and/or the wave energy (Escudero et al., 2019). These factors play an important role in controlling the balance between erosion and sediment deposition along both the distal end and the body of the sandspit. When wave energy increases, erosion and sediment redistribution tend to dominate, causing shortening and morphological changes. In contrast, when sediment supply and depositional processes are dominant, the sandspit experiences elongation.

We indicated that the shortening during the first and the third periods was caused by gradual erosion at the distal tip. Hence, the erosional processes exceeded the sediment supply during these periods. In the first period, the wave energy increased compared to early January. The west monsoon, which is characterized by dominant winds from the west-northwest, generates higher-energy wave conditions. Furthermore, the shortening observed during the third period corresponded with the peak of the east monsoon, which also showed relatively higher wave conditions. These conditions likely intensified erosional processes at the distal end and enhanced sediment redistribution along the shoreline.

In contrast, the shortening was more notable and occurred at a higher rate during the fourth period. Compared to the first period, relatively higher wave energy prevailed during this period. We indicated this condition triggered rapid erosion at the spit-platform tip within a short period, whereas the sediment supply may have remained insufficient to compensate for ongoing erosion at the distal end. Moreover, the elongation occurred in the second period during the transitional phase toward the east monsoon. Wave conditions during this period were relatively favorable for sediment deposition, allowing sediment supply to accumulate at the distal end of the sandspit.

Besides the changes in the sandspit's length, the changes in the distal end of the Perancak sandspit were observed. In general, the Perancak sandspit is oriented northwest with a large hooked sandspit type. In the first and fourth periods, the curvature at the distal end of the sandspit appeared to be pushed toward the east-northeast or landward migration. The direction change occurred because of the changes in the dominant direction and energy of prevailing waves originating from the west, which propagated into the estuary area, affecting and altering the Perancak spit-platform. The wave refraction and diffraction around the inlet mouth caused sediment transport pathways to shift landward and reorient the distal end curvature. In addition, the wave penetration into the estuary area during high-energy conditions increased the reworking of the sediment at the distal end. This reinforces the confidence that the Perancak sandspit developed within a wave-dominated inlet system. Such sandspits were commonly associated with the accumulation of sediments at their tips, which was introduced by longshore transport (Taveneau et al., 2024).

3.1.2 Sandspit Width

Fig. 7 shows the temporal variation of the width of the Perancak sandspit. In the first to second periods, January to June 2024, the width of the sandspit did not exhibit a significant change, remaining around 150 meters. During the first period, the sandspit experienced gradual erosion at the distal tip while maintaining a constant width. This condition suggests that the sediment redistribution occurred along the longitudinal axis, with erosion mainly concentrated at the distal tip rather than distributed across the entire body. Moreover, during the second period, the sandspit experienced elongation while maintaining a constant width. This condition indicates that the sediment deposition mainly occurred at the distal tip of the spit rather than at the entire body.

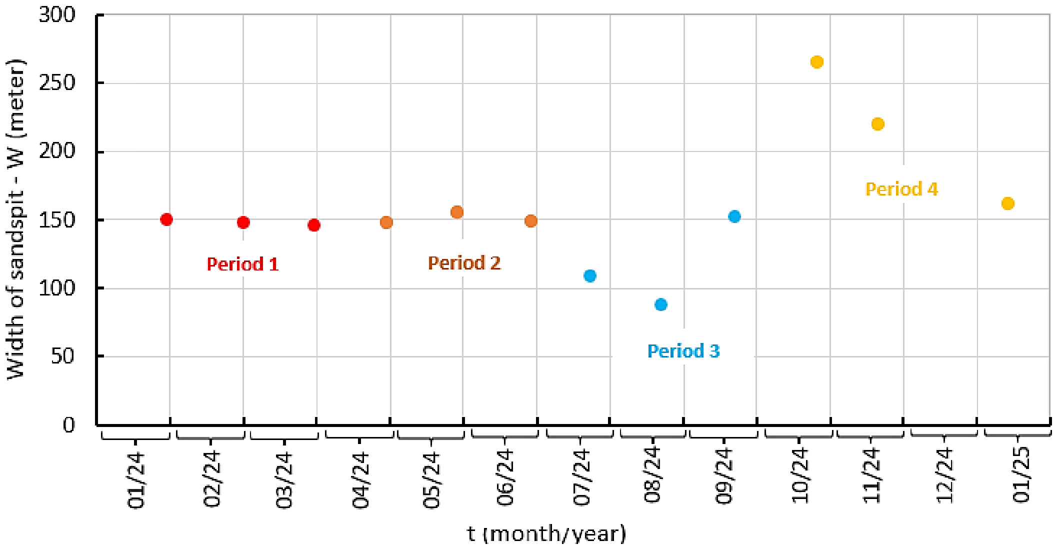

Fig. 7. Temporal variation of the Perancak sandspit's width from January 2024 to January 2025.

In the third period, July to September 2024, a larger change in the sandspit's width was observed and it did not occur uniformly throughout the entire period. From July to August 2024, the sandspit experienced a decrease in width. However, in September 2024, the curvature of the spit platform increased, and a significant widening was observed compared to the previous month. In August, the sandspit's width was only 87.26 meters, but it increased to 152 meters in September 2024. This widening continued to October 2024 with an additional increase of 112.19 meters.

Although shortening occurred in the third period, the morphological changes were not uniform. From July to August, both sandspit length and width decreased. This condition indicates that erosion occurred at both the distal end and lateral margins of the sandspit. However, in September 2024, the sandspit width increased despite the shortening trend, indicating that sediment redistribution temporarily shifted toward lateral deposition along the spit body.

A very distinct pattern was observed in October 2024, when the sandspit's length increased rapidly and the feature also widened. This condition is interpreted as a result of an increase in sediment budget accompanied by a reduction in wave energy. Subsequently, the sandspit's width decreased gradually during the fourth period, reaching 160.41 meters in January 2025. This reduction in width is likely due to the disruption of sediment supply and erosion of the sandspit tip. The width of the sandspit in that month did not differ considerably from that in January 2024.

3.2. Longshore Sediment Transport Rate and Sandspit Growth

As shown in **Fig. 6**, four distinct periods of the Perancak sandspit development were identified over one year. Based on the significant wave height and the wave period, the values of the beach berm elevation (D_B) and the depth of closure (D_C) were estimated at 0.78 m and 2.45 m, respectively. Therefore, the LSTR was calculated based on the elongation period derived from the image analysis. Using the elongation rate ($\Delta L/\Delta t$)) of the sandspit and Equation (7), the LSTR during the elongation period was estimated at 104,000 m^3/year. The results from this study indicate that the LSTR of the Perancak sandspit is in the order of 10^5 m^3/year with the LSTR estimations having an average error margin of $\pm 2.5 \times 10^4$ m^3/year.

Furthermore, the sandspit growth calculated using Equation (8) was estimated at 214 m/year, showing good agreement with the value derived from the satellite image analysis (215 m/year). This agreement suggests that the applied approach reasonably represents the morphological development of the Perancak sandspit. Nevertheless, the estimated LSTR may slightly overestimated due to the assumptions applied, particularly the assumption of negligible sediment losses at the tip.

Additionally, this study compares the characteristics of the Perancak sandspit with other sandspits worldwide, which were analyzed using similar approach, including the Badreveln in Sweden and the Fire Island in USA assessed by Hoan et al. (2011), the Sangomar in Senegal assessed by Palalane et al. (2014), Volta River in Ghana and Bouche du Roi in Benin studied by Lawson et al. (2021), as well as several sandspits in Vietnam, including the Loc An examined by Duc Anh et al. (2018), the Cua Loa examined by Duy et al. (2018), the Ly Hoa and the An Du examined by Duc Anh et al. (2020a), the Ken and the Phan examined by Duc Anh et al. (2020b), and the Song Tranh examined by Duy et al. (2023) (**Fig 8**, **Table 2**).

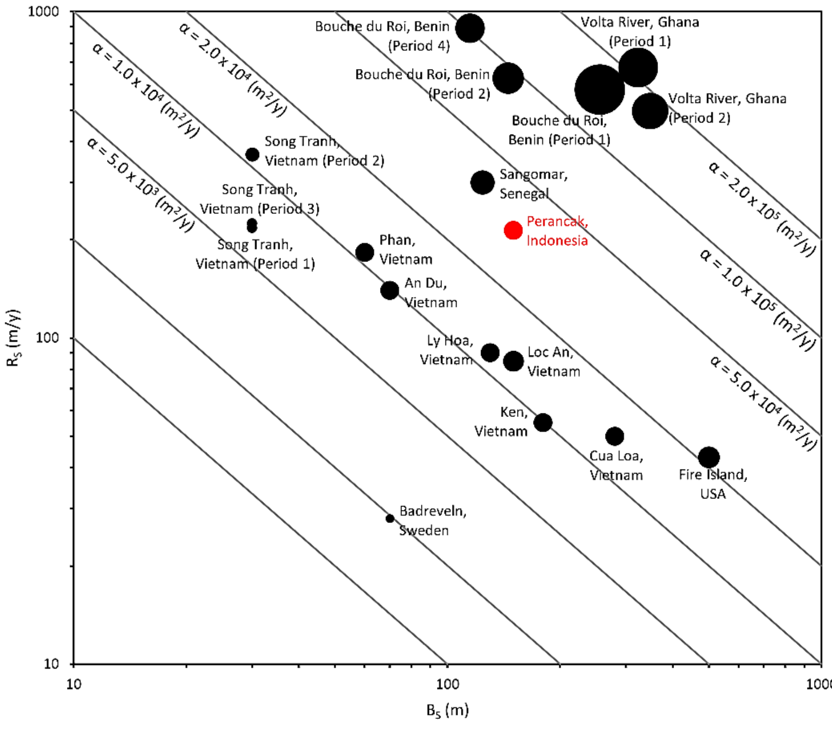

Fig. 8. Comparison of the sandspit growth rate and the sandspit width of the Perancak sandspit with that of other sandspits.

Based on the comparative data, the position of Perancak sandspit indicates a moderate category compared to other sandspits. The Perancak sandspit is narrower than the Volta River sandspit and the Bouche du Roi sandspit, although its growth rate remains relatively high. It indicates that an active accretion process and sediment supply occur in the area. In addition, the condition suggests that the longshore sediment transport plays an important role in the sandspit dynamics. Compared with several sandspits in Vietnam, the Perancak sandspit shows a higher growth rate at a similar width. It implies that the Perancak sandspit dynamics are more active and change rapidly.

Table 2.
Summary of morphodynamic properties of Perancak sandspit and other sandspits worldwide.

Study Area	B_S (m)	R_S (m/y)	LSTR (m^3/y)
Indonesia			
Perancak	150	214	104,000
Vietnam			
Loc An	150	85	200,000
Cua Loa	280	50	160,000
Ly Hoa	130	90	130,000
An Du	70	140	170,000
Ken	180	55	133,000
Phan	60	183	145,000
Song Tranh (Period 1)	30	217	39,000
Song Tranh (Period 2)	30	365	66,000
Song Tranh (Period 3)	30	224	40,000
Sweden			
Badreveln	70	28	10,000
USA			
Fire Island	500	43	220,000
Benin			
Bouche du Roi (Period 1)	255	578	1,980,000
Bouche du Roi (Period 2)	145	626	781,000
Bouche du Roi (Period 4)	115	889	734,000
Senegal			
Sangomar	124	300	465,000
Ghana			
Volta River (Period 1)	324	674	1,290,000
Volta River (Period 2)	348	496	1,210,000

Furthermore, the high dynamics of the sandspit may affect the stability of the river mouth through the inlet migration and sedimentation around the Perancak estuary. The sandspit dynamic may significantly influence the coastal community, fisheries activities, and mangrove habitat in the area. Thus, continuous monitoring of the sandspit dynamics is important to support sustainable coastal management and to mitigate the impacts on the surrounding area.

4. CONCLUSIONS

The analysis of morphological and geometrical changes of the Perancak sandspit, conducted using satellite imagery analysis from January 2024 to January 2025, shows several variations. The main findings can be summarized.

Three periods of shortening or reduction in sandspit length and one period of sandspit growth were identified. In the first period, January to March 2024, and the third period, July to September 2024, the sandspit experienced gradual shortening. Conversely, in the second period, April to June 2024, an elongation and growth phase occurred, and the sandspit width remained around 150 meters. In the fourth period, October 2024 to January 2025, both the length and width of the sandspit decreased, presumably due to reduced sediment supply and intensified erosion at the spit tip.

The orientation of the Perancak sandspit's hook shifted toward the east–northeast during this period, driven by changes in wave energy and strengthened waves and winds from the west–southwest impacting the sandspit.

Image analysis and empirical calculation based on a one-line model were used to estimate the LSTR along the sandspit in the elongation period. The result was 104,000 m^3/year.

Although the sandspit underwent considerable temporal variability within the year, the geometry of the Perancak sandspit in January 2025 did not differ from its condition in January 2024. This suggests that seasonal variation is the dominant factor controlling sediment supply, wave conditions, and longshore currents around Perancak Beach, thereby influencing the temporal variability of the Perancak sandspit geometry.

ACKNOWLEDGEMENT

This research was funded by the non-APBN DPA LPPM 2025, Universitas Diponegoro, under Contract No: 222-150/UN7 D2/PP/IV/2025, with Addendum No: 745/UN7.D2/PP/X/2025.

REFERENCES

Berlianty, D. & Yanagi, T. (2015) Tide and tidal current in the Bali Strait, Indonesia. *Marine Research in Indonesia*. 36 (2), 25–36. doi:10.14203/mri.v36i2.39.

Du, Y., Zhang, Y., Ling, F., Wang, Q., Li, W. & Li, X. (2016) Water bodies' mapping from Sentinel-2 imagery with modified normalized difference water index at 10-m spatial resolution produced by sharpening the SWIR band. *Remote Sensing*. 8 (4). doi:10.3390/rs8040354.

Duc Anh, N.Q., Duy, D. Van & Viet, N.T. (2018) Elongation of sand spit at Loc An river mouth, Southern Vietnam. *Journal of Japan Society of Civil Engineers Ser B3 (Ocean Engineering)*. 74.

Duc Anh, N.Q., Tanaka, H., Tam, H.S., Tinh, N.X., Tung, T.T. & Viet, N.T. (2020a) Comprehensive study of the sand spit evolution at tidal inlets in the central coast of Vietnam. *Journal of Marine Science and Engineering*. 8 (9). doi:10.3390/JMSE8090722.

Duc Anh, N.Q., Tanaka, H., Tinh, N.X. & Viet, N.T. (2020b) Sand spit morphological evolution at tidal inlets by using satellite images analysis: Two case studies in Vietnam. *Journal of Science and Technology in Civil Engineering (STCE) - NUCE*. 14 (2), 17–27. doi:10.31814/stce.nuce2020-14(2)-02.

Durkin, C.J., Seenath, A. & Knaapen, M.A.F. (2025) A critical review of closure depth theories and uncertainties: implications for shoreline modelling and coastal management. *Ocean and Coastal Management*. 267. doi:10.1016/j.ocecoaman.2025.107732.

Duy, D. Van, Tanaka, H., Mitobe, Y., Duc Anh, N.Q. & Viet, N.T. (2018) Sand spit elongation and sediment balance at Cua Lo inlet in Central Vietnam. *Journal of Coastal Research*. (81), 32–39.

Duy, D. Van, Ty, T. Van, Thanh, T.N., Minh, H.V.T., De, C. Van, Duong, V.H.T., Dan, T.C., Viet, N.T. & Tanaka, H. (2023) Sand spit morphology at an inlet on Phu Quoc Island, Vietnam. *Water (Switzerland)*. 15 (10). doi:10.3390/w15101941.

Escudero, M., Silva, R., Hesp, P.A. & Mendoza, E. (2019) Morphological evolution of the sandspit at Tortugueros Beach, Mexico. *Marine Geology*. 407, 16–31. doi:10.1016/j.margeo.2018.10.002.

Hallermeier, R.J. (1981) A profile zonation for seasonal sand beaches from wave climate. *Coastal Engineering*. 4 (4), 253–277.

Hallermeier, R.J. (1978) Uses for a calculated limit depth to beach erosion. In: *Coastal Eningeering, Proceedings of the 16th Conference on Coastal Engineering*. 1978 Hamburg, Germany, ASCE: Reston, VA, USA. pp. 1493–1512.

Hoan, L.X., Hanson, H., Larson, M. & Kato, S. (2011) A mathematical model of spit growth and barrier elongation: Application to Fire Island Inlet (USA) and Badreveln Spit (Sweden). *Estuarine, Coastal and Shelf Science*. 93 (4), 468–477. doi:10.1016/j.ecss.2011.05.033.

Huggett, R.J. (2007) *Fundamentals of Geomorphology*. 2nd edition. Routledge.

Lawson, S.K., Tanaka, H., Udo, K., Hiep, N.T. & Tinh, N.X. (2021) Morphodynamics and evolution of estuarine sandspits along the Bight of Benin Coast, West Africa. *Water*. 13 (21). doi:10.3390/w13212977.

Orford, J. (2006) Encyclopedia of Geomorphology. In: A.S. Goudie (ed.). *Encyclopedia of Geomorphology*. New York, Routledge, International Association of Geomorphologists. p.

Palalane, J., Larson, M. & Hanson, H. (2014) Analytical model of sand spit evolution. In: *34th International Conference on Coastal Engineering (ICCE 2014)*. January 2014 pp. 1187–1194.

Paluphi, W.R., Muskananfola, M.R. & Sugianto, D.N. (2020) Analysis of sediment dynamics in the waters Perancak and Pengambengan Beaches, Jembrana-Bali. *International Journal of Oceans and Oceanography*. 14 (2), 257–276.

Razak, M.Ab. & Khan, A.R. (2020) Development of a predictive closure depth equation using field data and wave refraction modelling. In: *IOP Conference Series: Materials Science and Engineering*. 29 May 2020 Institute of Physics Publishing. p. doi:10.1088/1757-899X/849/1/012093.

Taveneau, A., Almar, R. & Bergsma, E.W.J. (2024) On the cyclic behavior of wave-driven sandspits with implications for coastal zone management. *Estuarine, Coastal and Shelf Science*. 303. doi:10.1016/j.ecss.2024.108798.

Udo, K., Ranasinghe, R. & Takeda, Y. (2020) An assessment of measured and computed depth of closure around Japan. *Scientific Reports*. 10 (1). doi:10.1038/s41598-020-59718-5.

Xu, H. (2006) Modification of normalised difference water index (NDWI) to enhance open water features in remotely sensed imagery. *International Journal of Remote Sensing*. 27 (14), 3025–3033. doi:10.1080/01431160600589179.

Zhu, J., Shi, F., Cai, F., Wang, Q., Qi, H., Zhan, C., Liu, J., Liu, G. & Lei, G. (2022) Influences of beach berm height on beach response to storms: A numerical study. *Applied Ocean Research*. 121. doi:10.1016/j.apor.2022.103090.

Geographia Technica, Vol. 21, Issue 3, 2026, pp 132 to 149

OPTIMIZING BIOMETEOROLOGICAL COMFORT IN THE CENTRAL PEDESTRIAN AREA OF IAȘI CITY THROUGH VARIOUS URBAN DESIGN SCENARIOS IMPLEMENTED WITH ENVI-MET

Pavel ICHIM [1], ***Robert ȚURCANU*** [1,2] ***& Lucian SFÎCĂ*** [1*]

DOI: 10.21163/GT_2026.213.09

ABSTRACT

The paper analyses the biometeorological comfort of the main pedestrian area from the downtown area of Iași, Romania, during representative weather conditions for summer, aiming to identify sustainable strategies to mitigate or adapt to urban heat discomfort. Historical climate datasets were used to identify the thermal record high of the region, while microclimatic conditions were simulated with ENVI-met software. The work model was developed in ENVI-Met, allowing high-resolution (3×3×3 m grid) simulations of interactions between the lower atmosphere, built surfaces, vegetation, and in-depth soil characteristics. The analysis sampled August 7, 2012 weather conditions, identified as the hottest day between 1961 and 2025, with a recorded air temperature of 41.3°C at the Iași weather station. Three scenarios were simulated, and for each of them the model evaluated potential air temperature (PAT), mean radiant temperature (MRT), and additional biometeorological parameters derived using ENVI-met's BIO-met module, such as skin and clothing temperature with their variations along the selected pedestrian walk. Results show an average air temperature reduction of ~2°C by using cobblestone pavement and up to 20°C lower perceived temperatures, as indicated by MRT, in shaded areas. The complex scenario - represented by a mixture of cool pavement and urban greening - yielded the most significant improvements in thermal comfort, reducing MRT values and mitigating façade heat emissions by up to 9°C through vertical vegetation systems. The findings emphasize the effectiveness of integrated greening and shading strategies in reducing the urban heat island effect. Moreover, they revalidate the capability of ENVI-met-based biometeorological modelling to serve as a decision-support tool for the sustainable design and thermal optimization of urban public spaces.

Keywords: *Urban climate; ENVI-Met; Potential air temperature (PAT); mean radiant temperature (MRT), Iași.*

1. INTRODUCTION

In the context of accelerated urbanization and the intensification of climate change effects, biometeorological comfort in urban pedestrian spaces represents an essential element for ensuring the quality of life in the built environment (Nikoulopoulu et al., 2001). In recent years, numerous studies (Matzarakis et al., 2007, Ng, 2012, Park et al., 2021) have highlighted the role of urban morphology and its components - buildings, surface materials, vegetation - in modifying local microclimatic parameters and, implicitly, influencing the population's thermal perception. At the international level, urban heat island (UHI) effects have been widely documented (Masson et al., 2020), being strongly associated with rapid urban expansion, land-use change, and the increasing dominance of impervious surfaces, all of which contribute to intensified thermal stress in urban environments (Faragallah & Ragheb, 2022).

---

[1] *„Alexandru Ioan Cuza" University of Iași, Faculty of Geography and Geology, Department of Geography, Iași, Romania, pavel.ichim@uaic.ro, lucian.sfica@uaic.ro*

[2] *Department of Climatology, National Meteorological Administration, Bucharest, Romania, turcanu@meteoromania.ro*

[*] *Corresponding author: lucian.sfica@uaic.ro (All authors are equally considered the main author of the article).*

At the European and regional scales, numerous studies have emphasized that urban form and land-use structure play a key role in shaping microclimatic conditions, with compact urban areas generally associated with higher temperatures due to reduced ventilation and increased heat storage (Gusson & Duarte, 2016; Kotharkar & Dongarsane, 2024). Similar findings have been reported in Romanian cities, where urban morphology and the balance between built-up areas and vegetation significantly influence the spatial variability of thermal conditions and the intensity of the UHI effect (Urițescu et al., 2019; Grigoraș & Urițescu, 2024). These results highlight the need for detailed, site-specific analyses of urban microclimates, particularly in rapidly developing urban environments.

The Municipality of Iași, located in the northeastern part of Romania, represents a relevant example for analyzing the interactions between urban structure and the thermal comfort of public spaces. Over the past decades the city has experienced a continuous process of spatial expansion and functional transformation, marked by an increase in built-up surfaces, densification of urban fabric, and changes in land-use patterns (Ursu et al., 2016; Bănică et al., 2017). These processes are widely recognized as major drivers of UHI development, as they reduce evapotranspiration capacity and increase heat storage in urban materials. The city exhibits a well-contoured urban heat island (UHI) both at canopy (Sfîcă et al., 2018) and at the surface (Sfîcă et al., 2023) levels, while recording a high number of days with heat related thermal discomfort (Sfîcă et al, 2017). Simultaneously, the city faces consistent challenges related to the balance between built-up areas and vegetation cover (Foșalău et al., 2024). The central area of the city, corresponding to the Ștefan cel Mare pedestrian boulevard, represents a distinct combination of historical heritage and contemporary urban development, being entirely integrated in the UHI's core. In this area, microclimatic features derived from the UHI manifest intensely during the warm period of the year, influencing the level of thermal comfort for pedestrians and, consequently, the usability of the public space (Sfîcă et al., 2023).

Biometeorological comfort in this type of urban space is conditioned by local factors such as the streets orientation, height of buildings, the type of paving materials with their specific albedo, the presence of vegetation, the wind variability, and the exposure to direct solar radiation (Lau et al., 2015). Within the central area of Iași, these elements interact in a complex way, leading to a high variability of the thermal comfort state depending on synoptic weather conditions and the time of day.

One of the primary applications of ENVI-met consists in evaluating the impact of urban morphology on local temperatures. Numerous research has shown that building density and land-use patterns strongly influence the thermal environment, with compact urban forms exhibiting higher temperatures due to reduced ventilation and increased heat storage in impervious surfaces (Gusson & Duarte, 2016; Urițescu et al., 2019). At the same time, scenario-based simulations have highlighted the important role of green infrastructure in mitigating urban heat stress. Increasing tree canopy coverage, as well as the implementation of green roofs and vegetated façades, has been shown to significantly improve thermal comfort and reduce the UHI effect (Yang et al., 2021; Kotharkar & Dongarsane, 2024).

Surface materials also play a critical role in urban heat regulation. Studies have demonstrated that cool paving materials, such as permeable surfaces and grass grid pavers, can significantly reduce surface and air temperatures, while reflective materials may decrease heat accumulation depending on urban geometry and exposure conditions (Faragallah & Ragheb, 2022; Eingrüber et al., 2024; Sinsel et al., 2022).

In outdoor urban environments, thermal comfort is inherently dynamic, as individuals are exposed to continuously changing microclimatic conditions and rarely reach thermal equilibrium. However, due to the complexity of modelling transient physiological responses and the dependence on individual thermal history, steady-state approaches are commonly applied in urban microclimate studies, offering a practical compromise for thermal comfort assessment (Fischereit & Schlünzen, 2018).

The present work aims to analyze the influence of the urban environment on biometeorological comfort in the Ștefan cel Mare pedestrian area, by evaluating specific microclimatic parameters and advancing some possible solutions to optimize thermal comfort. This topic is relevant also from the citizen perspective, since the renewal of the urban center ignited in the past years a public debate involving also urban climate implications. The study also seeks to identify urban configurations and design solutions that can contribute to reducing biometeorological discomfort and promoting a more sustainable and attractive public space.

2. STUDY AREA

The study area is located in Iași city (**Fig. 1**), northeastern Romania - with its central area located at 47.1° N and 27.5° E - situated within the Moldavian Plateau developed primarily on the lower terraces of the Bahlui River (Minea, 2010; Sfîcă et al., 2023).

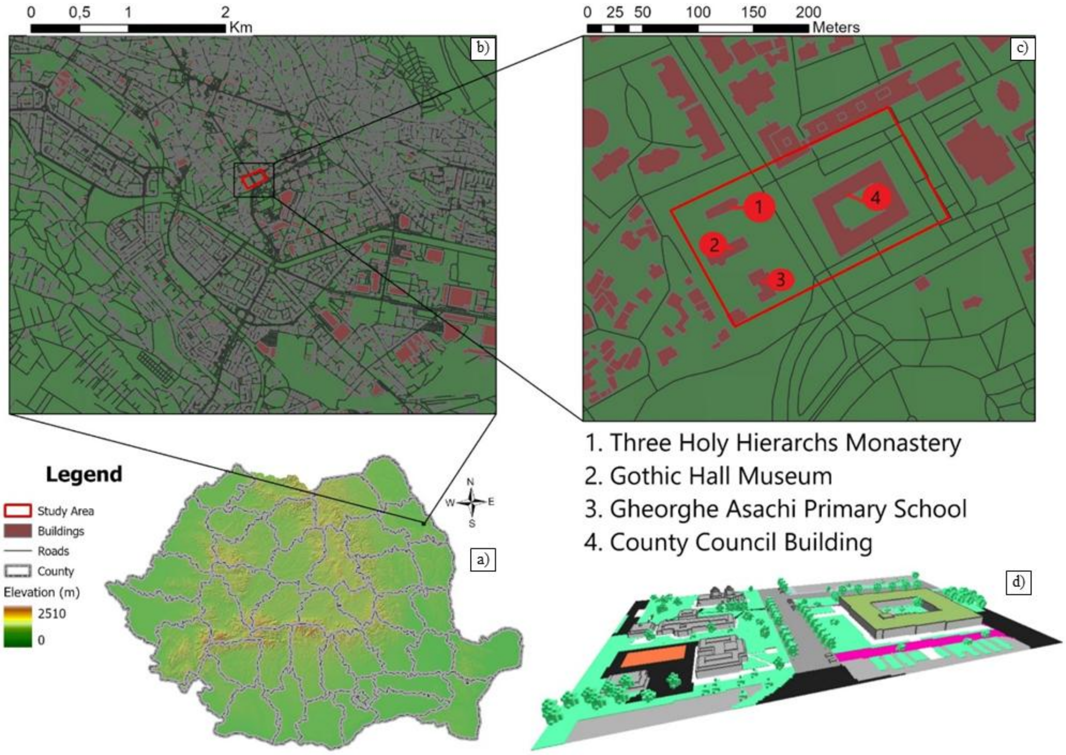

Fig. 1. Location map of the study area in Romania (a), in Iași (b), the selected study area (c) and its built Envi-Met spatial 3D model (d).

Although Iași is classified as Dfb under the Köppen‑Geiger system, recent studies and updated high-resolution climate datasets (Belda et al., 2014; Beck et al., 2018) indicate that parts of Romania, including major urban centers, may exhibit transitional characteristics toward Cfa (Onțel et al., 2025).

Furthermore, the concentration of population, urban expansion, and the high degree of land surface transformation in large cities intensify local thermal conditions, enhancing the urban heat island effect and amplifying warm-season thermal regimes. These processes, combined with regional climate warming trends, support the interpretation of Iași as exhibiting emerging Cfa-like features, particularly in the context of urban climate conditions.

Recent years have recorded significant heat extremes, with 2007, 2012, 2015 and 2019 considered the hottest years especially during summer when heat waves recorded high frequency and duration (Nagavciuc et al., 2022). In this context, in 2012, following a very hot month of July, on August 7, 2012 - when Romania's territory was placed under a strong tropical atmospheric ridge - Iași weather station recorded a maximum temperature of 41.3°C, which represents the highest value observed for the period 1961-2015 (Iordache et al., 2017). It should be underlined that this value also remains the highest recorded up to 2025, based on available observational data. In this context, the simulations presented in the current study can be considered highly relevant for assessing present-day summer thermal discomfort conditions, as well as for indicating potential future extreme heat stress scenarios.

The specific research site covers a 130-meter sector along and nearby the eastern sector of the Ștefan cel Mare pedestrian boulevard, spanning approximately over 30,000 m^2. The perimeter includes the County Council Building (CCB) and two asphalt-paved parking lots to the east, while the southern and northern boundaries are marked by the Gheorghe Asachi Primary School and the Three Holy Hierarchs Monastery, respectively.

3. DATA AND METHODOLOGICAL SETUP

ENVI-met is a three-dimensional non-hydrostatic microclimate model that simulates surface-plat-air interactions at high fluid dynamics, radiation fluxes, thermodynamics, vegetation processes, and soil-atmosphere exchanges (ENVI-Met, 2025). Unlike models focusing on isolated factors like airflow or radiation modeling (OpenFOAM, Radiance, i-Tree Eco), ENVI-met employs a unified approach to simulate holistic environmental changes.

The present analysis focuses on the spatial distribution of Potential Air Temperature (PAT) and Mean Radiant Temperature (MRT), two key variables controlling human thermal perception (Sinsel, 2022). While PAT reflects the thermal state of the air mass independent of pressure variations, MRT represents the combined effect of shortwave and longwave radiation fluxes and is a critical parameter in the assessment of thermal comfort indices indicating the heat load received by the human body. Therefore, MRT is calculated based on the integration of shortwave and longwave radiation fluxes from multiple directions, following the Stefan–Boltzmann law (Sinsel et al., 2022).

In the ENVI-met framework, Potential Air Temperature (PAT) is defined as the air temperature at a reference pressure (model default), and for practical purposes within the 3D model it can be treated as equivalent to the absolute air temperature. Thus, although PAT is formally derived from thermodynamic principles, in near-surface urban simulations it behaves similarly to the standard air temperature (Ta), with only minor differences due to pressure effects (ENVI-Met, 2025).

Mean Radiant Temperature (MRT) represents the integrated effect of all radiative fluxes exchanged between the human body and its surrounding environment and is a key parameter controlling outdoor thermal comfort. It can be expressed as:

$$T_{mrt} = \left(\frac{S_{str}}{\varepsilon_p \cdot \sigma}\right)^{1/4} - 273.15,$$

where S_{str} is the total absorbed radiation flux (including shortwave and longwave components), ε_p is the emissivity of the human body (≈0.97), and σ is the Stefan–Boltzmann constant (Sinsel et al., 2022).

In addition to microclimatic variables, the analysis includes biometeorological outputs related to the human energy balance simulated by ENVI-met (Salata et al., 2016). These include: (1) Tskin (skin temperature), representing the temperature of the body surface in direct interaction with the environment; (2) Tcore (core temperature), referring to the internal body temperature maintained by physiological regulation; (3) Tcl (clothing surface temperature), which describes the thermal state of the clothing layer acting as an interface between the body and the surrounding environment. Furthermore, static Tskin represents the skin temperature under steady-state conditions, assuming constant environmental forcing and no transient physiological adaptation (ENVI-Met, 2025; Sinsel, 2022). Together, these variables provide insight into the physiological response of the human body to outdoor thermal conditions by using dynamic comfort analyses in Bio-met extension of ENVI-met (Salata et al., 2016; ENVI-Met, 2025; Sinsel, 2022).

The model setup was performed using the ENVI-met Headquarters environment, where a dedicated project workspace and database were created to manage site-specific materials, vegetation types, and boundary conditions. The study area was constructed in the Spaces module based on geographic coordinates corresponding to Iași central area (47.16°N, 27.58°E).

The computational domain consists of a grid of 240 × 145 × 32 cells, with a horizontal resolution of 3 × 3 m, ensuring a detailed representation of urban morphology at the pedestrian scale. Such spatial resolutions are commonly applied in ENVI-met simulations to capture fine-scale urban microclimatic processes (Salata et al., 2016; Yang et al., 2021). To improve near-surface accuracy without significantly increasing computational cost, the lowest vertical layers were subdivided into five sub-cells, enhancing the simulation of air–surface interactions, as recommended in ENVI-met modelling practices (ENVI-Met, 2025).

To define the soil types and surface characteristics of the study area, the standardized soil profiles and surface materials provided by the ENVI-met software were used. The default soil type for the entire model domain was sandy-loam. Based on satellite imagery, paved streets were digitized using asphalt road surfaces. Pedestrian areas were represented with granite pavement (single stones), sidewalks with concrete pavement light, colored asphalt areas with asphalt road with red coating, and curbs and selected pedestrian connections with light concrete pavement (**Fig. 2**). This simplification is consistent with the soil characteristics of Iași, where natural soils such as Chernozems and Regosols exhibit predominantly loamy textures, while Fluvisols from the Bahlui floodplain tend toward finer clay-loam textures, while urban Technosols display a high spatial heterogeneity, often corresponding to sandy-loam or loamy compositions due to the mixture of natural and anthropogenic materials (Secu et al., 2015; Secu et al., 2016). In the context of ENVI-met, these conditions justify the use of a dominant sandy-loam soil type, which provides a balanced representation of soil hydraulic and thermal properties, while acknowledging local variability associated with urban land use.

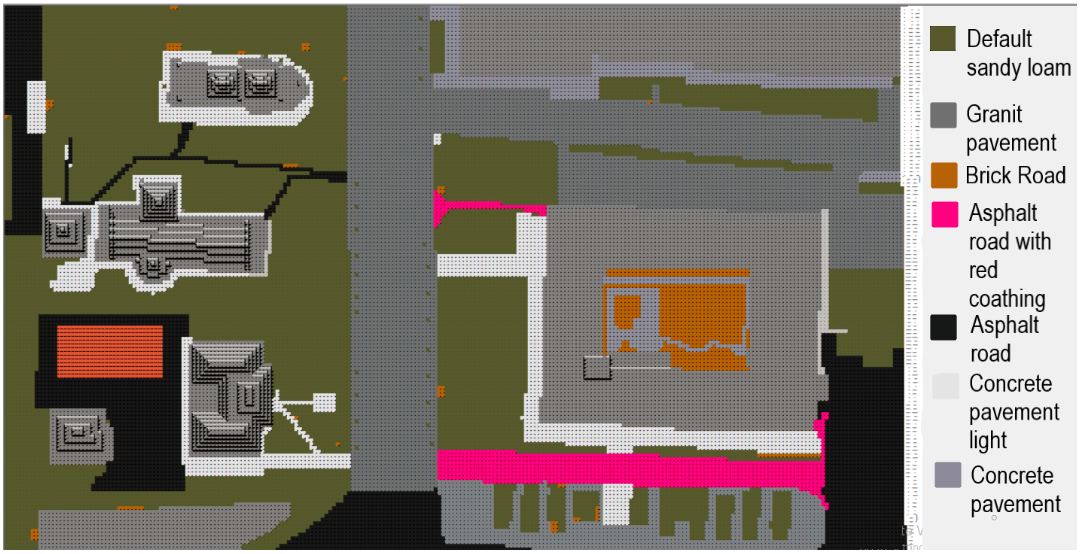

Fig. 2. Surface digitization interface in ENVI-met Spaces for the central area of Iași city.

Building foundations and basement areas were defined using the default cellar soil profile, which represents subsurface conditions beneath buildings and is required for outlining building footprints. Building geometry was then created using ENVI-met's grid-based building system, in which structures are represented by cells with variable heights. Building heights were determined using Google Earth Pro. For example, the CC building has a roof elevation of 73 m and a base elevation of 58 m; by neglecting terrain topography, the building was modeled with an absolute height of 15 m. Buildings with more complex geometries were modeled following the same approach, using three-dimensional building models as references for shape and height. To avoid modeling errors, building footprints were aligned with the previously defined basement profiles. Construction materials were assigned uniformly to all buildings. Due to the lack of detailed information on actual building compositions in the study area, the standard "Default Wall – moderate insulation" material was selected for both walls and roofs.

Vegetation was added using the ENVI-met plant library and was placed exclusively on natural soil profiles to prevent simulation errors. In total, 141 3D plants were included, representing linden (*Tilia cordata*), chestnut (*Aesculus hippocastanum*), black locust (*Robinia pseudoacacia*), thuja (*Thuja occidentalis*), silver fir (*Abies alba*), and Norway spruce (*Picea abies*). The remaining vegetated surfaces were modeled using the standard 25-cm grass surface from the simple plants category.

After completing the model of the study area and saving the model in *.inx* format, we used the ENVI-guide tool to start the simulation process of biometeorological factors. Using climatic gridded daily database from ROCADA (Dumitrescu &Bîrsan, 2015) and National Meteorological Administration of Romania (NMA RO) from SYNOP messages that were issued by official weather stations we identified the hottest day recorded in Iași, corresponding to 07.08.2012, with an absolute maximum temperature of 41.3°C at 17:00 (**Fig. 3**).

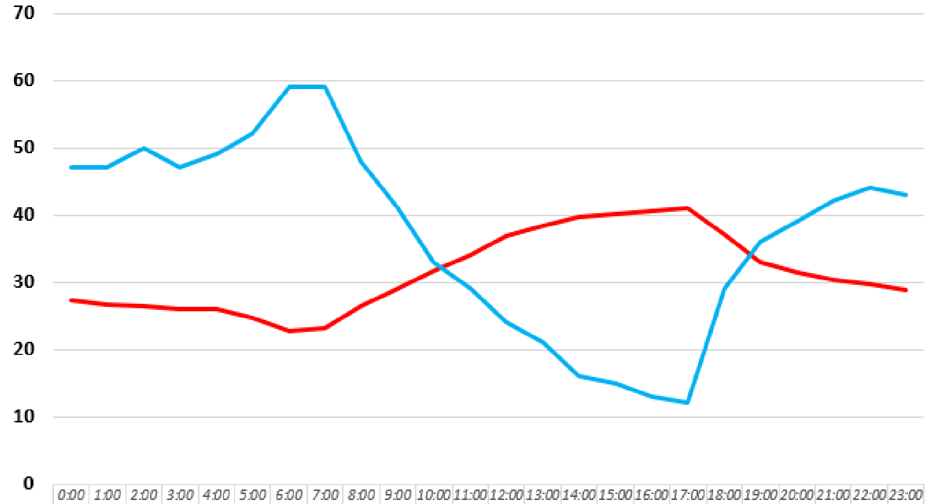

	0:00	1:00	2:00	3:00	4:00	5:00	6:00	7:00	8:00	9:00	10:00	11:00	12:00	13:00	14:00	15:00	16:00	17:00	18:00	19:00	20:00	21:00	22:00	23:00
Air temperature (°C)	27.4	26.7	26.4	26	25.9	24.6	22.8	23.1	26.5	29	31.7	34.1	36.9	38.3	39.8	40.2	40.6	41	37	33	31.4	30.3	29.6	28.8
Relative humidity (%)	47	47	50	47	49	52	59	59	48	41	33	29	24	21	16	15	13	12	29	36	39	42	44	43

Fig. 3. Values used in ENVI-guide for the Simple Forcing process tailored from the weather data recorded on 7 of August 2012

ENVI-guide uses the *.inx* project and a set of climatic data to create a simple forcing *.simx* file used in the subsequent steps. The first data we entered were the date, time, duration of the simulation, and the full and abbreviated names. We also entered the digital reference model (*.inx*) of the study area here. For our simulations, we used the "Multi Core" option, sacrificing the multitasking capacity of the computer used for higher performance and simulation speed (ENVI-MET GMBH, 26.03.2024). We used the "Meteorology" tab to enter climatic data through the "Simple Forcing" function, which requires temperature and humidity values. The entered values are displayed in the central graph. We saved the *.simx* project and entered it into the ENVI-core module for simulation. In ENVI-core, we selected the project database. The program loads all elements, a process that can take several minutes (depending on the spatial and temporal dimensions of the model). Then, we selected the *.simx* file and ran a "check model" module to identify any errors.

To create graphical representations of the results obtained from the simulations, we used "Leonardo" interface in which we imported the *.edx* files obtained after completing the simulation in ENVI-core, selecting the dataset corresponding to the time we wished to represent. To extract the data into a 2D map, we selected the desired parameter from the "Data" menu. For this work, we focused more on factors influencing the thermal comfort and discomfort of pedestrians. Under these conditions, the simulations performed and analyzed are characteristic of a height of 1.5m from the active surface, Leonardo allowing for the extraction of hourly data from points of interest (e.g., modeling on pedestrian routes, surface types, under trees, etc.) (ENVI-MET GMBH, 28.03.2024; ENVI-MET GMBH, 02.04.2024). The methodological workflow is presented in Figure S1 from the attached Supplementary Material.

4. RESULTS AND DISCUSSIONS

4.1. Microclimatic characteristics on current urban environment

To optimize processing time, microclimatic simulations were performed for the 16:00–18:00 local time interval, corresponding to the period of maximum values of air temperature recorded on August 7, 2012.

At 16:00 (**Fig. 4**), the average air temperature in the studied perimeter was 35.7°C, with minimum values of 34.4°C in shaded areas (east of the Three Holy Hierarchs Monastery and north of the Gheorghe Asachi School) and maximums of 37.0°C in the asphalt-paved parking lots north and southeast of the CCB. On the central pedestrian segment, covered with cobblestones, the values were approximately 35°C, indicating thermal variability determined by the differences in material (grass, asphalt and cobblestone) and their exposure to direct solar radiation.

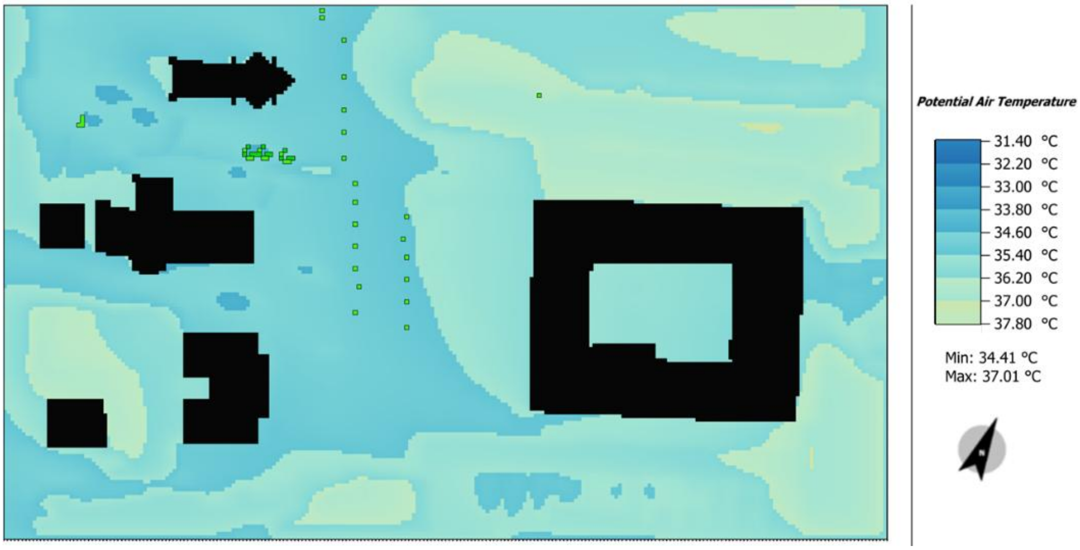

Fig. 4. Spatial distribution of PAT at 16:00 in the current conditions model.

At 18:00 (**Fig. 5**), the mean temperature dropped to 34.4°C, marking a reduction of 1.4°C over the two-hour interval. Maximum values of 35.7°C continued to be recorded on the asphalt surfaces, while shaded areas presented minimums of 33.1°C, as a result of the interplay between vegetation and buildings in moderating local temperatures (Sfîcă et al., 2023; Crețu et al., 2025).

Analyzing PAT values spatial distribution and variation we can observe their underestimation at local level when compared with the values reaching 41.3°C at the official weather station of Iași during the analyzed time interval. This could be explained by a combined result of the small differences between PAT and standard air temperature recorded in sheltered conditions at 2m height, but also of the cold pool island known to develop in very hot summer days in the central area of Iași (Sfîcă et al., 2018). As well, this underestimation indicates that ENVI-MET results could be improved by using local collected data, which is planned in our future work in urban climate modelling.

Fig. 5. Spatial distribution of PAT at 18:00 in the current conditions model.

The MRT presents significant spatial variations depending on local sun exposure. At 16:00 (**Fig. 6**), maximum values of 83.6°C were recorded in areas under the action of both direct solar radiation and heat reflected from the building façades. On the unshaded portions of the pedestrian area, the MRT is approximately 63°C, while in shaded areas, provided by either vegetation or buildings, values of approximately 32°C were obtained.

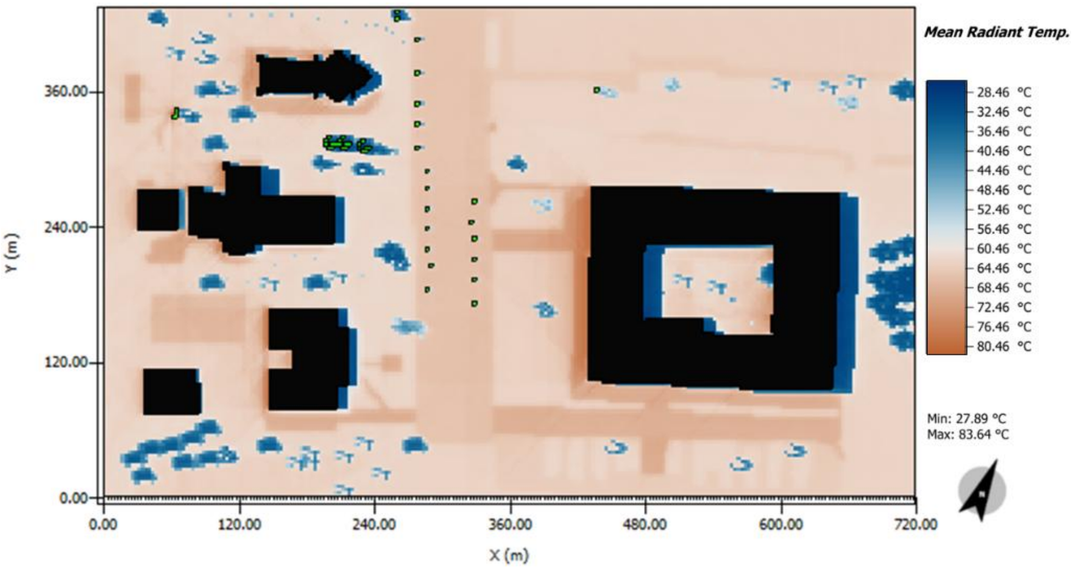

Fig. 6. Spatial distribution of MRT at 16:00 in the current conditions model.

At 18:00 (**Fig. 7**), maximum values decrease to 63.6°C. In the previously identified hotspots, this temperature is now driven by reflected radiation and heat released from building façades, particularly on their northwestern sides. Meanwhile, the pedestrian path averaged 48°C, maintaining a sharp contrast of up to 20°C between exposed and shaded surfaces.

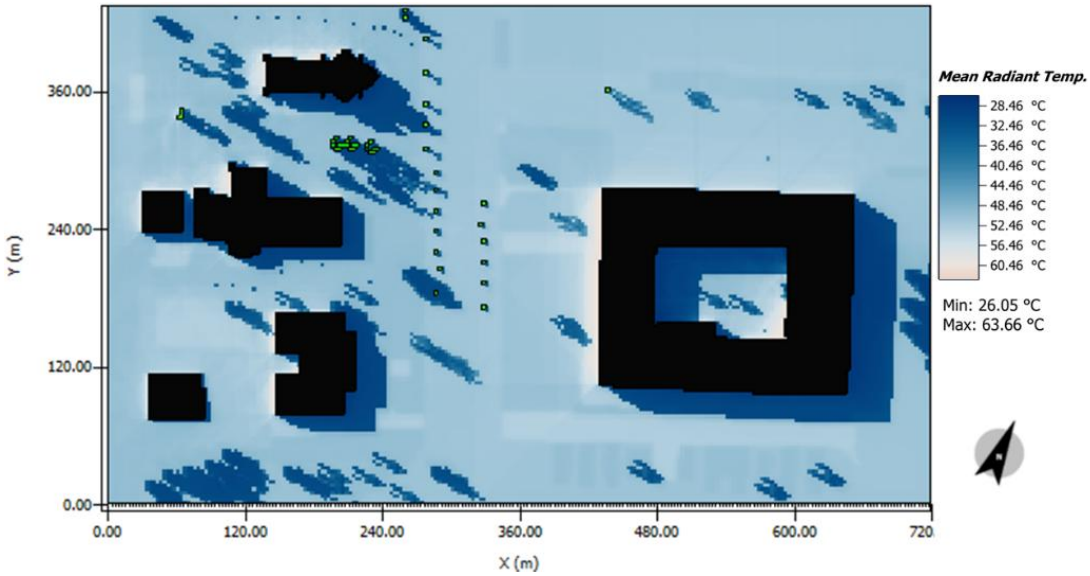

Fig. 7. Spatial distribution of MRT at 18:00 in the current conditions model.

4.2. Modification of the Study Area through Tree Planting and Active Surface Alteration

The analysis of the current situation highlighted significant differences between the thermal behavior of urban surfaces. Shaded areas exhibit temperatures lower by up to 1.3°C, due to the shadow offered by buildings and trees, which reduces the absorption and re-emission of solar radiation (Park et al., 2021). On the contrary, surfaces directly exposed to the sun radiation accumulate heat very fast and retain it for long periods, generating intensified thermal discomfort conditions.

To increase the level of shading, the proposed intervention scenario included planting Horse Chestnut trees (*Aesculus hippocastanum*) with an average height of 17.5m, positioned along the sides of the sidewalks and in the center of the parking lots (**Fig. 8**).

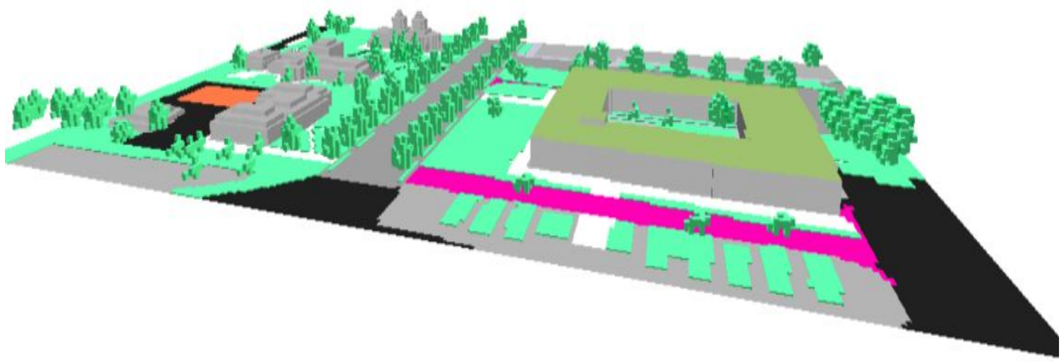

Fig. 8. 3D model of the study area with implemented chestnut trees.

The results obtained highlighted clear thermal differences between the materials used. At 11:00, the surfaces paved with cobblestone recorded an air temperature of 32.7°C, which was 2.3°C lower than that on black asphalt (35°C). The daily maximum temperatures were reached at 16:00, when the cobblestone reached 37.5°C, and the asphalt reached 39.1°C (**Fig. 9a**).

The average difference of~2°C between the two types of surfaces was maintained throughout the analyzed time interval. This supports the nowadays extensive use of cool pavements in urban renewal projects of many cities (Del Serrone et al., 2022), due to their capacity to mitigate the overheating effect during the daytime in maximum sunshine conditions.

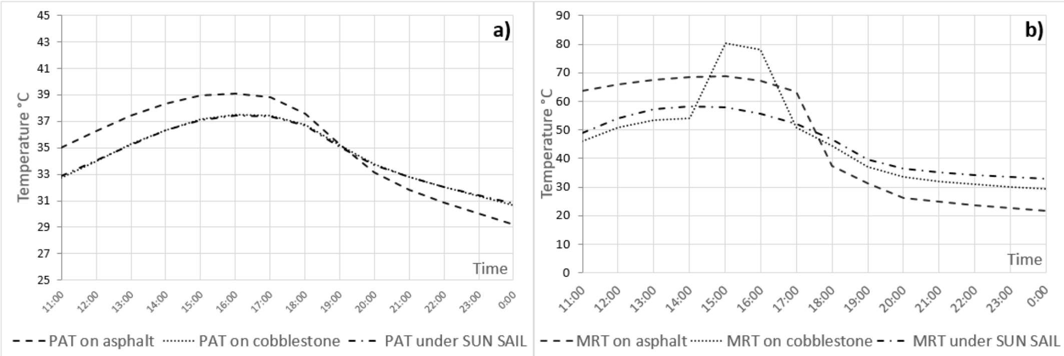

Fig. 9. (a) MRT diurnal evolution on asphalt surfaces, cobblestone pavement and sun sails for the central pedestrian area of Iași city; **(b)** PAT diurnal evolution on asphalt surface, cobblestone pavement and sun sails

The cobblestone exhibited a more favorable thermal response, maintaining felt temperatures (MRT) above 55°C for only 3 hours, compared to 6 hours for the asphalted areas (**Fig. 9b**). Nevertheless, the peak in felt temperature over cobblestone is higher at the time of maximum air temperature (17:00-18:00) and moreover, after 19:00, the MRT on the asphalted surfaces dropped below the PAT, while on the cobblestone the values remained close to it, indicating a slower but stable cooling, which could be also valuable for increasing thermal comfort during wintertime conditions.

Following the implementation of the developed scenario based on trees planting and replacing the asphalted surfaces with cobblestone, the average air temperature over the study region at 16:00 was 35.6°C, which is only 0.1°C lower than in the current situation. The minimum (34.2°C) and maximum (37.0°C) values were also lower than in current conditions, confirming a marginal improvement in thermal comfort (**Fig. 10**). The spatial distribution of temperatures at 16:00 indicates a reduction of approximately 2°C in the areas paved with cobblestone, compared to the original asphalt. Near the trees, the MRT values are 18–20°C lower than in the unshaded areas, confirming the effectiveness of vegetation shading in reducing thermal discomfort (Park et al., 2021).

Fig. 10. Spatial distribution of PAT at 16:00 in the chestnut trees model.

At 18:00 (**Fig. 11**), the average air temperature was 34.2°C, 0.1°C below the values of the initial model. The temperature distribution remains similar, with maximums values (35.4°C) appearing on the exposed surfaces, while minimums (33°C) are concentrated in the proximity of buildings and trees.

Fig. 11. Spatial distribution of PAT at 18:00 in the chestnut trees model

Although trees efficiently reduce direct radiation, the results show that localized shading does not constitute a "one size fits all" solution for reducing thermal discomfort at the pedestrian scale. In shaded segments, the felt temperatures are 18–20°C lower than those of neighboring surfaces, but the effect is limited to areas with consistent vegetation cover and is dependent on the accuracy of input tree data in Envi-Met (Simon et al., 2025), while the type of surface is assessed to be more important than the type of trees (Kaularachichi et al. 2020). However, the magnitude of the average overall differences (0.3°C) suggests that the general impact on the urban microclimate remains low, requiring additional scenarios to extend the shaded areas. As well, for improved accuracy of the results the climate modelling should use data from in-situ observations taking to account the limitations specific to model simulations (Yang et al., 2026). Using the BIOmet module, the thermal behavior of a human subject was compared in the two models: the Original Model (OM) (**Fig. 12**) and the Model with Chestnut Trees (CM) (**Fig. 13**).

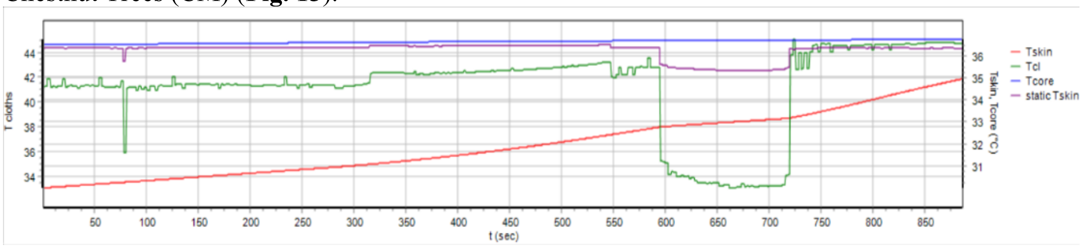

Fig. 12. BIOmet pedestrian route at 16:00 in the original model (OM).

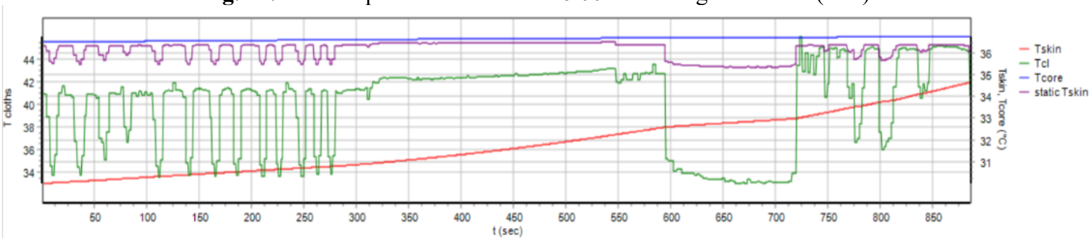

Fig. 13. BIOmet pedestrian route at 16:00 in the chestnut trees model (CM).

The air temperature (PAT) at 16:00 is similar in both cases (35.7°C). The temperature at the clothing level shows differences of 8°C between shaded and exposed areas over distances of 13 meters. In the unmodified segments (the south parking lot and the eastern area of CCB), the values remain identical between the models. The skin temperature is 30°C at the beginning of the route, reaching 35°C in the OM and 34.7°C in the CM after 15 minutes. The average difference of 0.1–0.3°C demonstrates a slight reduction in thermal stress due to the combined effect of shading and surface material modification.

The results confirm that localized interventions involving vegetation and replacing materials with less absorbent ones can generate punctual improvements in thermal comfort. The positive effects are more evident in the proximity of trees and on cobblestone paved surfaces, where the clothing temperature decreases by up to 10°C and the skin temperature is 0.2°C lower at the end of the route compared to the values of the original model.

4.3. Adaptation strategies based on artificial shading and green façades

Building on the results obtained from the tree-planting and surface modification scenario, a supplementary intervention was imagined to further reduce thermal discomfort at the pedestrian level. Although vegetation proved effective in lowering MRT locally, its influence remained spatially limited. To increase the extent and consistency of shaded areas, artificial shading structures of the Sun Sail type were introduced along the main pedestrian path (**Fig. 14**).

The use of sun sail shading systems has been documented in previous studies as an efficient strategy for improving outdoor thermal comfort, particularly in highly exposed urban spaces. Elgheznawy and Eltarabily (2021) demonstrated that covering approximately 60% of a courtyard surface with sun sails leads to significant reduction in thermal stress. In the present study, the economic component was not considered, and the analysis focused exclusively on microclimatic performance. In ENVI-met Spaces, the shading structures were modeled using the Single Wall function to approximate realistic physical behavior. Lateral elements were defined as PVC Sun Sail, providing structural support for a roof composed of photovoltaic panels mounted on aluminium frames (ENVI-MET GmbH, 13.02.2024). This configuration allowed the simulation of both shading and material-related radiative effects.

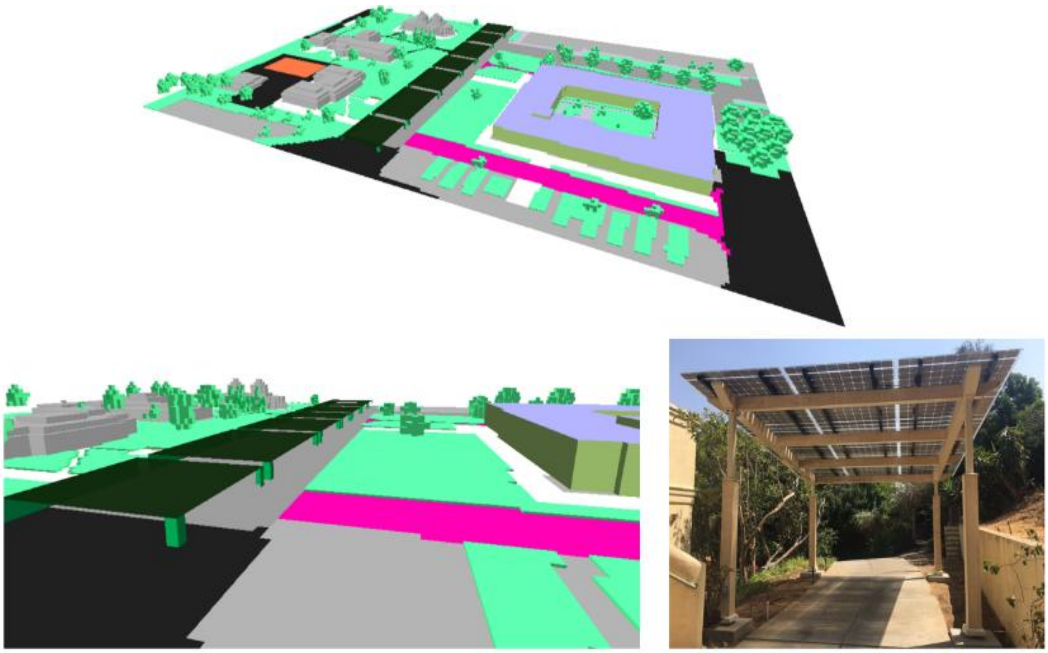

Fig. 14. 3D model of the study area in a scenario with sun sails and green façades.

Simulations at 16:00 revealed that the highest MRT values - reaching up to 68°C - were concentrated near the façades of the CCB. These elevated values are primarily attributed to the accumulation and re-emission of heat from the building envelope. To mitigate this effect, green-vegetated façades were applied to the CCB, as it represents the dominant radiative source influencing the pedestrian zone.

The effectiveness of green façades in reducing wall surface temperatures has been demonstrated by Vox et al (2018), who reported air-temperature reductions of up to 9°C during warm periods and improved insulation performance during colder seasons. In the present model, vegetation was applied exclusively to the CCB, due to its strong impact on adjacent pedestrian areas and the simplicity of modifying façade materials within the Spaces environment (ENVI-MET GmbH, 27.02.2024).

A direct comparison between the shaded model and the unmodified scenario indicates that the maximum PAT at pedestrian height (1.5 m) reached 37.4°C at 16:00, compared to 37.5°C in the original configuration (**Fig. 9a**). Although the difference in air temperature is marginal, the temporal evolution of thermal conditions shows a clear stabilization effect. The rapid temperature increase observed after 14:00 in the original model and the abrupt cooling after 16:00 were significantly buffered, resulting in a more uniform thermal profile throughout the day.

Maximum MRT in the shaded model did not exceed 58.2°C, compared to values of up to 80°C recorded in the original scenario (**Fig. 9b**). During the evening hours (19:00–24:00), perceived temperatures remained approximately 1°C higher than the actual air temperature, indicating residual heat storage within the artificial structures.

From a spatial point of view (**Fig. 15**), maximum values of PAT (36.1°C) were recorded on the asphalt surfaces of the south-eastern parking lot, where perceived temperatures reached approximately 65°C due to direct solar exposure. In contrast, the northern parking area, where asphalt has been replaced with cobblestone, exhibited a potential air temperature of 34.1°C. Excluding localized tree effects (0.2–0.3°C), the observed 2°C difference is attributed to the thermal properties of the paving material. Despite lower air temperatures, perceived temperatures (MRT) in the northern area reached approximately 70°C, reflecting the influence of prolonged solar exposure and radiative exchange. Under the sun sails, MRT were reduced to approximately 54°C, compared to 66°C east of the structures and 70–73°C west of them.

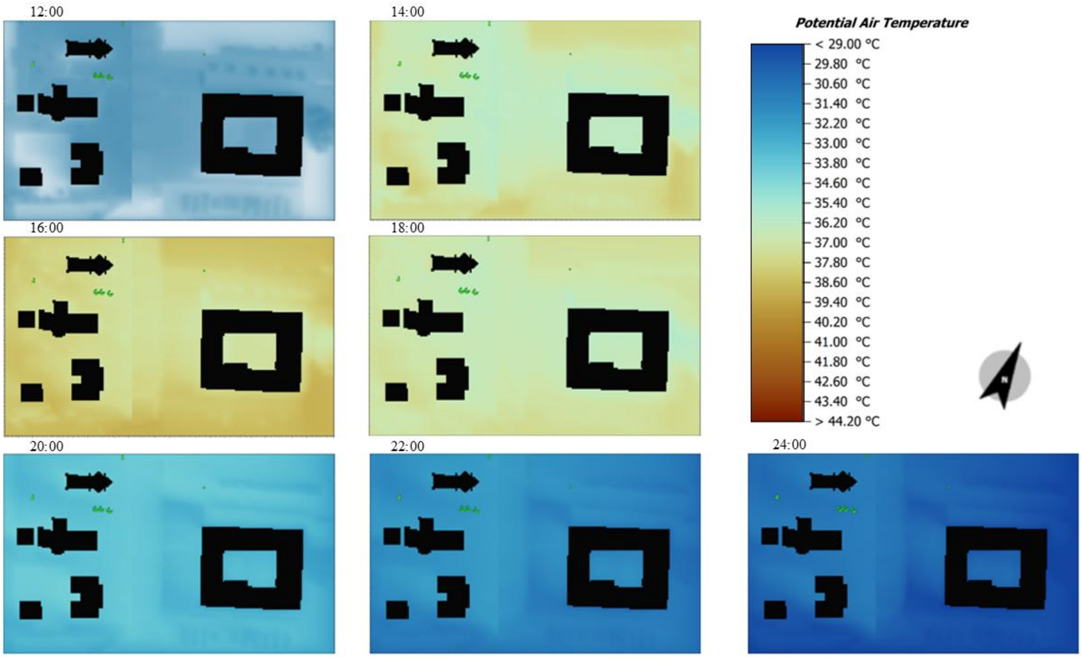

Fig. 15. Spatial distribution of PAT from 12:00 to 00:00 in the model with sun sails.

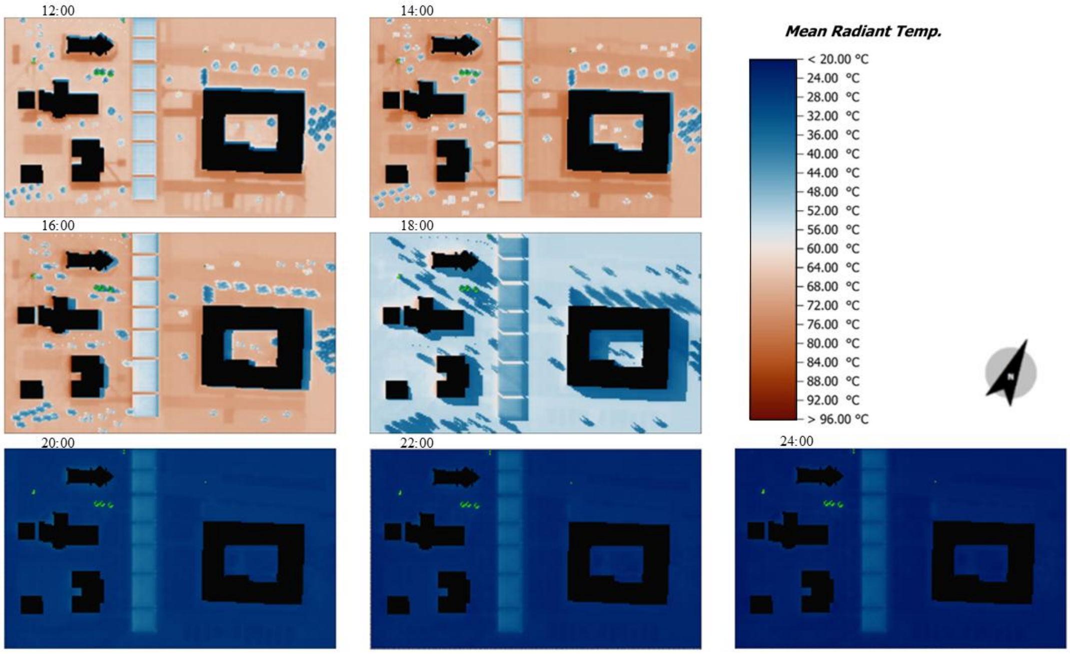

Fig. 16. Spatial distribution of MRT from 12:00 to 00:00 in the model with sun sails.

The highest MRT, up to 76°C, were observed on sidewalks paved with red concrete slabs, confirming the unfavorable thermal behavior of this material (Wardeh et al., 2024). Between 14:00 and 16:00, the average air temperature increased to nearly 38°C, while areas with temperatures below 37°C contracted spatially. Most locations exceeded 70°C in perceived temperature, particularly near west-facing façades. Under the sun sails, air temperature averaged 37°C, increasing to 38.5°C near the southern boundary due to the influence of adjacent asphalt surfaces (**Fig. 16**).

Perceived temperatures beneath the shading structures ranged from approximately 46°C in the eastern sector to 58°C in the western extremities, while minimum values of around 30°C were recorded along the eastern façades of buildings. After 18:00, average air temperatures decreased and spatial variability diminished. The combined influence of buildings and vegetation generated sharply defined shaded zones, where perceived temperatures were up to 15°C lower than in surrounding exposed areas. During the final analyzed interval (20:00–24:00), air temperatures declined uniformly across the study area. At this stage, vegetation no longer exerted a measurable influence on either air temperature or perceived temperature, while shaded areas under sun sails remained approximately 1.5°C warmer than uncovered surfaces due to residual heat emission.

Using the BIOmet module, a direct comparison was performed along an identical pedestrian route starting at 16:00. Skin temperature at the beginning of the route was 30°C in both models. In the original configuration (see Figure 12), it increased to 35°C, whereas in the modified model the increase was slower, reaching a maximum of 34.5°C (**Fig. 17**).

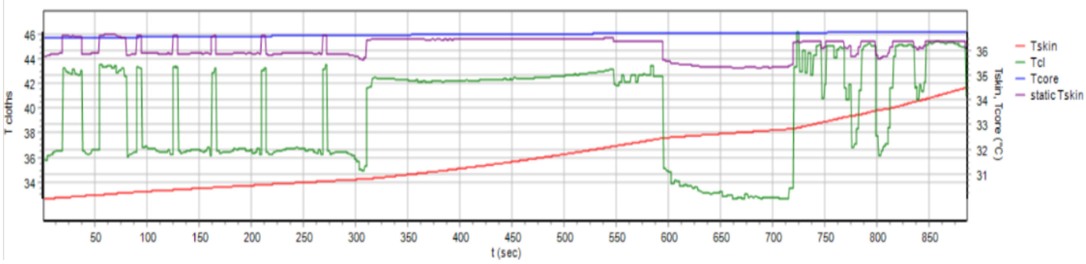

Fig. 17. BIOmet pedestrian route at 16:00 in the model with sun sails.

Clothing-level temperature clearly reflects the influence of artificial shading. When passing beneath sun sails, values decreased from approximately 42°C to 37°C, a pattern consistently observed at each structure. Outside shaded segments, temperature values remained similar to those recorded in the chestnut-only scenario, as the northern CCB parking area was treated identically.

5. CONCLUSIONS

Our analysis proves that ENVI-met has several key advantages when solutions to mitigate or to adapt heat stress are tested, including high-resolution and accurate data, the ability to assess sites without in-situ measurements, and the option to reproduce custom materials, soil profiles, and vegetation.

This study aimed to investigate strategies for enhancing thermal comfort in an urban pedestrian area with a high vulnerability to excessive heat during summer. Initially, vegetation was used to expand shaded surfaces, and paving materials were modified in microclimatically sensitive zones. The results of this approach were mixed. Tree planting had a marginal effect on air temperature, with differences below 0.5°C along the pedestrian area. However, the most notable impact was observed in perceived temperatures during the afternoon due to increased shading. As well, replacing asphalt with cobblestone produced a reduction of approximately 2°C in air temperature. The combined effect of vegetation and improved paving demonstrated promising potential for increasing thermal comfort in the study area.

Following these findings, a more substantial intervention was implemented. Artificial shading structures composed of PVC, aluminium, and photovoltaic panels were installed along the pedestrian corridor, while previously modified areas were retained due to their positive performance. The introduction of these structures resulted in significant improvements: air temperature (PAT) along the pedestrian zone remained below 37°C throughout the day, and perceived temperatures (MRT) under the sun sails were up to 20°C lower than surrounding exposed areas. However, despite of its microclimatic benefits, this method is difficult to be implemented due to its problematic integration in the urban design. As well, a temporary implementation only during summer could be envisaged since during the rest of the year the thermal comfort benefits are null.

Another important conclusion of our work is that ENVI-Met modelling should be based on fine scale weather measurements used both for running the model but also to validate its results.

ACKNOWLEDGEMENT

This work was supported by a grant of the Ministry of Research, Innovation and Digitization, CNCS-UEFISCDI, project number PN-IV-P1-PCE-2023-0897, within PNCDI IV.

Data processing and analysis in this paper were supported by the Competitiveness Operational Programme Romania, under project SMIS 124759 - RaaS-IS (Research as a Service Iasi).

REFERENCES

Alexe, C. (2012). *Climate and topoclimate of Iași municipality and metropolitan area (in Romanian)*. PhD Thesis. Iaşi.

Arnfield, A.J. (2023). *Köppen climate classification.* Encyclopedia Britannica, Available from: https://www.britannica.com/science/Koppen-climate-classification [Accessed 4 February 2024].

ASHRAE (2001). *ASHRAE Fundamentals Handbook*. American Society of Heating, Refrigerating, and Air-Conditioning Engineers, ISBN: 1883413885.

Bănică, A., Roșu, L., Muntele, I., & Grozavu, A. (2017). Towards urban resilience: A multi-criteria analysis of seismic vulnerability in Iasi City (Romania). Sustainability, 9(2), 270. Available from: https://doi.org/10.3390/su9020270.

Beck, H. E., Zimmermann, N. E., McVicar, T. R., Vergopolan, N., Berg, A., & Wood, E. F. (2018). Present and future Köppen-Geiger climate classification maps at 1-km resolution. Scientific data, 5(1), 180214. Available from: https://doi.org/10.1038/sdata.2018.214

Belda, M., Holtanová, E., Halenka, T. & Kalvová, J. (2014). Climate classification revisited: From Köppen to Trewartha. *Climate Research*, 59, 1–13. Available from: doi: 10.3354/cr01204.

Bruse, M. (2023). *ENVI-met 5.5* [Computer software]. ENVI-met GmbH. https://www.envi-met.com

Crețu, ȘC., Sfîcă, L., Ichim, P., Amihăesei, V.A., Breabăn, I.G. & Roșu, L. (2025). Warm season land surface temperature and its relationship with local climate zones in post-socialist cities. *Theoretical and Applied Climatology*, 156, 191. Available from: doi: 10.1007/s00704-025-05409-y.

Del Serrone, G., Peluso, P. & Moretti, L. (2022). Evaluation of microclimate benefits due to cool pavements and green infrastructures on urban heat islands. *Atmosphere*, 13(10), p.1586. Available from: https://doi.org/10.3390/atmos13101586.

Dumitrescu, A. & Birsan, M. V. (2015). ROCADA: a gridded daily climatic dataset over Romania (1961–2013) for nine meteorological variables. *Natural Hazards*, 78, 1045–1063. Available from: doi.pangaea.de/10.1594/PANGAEA.833627.

Eingrüber, N., Berg, P., Korres, W., Löhnert, U., & Schneider, K. (2024). Parameterization and Validation of a High-Resolution Microclimate Model to Identify Temperature Patterns in a Climate Change Adapted Urban High-Density Area. *Available at SSRN 4912045*. Available from: https://doi.org/10.1016/j.cacint.2026.100302.

Elgheznawy, D. & Eltarabily, S. (2021). The impact of sun sail-shading strategy on the thermal comfort in school courtyards. *Building and Environment*, 202, 108046. Available from: https://doi.org/10.1016/j.buildenv.2021.108046.

ENVI-met., (2025). Leading 3D Modelling Software for Urban Cooling and Climate Adaptive Planning. Accessed [2025], https://envi-met.info/doku.php?id=start

Faragallah, R. N., & Ragheb, R. A. (2022). Evaluation of thermal comfort and urban heat island through cool paving materials using ENVI-Met. *Ain Shams Engineering Journal*, *13*(3), 101609. Available from: https://doi.org/10.1016/j.asej.2021.10.004.

Ferrari, A., Kubilay, A., Derome, D. & Carmeliet, J. (2020). The use of permeable and reflective pavements as a potential strategy for urban heat island mitigation. *Urban Climate*, 31, p.100534. Available from: https://doi.org/10.1016/j.uclim.2019.100534.

Fischereit, J., Schlünzen, K.H. (2018). Evaluation of thermal indices for their applicability in obstacle-resolving meteorology models. *Int J Biometeorol* 62, 1887–1900. Available from: https://doi.org/10.1007/s00484-018-1591-6

Foșalău, C.M., Roșu, L., Iațu, C., Dinter, O.V. & Cristodulo, P.M. (2025). Mapping urban changes through the spatio-temporal analysis of vegetation and built-up areas in Iași, Romania. *Sustainability*, *17*(1), p.11. Available from: https://doi.org/10.3390/su17010011.

Grigoraș, G., & Urițescu, B. (2024). Analysis of urban thermal environments using satellite data and urban microclimate modeling. *INCAS Bulletin*, *16*(3), 39-49. DOI: 10.13111/2066-8201.2024.16.3.4

Gusson, C. S., & Duarte, D. H. (2016). Effects of built density and urban morphology on urban microclimate-calibration of the model ENVI-met V4 for the subtropical Sao Paulo, Brazil. Procedia engineering, 169, 2-10. https://doi.org/10.1016/j.proeng.2016.10.001.

Ichim, P. & Sfîcă, L. (2020). The influence of urban climate on bioclimatic conditions in the city of Iași, Romania. *Sustainability*, 12(22), 9652. Available from: https://doi.org/10.3390/su12229652.

Iordache, I., Apostol, L. & Ichim, P. (2017). The land surface temperature distribution during 7th August 2012 using MODIS imagery in Iasi metropolitan area. *Air and Water Components of the Environment Conference*, March 2017, 11–17. Available from: doi: 10.24193/AWC2017_02.

Kaularachichi, T.U.N., Tjoelker, M.G. & Pfautsch, S. (2020). Temperature reduction in urban surface materials through tree shading depends on surface type not tree species. *Forests*, 11(11), p.1141. Available from: https://doi.org/10.3390/f11111141.

Kotharkar, R., & Dongarsane, P. (2024). Investigating outdoor thermal comfort variations across Local Climate Zones in Nagpur, India, using ENVI-met. *Building and Environment*, *249*, 111122. Available from: https://doi.org/10.1016/j.buildenv.2023.111122

Lau, K.K.L., Lindberg, F., Rayner, D. & Thorsson, S. (2015). The effect of urban geometry on mean radiant temperature under future climate change: a study of three European cities. *International Journal of Biometeorology*, *59*(7), pp.799-814. Available from: https://doi.org/10.1007/s00484-014-0898-1.

Nagavciuc, V., Scholz, P. and Ionita, M., (2022). Hotspots for warm and dry summers in Romania. *Natural Hazards and Earth System Sciences*, 22(4), pp.1347-1369.

Nikolopoulou, M., Baker, N. & Steemers, K. (2001). Thermal comfort in outdoor urban spaces: understanding the human parameter. *Solar Energy*, 70(3), pp.227-235. Available from: https://doi.org/10.1016/S0038-092X(00)00093-1.

Masson, V., Lemonsu, A., Hidalgo, J., & Voogt, J. (2020). Urban climates and climate change. Annual Review of Environment and Resources, 45(1), 411-444. Available from: https://doi.org/10.1146/annurev-environ-012320-083623

National Meteorological Administration of Romania (NMA RO) data source: www.meteomanz.com who is the ftp server of the National Oceanic and Atmospheric Administration (NOAA). [Accessed: January 2026].

Minea, I. (2010). The evaluation of the water chemistry and quality for the lakes from the south of the Hilly Plain of Jijia (Bahlui drainage basin). *Lakes Reservoirs and Ponds*, 4(2), 131–144.

Ng, E. (2012). Towards planning and practical understanding of the need for meteorological and climatic information in the design of high-density cities: A case-based study of Hong Kong. *International Journal of Climatology*, 32(4), pp.582-598. Available from: https://doi.org/10.1002/joc.2292.

Onțel, I., Amihăesei, V., Micu, D., Dumitrescu, A., & Cheval, S. (2025). Influence of environmental factors on land surface temperature and surface urban heat island. A cross-country analysis in Romania. Sustainable Cities and Society, 128, 106454. Available from: https://doi.org/10.1016/j.scs.2025.106454

Park, Y., Guldmann, J.M. & Liu, D. (2021). Impacts of tree and building shades on the urban heat island: Combining remote sensing, 3D digital city and spatial regression approaches. *Computers, Environment and Urban Systems*, *88*, p.101655. Available from: https://doi.org/10.1016/j.compenvurbsys.2021.101655.

Sandu, I., Mateescu, E. & Vătămanu, V. (2008) *Climate of Romania* (in Romanian), National Meteorological Administration, Academy Publishing House.

Salata, F., Golasi, I., de Lieto Vollaro, R., & de Lieto Vollaro, A. (2016). Urban microclimate and outdoor thermal comfort. A proper procedure to fit ENVI-met simulation outputs to experimental data. *Sustainable Cities and Society*, *26*, 318-343. Available from: https://doi.org/10.1016/j.scs.2016.07.005

Sinsel, T. (2022). Advancements and applications of the microclimate model ENVI-met. Dissertation zur Erlangung des Grades "Doktor der Naturwissenschaften" im Promotionsfach Geographie am Fachbereich Chemie, Pharmazie, Geographie und Geowissenschaften der Johannes Gutenberg-Universität Mainz, Available from: http://doi.org/10.25358/openscience-6716

Sinsel, T., Simon, H., Ouyang, W., dos Santos Gusson, C., Shinzato, P., & Bruse, M. (2022). Implementation and evaluation of mean radiant temperature schemes in the microclimate model ENVI-met. *Urban Climate*, *45*, 101279. Available from: https://doi.org/10.1016/j.uclim.2022.101279.

Secu, C. V., Minea, I., & Stoleriu, I. (2015). Geostatistical modeling of water infiltration in urban soils. Carpathian Journal of Earth and Environmental Sciences, 10, 95-104.

Secu, C. V., Juravle, D. T., Paiu, M., Lesenciuc, D. C., Costică, M., Negru, D., & Breabăn, I. G. (2016). Potentially toxic elements in urban soils of Iasi (Romania). Environmental Engineering and Management Journal, 15(3), 687-698. Available from: 10.30638/eemj.2016.074

Sfîcă, L., Croitoru, A.E., Iordache, I. & Ciupertea, A.F. (2017). Synoptic conditions generating heat waves and warm spells in Romania. *Atmosphere*, 8(3), p.50. Available from: https://doi.org/10.3390/atmos8030050.

Sfîcă, L., Ichim, P., Apostol, L. & Ursu, A. (2018). The extent and intensity of the urban heat island in Iași city, Romania. *Theoretical and Applied Climatology*, *134*(3), pp.777-791. Available from: https://doi.org/10.1007/s00704-017-2305-4.

Sfîcă, L., Crețu, C.Ș., Ichim, P., Hrițac, R. & Breabăn, I.G. (2023). Surface urban heat island of Iași city (Romania) and its differences from in situ screen-level air temperature measurements. *Sustainable Cities and Society*, 94, 104568. Available from: https://doi.org/10.1016/j.scs.2023.104568.

Simon, J., Oster, J. & Beck, C. (2025). Exploring the Role of Urban Green Spaces in Microclimate Modeling: Insights from ENVI-met Simulations in Augsburg, Germany, *EGU General Assembly 2025*, Vienna, Austria, 27 Apr–2 May 2025, EGU25-17996. Available from: https://doi.org/10.5194/egusphere-egu25-17996.

Urițescu, B., Grigoraș, G. (2022). The Influence of Building Envelope on the Local Microclimate. 2022 ”Air and Water – Components of the Environment” Conference Proceedings, Cluj-Napoca, Romania, p. 140153, DOI: 10.24193/AWC2022_14.

Ursu, A., Andrei, M., Chelaru, D. A., & Ichim, P. (2016). Built-up area change analysis in Iasi city using GIS. Present Environment and Sustainable Development, (1), 201-216. DOI 10.1515/pesd-2016-00 18

Vox, G., Blanco, I. & Schettini, E. (2018). Green façades to control wall surface temperature in buildings. *Building and Environment*, 129, 154–166. Available from: https://doi.org/10.1016/j.buildenv.2017.12.002.

Wardeh, Y., Rahme, P., Escadeillas, G., Kinab, E. & Ginestet, S. (2024). Cooling potential of cement concrete pavements based on their thermophysical properties. *Case Studies in Construction Materials*, 21, p.e04018. Available from: https://doi.org/10.1016/j.cscm.2024.e04018.

Yang, J., Hu, X., Feng, H., & Marvin, S. (2021). Verifying an ENVI-met simulation of the thermal environment of Yanzhong Square Park in Shanghai. Urban Forestry & Urban Greening, 66, 127384. Available from: https://doi.org/10.1016/j.ufug.2021.127384.

Yang, X., Li, B., Li, N. & Ma, X. (2026). A study of the cooling effect of urban trees: Influencing factors, assessment methods, planning strategies, and impacts. *Theoretical and Applied Climatology*, 157(1), p.31. Available from: https://doi.org/10.1007/s00704-025-05904-2.

GEOSTATISTICAL VARIABLES INFLUENCING *LIVESTOCK GUARDIAN DOGS* (LGDs) MOVEMENT IN MOUNTAIN SETTINGS. A PREDICTIVE MAPPING CASE STUDY FROM NORTHERN ROMANIA

Silviu Vasile BUMBAK [1]

DOI: 10.21163/GT_2026.213.10

ABSTRACT

In Romania, a Carpathian nation by definition, pastoralism represents a cultural reference and, as such, its proxies are seen as ancestral users of mountain spaces. The cultural reference extends to the livestock guardian dogs (LGDs) present at the sheepfolds across the landscape. The dogs are seen as an integral part of pastoralism, providing security in an environment populated with large carnivores. However, through mountain tourism, a new category of landscape users is increasingly making its presence known, as many outdoor recreational activities in the mountains overlap with the pastoral calendar. This situation creates a potential for conflict between two distinct categories of landscape users. The research hypothesis states that the flock and the dog's presence are not randomly distributed but follow a spatial pattern characterized by key geostatistical variables, with varying degrees of significance and predictive power. To demonstrate this in a GIS environment (QGIS), 9 geostatistical variables (topographic, environmental and control variables) were selected as representative for a 113 km2 area used by two LGDs from two sheepfolds in the lowlands of Igniș Mountains, Maramureș Land, northern Carpathians. All geovariables were reclassified as categorical data using a 1-5 rules-based risk scale. The reclassified geovariables were used to build a weighted theoretical model mapping the areas where the probability of their presence is high. Using telemetry data collected during a 60-day monitoring campaign of the two LGDs for validation (over 1200 daytime observation points), the analysis shows that over 78% of the daytime LGD activity was concentrated in areas with medium to high (over 3.5) probability risk. These results indicate that topographic variables can influence LGD presence and serve as predictors of occurrence. The environmental variables can highlight areas of high occurrence, while the high density of observations near the control variables shows how they act as anchors, concentrating the dogs' movement in their vicinity. Case studies of this kind have the potential to contribute to the design process of smart solutions for trail management instruments based on predictive mapping, integration of results into dedicated trail apps, spatial planning and design trails, information, and signaling infrastructure.

Keywords: *Livestock guardian dogs (LGD); Telemetry data; Mountain tourism; Geostatistical variables; Potential for conflict; Predictive mapping; Trail management.*

1. INTRODUCTION

In the last decades, mountain landscapes have become increasingly multifunctional, as grazing areas overlap with those frequented by mountain tourism practitioners, leading to spatial superposition and interactions between the shepherds and their dogs and the practitioners of mountain tourism (Landry & Drouilly, 2020; Gehring et al., 2010). This type of interaction can generate mixed effects: convergent effects such as the touristification of the sheepfolds that capitalize on the presence of the tourists, selling produce and services. These effects are best seen on highly developed, marketized trails such as the newly developed Via Transilvanica, a long-distance, cross-country trekking and biking trail (Tășuleasa Social, 2026). At the other end, divergent effects are occurring across the majority of Romanian mountain areas, at least in part due to often problematic encounters in the field between tourists and livestock guardian dogs that protect flocks (Bailly et al., 2025). This type of land-use conflict encourages avoidance and fear-based perceptions that can develop in the minds of tourists into true "landscapes of fear" (Gaynor et al., 2019; van Bommel et al., 2023; Tuan, 2013).

----

[1] *Babeș-Bolyai University of Cluj-Napoca, Faculty of Geography, Department of Human Geography and Tourism (Sighetu Marmației Extention), Romania, silviu.bumbak@ubbcluj.ro*

Many incidents have occurred over the years (Ivașcu & Biro, 2020), mainly because mountain trails overlap the pastoral trails and their summer grazing calendar. This is one of the reasons why this paper focuses on this second category, as the presence of the LGD's, even though essential for the pastoral activities (Spencer et al., 2020; van Bommel & Johnson, 2024), represents a serious risk factor and a psychological barrier for the tourists, posing challenges for mountain activities management, safety, and overall experience.

From academic and practical spatial management perspectives, efforts should be directed toward identifying synergies that addresses this issue in a predictive and proactive manner and focus on smart coexistence and smart spatial co-management frameworks. One such synergy can come from the area of animal movement analysis in heterogeneous geographical spaces. These analyses can substantiate future predictive modeling efforts that offer a new perspective on spatial trail management in mountain areas that accommodate both user categories.

The main objective of the study is to predict LGD occurrence by conceptualizing a GIS-based modeling approach that combines selected key geostatistical variables of the land used in the grazing system at two sheepfolds in the Igniș Mountains, north of Romania. The study's purpose is to explain and understand the influence of these geovariables on LGD distribution. The results are presented as a predictive map highlighting areas of LGD occurrence probability. It was hypothesized that their movement is not random and can be determined by studying the spatial characteristics of the terrain used to navigate between grazing domains. Considering the LGD as a proxy for the sheep, it can be assumed that they move alongside them, following a spatial movement pattern influenced by those variables. As such, the flock's and the dog's presence are not randomly distributed but follow a spatial pattern characterized by key physical and environmental predictors with different degrees of significance.

One important element regarding the spatial dynamics of the LGDs, a proxy for the sheep, is that these animals do not exhibit full natural behavior. Their spatial dynamics are influenced by the shepherd's decisions. We assume that these decisions are based on choices, knowledge, possibly restrictions, and that the geovariables we choose are representative of the decision-making processes in traditional pastoral landscapes. For exploratory validation of the model, the selected geovariables were combined with telemetry data from a field monitoring campaign of two LGDs at the two sheepfolds involved in the study.

Even though this is a case study, it presents a conceptual and methodological approach to better understand the spatial probability of LGD occurrence. It highlights the LGD as an important element of the pastoral system, while also acknowledging them as a source of friction in their interactions with people. This is important because the area of LGD-human interactions represents an understudied field, especially regarding the Carpathian Mountains. This is the case mainly because the academic interests have focused more on human-wildlife (especially large carnivores such as bears) conflicts. The reactive outcomes of such encounters, even though rare compared with incidents involving LGDs, have often been reported in a sensationalist manner in the press.

Findings of this type can also contribute to a shift in perspective by moving towards proactive conflict-management solutions that favor coexistence. Regarding the spatiality of LGD occurrence, the findings also demonstrate the real spatial footprint of traditional pastoral practices in heterogeneous landscapes, highlighting preferred areas of activity and providing a better understanding of the geographical context that favors them.

From an outdoor recreation planning perspective, they can contribute to predictive mapping of the vulnerability of tourist trails to LGD occurrence. This area of recreation planning usually relies on input on general mountain safety criteria, such as static potential risks, avalanche risk assessments, various geomorphological risks (e.g., rockfall), trail difficulty and technicality, etc. In a paper-to-practice scenario, predictive mapping of LGD occurrence can represent a tangible tool in the decision-making process and design of smart solutions of trail management and safety in mountain areas, such as trail routing and rerouting options, maps highlighting trail vulnerability to this kind of danger, integration of results into dedicated trail apps, and spatial planning of information and signaling infrastructure.

1.1. Description of study area and sheepfolds involved in the field monitoring campaign

The findings from a previous study focused on a primary analysis of movement of two LGDs (Bumbak et al., 2024) were also used to delineate the area of interest for this exploratory study. We used the maximum extent of their whereabouts (home range) from the telemetry data interval and expanded it by about 2–3 kilometers in each cardinal direction to define an area of approximately 113 km2, considered suitable for the study's purposes. This section of land is situated in the northern Carpathians, north of Romania, in the western part of the region known as Maramureș Land, with strong cultural, identitarian, and pastoral traits.

The region is a part of the external EU border territorial system with Ukraine (Ilieș & Grama, 2010). The local geography features a sedimentary piedmont with moderate fragmentation, bordering the Igniș volcanic mountains to the east. It decreases in altitude towards the eastern lowlands of the Mara River, one of the region's main systemic axes, where small to medium rural settlements are found. The altitudes of the area of interest range between 270 meters in the Mara River valley to approximately 1060 meters in the western highlands, with a median altitude of around 500 meters. The area represents the typical agricultural landscapes of the Carpathians, with a mosaic of natural vegetation (forests, natural grasslands, and shrubs) interspersed with patches of agricultural land and pastures.

Climatically, the area is representative of the Dfb Koppen classification, characterized by strong continental features (Kottek et al., 2006). It is also traversed east-west by local roads and trails that lead up to the highlands of the Ignis Mountains. These mountains have also become a popular hiking and biking destination for both local recreationists and tourists (see **Fig. 1**).

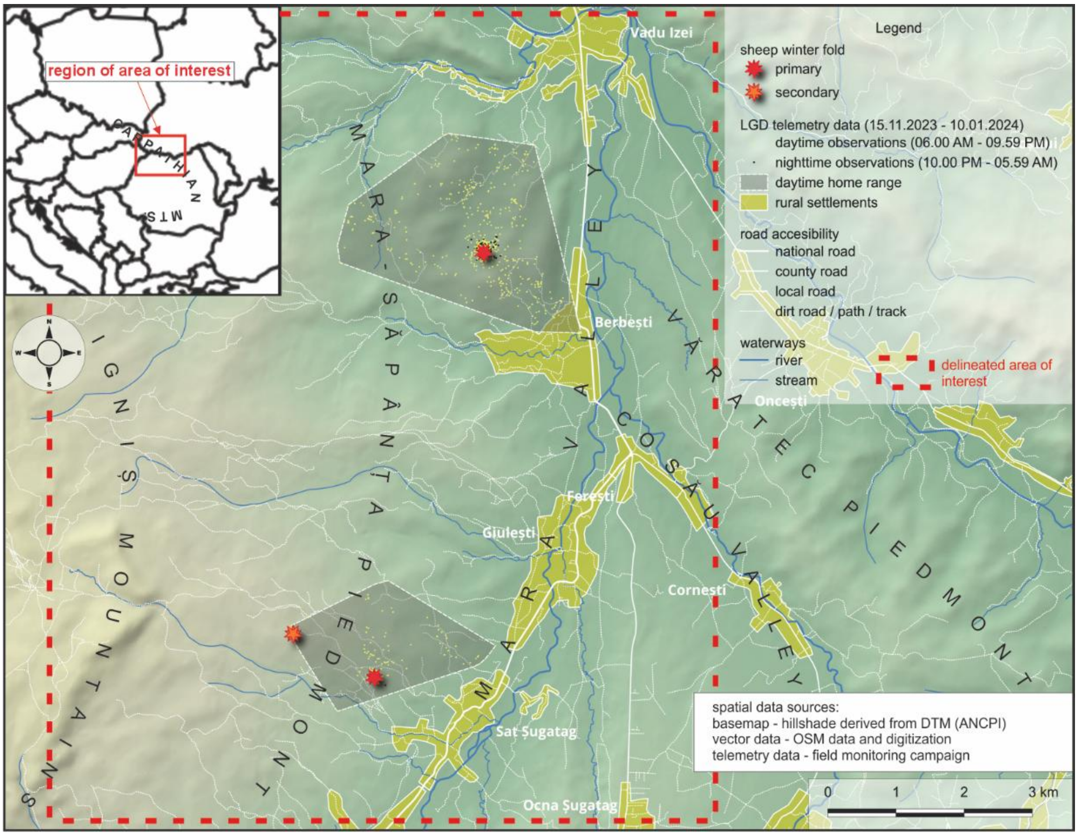

Fig.1. Delineation of area of study, location of sheepfolds and LGD field telemetry data.

2. LITERATURE REVIEW

The identification and parametrization of geostatistical and other predictors of animal movement in different environments, and proactive movement model build-up, represents a fertile research avenue in many academic fields (Laffan et al., 2012; Edelhoff et al., 2016; Rew et al., 2019; Khayli et al., 2021; Jacobson et al., 2024). Usually, this requires an interdisciplinary approach that combines statistics, modelling, and geographical analysis of terrain, land features, climate and weather features, other environmental and anthropic features, and animal ethology. This is frequently done in a GIS environment (Dănilă et al., 2024).

Papers covered subjects related especially to quantifiable spatial predictors (Avgar et al., 2013) of animal movement in mountain regions, such as topographic (Valderrama-Zafra et al., 2024) and land-use factors, habitat selection criteria and analysis (Avgar et al., 2016; Thurfjell et al., 2014), movement pattern identification (Preisler et al., 2013), tracking data representation and analysis (Seidel et al., 2018), and solutions applied in spatial management of interactions in areas frequented by people.

Another category included works related to the use of guardian dogs (Vercauteren et al., 2011; Rigg, 2001), their movement in mountain environments (Smith et al., 2026), flock and LGD spatial dynamics, and LGD's overall ethology during interactions with tourists in mountain settings (Bailly et al., 2026). It also accepted, as a proxy, a set of general features from previous research on animal movement, even when these were not directly related to other species. These features served as a methodological guideline, as they could be extrapolated to the present approach.

Environmental and topographical drivers were identified (Avgar et al., 2013) as influencing animal movement in a deterministic way by combining spatial variables (NDVI, land cover categories, distance to various landscape features, etc.) with temporal dynamic variables (precipitation, temperature, snow cover, length of day, etc.) in relation to the functional characteristics of the landscape in a cost-risk-benefit relationship. In another study, Avgar and his team examined resources as attractors that influence animal behavior and time spent in a given location using integrated step-selection analysis (Avgar et al., 2016).

Other papers mathematically demonstrate the utility of various habitat selection models, such as the step selection function, by considering real versus available spaces based on the animal's actual movement possibilities in a geographically heterogeneous environment (Fieberg et al., 2021). In other examples, authors highlight the importance of topographic factors such as natural or human-made obstacles‒rivers, ravines, roads, fences, etc. ‒in restricting, conditioning, or guiding animal movement (Lempidakis et al., 2018), or propose a guideline for structural decomposition of the land (Panzacchi et al., 2016) based on primary topographical attributes (elevation, slope, terrain roughness index, etc.). All these spatial predictors influence the movement of animals from different species, which tend to adopt a least-cost, energy-saving movement pattern and to repeatedly use suitable movement corridors (Valderrama-Zafra et al., 2024).

Some researchers focused on the limitations of many predictive models, highlighting their predictive inadequacy outside the temporal and spatial sampling of the telemetry data or outside the parameter-defined environment (Winter et al., 2024). As a result, suggestions have been made to cross-reference telemetry data with, for example, spatial surveys or observations to improve the accuracy of predictive models (Lauret et al., 2025). Other authors highlight the importance of telemetry data abundance, sampling intensity, and the time frame over which the spatial data were collected for accurate predictions (Gerber et al., 2019).

Another aspect that caught our attention during the literature review was the importance of including correction variables (control variables), such as distance to specific landscape features, to avoid over- or underestimating landscape variables (Forester et al., 2009).

As the study's interest gravitated towards LGD ethology, which does not represent natural behavior but rather a controlled one aligned with the priorities of the sheepfold, we are aware that LGD movement is highly dependent on the shepherd's decisions. As such, any telemetry data from the dogs carries a certain degree of bias, as they represent instances of guided behavior.

A recent applied study on the movement patterns of LGDs across several Carpathian massifs (Smith et al., 2026) found that telemetry data indicate LGDs tend to stay close to the sheep, reinforcing their guarding instinct. This finding underscores the idea that dogs are seen as proxies for sheep. However, in the same study, the authors found that the "LGDs were separated from the sheep at some point each day" and that their own roaming behavior (not parametrized in this paper) took them several kilometers away, increasing the risk of encounters with other landscape users such as recreationists or tourists. Highlighting these hazards, the authors suggest buffer zones of several hundred meters around popular trails, a sound recommendation that must be adapted to specific local conditions. We also looked at papers on the issue of the large numbers of LGDs found around sheepfolds and some of the effects they have on dog behavior. For example, the pack effect (not parametrized in this paper) around a single flock that instinctively protects it. In situations like this, the dogs can become an issue (Gehring et al., 2010), as they can easily enter into conflicts with people engaged in recreational activities in the same areas (Mosley et al., 2020). These situations also speak volumes about the micro-management solutions adopted by the shepherd and about dog training.

3. METHODOLOGY

A better understanding of the land characteristics is necessary to substantiate the previous findings and highlight the geographical characteristics of the areas where the LGDs spent more time. For this purpose, we conceptualized a methodological flow (see **Fig.2**) and identified the main spatial characteristics of the geographical context using a set of 9 geostatistical variables (see **Table 1** and **Fig. 2**) that reflect the concept of animal-guided behavior, as determined by the shepherd's decisions. The selected geovariables were grouped into three categories based on literature inputs considered suitable for the study's objectives. Firstly, a set of 4 topographical variables was considered ‐ slope, aspect, TRI (Terrain Ruggedness Index), and TPI (Terrain Positioning Index) - followed by 2 environmental variables ‐ NDVI (Normalized Difference Vegetation Index) and CLC (Corine Land Cover).

These were supplemented by 3 logistical variables, considered control variables‒distance to sheepfolds (the most important control variable for the study), distance to streams, and distance to access routes‒to avoid over- or underestimating the importance of the selected topographical and environmental variables. With the exception of CLC data obtained in vector format, all other data are categorical and represented in raster format.

Aside from the own vector data, open-source spatial data (roads/trails and streams) was also used to create a database in QGIS 3.44.8 (QGIS Development Team, 2026). For the continuous spatial data, since several topographic variables were considered as defining for the analysis, a high-resolution digital terrain model (DTM) was paramount. In this analysis, we assume that a dog's spatial predictability is influenced by the sheep's movement under the shepherd's guidance in search of patches with good food sources, while accounting for terrain accessibility. Therefore, deriving reliable topographical variables describing terrain's accessibility represented an important methodological step. We searched for several reliable open-source datasets and ultimately settled on DTM data tiles available from the Romanian National Agency for Cadastre and Land Registration (ANCPI, 2026). The resolution of the tiles covering the area of interest is 5 meters x 5 meters, offering good granularity of topographically derived information - slope, aspect, TRI, and TPI. For the study area, the TPI values range from -4.55 m to 4.06 m and, together with TRI values between 0 m and 19.2 m, indicate a fragmented landscape with clear topographical variations and induced differentiation of suitable grazing surfaces (TPI> 0.5 m and TRI between 0 m and 6 m).

These are important geostatistical variables influencing movement in a least-cost, energy-saving scenario, as sheep, like most gregarious animals, usually do not prefer steep or highly fragmented terrain, as it can impede or narrow movement to certain terrain corridors. They also favor, especially during periods outside the main grazing calendar, open, southern, sunny, low-inclined slopes (between 0^o and 15^o), avoiding narrow valleys used mainly as transit areas between feeding domains.

Table 1.

Selected geostatistical variables

geostatistical variable	data source	short description in the context of traditional shepherding
slope (^{0})	derived from DTM 5 m resolution (ANCPI)	indicates topographical features facilitates / limits access to feeding grounds influences accessibility and effort of movement influences site selection for sheepfold placement influences visibility
aspect	derived from DTM	indicates micro-climate characteristics Influences site selection for sheepfold placement Influences daily related movements influences vegetation structure
TRI (m)	derived from DTM	indicates natural suitable areas for movement usually, areas with high TRI values will be avoided facilitates / limits access to feeding grounds influences visibility
TPI (m)	derived from DTM	indicates natural suitable areas for movement and observations usually, areas with positive high TPI values will be favoured influences visibility
NDVI (-1.00 to 1.00)	derived from Landsat 8 tiles EROS Archive (USGS Earth Explorer)	valuable resource indicator indicates predominant vegetation indicates available areas for grazing (0.20 – 0.40) influences visibility
distance to sheepfolds (m)	field GPS location	spatial anchor and home range center indicates areas of high sheep and LGD activity influences the probability of occurrence (the probability decreases with distance from sheepfold)
distance to streams (m)	OSM data own digitization	valuable resource indicates priority areas near the grazing domains influences site selection for sheepfold placement implications on the daily movement (maximum distance)
distance to access routes (m)	OSM data own digitization	influences site selection for sheepfold placement indicates accessible corridors of movement, even in rough terrain increases speed of movement increases access to isolated areas indicates multi-use areas (vehicles, recreationists, tourists etc.)
CLC (classes)	European Environment Agency (EEA)	indicates the predominant land cover types and habitats indicates landscape features and fragmentation indicated favoured grazing areas – open meadows, grasslands. influences visibility

The NDVI data were obtained from Landsat 8 tiles downloaded using the USGS Earth Explorer web tool (EROS, 2020) for a suitable time interval relative to the field monitoring campaign - November 2024. Using the dedicated formula (NIR-R)/(NIR+R), we obtained the necessary spatial raster data at a resolution of 30 meters by 30 meters, the best available. Optimal NDVI values (0.20-0.40) indicate a direct indicator of biomass location. As the field campaign took place outside the main summer grazing season, we considered that the NDVI data should be supported by a supplementary geostatistical variable defining the local habitats. For this purpose, we used the 2018 vector format Corine Land Cover data, downloaded from the Copernicus mission (European Environment Agency, 2020). The CLC data clearly differentiates the habitats, thus adding the necessary nuance. Other data were obtained in vector format (water streams/access ways) and represent OSM data (OpenStreetMap contributors, 2026), downloaded in QGIS and annotated through digitization where the data were incomplete. For digitization, georeferenced topographic map tiles 1 to 25.000 (MTD, 1980) were used, alongside open-source satellite imagery (Bing Virtual Earth, 2026; Esri Imagery, 2026). The vector data representing water streams and access routes were treated as non-hierarchical and used to derive two important control variables: distance to streams and distance to access routes. The distance to streams is an important control variable, as it indicates the distance to the nearest water sources, since the flock must remain in close proximity for watering. They also tend to move alongside existing roads and trails.

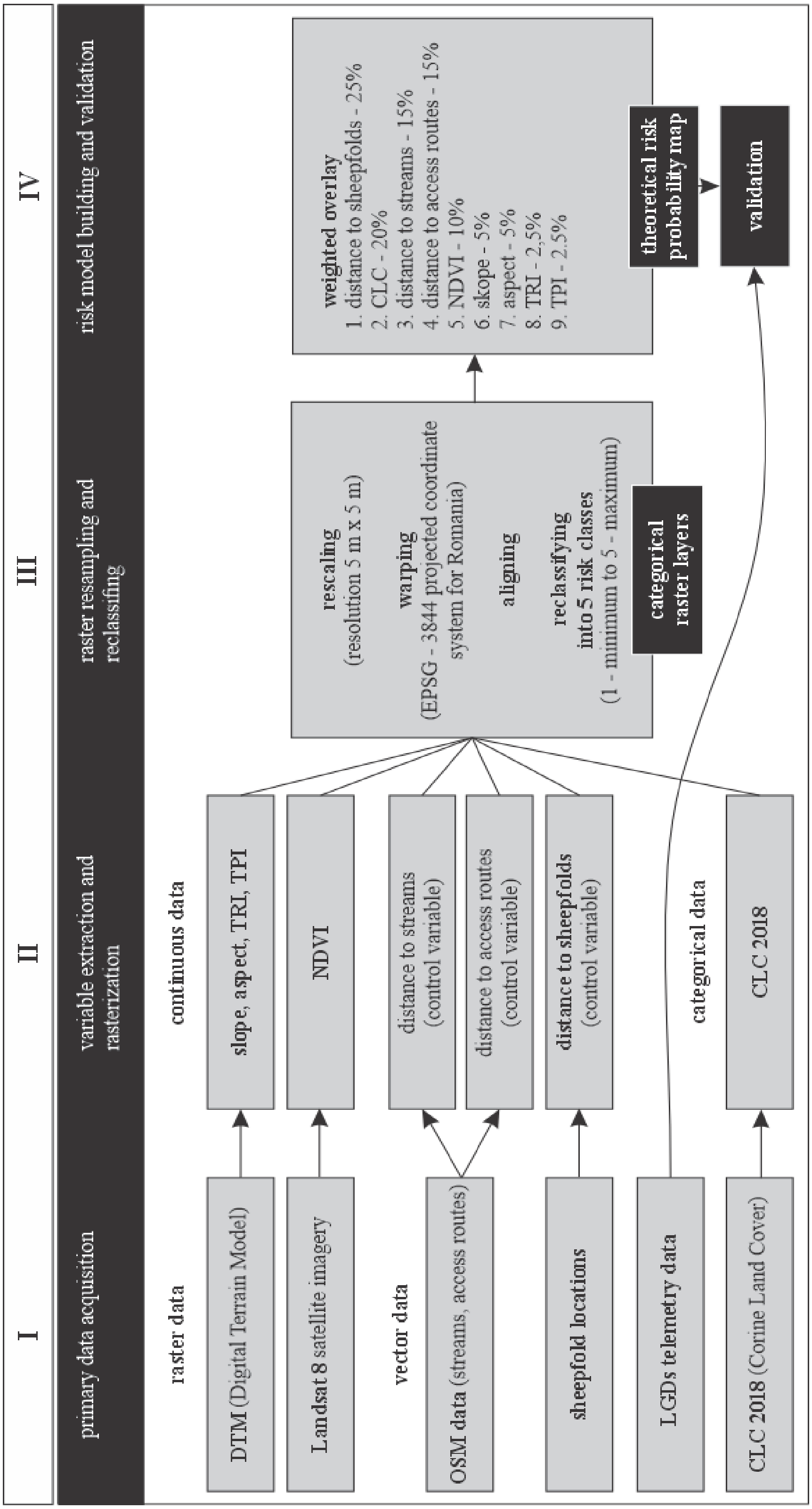

Fig.2. The main methodological stages of the case study.

Therefore, the distance to access routes was considered another important spatial predictor, with the shortest distances deemed critical, as these are the areas where encounters between dogs and people are most likely to occur. The most important control variable was derived from the own vector data representing the location of the sheepfolds - distance to sheepfolds. Based on the specificities of the pastoral system, the sheepfold was considered to act as a gravitational center, governing the entire sheepfold's activity and influencing the daily movements of the sheep and LGD's that tend to stay in or near the fold. For example, in the previous study (Bumbak et al., 2024), it was found that during the monitoring campaign, the LGDs patrolled areas of up to 6.6 km2 (LGD 1) and 3.2 km2, respectively, suggesting radial movement with gravitational tendencies.

To obtain the 3 key control predictors, the vector layers were rasterized using a proximity function based on Euclidean distance, where each cell represents the shortest distance to the features in question.

In order to better aggregate the data, next, the raster files were trimmed to the same extent and resampled at the best resolution available from the data - 5 meters x 5 meters. While doing so, all layers were reprojected to the Stereo 70 projection system (EPSG:3844), which is used in Romania. This system was preferred for this study due to its minimal spatial distortions and metric precision.

Considering the different units each of these raster files has, a risk scale was defined, ranging from 1 (low risk of encounter) to 5 (maximum risk of encounter) for each geostatistical variable, through a set of classification rules that were applied using the reclassification by table function in QGIS (see **Table 2**).

Table 2.

Raster data reclassification rules representing explicit thresholds related to the probability of LGD occurrences

geostatistical variable	**risk categories** **1** **low risk**	**2** **low to medium risk**	**3** **medium risk**	**4** **medium to high risk**	**5** **high risk**
slope (^{0})	> 45	30 – 45	15 – 30	5 – 15	0 – 5
aspect	N	NV / NE	W	E / SE	S / SW
TRI (m)	>15	10 – 15	6 – 10	2.5 – 6	0 – 2.5
TPI (m)	< -1.5	-1.5 – -0.5	-0.5 – 0.5	0.5 – 1.5	>1.5
NDVI (-1.00 to 1.00)	<0.20	0.75 – 1.00	0.55 – 0.75	0.40 – 0.55	0.20 – 0.40
distance to sheepfolds (m)	>2000	1000 – 2000	500 – 1000	200 – 500	0 – 200
distance to streams (m)	>1000	600 – 1000	300 – 600	100 – 300	0 – 100
distance to access routes (m)	>600	300 – 600	150 – 300	50 – 150	0 – 50
CLC (classes defined by the official nomenclature)	112 – dicontinuous urban fabric	311 – broad-leaved forests 313 – mixed forests	242 – complex cultivation patterns 243 – land occupied by agriculture with areas of natural vegetation	324 transitional woodland-shrubs	231 - pastures 321 – natural grasslands
category descriptors	**avoided areas**	**rare peripheral occurrence areas**	**transition areas with temporary occurrences**	**transition areas with frequent occurrences**	**core pastoral areas with permanent occurrences**

In total, 9 raster layers (see **Fig. 3**) representing essential spatial characteristics as important predictors of the occurrence of the sheep and their proxies, the LGD's, were obtained (8 continuous raster layers and 1 categorical raster layer).

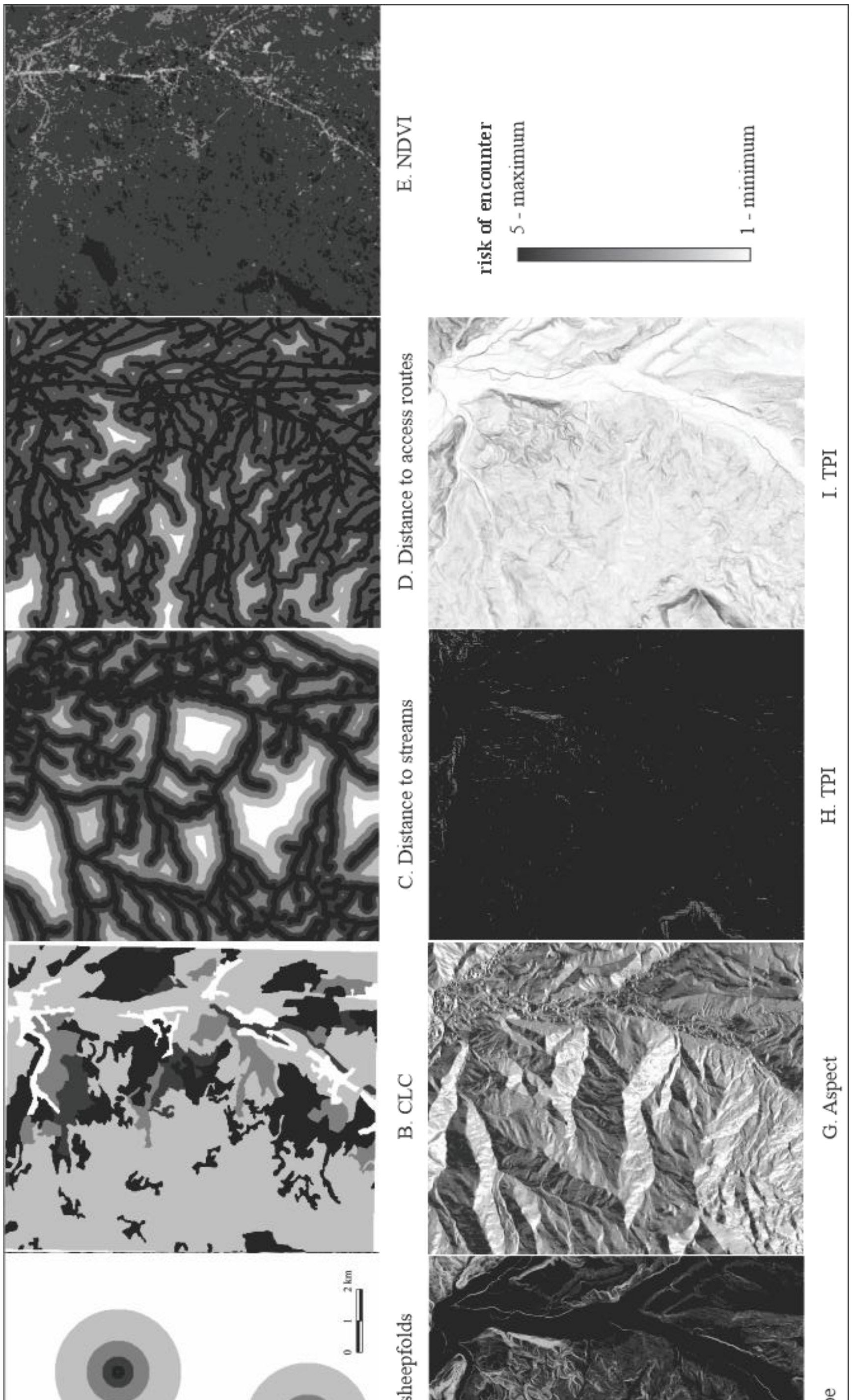

Fig. 3. Reclassified geostatistical variables representing essential spatial features for mapping the probability of encounter with sheep and LGD`s .

The five risk of occurrence categories (see **Table 2**) define explicit thresholds for each geovariable according to its own specificity, that conceptualize the spatial context of LGD occurrence probability.

For example, the 1st risk category (low risk) represents unsuitable areas with a very low theoretical probability of occurrence. This is mainly due to the topography's restrictiveness (very steep slopes, deep ravines), the northern exposure, the lack of vegetation, the presence of built areas (villages), and large distances from the three control variables.

The 2nd risk category (low to medium risk) refers to areas situated at the periphery of the usual grazing domains, where sheep or LGD occurrences can rarely be observed. This category is characterized by lower terrain, moderate to high terrain fragmentation, slope steepness and NW and NE exposure. These terrains are dominated by forestry vegetation (in the area in question, broad-leaved and mixed forests) and are situated far from the sheepfold compounds, water sources, or access routes.

In the 3rd risk category (medium risk) are areas with complex cultivation patterns, used as transition zones between grazing domains. These terrains are characterized by moderate steepness and terrain ruggedness and a predominantly western exposure, a feature exploited by the shepherds, especially in the afternoon. These terrains are situated at a moderate distance from the sheepherding infrastructure, access routes, and water sources, in a landscape dominated by mosaic agricultural lands interspersed with patches of natural vegetation.

The 4th category (medium to high risk) includes areas with gentle, low inclined upper slopes, predominantly with an eastern and south eastern exposure, favouring high chances of occurrence in the early hours of the day. These areas are situated close to the sheepfolds, water sources and access routes. The moderate NDVI values, combined with a mixed vegetation structure (forests and semi-natural areas with shrubs), make these areas highly prone to LGD occurrences, given the open transitional zones between forests and pastures.

The 5th risk category (high risk) indicates areas of very high LGD occurrence probability with favorable topographical, environmental and micro-climatic conditions for sheepfold infrastructure. These areas are found near permanent water and food sources (NDVI values of 0.20-0.40) and are characterized by terrain dominated by natural, spontaneous meadows and permanent grasslands used for grazing. Closeness to roads and trails facilitates the flock's movement during daily feeding routines.

For empirical validation purposes of the model, during November 15th of 2023 and 10th of January 2024, telemetry data were obtained from a field monitoring campaign of these livestock guardian dogs at two sheepfolds situated in proximity of one another, whose owners have agreed to participate in the study during two months in the winter period. The sheepfolds were managed at the time by two families, each possessing over 150 sheep and around 10 LGDs. At the time, we selected a young male (2 to 6 years of age) dog of Romanian traditional breeds from each sheepfold, based on several criteria discussed with the sheep owners.

This timeframe was selected following verbal negotiations and a process of trust-building. Approximately 60 days of high-intensity discrete telemetry data were gathered, with locations recorded every 30 minutes, using professional GPS trackers with GSM technology purchased from Digitanimal, a company specializing in livestock monitoring based in Spain (Navarro et al., 2021). The first findings and the subsequent methodology were detailed in another paper published shortly after that (Bumbak, et al., 2024).

The telemetry data were used to compute home ranges and identify the most frequented areas by the animals during the night (10.00 PM ‑ 05.59 AM) and the day (06.00 AM ‑ 09.59 PM). In the previous study, the Kernel Density Estimation method was applied. It helped identify clusters of LGD presence near the winter folds, as well as other clusters in areas hundreds of meters away from the main compound, in certain locations (Bumbak et al., 2024). Questions remained about why these clusters were found in some areas but absent in others. Therefore, we considered that further insights could be gained by examining the defining features of the land that influence their spatial movement.

The next methodological step involved a weighted model built using a summing expression the raster calculator function in QGIS. It arithmetically combined each essential geostatistical variable multiplied with its assigned significance factor (%) as weights to obtain a theoretical occurrence probability map (see **Figs. 2** and **4**) that represents areas where the occurrence of sheep and, invariably, dogs can be high. We then superimposed the telemetry data and applied the zonal statistics algorithm in order to extract statistics and compare the data for validation.

4. RESULTS

The weighted, quantitative analysis of these geovariables using the raster calculator function in QGIS, combined with telemetry data on LGD movement, can highlight a spatial signature of high encounter rates, substantiating the development of predictive models for proactive management of mountain trails. To do so, a significance hierarchy was established for all 9 variables considered in the study. The weights corresponding to their significance (see **Fig. 3)** reflect personal and literature-based insights into sheep and LGD ethology at sheepfolds, as well as the traditional approach to shepherding in this part of the Carpathians.

In the proposed risk probability model, the control variables were ranked as most significant, totalizing 55%, while the environmental (30%) and topographical factors (15%) amounted for 45%. The distance to sheepfolds was considered the most important predictive variable with the highest significance (25%). The high percentage value reflects the importance of the geovariable acting as a true gravitational center and spatial anchor, reflecting the animals' immediate territorial reality.

The other two control variables distance to streams (15%) and distance to access routes (15%) were considered as defining variables representative of the dynamics of movement. Watering is as important as feeding, and it is assumed that the chances of encounter increase as the sheep and the dogs approach a water source. The distance to access routes is a multifunctional variable, as it defines the least-cost movement corridors for both categories of landscape users.

The environmental geovariables represented by the CLC (20%) and NDVI data (10%) – totalizing 30%, were considered defining variables representing habitat, land-use structure, and food resource. The difference in proportions is explained by the field monitoring campaign occurring during winter, when NDVI is less representative of the field conditions.

Of the proposed topographical geovariables for this model, the slope (5%) and aspect (5%) were considered conditional variables, while TRI (2.5%) and TPI (2.5%) were considered nuance variables influencing movement choices in a least-cost, energy-saving movement scenario.

Overall, the obtained risk probability map (see **Fig. 4**) emphasizes a strong interdependence between topography and the resource's location and availability.

It confirms that topographical variables predict movement, either restricting or facilitating it. The environmental variables included in this study serve as indicators of food availability for the sheep, highlighting areas of high occurrence. The high density of observation points near the control variables indicates that they act as anchors, limiting the dogs' movement in their vicinity.

In our preliminary analysis, the data were split into time intervals, with the focus mainly on the daytime interval (06.00 AM – 22.59 PM), as this time frame is typically associated with recreational outdoor activities.

For validation purposes, we used this data set to obtain relevant results. The validation process assumed the overlay of over 1200 (N=1239) daytime observations covering 60 days from both LGDs. Firstly, over 78% of the total number of daytime observations (939 observation points) were recorded in areas categorized as at least 3.5 on the probability risk scale. Thus, this skew towards high values provides statistical validation of the theoretical risk model's high fidelity. The 3.9 to 4.2 median, corroborated by a 0.35 to 0.37 standard deviation, indicates that the observed LGD locations are strongly associated with the medium (category 3) and high-occurrence areas (categories 4 to 5) identified in the occurrence probability model. Another important aspect substantiating the model is the minimum value of 2.6, indicating that the dogs avoided almost completely the areas identified in the model as low (category 1) and low to medium risk (category 2).

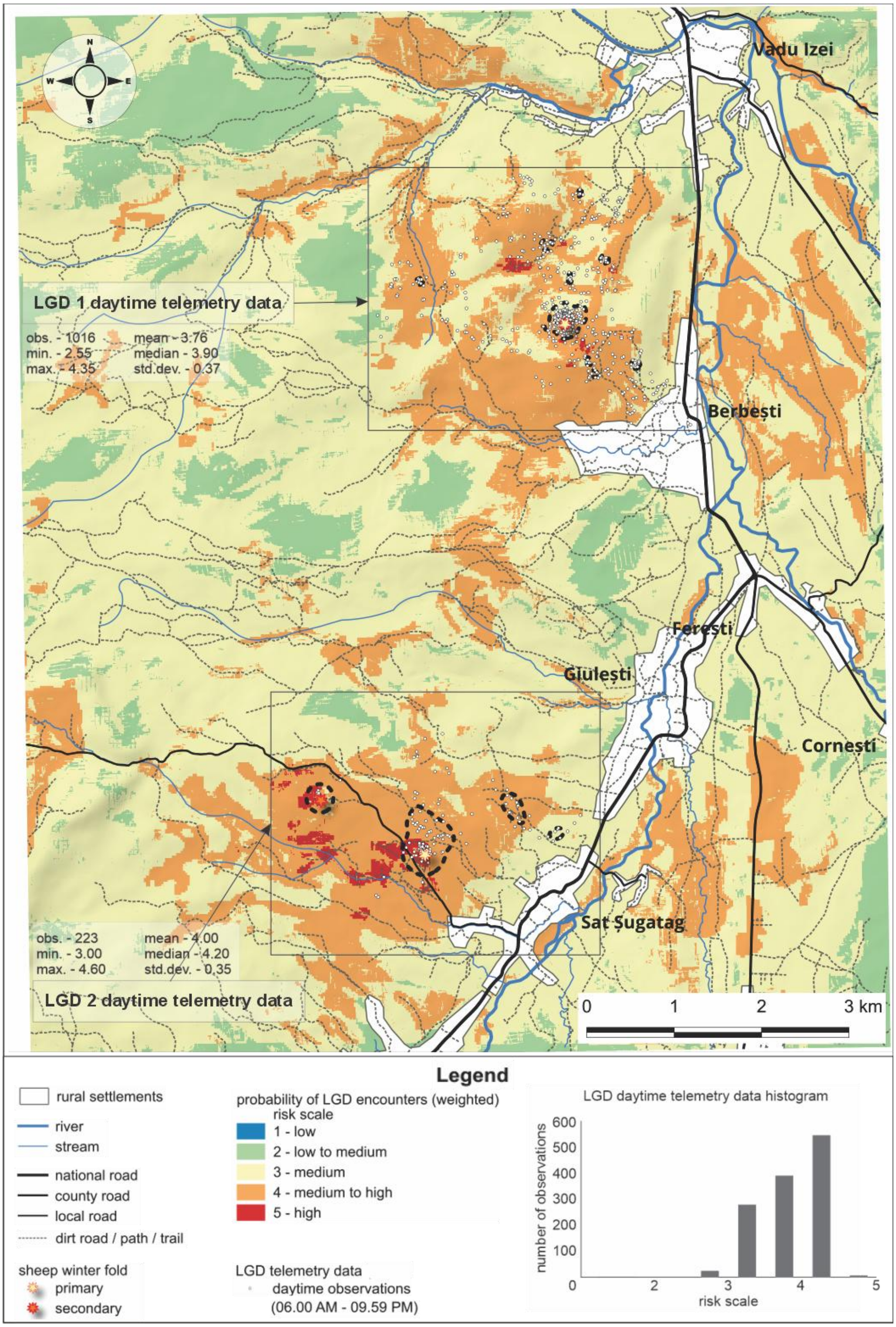

Fig. 4. Weighted theoretical occurrence probability map (9 weighted resampled geovariables) with overlay LGD daytime telemetry data used for validation purposes (spatial data sources: OSM data and field-collected telemetry data).

It also validated the criteria used to build rule-based risk categories (1 - minimum to 5 - maximum) by highlighting the avoidance of topographical areas with high slopes, dense wooded vegetation, or long distances relative to interest points/areas (sheepfold locations, water availability, and accessibility).

The study demonstrates that, even if the dog's movement is acknowledged as induced by the shepherd's decisions (which are not parametrized or otherwise accounted for in this study), it can still be considered highly predictable. This statement is also supported by the geostatistical variables selected and their overall significance in the model design, despite the telemetry data covering a winter interval, which is more representative of low-season outdoor activity.

To further support this, we tested our findings against a null model assuming LGD occurrences are randomly distributed and against our own model assuming they are not (see **Table 3**). For this purpose, the data analysis capabilities from M.Excel were used. A vector layer of randomly distributed points was generated to simulate the real daytime observations (N=1239). To parametrize and obtain an accurate estimate of the mean distance between the random points, the mean distance for the real observational points (171.5 m) was first calculated. This random points layer was sampled against the raster layer representing the theoretical occurrence probability map. Using the t.Test function, we ran a comparison to obtain a p-value < 0.001, as shown below.

Table 3.
Null hypothesis testing using the *t* Test: two-sample assuming unequal variances function (M.Excel).

parameters	LGD (1 and 2) real obs. points	random obs. points
mean	3.799416666	3.079691411
variance	0.145256123	0.149505836
observations	1239	1239
hypothesized Mean Difference	0	
df	2396	
t Stat	45.9123803	
P(T<=t) one-tail	0.000	
t Critical one-tail	1.645489838	
P(T<=t) two-tail	**0.000**	
t Critical two-tail	1.960954573	

The results confirm that the proposed model instead follows an intentional pattern of preferred spaces. The model is statistically significant, and LGD spatial occurrences do not exhibit wandering behavior.

4.1. Limitations

Although the results are encouraging, the study encountered several limitations. Given that the monitoring campaign took place in winter, outside the main pastoral season, questions can be raised about the validity of the winter spatial movement pattern relative to the summer pattern and its implications for the tourist dynamic in those areas, as summer is the prime outdoor season. This fact influenced the predictive power of another important variable ‑ the NDVI, which was computed using autumn satellite imagery. Our findings validate low-season spatial movement characteristics.

Secondly, the field campaign produced 60 days of high-intensity spatial data, which is insufficient to substantiate a robust predictive risk probability model. The short timeframe, while valuable for an exploratory study such as this, limits the model's ability to infer long-term LGD patterns by failing to capture essential details and shifts that occur over a full year or at least a full pastoral season. Future field campaigns should focus on obtaining spatial data over a wider time interval.

Thirdly, in the campaign, only two large guardian dogs from two sheepfolds were involved. Again, pertinent questions can be raised regarding the robustness of the output model. In the future, field campaigns should involve a larger number of LGDs from sheepfolds situated farther apart in Carpathian settings with nuanced physical, environmental, and logistical characteristics. Also, future approaches will focus on treating control variables as hierarchical spatial structures to avoid spatial simplification of key movement predictors.

5. CONCLUSIONS

The study tested the hypothesis that the spatial distribution of LGDs, proxies for sheep, is not random but is governed by landscape features with predictive power. Using an integrated spatial approach, the landscape of the area of interest was defined by 9 geostatistical variables, each with a certain degree of significance. All variables, once defined and cartographically represented, were reclassified as categorical data using a 1-5 rules-based occurrence risk scale. The reclassified layers were used to build a weighted theoretical probability risk map that highlights areas with a high occurrence of LGD. Using telemetry data for validation, the analysis shows that over 78% of daytime LGD activity was concentrated in areas with medium to high (over 3.5) risk probability. The model demonstrates high fidelity and can serve as a starting point for a methodological discussion in the predictive mapping of the vulnerability of trails used by recreationists. Even if the dog's movement is acknowledged as being induced by the shepherd's decisions, it can be considered as having a high degree of predictability, and, using key geostatistical variables, it can highlight a movement pattern with preferred and avoided spaces. These models and their associated cartographic outputs represent valuable spatial management tools that can support decision-making. The models can be used in the process of designing trails, spatial planning tools for mountain activities, information advisories, and complementary signaling infrastructure. They can also be used for trail management and safety in mountain areas (trail routing and rerouting options), for maps highlighting trail vulnerability to LGD occurrences, or integration of results into dedicated trail apps, at least in mountain areas with similar spatial, environmental, and logistical features to the area in question in this study.

REFERENCES

Avgar, T., Mosser, A., Brown, G. S. & Fryxell, J. M. (2013) Environmental and individual drivers of animal movement patterns across a wide geographical gradient. *Journal of Animal Ecology,* 82(1), pp. 96-106. Available from: https://doi.org/10.1111/j.1365-2656.2012.02035.x.

Avgar, T., Potts, J. R., Lewis, M. A. & Boyce, M. S. (2016) Integrated step selection analysis: bridging the gap between resource selection and animal movement. *Methods in Ecology and Evolution,* 7(5), pp. 619-630. Available from: https://doi.org/10.1111/2041-210X.12528.

Bailly, N., Lecuyer, L., Ba, M. & Perrin-Malterre, C. (2026) Understanding encounters between recreationists and livestock guardian dogs as a basis for conflict management. *Journal of Outdoor Recreation and Tourism,* Volume 54. Available from: https://doi.org/10.1016/j.jort.2026.101043.

Bailly, N., Perrin-Malterre, C. & Chanteloup, L. (2025) Tourists and livestock in mountain areas. A cycle of attraction, avoidance and mediation. *OpenEdition Journals,* Issue 28. Available from: https://doi.org/10.4000/160oc.

Bumbak, S. V., Ilieș, M., Hotea , M. & Hassan, T. H. (2024) Analysis of movement data from GPS-monitored livestock guardian dogs (LGDs) at two sheepfolds in the north-western Maramures Land, Romania using the Kernel Density Estimation method. Implications for outdoor tourism. *Geojournal of Tourism and Geosites,* 54(2spl), pp. 811-820. Available from: https://doi.org/10.30892/gtg.542spl05-1256.

Dănilă, G., Cătănoiu, S., Roșca, S. & Coșofreț, C. (2024) GIS analysis of the spatial distribution of European bison (Bison bonasus L.) in Vânători Neamț Natural Park, Romania, between 2014 and 2019. *Geographia Technica,* 19(1), pp. 135-150. Available from: https://doi.org/10.21163/GT_2024.191.10.

Edelhoff, H., Singer, J. & Balkenhol, N. (2016) Path segmentation for beginners: an overview of current methods for detecting changes in animal movement patterns. *Movement Ecology,* 4(21). Available from: https://doi.org/10.1186/s40462-016-0086-5.

Earth Resources Observation and Science (EROS) Center. (2020) Landsat 8-9 Operational Land Imager / Thermal Infrared Sensor Level-2, Collection 2 [dataset]. U.S. Geological Survey. Available from: https://doi.org/10.5066/P9OGBGM6 [Accessed: March 2026].

Esri. (2026) World Imagery Basemap [digital map]. Retrieved using HCMGIS plugin in QGIS. Available from: https://server.arcgisonline.com/arcgis/rest/services/World_Imagery/MapServer/tile/{z}/{y}/{x} [Accessed: March 2026].

European Environment Agency (EEA). (2020) CORINE Land Cover 2018 (vector), Europe, 6-yearly - version 2020_20u1. Available from: https://doi.org/10.2909/71c95a07-e296-44fc-b22b-415f42acfdf0 [Accessed: March 2026].

Fieberg, J., Singer, J., Smith, B. & Avgar, T. (2021) A 'How to' guide for interpreting parameters in habitat-selection analyses. *Journal of Animal Ecology,* 90(5), pp. 1027-1043. Available from: https://doi.org/10.1111/1365-2656.13441.

Forester, J. D., Kyung Im, H. & Rathouz, P. J. (2009) Accounting for animal movement in estimation of resource selection functions: sampling and data analysis. *Ecology,* 90(12), pp. 3554-3565. Available from: https://doi.org/10.1890/08-0874.1.

Gaynor, K. M., Middleton, A. D., Power, M. E. & Brashares, J. S. (2019) Landscapes of Fear: Spatial patterns of risk perception and response. *Trends in Ecology&Evolution,* Issue 34, pp. 355-368. Available from: https://doi.org/10.1016/j.tree.2019.01.004.

Gehring, T. M., VerCauteren, K. C. & Landry, J.M. (2010) Livestock Protection Dogs in the 21st Century: Is an Ancient Tool Relevant to Modern Conservation Challenges?. *Bioscience,* 60(4), pp. 299-308. Available from: https://digitalcommons.unl.edu/icwdm_usdanwrc/919.

Gerber, B. D. et al. (2019) Extreme site fidelity as an optimal strategy in an unpredictable and homogeneous environment. *Functional Ecology,* 33(9), pp. 1695-1707. Available from: https://doi.org/10.1111/1365-2435.13390.

Ilieș, A. & Grama, V. (2010) The external Western Balkan border of the European Union: premises for building functional transborder systems. *Annales, Ser Historia & Sociologia,* 20(2), pp. 457-468. Available from: https://doi.org/10.3390/rs15245763.

Ivașcu, C. M. & Biro, A. (2020) Coexistence through the Ages: the Role of Native Livestock Guardian Dogs and Traditional Ecological Knowledge as Key Resources in Conflict Mitigation between Pastoralists and Large Carnivores in the Romanian Carpathians. *Journal of Ethnobiology,* 40(4), pp. 465-482. Available from: https://doi.org/10.2993/0278-0771-40.4.465.

Jacobson, O. T., Barrett, B.J., Perry, S.E., Finerty, G.E., Tiedeman, K.M., Crofoot, M.C. (2024) A new approach to geostatistical synthesis of historical records reveals capuchin spatial responses to climate and demographic change. *Ecology Letters,* 27(5). Available from: https://doi.org/10.1111/ele.14443.

Khayli, M., Lhor, Y., Bengoumi, M., Zro, K., El Harrak, M., Bakkouri, A., Akrim, M., Yaagoubi, R., El Berbri, I., Kichou, F., Berrada, J., Bouslikkhane, M. (2021) Using geostatistics to better understand the epidemiology of animal rabies in Morocco: what is the contribution of the predictive value?. *Helyion,* 7(1). Available from: https://doi.org/10.1016/j.heliyon.2021.e06019.

Kottek, M., Grieser, J., Beck, C., Eudolf, B., Rubel, F. (2006) World Map of the Köppen-Geiger climate classification updated. *Meteorol. Z.,* Volume 15, pp. 259-263. Available from: https://doi.org/10.1127/0941-2948/2006/0130.

Laffan, S. W., Skidmore, A. K. & Franklin, J. (2012) Geospatial analysis of species, biodiversity and landscapes: Introduction to the second special issue on spatial ecology. *International Journal of Geographical Information Science,* 26(11), pp. 2003-2007. Available from: https://doi.org/10.1080/13658816.2012.721557.

Landry, J. M. & Drouilly, M. (2020) Interactions between livestock guarding dogs and wolves in the southern French Alps. *Journal of Vertebrate Biology,* Volume 69(3), pp. 20078.1-18. Available from: https://doi.org/10.25225/jvb.20078.

Lauret, V., Courbin, N. & Besnard, A. (2025) Integrating individual tracking data and spatial surveys to improve estimation of animal spatial distribution. *Ecosphere,* 16(5). Available from: https://doi.org/10.1002/ecs2.70283.

Lempidakis, E., Wilson, R. P., Luckman, A. & Metcalfe, R. S. (2018) What can knowledge of the energy landscape tell us about animal movement trajectories and space use? A case study with humans. *Journal of Theoretical Biology,* 457(14), pp. 101-111. Available from: https://doi.org/10.1016/j.jtbi.2018.08.024.

Microsoft. (2026) Bing Virtual Earth Basemap [digital map]. Retrieved using HCMGIS plugin in QGIS. Available from: https://ecn.t3.tiles.virtualearth.net/tiles/a{q}.jpeg?g=1 [Accessed: March 2026].

Military Topographic Directorate (1980) [Military Topographic Map of Romania]. Scale 1:25,000. Stereographic 1970 Projection. Sheets L-34-012-B-c; L-34-012-B-d; L-34-012-D-b; L-34-012-D-a. Bucharest: Military Topographic Directorate.

Mosley, J. C., Roeder, B.L., Frost, R.A., Wells, S.L., McNew, L.B., Clark, P.E. (2020) Mitigating Human Conflicts with Livestock Guardian Dogs in Extensive Sheep Grazing Systems. *Rangeland Ecology & Management,* 73(5), pp. 724-732. Available from: https://doi.org/10.1016/j.rama.2020.04.009.

Navarro, J., Martín de Diego, I., Carballo Pérez, P. & Ortega, F. (2021) Outlier detection in animal multivariate trajectories. *Computers and Electronics in Agriculture,* Volume 190. Available from: https://doi.org/10.1016/j.compag.2021.106401.

National Agency for Cadastre and Land Registration (ANCPI). (2026) Download MNT tiles application. [Dataset] Available from: https://geoportal.ancpi.ro/portal/apps/webappviewer/index.html?id=50289a41a afc4e01a efd131c2105e374 [Accessed: March 2026].

OpenStreetMap contributors. (2026) OpenStreetMap data extract for western Maramureș [Data file]. Extracted using QGIS. Available from: www.openstreetmap.org. [Accessed: April 2026].

Panzacchi, M., van Moorter, B., Strand, O., Saerens, M., Kivimäki, I., St.Clair, C.C., Herfindal, I., Boitani, L. (2016). Predicting the continuum between corridors and barriers to animal movements using Step Selection Functions and Randomized Shortest Paths. *Journal of Animal Ecology,* 85(1), pp. 32-42. Available from: https://doi.org/10.1111/1365-2656.12386.

Preisler, H. K., Ager, A. A. & Wisdom, M. J. (2013) Analyzing animal movement patterns using potential functions. *Ecosphere,* 4(3), pp. 1-13. Available from: https://doi.org/10.1890/ES12-00286.1.

QGIS Development Team. (2026). QGIS Geographic Information System (version 3.44.8). QGIS Association. Available from: https://www.qgis.org [Accessed: March 2026].

Rew, J., Park, S., Cho, Y., Jung, S., Hwang, W. (2019) Animal Movement Prediction Based on Predictive Recurrent Neural Network. *Sensors,* 19(20). Available from: https://doi.org/10.3390/s19204411.

Rigg, R. (2001) *Livestock guarding dogs: their current use world wide.* Oxford: IUCN/SSC Canid Specialist Group Occasional Paper. Available from: http://www.canids.org/occasionalpapers/.

Seidel, D. P., Dougherty, E., Carlson, C. & Getz, W. M. (2018) Ecological metrics and methods for GPS movement data. *International Journal of Geografical Information Science,* 32(1), pp. 2272-2293. Available from: https://doi.org/10.1080/13658816.2018.1498097.

Smith, B. R., Yarnell, R.W., Whitehouse-Tedd,K., Marginean, M., Popa, R., Trewby, I., Faur, M., Uzal, A. (2026) So close yet so far: Movement patterns of livestock guarding dogs in a shared landscape in Romania. *Ecological Solutions and Evidence,* 7(2). Available from: https://doi.org/10.5441/001/1.739.

Spencer, K., Sambrook, M., Bremner-Harrison, S., Cilliers, D., Yarnell, R.W., Brummer, R., Whitehouse-Tedd, K. (2020) Livestock guarding dogs enable human-carnivore coexistence: First evidence of equivalent carnivore occupancy on guarded and unguarded farms. *Biological Conservation,* Volume 241. Available from: https://doi.org/10.1016/j.biocon.2019.108256.

Tășuleasa Social. (2026) *Via Transilvanica - Traveller Guide* [Online]. Available from: https://www.viatransilvanica.com/en/vt-guide/ [Accessed: April 2026].

Thurfjell, H., Ciuti, S. & Boyce, M. S. (2014) Applications of step-selection functions in ecology and conservation. *Movement Ecology,* 2(4). Available from: https://doi.org/10.1186/2051-3933-2-4.

Tuan, Y.-F. (2013) *Landscapes of Fear* [Online]. University of Minnesota Press. Available from: https://www.scribd.com/document/960679466/TUAN-Yi-Fu-Landscapes-of-Fear [Accessed: April 2026].

Valderrama-Zafra, J. M., Rubio-Paramio, M.A., Garcia-Molina, D.F., Mercado-Colmenero, J.M., Oya, A., Carrasco, R., Azorit, C. (2024) Impact of topographic factors on animal field pathings: Analysis and prediction of deer movement patterns. *Ecological Informatics,* Volume 80. Available from: https://doi.org/10.1016/j.ecoinf.2024.102487.

van Bommel, L. & Johnson, C. N. (2024) Still a good dog! Long-term use and effectiveness of livestock guardian dogs to protect livestock from predators in Australia's extensive grazing systems. *Wildlife Research,* 51(1). Available from: https://doi.org/10.1071/WR23008.

van Bommel, L., Magrath, M., Coulson, G. & Johnson, C. N. (2023) Livestock guardian dogs establish a landscape of fear for wild predators: Implications for the role of guardian dogs in reducing human–wildlife conflict and supporting biodiversity conservation. *Ecological Solutions Evidence,* 5(1). Available from: https://doi.org/10.1002/2688-8319.12299.

Vercauteren, K. C., Gehring, T. M. & Landry, J. M. (2011) The dynamic role of livestock protection dogs in a changing world. *Journal of Veterinary Behavior: Clinical Applications and Research,* 6(1), p. 73. Available from: DOI:10.1016/j.jveb.2010.09.026.

Winter, V. A., Smith, B.J., Berger, D.J., Hart, R., Huang, J., Manlove, K., Buderman, F.E., Avgar, T. (2024) Forecasting animal distribution through individual habitat selection: Insights for population inference and transferable predictions. *Ecography, 2024(11), p. e07225.* Available from: https://doi.org/10.1111/ecog.07225.

Geographia Technica, Vol. 21, Issue 3, 2026, pp 167 to 181

GEOHAZARD MAPPING WITH MICROTREMOR WAVES USING THE HVSR METHOD. CASE STUDY: SOUTHERN SEMARANG AREA, CENTRAL JAVA, INDONESIA

***M. Irham NURWIDYANTO* [1*], *Gatot YULIYANTO* [1] *& Gregorius Alvin FERNANDO* [1]**

DOI: 10.21163/GT_2026.213.11

ABSTRACT

Semarang City is located in an area influenced by several active fault systems in Central Java, Indonesia. Semarang City has a historical record of being an area with relatively low seismic activity. Geological investigations and several recent sources of information indicate the presence of active faults around the city, thus increasing the potential for seismic hazards. This study aims to describe the potential seismic hazards in the southern part of Semarang using microtremor measurements analyzed through the Horizontal-to-Vertical Spectral Ratio (HVSR) method. Data collected in this study were 119 microtremor measurement stations placed to determine several location response parameters. The parameters used for analysis include the dominant frequency (f_0), amplification factor (A_0), seismic vulnerability index (SVI), Peak Ground Acceleration (PGA), and Ground Shear Strain (GSS). The results show that the dominant frequency value is influenced by the thickness of the sediment in a particular area. The South Semarang area has a dominant frequency value ranging from 0.13 to 9.21 Hz, with an average of 1.17 Hz at 119 microtremor stations. The amplification factor (A_0) values in the South Semarang region ranged from 0.53 to 6.94, with an average of 2.77. The seismic vulnerability index is used in seismic microzoning studies to map areas most at risk of structural damage due to geological conditions. The seismic vulnerability index in the South Semarang region ranged from 0.17 to 260.09 $\mu cm^2/s$, with an average of 32.29 $\mu cm^2/s$. Another calculation parameter used in this study was the PSDA (Deterministic Seismic Hazard Analysis) method, with PGA values in the South Semarang region ranging from 5.87 to 49.17 gal, with an average of 13.85 gal. The ground shear strain value affects post-earthquake conditions. The GSS value in the South Semarang region ranged from $1.3x10^{-5}$ to $3.59x10^{-4}$, with an average of $1.3x10^{-4}$. Spatial analysis shows that several sub-districts, particularly Tembalang, Banyumanik, and Pedurungan, have higher earthquake vulnerability than surrounding areas. Furthermore, more in-depth technical studies are needed in the geotechnical field in several locations with high seismic hazards (contained in the A_0, f_0, PGA, SVI, and GSS maps), and locations around faults in the Semarang area.

Keywords: *A_0; F_0; SVI; PGA; GSS; Microtremor; Seismic.*

1. INTRODUCTION

The geological conditions of Semarang City are situated at the intersection of alluvial plains (coastal) and volcanic hills, which are equipped with significant seismic potential due to the presence of active fault structures that cover Semarang City (Thanden et al., 1996). The comparison between the North Java and South Java faults lies in their activity, where the faults in North Java (including the Semarang City area) have a relatively low seismic activity. Based on historical records and geological studies, Semarang City is surrounded by significant active earthquake sources (Partono et al., 2018). Additionally, according to Newcomb and McCann (1987), the Central Java region has experienced several destructive earthquakes since the 19th century.

[1] *Department of Physics, Faculty of Science and Mathematics, Diponegoro University, Semarang, Indonesia. Corresponding author: irhammn@lecturer.undip.ac.id (MIN); gatoty@fisika.fsm.undip.ac.id (GY); gregoriusalvinfernando@gmail.com (GAF).*

Historical records show that there was an earthquake in 1867, which was thought to originate from a land fault (possibly from the Semarang fault or the Kaligarang fault), which caused severe damage to colonial buildings in Semarang and its surroundings, and caused many casualties. Other disasters that occurred in this city were local landslides and vibrations from the subduction zone (megathrust) in southern Java.

The presence of faults significantly increases the potential for earthquakes in the surrounding area because they act as weak zones in the Earth's crust and serve as reservoirs of tectonic energy (Scholz, 2019). As the Earth's plates continue to move, rocks along the fault planes interlock and rub against each other, causing mechanical stress to build up over time. This sudden, massive release of energy, which propagates to the surface in the form of seismic waves, can trigger earthquakes (Shearer, 2009). Because the rock structure in fault zones is fragile and has undergone deformation, this makes the area vulnerable to seismic activity. The presence of local faults that divide or are located near the Semarang area (Koesuma et al., 2022) increases the regional seismic risk, where even the slightest shift in a subsurface rock segment can trigger a shallow earthquake, the destructive power of which tends to be higher at the surface. This risk is exacerbated by the geological conditions of Semarang's environment, particularly in the northern part of Semarang and the lowlands, which are dominated by thick, incompletely compacted layers of alluvium or Quaternary sediment (Thanden et al., 1996). When seismic waves from the fault propagate through this soft soil layer, an amplification phenomenon occurs, where the amplitude of the earthquake waves actually increases, thereby amplifying the shaking felt at the surface.

Geotechnically, the presence of the Semarang Fault creates a shear zone that destabilizes the surrounding rock. This contributes to the high frequency of landslides in hilly areas such as Gombel and Candi. Furthermore, this fault activity also interacts with the land subsidence phenomenon in North Semarang (Marfai & King, 2007); although land subsidence is dominated by loading and groundwater extraction, the structural control of the Semarang Fault is believed to also influence the pattern of bedrock subsidence beneath the alluvium layer (Abidin et al., 2013).

Based on this, a method capable of explaining seismicity in Semarang is needed. The HVSR method, using microtremors, is one such geophysical method capable of explaining seismicity (Nurwidyanto et al., 2024; Simanjuntak et al., 2017). Microtremors are very subtle harmonic ground vibrations that occur continuously on the Earth's surface, while HVSR is a technique for analyzing microtremor data to obtain the physical characteristics of the soil. The parameters used in the HVSR method include dominant frequency, amplification factor, Seismic Vulnerability Index (Sasongko et al., 2019), Peak Ground Acceleration (Nurwidyanto et al., 2023), and Ground Shear Strain (Nurwidyanto & Yuliyanto, 2024). These parameters will be a reference for potential building damage and ground deformation during an earthquake in the city of Semarang. Although Semarang is one of the cities with a high seismic risk due to the presence of faults in Semarang, there is no comprehensive microzonation map that covers the entire administrative area of the city with a high density of observation points. Research for the South Semarang area is still very minimal, in addition, the characteristics of the sedimentary layer in the transition area to the hills have not been identified in detail. This research is expected to explain and understand the potential geohazards in the South Semarang area.

2. STUDY AREA

This research was conducted in the southern region of Semarang City, Central Java, Indonesia which is geographically located at 7°0'1.47"S & 110°23'20.59"E to 7°3'15.45"S & 110°28'47.93"E. **Fig.1** shows the location of the microtremor station area and the presence of faults in Semarang. Thanden (1996) revealed that in Semarang there are several faults located around the research area, namely the Kendang-Baribis fault, the Kaligarang fault, and the Semarang fault. There are 8 earthquakes that have occurred around the research area over the past 50 years. The magnitude of the earthquake has a range of 3.7 - 4.8 mb. The largest earthquake occurred in 1986 located in the western side of the Semarang area. This picture explains the potential seismic hazards that will always be faced by the community in this area.

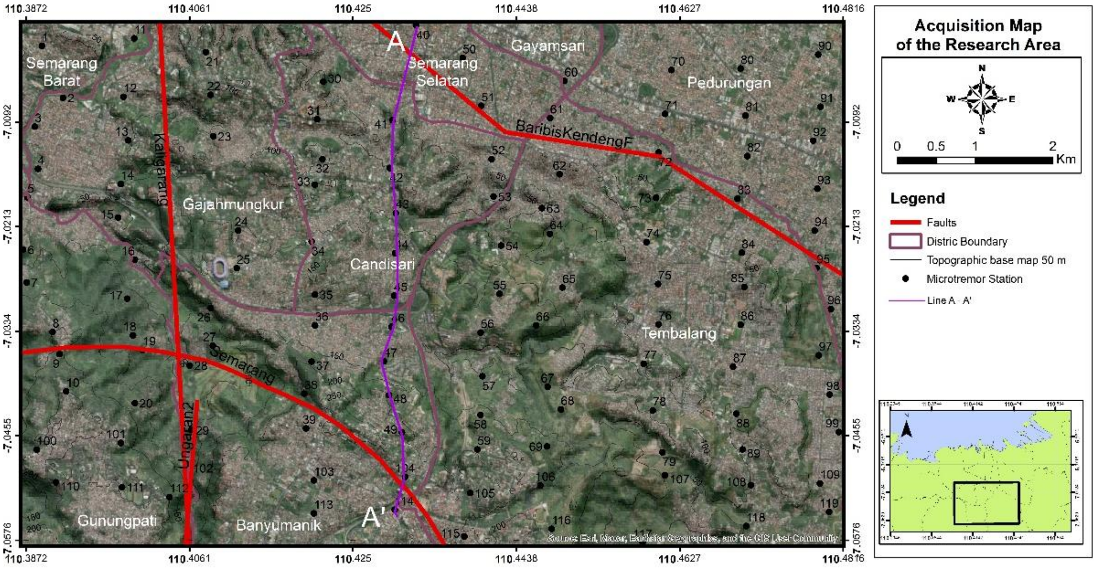

Fig. 1. Map of research location and faults.

Based on the latest data from the BRIN geological expedition (2025), several active fault zones pose a real threat. The Semarang Fault stretches approximately 34 km from north to south. Its characteristics are reverse faults with a potential maximum magnitude of 6.5 to 6.9 Mw (Partono et al., 2020). Traces of these faults are visible in several central points of the city, such as around the Giri Tunggal Heroes' Cemetery (TMP) area, where a fault scarp several meters high was found. The Kaligarang Fault has a path that runs parallel to the flow of the Kaligarang river (Hidayat, 2013). This fault has been active since the Tertiary period and showed reactivity during the Quaternary period as a sinistral strike-slip fault. Poedjoprajitno et al. (2018) noted that the steep morphology around the Kaligarang River, combined with this active fault structure, often triggers slope instability, especially during high rainfall. The National Center for Earthquake Studies (PusGen, 2017) recognized the Kaligarang Fault as part of a fault framework with the potential to produce critical magnitude earthquakes (up to 6.5). The Semarang Fault is part of a larger structure, the Kendeng Fault Zone, which amplifies from West Java to East Java. The section around Semarang-Demak appears clear land elevate.

3. DATA AND METHODS

3.1. Geology of the Research Area

The geological conditions of the research area in Semarang City consist of Alluvial Deposits (Qa), Damar Formation, Kalibeng Formation, Kaligetas Formation, and Kerek Formation. According to Thanden et al. (1996), this alluvial lithology consists of loose sedimentary material in the form of clay, mud, sand, and gravel with varying thicknesses, even reaching more than 50 meters near the coastline (**Fig. 2**). Alluvial deposits contribute to the high rate of land subsidence in North Semarang, due to the vulnerability of the soil to consolidation due to building loads and excessive groundwater extraction (Abidin et al., 2013). The Damar Formation was formed during the Pleistocene and is of volcanic origin. Its lithology is very diverse, consisting of tuff sandstone, conglomerate, and volcanic breccia that have undergone significant consolidation. Van Bemmelen (1949). The existence of the Damar Formation has a significant impact on the hydrogeology of Semarang City because its sandstone layer functions as a productive aquifer (air-bearing layer). Although in some locations, the slope conditions of this formation are susceptible to landslides. The Kalibeng Formation formed during the Pliocene and is altered by a lithology consisting of marl, tuff sandstone, and limestone intercalations rich in foraminifera fossils (Thanden et al., 1996). The rocks in this formation tend to undergo rapid weathering and exhibit high swelling and shrinkage, often acting as shear surfaces that cause landslides in several hilly areas of Semarang.

The Kaligetas Formation is a volcanic rock unit formed during the Pleistocene. According to Thanden et al. (1996), this lithology consists of volcanic breccia, lava, tuff, tuff sandstone, and mudstone. The material in this formation is largely derived from the ancient volcanic activity of Mount Ungaran, which subsequently underwent remodeling (Van Bemmelen, 1949). Weathering of this formation produces thick clay residues on steep slopes, often posing a risk of landslides (Sitorus et al., 2017). The Kerek Formation was formed during the Middle to Late Miocene, reflecting an open marine depositional environment (upper bathyal zone). The lithology of this formation is characterized by a very distinctive alternation of mudstone, marl, tuffaceous sandstone, and sandy limestone (Thanden et al., 1996). Van Bemmelen (1949) suggested that the Kerek Formation is part of a thick sedimentary sequence in the North Java geosyncline that experienced strong tectonic deformation, so that its layers are often found in a sharply inclined or folded position.

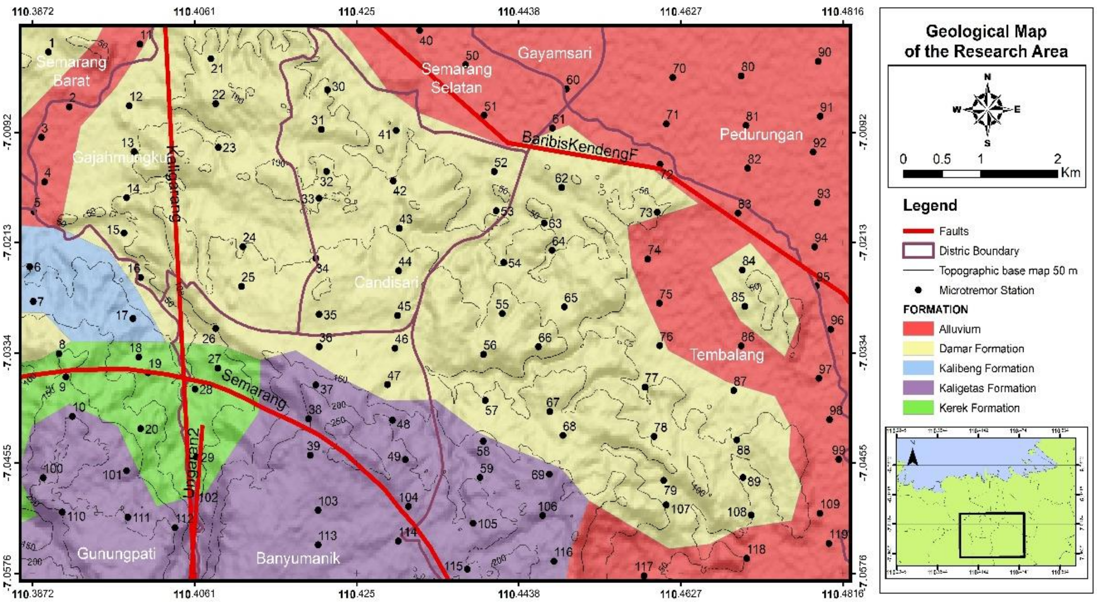

Fig. 2. Geological map of the southern area of Semarang.

3.2. HVSR and Microtremor

Microtremors are exceptionally small natural harmonic vibrations of the ground (micron amplitude) that begin from natural activities such as sea waves and wind, as well as human exercises such as activity and mechanical apparatus. Soil characteristics can be determined by comparing the horizontal and vertical wave spectra of microtremor recordings, commonly known as the Horizontal-to-Vertical Spectral Ratio (HVSR) (Nakamura, 1989). This method is very effective for determining the resonance frequency and intensification factor of an area.

Based on the application, the HVSR method works on the assumption that the vertical component of the microtremor is not essentially amplified when passing through the sedimentary layer, whereas the horizontal component is intensified due to the impedance difference between the soft soil layer and the bedrock. Konno & Ohmachi (1998) emphasize that this spectral ratio can give an outline of the sedimentary layer thickness and the seismic vulnerability of a region. In areas such as Semarang, the use of this method is crucial for mapping the distribution of alluvial layers and identifying zones at risk of severe damage during earthquakes due to local soil amplification effects (SESAME, 2004).

3.2.1. A_0 and f_0

The frequency that frequently occurs in the research area is the dominant frequency and is considered the natural frequency of the rocks in that area. An area experiencing an earthquake or vibration with a frequency similar to the natural frequency will experience resonance, resulting in amplification of seismic waves in that area (Cakici et al., 2021). Buildings with a low dominant structural frequency are therefore susceptible to long-period vibrations and can potentially cause damage due to resonance if the building is constructed in an area with a low dominant frequency (Ilgac et al., 2026). When planning earthquake-resistant building structures, it is necessary to understand the distribution of frequency values in an area to reduce the risk of building damage due to earthquake vibrations (Widodo, 2012). The classification of f_0 values can be found in **Table 1** using the classification of Kanai (1983).

Table 1.

Frequency value classification (Kanai, 1983).

No	Soil Classification Types	Natural Frequency	Description
1	Type 4	< 2.5	The thickness of the surface sediment is very thick
2	Type 3	2.5 – 4	Surface sediment thickness is approximately 10 to 30 m
3	Type 2	4 – 10	Medium surface sediment, thickness around 5 to 10 m
4	Type 1	6.667 - 20	Surface sediments that have a very thin depth

Amplification is the contrast of wave propagation parameters (density and velocity) between the bedrock and the sediment in the overlying layer. Seismic waves will experience amplification if they propagate from a harder medium to a softer medium. This amplification value is closely related to the comparison of the impedance contrast of the rock layers, when the impedance contrast of the two layers is high, the amplification value will also be higher, and vice versa (Nakamura, 2000). The amplification factor explains the change or amplification of the acceleration of ground motion from bedrock to the surface of the soil caused by the difference in shear wave movement speed (v_s) in the bedrock and the soil layer (sediment). The amplification of the acceleration of ground motion on the surface is indicated by the increasing amplification value (Partono et al., 2013). The amplification value can be written as a function of the comparison of the contrast values with the equation (Arifin et al., 2014):

$$A_o = \frac{\rho_b\, v_b}{\rho_a\, v_a} \tag{1}$$

where:

A_0 - Amplification Factor;

ρ_b - Bedrock density value (g/cm^3);

v_b - Wave propagation velocity in bedrock (m/s);

ρ_a - Mass density of soft rock (g/cm^3);

v_a - Wave propagation speed in soft rock (m/s).

3.2.2. Seismic Vulnerability Index (SVI)

The seismic vulnerability index could be a parameter closely related to the level of vulnerability of a zone to the threat of earthquake risks, the value of which shows a linear relationship with the level of hazard of damage caused by earthquakes. The geological conditions of the local region are a factor that should be taken into consideration when calculating the value of the seismic vulnerability index of an area (Roser & Gosar, 2010). A thick sedimentary layer accompanied by high amplification will result in a high seismic vulnerability index. The higher the seismic vulnerability index, the greater the potential for structural damage due to weak soil strength. Conversely, a low seismic vulnerability index will reduce the potential for structural damage due to strong soil strength (Hadi et al., 2012).

$$K_g = \frac{A_0{}^2}{f_0} \tag{2}$$

where:

- K_g - Seismic vulnerability index (μcm²/s);
- A_0 - Amplification Factor;
- f_0 - Dominant Frequency (Hz).

3.2.3. Peak Ground Acceleration (PGA)

Peak Ground Acceleration is defined as the maximum ground acceleration value that has ever occurred in an area caused by earthquake waves, calculated empirically based on the strength of the earthquake magnitude, the distance of the earthquake source from the measurement point, and the dominant period value of the soil in the area.The resulting maximum ground acceleration value indicates the level of disaster risk that occurs (Nakamura, 1997). According to Douglas (2022), the formulation of the PGA value proposed by Kanai (1996) is that the ground vibration acceleration on the surface becomes maximum with the magnitude of the high wave magnification value, with a period function written in the following equation:

$$\alpha_g = \frac{5}{\sqrt{T_0}} 10^{\left(0{,}61M - \left(1{,}66 + \frac{3{,}66}{R}\right)\log R + 0{,}167 - \frac{1{,}88}{R}\right)} \tag{3}$$

where:

- α_g - Peak Ground Acceleration at observation point (gravitational acceleration = gal);
- T_0 - Dominant period of land observation point (s);
- M - Moment Magnitude
- R - Epicenter distance (km)

3.2.4. Ground Shear Strain (GSS)

The ability of soil layers to shift or stretch during an earthquake is called Ground Shear Strain (GSS). The GSS value is obtained by multiplying the PGA and SVI. High levels of vulnerability in an area increase the risk of earthquake-induced ground movement, such as ground cracks, landslides, land subsidence, and liquefaction.The effective value of ground shear strain has an influence on conditions after an earthquake. The potential for deformation, landslides, or liquefaction is shown in **Table 2** (Nakamura, 1997).

Table 2.
Relationship between strain and dynamic properties of soil (Nakamura, 1997).

<table>
<tr><td>Size of Strain γ</td><td>10^{-6}</td><td>10^{-5}</td><td>10^{-4}</td><td>10^{-3}</td><td>10^{-2}</td><td>10^{-1}</td></tr>
<tr><td>Phenomena</td><td colspan="2">Wave, Vibration</td><td colspan="2">Crack, Settlement</td><td colspan="2">Landslide, Soil Compaction, Liquefaction</td></tr>
<tr><td rowspan="2">Dynamic Properties</td><td colspan="2" rowspan="2">Elasticity</td><td colspan="2" rowspan="2">Elasto-Plasticity</td><td colspan="2">Collapse</td></tr>
<tr><td colspan="2">Repeat- Effect, Speed- Effect of Loading</td></tr>
</table>

3.3. Data Collection Method

This study, conducted to determine seismic vulnerability in the upper part of Semarang City, involved recording microtremor signals at 119 locations. The recording equipment used in this study consisted of three sets of microtremor devices, each with a data logger, a VHL PS 2B 3-component seismograph, a GPS, and a compass to determine the North-South direction of the data collection. In addition to the hardware, the software used for data processing in this microtremor (HVSR) method includes Microsoft Excel, Notepad, Notepad++, Geopsy, and Dinver (Irham et al., 2021; Arintalofa et al., 2022). The initial results of the microtremor data recording are raw data, which are obtained in CSV format and can be opened in Microsoft Excel. This data demonstrates the microtremor reaction, revealing a subsurface image with three components (Yulianto & Yuliyanto, 2023): the East-West level component, the North-South horizontal component, and the vertical component (**Fig. 3**). These three components will then be processed using Geopsy software to create an HV curve (**Fig. 4**), which produces A_0 and f_0 values.

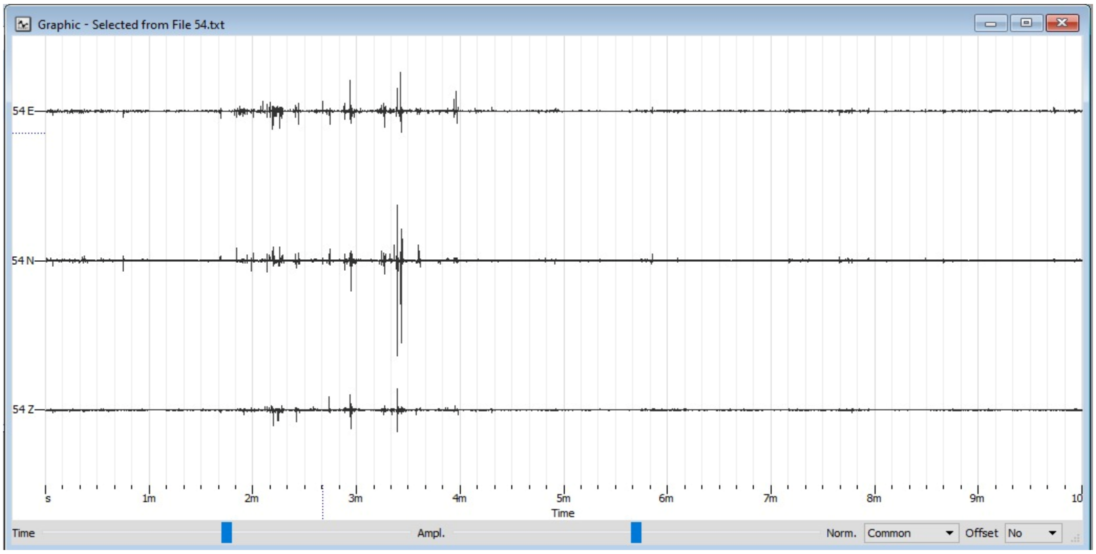

Fig. 3. Microtremor Raw Data.

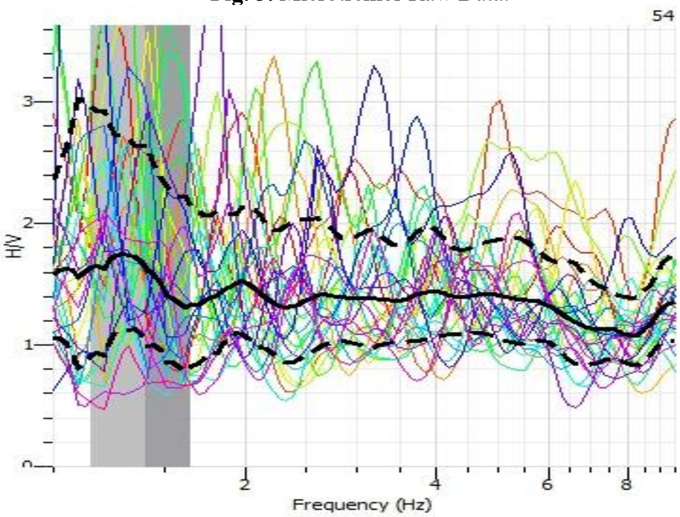

Fig. 4. HVSR processing results.

4. RESULTS

4.1. f_0 (Dominant frequency)

The frequency value of the rock layer in a region can be interpreted as a dominant frequency, which indicates the thickness of the soft layer in that area. Based on the classification explained by Kanai (1983), a higher f_0 value indicates the presence of hard rocks in shallow areas and a thinner surface layer. Meanwhile, greater thickness and softer sediments are associated with smaller dominant frequency values. The southern Semarang area has a dominant frequency value in the range of 0.13 – 9.21 Hz, with an average at 119 station locations of 1.17 Hz, as shown in **Fig.5**. In general, the research area has a dominant frequency classification of f_0 <2.5 Hz, indicating that most areas are classified as soft soil with a depth of 30 m. Dominant frequencies with a range of 2.5 < f_0 < 6.67 Hz are found at stations 36, 70, 77, 87, and 118, indicating the presence of soft soil with a thickness of 5 m and consisting of gravelly sand, hard sandy loam, clay, and clay. The f_0 value with a range of 6.667 < f_0 < 20 Hz is found in the central part of Pedurungan District (station 91), the Southwest part of Pedurungan District (station 72), the northeastern and northern parts of Tembalang District (stations 83, 62), and the southern and western parts of Gajahmungkur District (stations 4 and 15). This classification indicates the presence of a classification of Tertiary or older rocks consisting of hard gravelly sandstone.

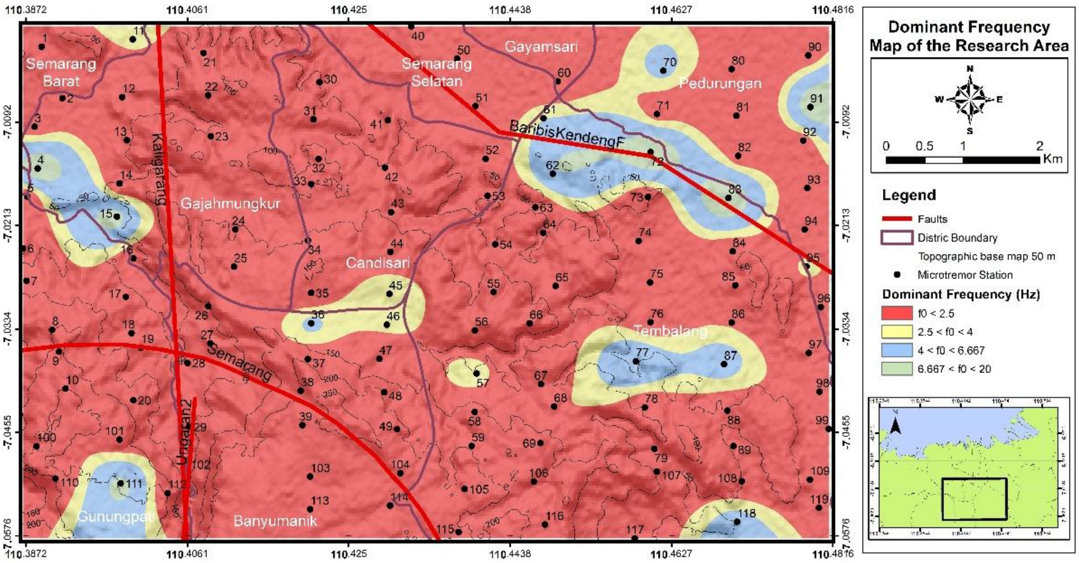

Fig. 5. Dominant frequency map of the research area.

4.2. A_0 (Amplification Factor)

The amplification factor can be defined as a phenomenon where earthquake waves experience an increase in amplitude (shaking strength) as they propagate through certain soil layers, especially soft soil or sediment (Elbshbeshi et al., 2022). This occurs because earthquake waves possess energy. When waves move from a hard medium (high propagation velocity) to a soft medium (low propagation velocity), their speed decreases. To maintain constant energy, the amplitude (wave height) must increase drastically. The greater the impedance difference between the bedrock and the surface soil layer, the greater the amplification factor (Farahani & Zare, 2014). The dependent variables in the amplification factor are sediment thickness, lithology, topography, and resonance. The amplification factor (A_0) value in the southern Semarang area ranges from 0.53 to 6.94 with an average of 2.77 (**Fig. 6**). Based on this, the research area is dominated by amplification classifications

$A_0 < 3$ and $3 < A_0 < 6$. However, in the Northwest part of Tembalang District (station 54), there is a classification of $6 < A_0 < 9$, which is classified as high amplification and requires special attention and handling.

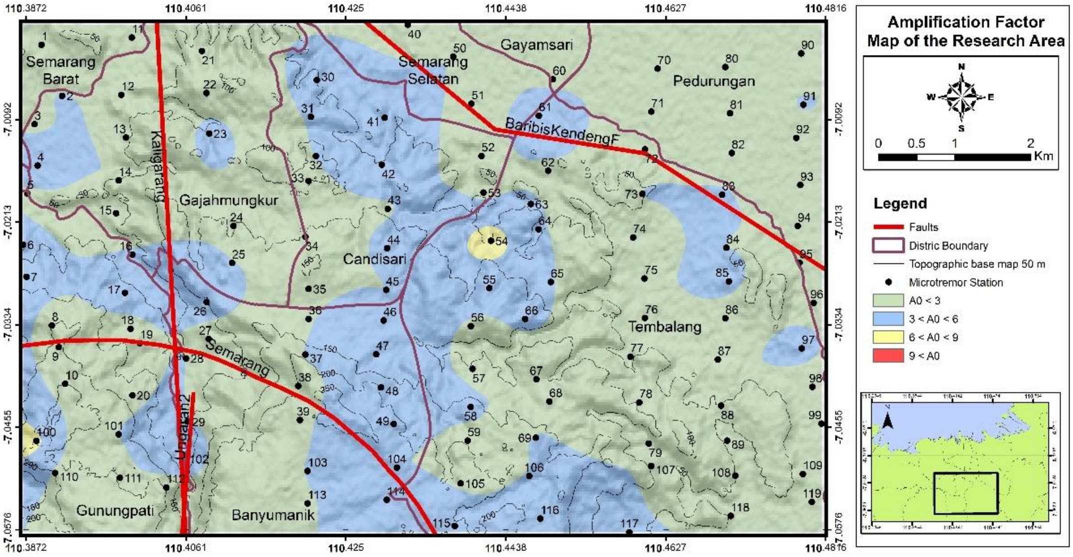

Fig. 6. Amplification Factor Map of the research area.

4.3. SVI (Seismic Vulnerability Index)

The Seismic Vulnerability Index (SVI) can be defined as a numerical parameter used to identify the level of vulnerability of a soil layer to deformation during an earthquake. This index is an important indicator in seismic microzonation studies to map areas most at risk of structural damage due to their geological conditions (Elbshbeshi et al., 2022). The potential impact and hazard of an earthquake increase with the value of the seismic vulnerability index of a region. The thickness of the sediment layer below the ground surface, the surface wave velocity, and the wave velocity below the ground surface are variables used to calculate the seismic vulnerability index value. The Seismic Vulnerability Index value in the southern Semarang region ranges from 0.17 to 260.09 $\mu cm^2/s$ with an average of 32.29 $\mu cm^2/s$. Based on **Fig. 7**, low classification in zone 1 with a range of values 5 $\mu cm^2/s$ > SVI was found in West Semarang District (station 11), Gajahmungkur District (stations 4, 15, and 24), South Gunungpati District (station 111), South Candisari District (stations 36, 45, 46), North, Central and South Tembalang District (stations 62, 72, 68, 77, 87, 118, 98) and South and Central Pedurungan District (stations 70, 71, 82, 91, 92, 93, 95). Medium classification is in zone 2 with a range of values $5 < SVI < 25$ $\mu cm^2/s$, and high classification, $SVI > 25$ $\mu cm^2/s$ is the dominant classification found in the South Semarang area.

4.4. PGA (Peak Ground Acceleration)

PGA can be defined as the maximum ground vibration acceleration value that occurs at a location during an earthquake. Unlike magnitude, which measures the energy at the epicenter (focal point), PGA measures what is actually felt and experienced by the ground surface at a specific location (Fahrezi et al., 2025). Factors that influence the PGA value are the earthquake source, trajectory, and local conditions. The calculation method in this study uses the PSDA (Deterministic Seismic Hazard Analysis) method, which calculates the worst-case scenario from a specific earthquake source (Kanai, 1996).

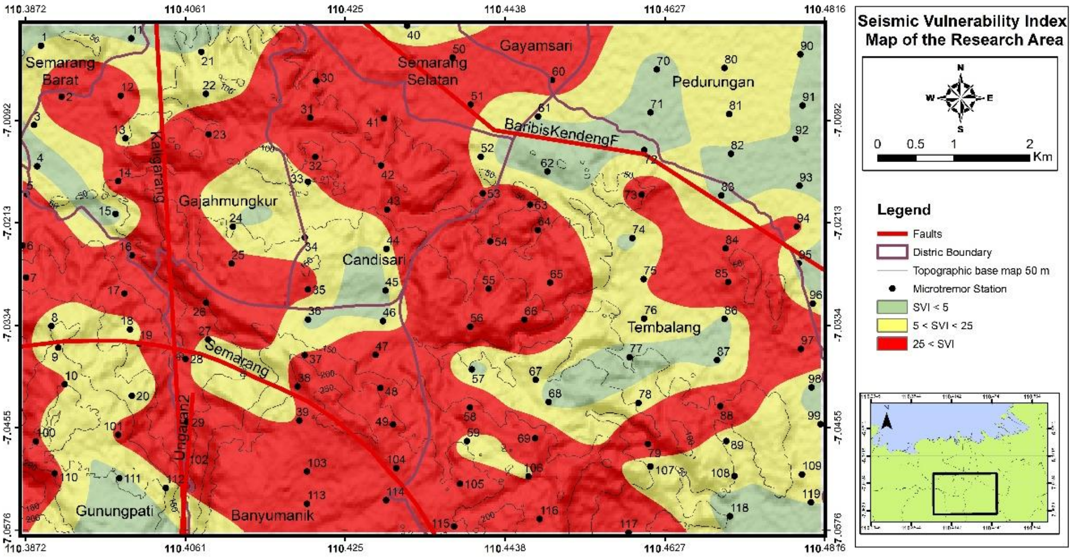

Fig.7 Seismic Vulnerability Index Map of the study area

The earthquake used in this analysis was an earthquake that occurred in Yogyakarta with a magnitude of 6.3. Despite its considerable distance, the presence of a thick and soft alluvial layer in North Semarang causes seismic wave amplification (Partono et al., 2015). This was demonstrated in the 2006 Yogyakarta earthquake (magnitude 6.3), where the tremors were felt quite strongly in Semarang and caused cracks in several building structures, even though the epicenter was hundreds of kilometers from Semarang City.

The presence of active faults that encompass dense organizational and industrial areas can increase the city's seismic risk profile (Azizah et al., 2018), mainly due to the combination of earthquake threats in the environment and soil conditions that are susceptible to land subsidence.

Based on **Fig. 8**, the PGA value in the southern Semarang area ranges from 5.87 to 49.17 gal with an average of 13.85 gal.

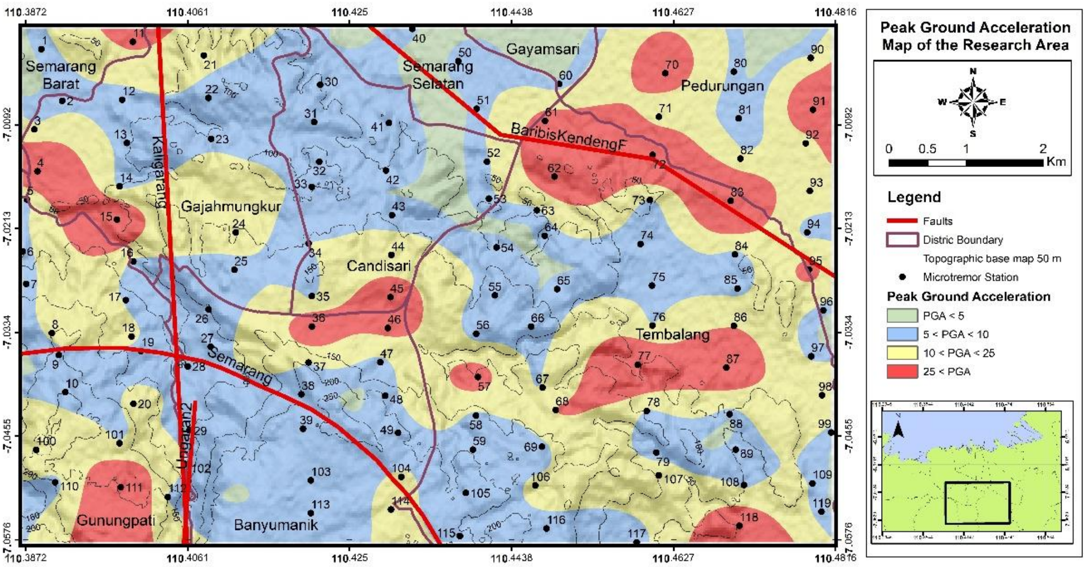

Fig. 8. PGA map of the research area.

The dominant classifications found in the southern Semarang area are 5 < PGA < 10 gal and 10 < PGA < 20 gal, which indicate a moderate area. There are PGA values with high classification, namely in the western part of Gajahmungkur District (stations 4, 15), the southern part of West Semarang District (station 11), the northern part of Banyumanik District (stations 36 and 46), the southern part of Candisari District (station 45), the northern, southern and central districts (stations 61, 62, 72, 83, 57, 77, 87, and 118), the western part of Pedurungan District (stations 70, 91, and 95), the southern part of Gunung District (station 111).

4.5. GSS (Ground Shear Strain)

Ground Shear Strain (GSS) is a critical parameter for assessing the risk level of soil deformation, especially due to dynamic loads such as earthquakes. High GSS values in an area increase the risk of ground movement due to earthquakes, such as ground cracks, landslides, land subsidence, and liquefaction (Nakamura, 1997). The effective value of ground shear strain has an influence on conditions after an earthquake. The classification used in determining the GSS value uses the Nakamura 1997 classification. The GSS value in the southern Semarang area, based on **Fig. 9**, has a range of 1.3×10^{-5} - 3.59×10^{-4} with an average of 1.3×10^{-4}. Most of the southern Semarang area is classified as $1 \times 10^{-4} < GSS < 1 \times 10^{-4}$, which has the phenomenon of ground cracks and land subsidence, and has elastic-plastic dynamic properties with the effects of repeated loading and speed effects. There is an area with a GSS classification of $<1 \times 10^{-4}$, namely in the Central Pedurungan area (station 90). This area experiences wave phenomena, vibrations, and has plastic dynamic properties.

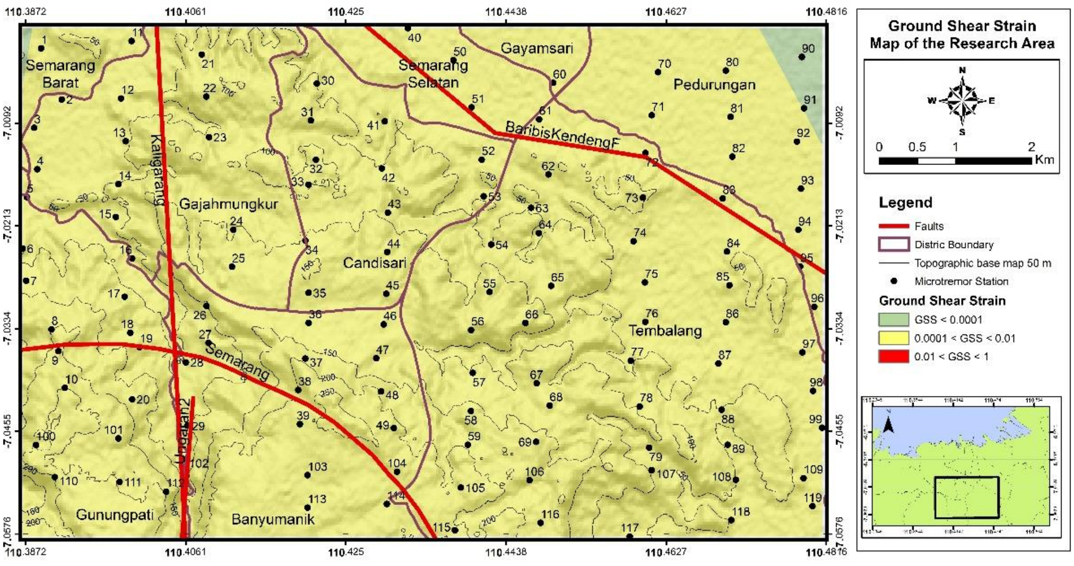

Fig. 9. GSS map of the research area

5. DISCUSSION

Based on the correlation analysis results of the HVSR method (**Fig. 9**) parameters in the form of dominant frequency (f_0), amplification factor (A_0), seismic vulnerability index (SVI), Peak Ground Acceleration (PGA), and Ground Shear Strain (GSS), a close relationship was obtained in describing the subsurface characteristics and the level of earthquake vulnerability in the southern Semarang region. Line A-A' in **Fig. 1** includes several microtremor stations, namely stations 40, 41, 42, 43, 44, 45, 46, 47, 48, 49, 104, 114.The dominant frequency (f_0) value in the study area is dominated by a range of less than 2.5 Hz, with an average of 1.17 Hz. This value indicates that most of the area is composed of a soft sediment layer with a relatively large thickness. This condition causes the soil's ability to respond to seismic waves to be greater, especially in the form of wave amplitude amplification. The f_0 value is closely related to bedrock depth, with low f_0 values indicating deep bedrock and thick sediment layers. Similar research (in the northern region of this study) indicates low f_0 values (Nurwidyanto et al., 2023). This is in line with the distribution of amplification factor (A_0) values in the study area, which are dominated by low to moderate classifications ($A_0 < 3$ and $3 < A_0 < 6$), with several locations showing high amplification values ($A_0 > 6$). The presence of a significant impedance contrast between the bedrock and the overlying sedimentary layer indicates a high amplification factor. The decrease in seismic wave velocity, coupled with constant wave energy, indicates that seismic waves propagate from a hard to a soft medium. Therefore, this correlation indicates that areas with low f_0 values have high A_0 values.

The correlation between f_0 and A_0 is reflected in the seismic vulnerability index (SVI) values (**Fig. 9**), which show a predominance of high classifications (SVI > 25 µcm²/s) in most of the study area. A low f_0 value combined with a high A_0 value results in high seismic vulnerability, or susceptibility to earthquake shaking. The SVI value in an area can be used as a reference parameter for seismic vulnerability, as evidenced by research by Nurwidyanto et al. (2024) conducted in the coastal area of Demak. This study showed low SVI values in most of the study areas. These values can also be used as geotechnical recommendations for several areas with high potential seismic vulnerability. The PGA value is influenced by the earthquake source and the distance from the source to the study site. Local conditions such as soil type and sediment thickness also play a role in modifying the acceleration felt at the surface. The Peak Ground Acceleration (PGA) value in the southern Semarang area is classified as moderate to high ground motion. Local soil conditions play a significant role in increasing the intensity of the perceived shaking.

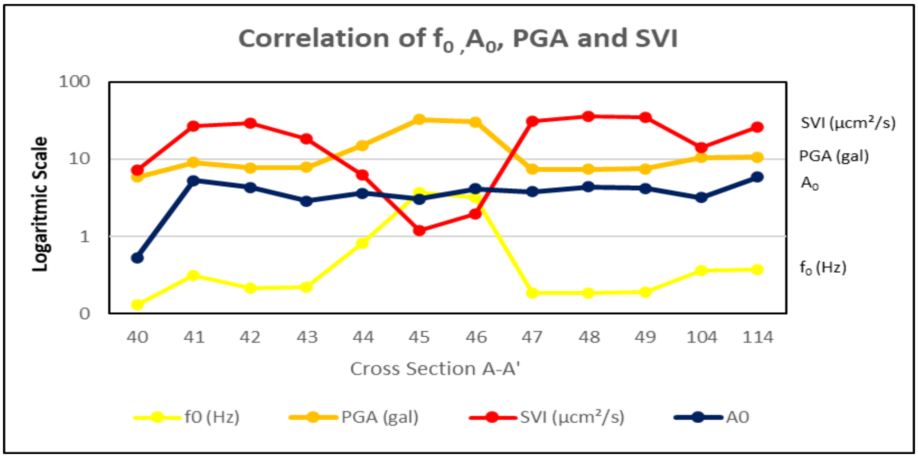

Fig. 9. Correlation between f_0, A_0, PGA and SVI in Line A – A'.

The Ground Shear Strain (GSS) value in the study area is in the range of 10^{-4}, which indicates that most areas have the potential for significant deformation. The GSS value indicates the potential for phenomena and dynamic properties experienced by an area. Several previous studies, such as Nurwidyanto et al. (2023), on earthquake microzonation using the HVSR method in the northern area of this study, indicate that most of the northern coast of Semarang is dominated by moderate vulnerability. Meanwhile, several areas across Semarang City, from north to south, have low earthquake vulnerability. These results are based on GSS calculations in various areas.

Therefore, it can be concluded that the GSS value has a positive correlation with SVI and A_0, and a negative correlation with f_0. The relationship between parameters shows that the dominant frequency (f_0) is inversely proportional to other vulnerability parameters, while the amplification factor (A_0), seismic vulnerability index (SVI), Peak Ground Acceleration (PGA), and Ground Shear Strain (GSS) are directly proportional. Based on the relationship analysis, it can be concluded that the southern Semarang region is dominated by geological conditions in the form of soft sediment with a fairly large thickness, which causes the potential for wave amplification and high vulnerability to earthquakes. This condition requires attention in spatial planning and disaster mitigation, especially in areas with high amplification values and vulnerability indexes.

6. CONCLUSIONS

Based on several parameters used to determine seismic hazard potential, the upper part of Semarang City has a relatively high seismic vulnerability index in several areas. Furthermore, spatial analysis also shows that several sub-districts, particularly Tembalang, Banyumanik, and Pedurungan, have a higher earthquake vulnerability than the surrounding areas. These findings provide important information for seismic microzonation, supporting urban planning and information related to disaster mitigation in Semarang City. Furthermore, more in-depth technical studies are needed in the geotechnical field in several locations with high seismic hazards (contained in the A_0, f_0, PGA, SVI, and GSS maps), and locations around faults in the Semarang area.

REFERENCES

Abidin, H. Z., Andreas, H., Gumilar, I. & Brinkman, J. J. (2013) Land subsidence and urban development in Jakarta (Indonesia). Geohazards, 18(1), 148-154.

Arifin, S.S., Mulyatno, B. S., Mujiyono, and Setianegara, R. 2014. Determination of Earthquake Disaster Prone Zones Based on Analysis of Microtremor HVSR Amplification Values and Analysis of Dominant Periods in the Liwa Area and Surrounding Areas. Jurnal Geofisika Eksplorasi, 2(1). https://doi.org/10.23960/jge.v2i01.217

Arintalofa, V., Yuliyanto, G. & Harmoko, U. (2020) Subsurface characterization of Diwak Derekan geothermal field by HVSR analysis method based on microtremor data. AIP Conference Proceedings, 2296(1). https://doi.org/10.1063/5.0030356

Azizah, L., Chintami R. D., Partono, W. & Sukamta. (2018) Analysis study of building vulnerability levels to earthquakes with a maximum strength of 6.9 Mw. Jurnal Karya Teknik Sipil, 7(1), 62-75.

BRIN, (2025) BRIN Geological Expedition Reveals Potential Active Faults in Semarang and Surrounding Areas, Last access on February 2026, https://www.brin.go.id/news/124219/ekspedisi-geologi-brin-ungkap-potensi-sesar-aktif-di-semarang-dan-sekitarnya

Cakici, H., Kocadagistan, M. E., Ozer, C. & Zaimoglu A. S., (2021) Investigation of the Effects of Waste Tire, Water Content, and Relative Density on Soil Dominant Frequency in Separate Grained Soils by Microtremor Method, Journal of Engg. Research, 11(3), 33-42. https://doi.org/10.36909/jer.14659

Douglas, J. (2022) Ground motion prediction equations 1964-2021, University of Strathclyde, UK. https://doi.org/10.6084/m9.figshare.26827750

Elbshbeshi, A. Gomma, A. Mohamed, A. Othman, A. & Ghazala, H. (2022) Seismic hazard evaluation by employing microtremor measurements for Abu Simbel area, Aswan, Egypt. Journal of African Earth Sciences, 196, 104734. https://doi.org/10.1016/j.jafrearsci.2022.104734

Fahrezi, Z., Misliniyati, R., Amri, K., Mase, L. Z. & Hardiansyah. (2025) Earthquake Hazard Evaluation Study on the Central Area of Selebar District, Bengkulu City, based on Seismic Response Analysis. Riset Geologi dan Pertambangan 35, 1, 11–24. https://doi.org/10.55981/risetgeotam.2025.1331

Farahani, J. V. & Zare, M. (2014) Site characterizations for the Tehran network (TDMMO) in Tehran Region Using Micro-Earthquake, Microtremor and Quarry Blast Data. Soil Dynamics and Earthquake Engineering. 63, 235–247 http://dx.doi.org/10.1016/j.soildyn.2014.03.013

Hadi, A.I., Farid, M. & Fauzi, Y. (2012) Mapping of Maximum Ground Vibration Acceleration and Seismic Vulnerability Due to Earthquakes to Support the Spatial and Regional Planning (RTRW) of Bengkulu City, Jurnal Ilmu Fisika Indonesia, 1(2D).

Hidayat, E. (2013). Identification of Active Fault Along the Path Kaligarang, Semarang. *JSD.Geol.* 23, 1. https://doi.org/10.33332/jgsm.geologi.v23i1.97

Ilgac, M., Vantassel, J. P. & Zekkos A. A. (2026) Influence of processing technique on the agreement of site fundamental frequency (f0) from earthquake and microtremor horizontal-to-vertical spectral ratio. Engineering Geology, 363, 08573. https://doi.org/10.1016/j.enggeo.2026.108573

Kanai, K. (1983) Engineering Seismology. Tokyo University: Japan.

Koesuma S., Viola, F., & Sunardi B. (2022). Identifikasi zona bahaya gempa bumi berdasarkan percepatan tanah maksimum di Kota Semarang. Indonesian Journal of Environment and Disaster (IJED), 1(2), 65-72. https://doi.org/10.20961/ijed.v1i2.428

Konno, K., & Ohmachi, T. (1998) Ground-motion characteristics estimated from spectral ratio between horizontal and vertical components of microtremor. Bulletin of the Seismological Society of America, 88(1), 228-241.

Marfai, M. A. & King, L. (2007) Monitoring land subsidence in Semarang, Indonesia. Environmental Geology, 53(3), 651-659. https://doi.org/10.1007/s00254-007-0680-3

Nakamura, Y., (1997) Seismik Vulnerability Indices for Ground And Structures Using Microtremor, World Congress on Railway Research, Florence.

Nakamura, Y. (1989) A Method for Dynamic Characteristics Estimation of Subsurface using Mikrotremor on Ground Surface, QR of RTI, 30, 1

Nakamura, Y. (2000) Clear Identification of Fundamental Idea of Nakamura's Technique And Its Applications, System and Data Research Co. Ltd., 3(25), 3

Newcomb, K. R., & McCann, W. R. (1987) Seismic history and seismotectonics of the Sunda Arc. Journal of Geophysical Research: Solid Earth, 92(B1), 421-439. https://doi.org/10.1029/JB092iB01p00421

Nurwidyanto, M. N., Harmoko, U., Gernowo, R., Fernando, G. A., & Koesuma, S. (2024) Analysis of earthquake vulnerability of the Demak coastal area based on the HVSR (Horizontal to Vertical Spectral Ratio) method. Indonesian Journal of Applied Physics, 14(2). https://doi.org/10.13057/ijap.v14i2.90703

Nurwidyanto, M. N. & Yuliyanto, G. (2024) Landslide delineation using shear wave velocity, poisson’s ratio, and GSS parameter analysis for the case study of the Ngasinan landslide, Banyumanik, Semarang Indonesia. ARPN Journal of Engineering and Applied Sciences, 19 (7), 426-433.

Nurwidyanto, M. N., Zainuri, M., Wirasatriya, A. & Yulianto, G. (2023) Microzonation for earthquake hazards with HVSR microtremor method in the coastal areas of Semarang, Indonesia. Geographia Technica, 18(1), 177–188. http://doi.org/10.21163/GT_2023.181.13

Nurwidyanto, M. N., Zainuri, M., Wirasatriya, A. & Yulianto, G. (2023) Subsurface Structure of Semarang Coast Based on HVSR Method. Indonesian Journal of Applied Physics (IJAP), 13 (1) - 117. https://doi.org/10.13057/ijap.v13i1.66864

Nurwidyanto, M, I., Zainuri, M., Yuliyanto, G. & Wirasatriya, A. (2021) Measurement of ground response of Semarang coastal region risk of earthquakes by Horizontal to Vertical Spectral Ratio (HVSR) microtremor method. IOP Publishing Journal of Physics: Conference Series, 1943(1):012033. http://doi.org/10.1088/1742-6596/1943/1/012033

Partono, W., Irsyam, M., Prabandiyani, R. W. S. & Maarif, S., (2013) Application of the HVSR Method in Calculating Soil Amplification Factors in Semarang City. Jurnal Ilmu dan Terapan Bidang Teknik Sipil, 19, 2

Partono, W., Irsyam, M., Sengara, I. W., & Asrurifak, M. (2019) Seismic microzonation of Semarang, Indonesia, based on probabilistic and deterministic combination analysis. GEOMATE Journal, 16 (57), 176–182. https://doi.org/10.21660/2019.57.8323

Partono, W., Irsyam, M., Wardani, S. P. R. & Maarif, S. (2015) Perception of the Development of the Semarang City Earthquake Hazard Map through Deterministic Earthquake Hazard Research. Teknik, 36, 1, 24-31,. https://doi.org/10.14710/teknik.v36i1.7701

Partono, W., Irsyam, M., Sengara, I. W., Asrurifak, M., Pradipta, M., & Djarwodiningrat, S. (2020). Development of seismic hazard maps for Semarang, Indonesia due to shallow crustal fault earthquake sources. International Journal of Technology, 11(4), 785-795. https://doi.org/10.1051/matecconf/201815901011

Poedjoprajitno, S., Wahyudiono, J. & Cita, A. (2008) Reactivation of the Kali Garang Fault, Semarang. Jurnal Geologi Indonesia, 3(3), 129-138.

Pusat Studi Gempa Nasional - PusGen. (2017) Map of Indonesian Earthquake Sources and Hazards in 2017. Kementerian Pekerjaan Umum dan Perumahan Rakyat, Jakarta.

Rošer, J. & Gosar, A. (2010) Determination of Vs30 for Seismik Ground Classification in the Ljubljana Area, Slovenia. Acta Geotechnica Slovenica, 7(1), 61–76.

Sasongko, D. P., Yuliyanto, G. & Arifin, Z. (2019) Vibration Vulnerability Identification in Kota Lama Semarang using Microtremor Method. Indonesian Journal of Applied Physics, 9(2), 105

Scholz, C. H. (2019). *The Mechanics of Earthquakes and Faulting* (3rd ed.). Cambridge University Press. https://doi.org/10.1017/9781316681473

SESAME. (2004). Guidelines for the implementation of the H/V spectral ratio technique on ambient vibrations: measurements, processing and interpretation. European Commission – Research General Directorate.

Shearer, P. M. (2009). *Introduction to Seismology* (2nd ed.). Cambridge University Press. https://doi.org/10.1007/978-3-0348-5283-8

Simanjuntak, A. B., Yuliyanto, G. & Harmoko, U. (2017) Earthquake disaster risk analysis using microtremor data in Fulolo Village, Alasa District, North Nias Regency. Youngster Physics Journal, 6(4), 360-367.

Sitorus, N., Purwanto, S. & Utama, W. (2017) Analysis of Natural Frequency Values and Amplification in Olak Alen Village, Blitar Using the HVSR Microtremor Method. Jurnal Geosaintek. 3(2), 89

Thanden, R. E., Sumadirdja, H., Richards, P. W., Sutisna, K. & Amin, T. C. (1996) Geological Map of Magelang and Semarang Sheet, Java. Pusat Penelitian dan Pengembangan Geologi, Bandung.

U.S. Geological Survey. (2026) Search Results for Earthquake Data. Earthquake Hazards Program. Retrieved February 7, 2026, from ttps://earthquake.usgs.gov/earthquakes/search/

Van Bemmelen, R. W. (1949) The Geology of Indonesia. Vol. IA: General Geology of Indonesia and Adjacent Archipelagoes. Government Printing Office, The Hague.

Widodo, P. (2012) Engineering Seismology and Earthquake Engineering, Pustaka Pelajar, Yogyakarta.

Yulianto, T. & Yuliyanto, G. (2023) Microtremor data and HVSR method in the kaligarang fault zone Semarang, Indonesia. Data In Brief, 49, 109428. https://doi.org/10.1016/j.dib.2023.109428

Yuliyanto, G. & Yulianto, T. (2023) Microtremor data and HVSR method of geothermal manifestation of Mt. Telomoyo, Central Java, Indonesia. Data In Brief, 51, 109721. https://doi.org/10.1016/j.dib.2023.10972

Geographia Technica, Vol. 21, Issue 3, 2026, pp 182 to 195

SEASONAL REORGANIZATION OF CLIMATE SIMILARITY IN THE CARPATHIAN BASIN: A TIME-BASED CLIMATE NETWORK APPROACH

***Attila MAGYARI-SÁSKA*[1]**

DOI: 10.21163/GT_2026.213.12

ABSTRACT

This study examines changes in the seasonal organisation of climate in the Carpathian Basin using a time-based climate-network approach. In contrast to conventional climate networks, where nodes usually represent spatial locations, the present method defines individual year–month observations as network nodes. Edges describe multidimensional climatic similarity based on monthly values derived from daily temperature, precipitation, humidity and radiation data. The analysis uses E-OBS gridded observational data for ten selected locations and compares two 30-year periods: 1961–1990 and 1995–2024. The results show that the annual climatic cycle remained broadly recognisable in the recent period, with stable winter and summer components still present in the network structure. However, the boundaries between seasonal groups became less sharply defined. The strongest changes were associated with transition months, especially February, March, April, September and October. Shannon entropy indicates that some of these months became more fragmented, while prototype similarity matrices reveal stronger cross-seasonal relationships between spring and autumn states. Percolation analysis shows only minor changes in overall network robustness, suggesting that the observed transformation should not be interpreted as a collapse of the seasonal structure, but rather as a moderate reorganisation of the relationships between monthly climatic states. The study demonstrates that time-based climate networks can complement conventional trend-based climate analyses by highlighting structural changes in the temporal organisation of seasonality.

Keywords: *time-based climate networks; seasonal reorganisation; Carpathian Basin; climatic similarity; Shannon entropy; percolation analysis*

1. INTRODUCTION

Climate change is usually described through changes in individual climatic variables, such as temperature, precipitation, humidity or radiation (Stine et al., 2009; Stine and Huybers, 2012). These variables are commonly analysed by trends, anomalies, extremes or spatial patterns, and such approaches remain essential for understanding regional climate dynamics. At the same time, climate is not experienced as a set of isolated variables. It is organised through recurring seasonal states, transitions between months, and similarities between different parts of the annual cycle. For this reason, changes in climate may also appear as changes in the internal structure of seasonality: some months may become more similar to others, some transitional periods may become less clearly defined, and the stability of the annual cycle may be modified even when the general seasonal order remains recognisable (Stine et al., 2009; Hajek et al., 2022).

This structural perspective is particularly relevant in regions where several climatic influences meet like in the Carpathian Basin (Spinoni et al., 2015b). Situated between Central and South-Eastern Europe, it is shaped by oceanic, continental and local topographic influences. Its climate is therefore not only spatially heterogeneous, but also strongly seasonal. The basin includes lowland areas, enclosed depressions, hilly regions and mountain-influenced zones, all of which may respond differently to ongoing climatic change.

[1] *Babeş-Bolyai University, Faculty of Mathematics and Computer Science, 400084 Cluj-Napoca, Romania,* magyari.saska.attila@gmail.com, attila.magyari@stud.ubbcluj.ro

Previous research has already shown that the region is sensitive to changes in temperature and precipitation regimes, with consequences for agriculture, water resources and environmental stability (Bartholy and Pongrácz, 2007; Spinoni et al., 2015a; Spinoni et al., 2015b; Jánosi et al., 2023; Megyeri-Korotaj et al., 2023). However, beyond changes in the magnitude of climatic variables, it is also important to ask whether the temporal organisation of the regional climate has changed. Network-based methods offer a useful framework for this type of question (Tsonis and Roebber, 2004; Tsonis et al., 2006; Donges et al., 2009). In climate research, networks are most often used to represent spatial relationships: nodes usually correspond to grid cells or meteorological stations, while edges describe statistical similarity, correlation or coupling between climatic time series (Tsonis and Roebber, 2004; Donges et al., 2009; Holme and Rocha, 2023). Such spatial climate networks have been applied to the study of teleconnections, climate regimes and large-scale atmospheric patterns, including phenomena such as El Niño (Ludescher et al., 2023). This line of research has shown that graph-based representations can reveal structural properties of the climate system that are not always visible through conventional statistical summaries. Changes in seasonal organisation may also have consequences beyond the physical climate system. The timing, duration and climatic distinctness of seasons influence climate-sensitive forms of outdoor recreation and tourism, including hiking and geotourism, because temperature, precipitation, humidity, wind and extreme events affect activity suitability, visitor comfort and safety (Martínez Ibarra et al., 2019; Pröbstl-Haider et al., 2021; Gordon, 2023). In mountain and protected areas, structural changes in the shoulder seasons may therefore have practical relevance even where the core annual climatic cycle remains recognisable.

The temporal dimension of climate similarity has received less attention (Holme and Saramäki, 2012; Mucha et al., 2010). If spatial climate networks ask how different places are connected through climate behaviour, a time-based climate network asks a different question: how are different time periods connected to each other? From this perspective, months or seasons can be treated as elements of a climatic system (Holme and Saramäki, 2012; Stine et al., 2009). Their relationships can be described by the similarity of their multidimensional climatic conditions. Such an approach is especially suitable for investigating whether the annual cycle has become more fragmented, more internally differentiated, or more strongly reorganised over time.

The study is guided by three main questions. First, can a time-based network representation reveal changes in the seasonal organisation of climate in the Carpathian Basin? Second, which parts of the annual cycle show the strongest structural reorganisation between the two periods? Third, do these changes indicate a general weakening of the climatic network, or rather a reconfiguration of seasonal relationships while the overall annual structure remains stable? By addressing these questions, the paper contributes both to regional climate analysis and to the methodological development of climate-network research. Its regional contribution lies in identifying how the internal seasonal structure of the Carpathian Basin has changed during the last six decades. Its methodological contribution lies in adapting established tools of network analysis, including similarity-based graph construction, community detection, entropy measures and percolation analysis, to a temporal-node framework (Fan et al., 2018). This makes it possible to study climate not only as a spatially connected system, but also as a temporally organised structure.

2. STUDY AREA AND DATA

The analysis focuses on the Carpathian Basin, a climatically diverse region situated in Central and South-Eastern Europe. The ten locations were selected using a stratified, purposive design intended to span the principal geographical and climatic contrasts of the basin rather than to constitute a statistically representative sample of all grid cells. Győr and Keszthely represent the western sector of the basin, including more pronounced western atmospheric influences and, in the case of Keszthely, the vicinity of Lake Balaton. Kecskemét represents the open central Pannonian lowland, while Pécs represents the southern foothill zone. Košice and Oradea cover the northern and eastern margins of the Pannonian lowland and its transition toward the surrounding mountain system. Cluj-Napoca and Deva represent Transylvanian hilly and valley environments, whereas Gheorgheni and Brașov represent elevated, enclosed intra-mountain depressions. Together, the selected locations cover open plains, foothill transition zones, hilly and valley environments, and mountain-controlled basins. This design makes it possible to examine whether the inferred changes in seasonal climate-network organisation recur across contrasting regional settings. The study locations should therefore be regarded as physiographically and climatically contrasting case-study sites rather than as an area-weighted sample of the entire Carpathian Basin (Fig. 1).

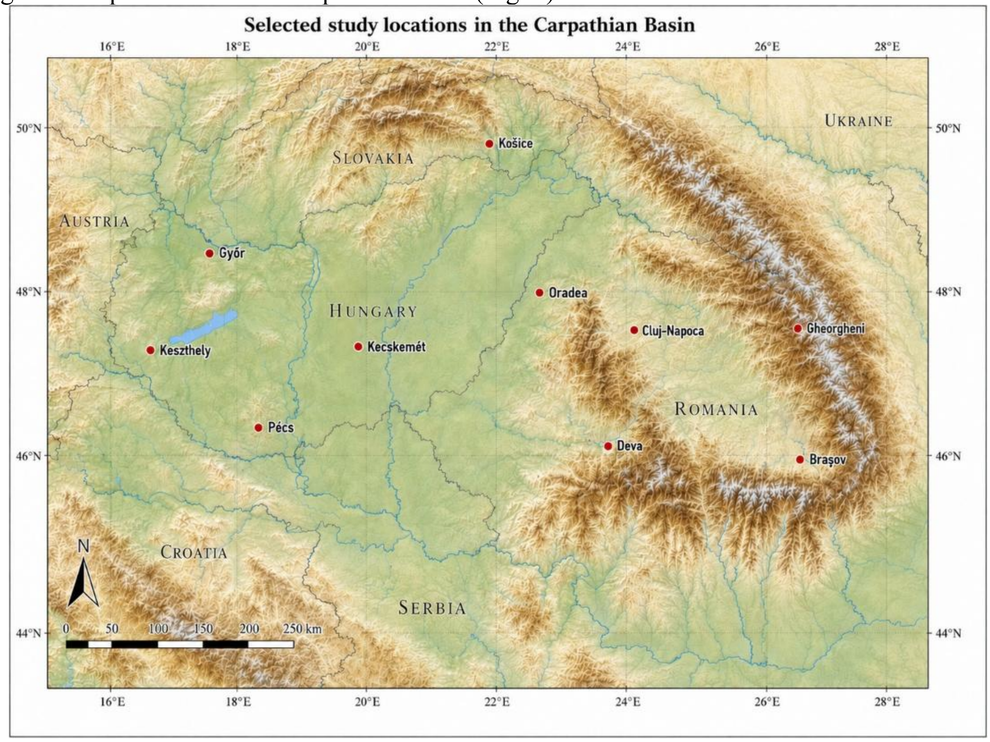

Fig. 1. Study locations in the Carpathian Basin

For each location, the corresponding grid cell of the E-OBS gridded observational dataset was used. The analysis was based on the 0.1° × 0.1° regular latitude–longitude grid version 31.0e, obtained from the Copernicus Climate Data Store. The data were obtained from the Copernicus Climate Data Store. E-OBS consists of station-based daily observations spatially interpolated to a regular European grid. Six daily variables were extracted for each selected location: daily mean temperature (TG), daily minimum temperature (TN), daily maximum temperature (TX), daily precipitation sum (RR), daily mean relative humidity (HU) and daily mean global radiation (QQ) to describe each month as a multidimensional climatic state.

Each month in each year therefore became one observation described by a six-dimensional climatic vector. The temporal coverage was divided into two 30-year periods. The early period extends from January 1961 to December 1990, while the late period extends from January 1995 to December 2024. These two intervals were selected to compare a historical baseline with a more recent climatic period of the same length.

3. METHODOLOGY

Since the six variables have different units and numerical ranges, the monthly feature vectors were first standardised. This step prevents variables with larger absolute values, such as precipitation totals, from dominating the distance calculation. After standardisation, Principal Component Analysis (PCA) was applied to reduce the six-dimensional space to two dimensions to obtain a compact space in which the main multidimensional differences between months are preserved. Similarity was then calculated from the Euclidean distance between monthly observations in this reduced PCA space. For two nodes (i) and (j), with projected coordinates (p_i) and (p_j), the distance was calculated as (Eq. 1):

$$d(i,j) = \sqrt{\left(p_{i,1} - p_{j,1}\right)^2 + \left(p_{i,2} - p_{j,2}\right)^2} \tag{1}$$

The distances were transformed into similarity values using min–max scaling followed by inversion (Eq. 2):

$$S(i,j) = 1 - \frac{d(i,j) - d_{min}}{d_{max} - d_{min}} \tag{2}$$

Thus, a value close to 1 means that two months occupy a very similar position in the reduced climatic space, while lower values indicate more distinct monthly states. For the early and late networks, the same reference scale was used. The minimum and maximum distances used in the transformation were derived from the full available period, so that similarity values in the two networks remained directly comparable.

The pairwise similarity calculation initially produces a complete weighted graph, where each month is connected to all other months. For a meaningful interpretation a pruning step was applied to extract the main structural backbone of the network. All edges were ranked according to their similarity values, and the weakest edges were removed until a predefined average degree was reached. For this, instead of using a fixed similarity threshold, the method therefore keeps network density comparable between locations and periods. The target average degree was defined as (Eq. 3):

$$\langle k \rangle = 3Y - 1 \tag{3}$$

where (Y) is the number of years in the analysed period. Since both comparison periods contain 30 years, this gives a target average degree of 89. The corresponding number of retained edges is (Eq. 4):

$$E_{target} = \frac{\langle k \rangle \times N}{2} \tag{4}$$

where (N) is the number of nodes in the network. This rule follows the assumption that, under stable seasonal conditions, a month should remain strongly connected to its own calendar-month occurrences in other years and to the neighbouring parts of the annual cycle. The weight of the weakest retained edge defines the empirical structural threshold of the given network.

The community structure analysis aim was to identify groups of month-year observations that form internally coherent climatic blocks. In this context, a community can be interpreted as a set of months that are more similar to each other than to the rest of the annual cycle (Newman, 2006). The Leiden algorithm was used for community detection, with edge weights included in the partitioning process (Traag et al., 2019). The resulting communities were not interpreted only as abstract graph clusters, but they were compared with calendar months in order to see whether the detected structure follows the expected seasonal order, and whether this order changes between the early and late periods. The quality of the detected partition was summarised by modularity, which measures how strongly nodes are grouped within communities compared with the connections expected in a random network. Higher modularity indicates more clearly separated seasonal blocks, while lower modularity indicates weaker separation and stronger overlap between seasonal communities.

To describe how stable or fragmented each calendar month is within the detected communities, Shannon entropy was calculated for every month (Shannon, 1948). For a given calendar month, the distribution of its 30 year–month observations across communities were used. The entropy of month (m) was calculated as (Eq. 5):

$$H_m = \sum_{c=1}^{C} p_{m,c} * ln(p_{m,c}) \tag{5}$$

where $(p_{m,c})$ is the proportion of observations of month (m) assigned to community (c), and (C) is the number of communities containing observations from that month. Higher entropy values indicate a more fragmented or transitional monthly position, while lower values indicate a more stable community membership.

Community detection and entropy describe the internal structure of each period separately. To compare the typical position of calendar months between the early and late periods, prototype similarity matrices were also calculated. For each location and each period, a monthly prototype was created for every calendar month, representing the average climatic state of that month over the 30-year period. The early and late prototypes were projected into the same PCA-based reference space used for the network construction. Similarities were then calculated between all early and late monthly prototypes, producing a 12 × 12 matrix.

Percolation analysis was used to describe the robustness of the entire network. The procedure examines how the network breaks apart when weaker edges are progressively removed. For each network, a series of increasing similarity thresholds was applied. At each threshold, only edges with weights equal to or higher than the threshold were kept. The size of the largest connected component was then calculated as a proportion of all nodes. As the threshold increases, the network gradually loses edges and eventually fragments. The critical percolation threshold was defined as the threshold before the largest drop in the size of the largest connected component. This point marks the similarity level at which the network loses a major part of its connectivity. A higher critical threshold means that the network remains connected even when only strong similarities are kept. A lower critical threshold indicates earlier fragmentation. To compare the two periods, a percolation index was calculated as (Eq. 6):

$$I_{perc} = \tau_c^{late} - \tau_c^{early} \tag{6}$$

where (τ_c^{early}) and (τ_c^{late}) are the critical thresholds of the early and late networks. Positive values indicate that the late network is more robust than the early one, while negative values indicate that it fragments at a lower similarity threshold.

4. RESULTS

4.1. General structure of the time-based climate networks

The comparison of the early and late time-based climate networks shows that the annual climatic cycle did not undergo a complete structural breakdown. In most cases, the detected communities still followed a broad seasonal logic. The networks were usually organised around three main blocks, corresponding to winter, summer and transitional months. In a few cases, a fourth community also appeared, but this did not represent a new stable seasonal regime. It was generally linked to the separation of one or a small number of isolated nodes. The more relevant change was not the number of communities itself, but the way in which these communities became connected to each other. Modularity decreased at all ten selected locations between the early and late periods (**Fig. 2**). This indicates that the seasonal blocks became less sharply separated in the contemporary period. The winter and summer cores remained identifiable, but the boundaries between the main seasonal groups became weaker.

This pattern is important as suggests a reorganisation of the seasonal structure rather than a simple increase or decrease in climatic variability. The annual cycle remained recognisable, but the internal separation between its main components became less clear. The most visible changes were connected to the months located near seasonal boundaries, especially late winter, spring and early autumn. The community-detection results therefore provide the first indication that the contemporary climate networks are not simply more fragmented in a general sense. Instead, they show a more subtle change: stable seasonal cores are preserved, while the transition zones between them become more flexible and less clearly delimited.

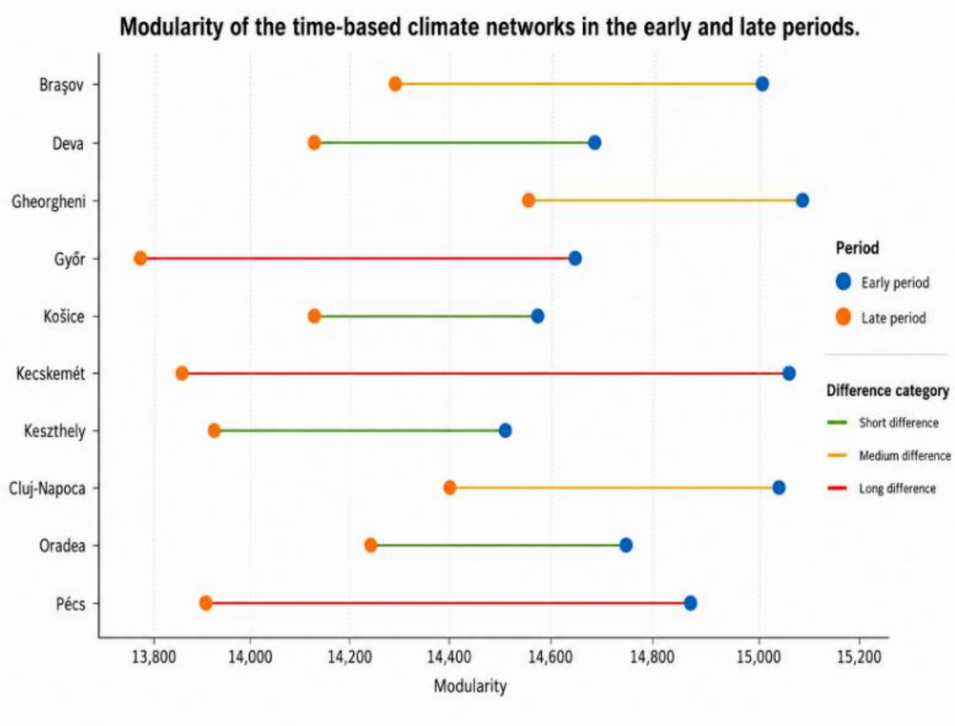

Fig. 2. Change in modularity between the early and late periods.

4.2. Monthly fragmentation based on Shannon entropy

Shannon entropy was used to describe how clearly the observations of a given calendar month belong to the detected communities. Low values indicate that the month is concentrated in one community, while higher values show that its observations are distributed across several communities. In this sense, entropy measures the stability or ambiguity of monthly community membership.

The monthly averages of the considered locations show that changes were concentrated in specific parts of the annual cycle rather than distributed evenly throughout the year (**Fig. 3**). January and December remained completely stable in both periods, with average entropy values of 0.000. The core summer months also changed only slightly, especially June, July and August. This confirms that the middle of winter and the middle of summer preserved a relatively coherent network position. The strongest changes were instead linked to the transition months.

The clearest increase occurred in February. Its average entropy rose from 0.078 in the early period to 0.328 in the late period, and this increase was visible at nine of the ten locations. The location-level heatmaps confirm that February became more fragmented almost everywhere, with the only exception being Košice, where entropy remained unchanged. This suggests that late winter became less consistently attached to a single winter community and more often shared similarities with transitional climatic states (**Fig. 4**).

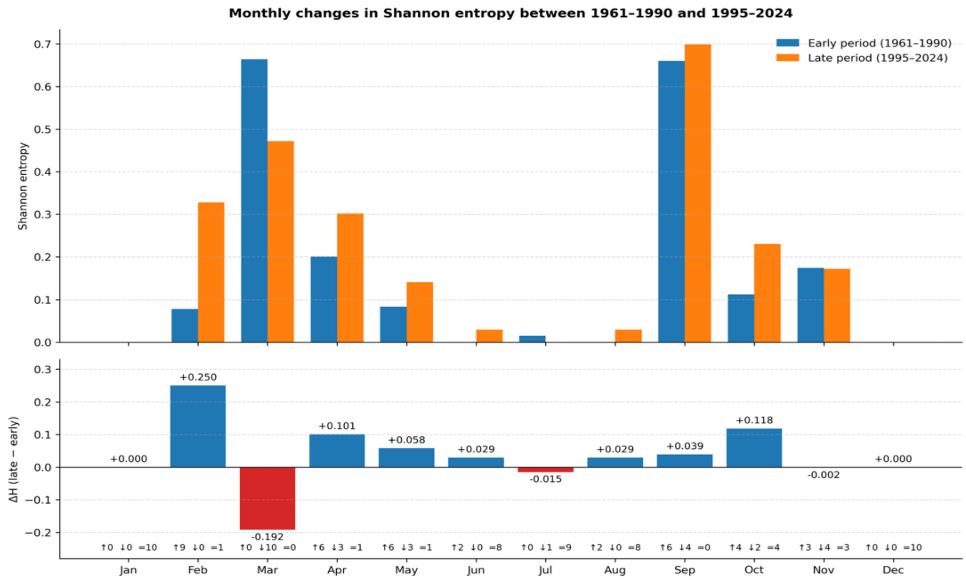

Fig. 3. Monthly Shannon entropy in the early and late periods.

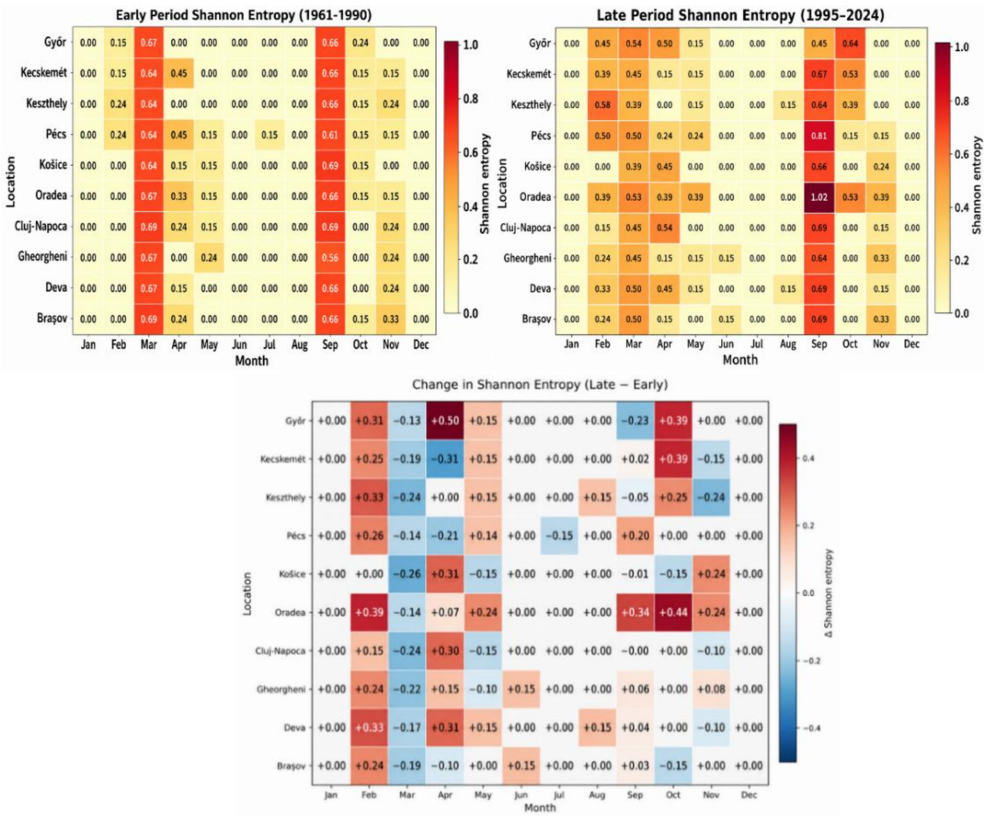

Fig. 4. Shannon entropy by location and month between the late and early periods.

March shows the opposite pattern. Its average entropy decreased from 0.664 to 0.472, and the decrease occurred at all selected locations. The heatmaps make this result especially clear: March was one of the most fragmented months in the early period, but its entropy became lower everywhere in the late period. This does not mean that the spring transition disappeared. Rather, it suggests that March became less divided between winter-like and spring-like communities and moved toward a more coherent transitional or early-spring position.

April and May show a more mixed spatial pattern. Their average entropy increased moderately, but the heatmaps reveal that this increase was not uniform across the basin. In April, entropy increased clearly at Győr, Košice, Cluj-Napoca and Deva, while it decreased at Kecskemét, Pécs and Brașov. May also shows both positive and negative changes depending on location. This means that the spring transition did not reorganise in a single regional direction. Instead, it changed through locally different adjustments in the position of individual months.

September remained one of the most complex months in the annual cycle. Its entropy was already high in the early period and remained high in the late period as well. The heatmaps show that September continued to have elevated entropy values at most locations, with particularly high late-period values at Oradea and Pécs. This confirms its persistent transitional character. September does not behave as a stable late-summer or early-autumn month only, but as a climatic boundary zone where different seasonal signals overlap.

October became more fragmented on average, but again with strong spatial differences. The largest increases appear at Győr, Kecskemét, Keszthely and Oradea, while Košice and Brașov show decreases. November remained almost unchanged in the basin-wide average, although the change heatmap shows that this apparent stability hides local contrasts: entropy increased at some locations, such as Košice and Oradea, but decreased at others, including Keszthely, Kecskemét, Cluj-Napoca and Deva.

Overall, the entropy results support the interpretation that the core months of winter and summer remained relatively stable, while the transition months underwent the strongest reorganisation. The annual cycle therefore changed mainly through the restructuring of its seasonal margins rather than through a uniform shift affecting all months equally.

4.3. Prototype similarities and cross-seasonal shifts

The prototype similarity matrices provide a direct comparison between the typical monthly climatic states of the early and late periods. They help to identify whether the same calendar months remained close to their earlier climatic position, or whether stronger cross-seasonal similarities appeared.

The general pattern confirms that the main annual structure was preserved. Winter months remained most similar to winter-like late-period states, and the summer months continued to form a clearly recognisable warm-season block. This means that the basic seasonal order did not disappear. The networks do not indicate a collapse of the annual cycle into an undifferentiated structure (**Fig. 6**).

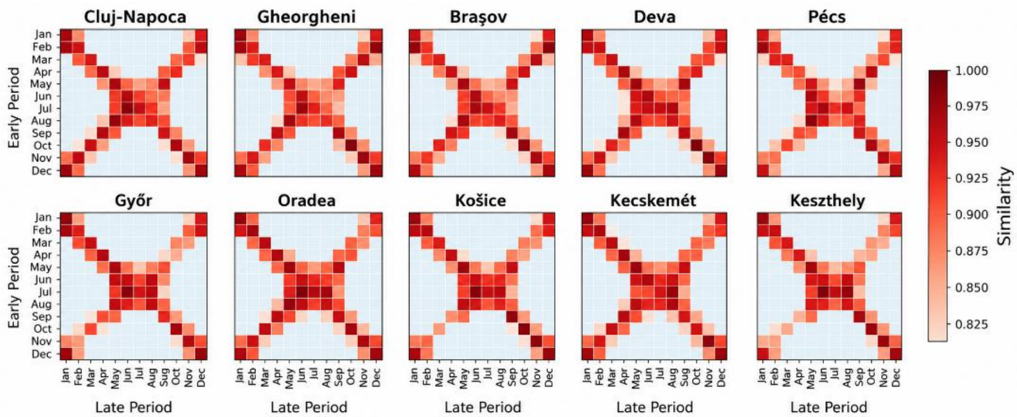

Fig. 6. Mean prototype similarity by location.

The most informative changes appear outside the diagonal of the prototype matrices. These off-diagonal similarities show where months from the early period became strongly connected to different months in the late period. After applying the structural thresholds, several spring–autumn and late-summer–autumn overlaps remained visible. This indicates that these similarities were not only weak background relations, but part of the stronger network structure.

The case of Pécs illustrates this pattern clearly (**Fig. 7**). In the thresholded prototype matrix, early April shows a very high similarity to late October, with a value of 0.95. Early May is most strongly linked to late September, with a similarity of 0.97. These values point to a stronger overlap between spring, late-summer and autumn transitional states. The result should not be interpreted as a direct replacement of one month by another, but rather as evidence that the climatic similarity field of transitional months became more interconnected.

Similar patterns also appear at other locations, although with different strength. The thresholded matrices show that even after removing weaker background similarities, the transition periods retain important cross-seasonal links. This is consistent with the entropy results: the largest changes are not located in the stable winter and summer cores, but in the months where seasonal identities are naturally less fixed.

The prototype analysis therefore adds an important layer to the results. Community detection shows that the seasonal blocks became less sharply separated, and Shannon entropy identifies which months became more or less fragmented. The prototype matrices show how this reorganisation appears in terms of direct month-to-month similarity between the two periods.

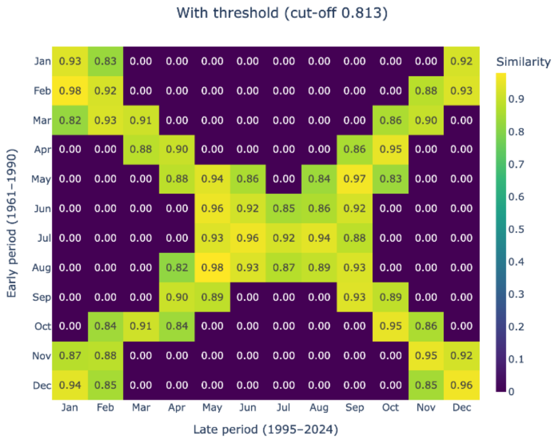

Fig. 7. Thresholded prototype similarity matrix of Pécs.

4.4. Percolation robustness

Percolation analysis was used to evaluate whether the observed seasonal reorganisation also involved a weakening of the whole network backbone. The percolation indices remained close to zero at the selected locations, indicating only moderate changes in global network robustness.

Across the ten locations, the percolation index ranged from −0.01419 to +0.01002, with an average value of −0.00257. The average direction of change was therefore slightly negative, meaning that the late-period networks tended to fragment at somewhat lower similarity thresholds considering the whole Carpathian Basin.

At the same time, different types of changes in this indicator can be observed at each location and they can be grouped into three broad categories (**Fig. 8**). The first group includes locations with negative percolation indices, where the late-period network became slightly more fragile. This group includes Brașov, Deva, Pécs, Košice, Kecskemét and Cluj-Napoca. The strongest negative shift was found in Brașov (**Fig. 9**), where the index reached −0.01419 and the critical threshold decreased from approximately 0.971 to 0.957. Deva also showed a relatively stronger negative value, while the changes at Košice, Kecskemét and Cluj-Napoca were smaller.

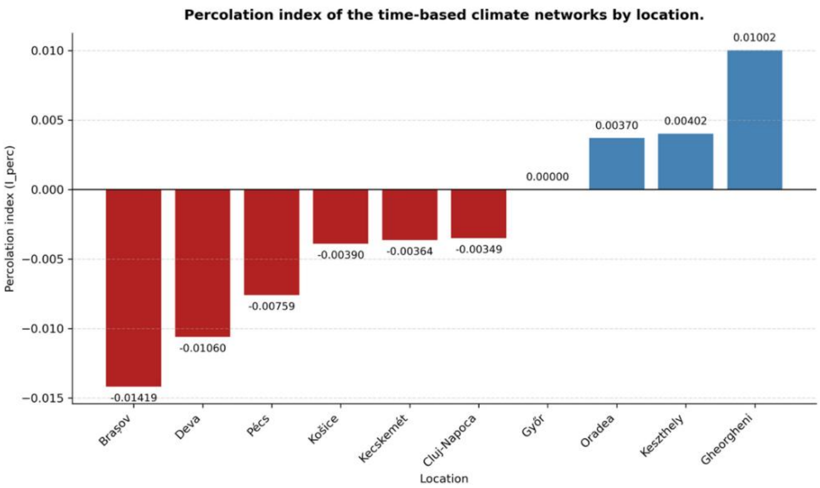

Fig. 8. Percolation index by location.

A second group includes location where the index was zero, in our case Győr. In this case, the late-period network remained connected up to a slightly higher similarity threshold. This shows that local or monthly reorganisation does not necessarily mean that the full network becomes weaker. A network can become more internally differentiated while its strongest connections remain stable or even slightly stronger.

The third group consists of locations where the percolation index presents positive values: Gheorgheni, Oradea and Keszthely. At these sites, the percolation curves suggest that a local gain in structural robustness is present.

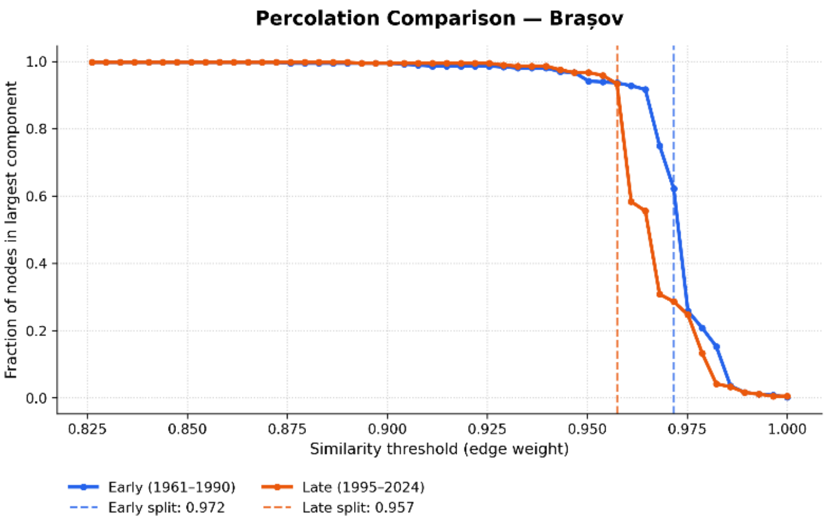

Fig. 9. Percolation Comparison for Brasov

5. DISCUSSION

The time-based climate network analysis demonstrates that recent climate change in the Carpathian Basin manifests not merely as a shift in isolated variables, but as a systemic structural reconfiguration of seasonality. The preservation of the core winter and summer communities across all ten locations indicates that the macro-level, seasonal cycle remains fundamentally intact. However, the universal decrease in network modularity reveals that the boundaries separating these seasonal blocks have become less distinct in the contemporary period. Rather than a collapse of the annual cycle or a simple increase in climate volatility, these findings point toward a highly organized, location-specific redistribution of climatic similarity, concentrated primarily at the margins of the traditional seasons.

The most coherent basin-wide signal emerges during the late winter and early spring transition, characterized by an asymmetry between February and March. In the historical baseline period, March was characterized by elevated Shannon entropy, acting as a volatile, fragmented bridge between winter-like and spring-like states. In the recent period, March has stabilized into a more consistent, coherent transitional position. Concurrently, February has experienced a profound surge in fragmentation across nine of the ten studied locations. This macro-regional inversion suggests a structural phase advancement in the onset of spring-like conditions, a phenomenon that echoes the large-scale seasonal changes observed across Europe by Stine et al. (2009). Late winter is no longer consistently anchored to the core cold-season regime; instead, it frequently fluctuates toward warmer, transitional states. This increased structural ambiguity in February matches the empirical findings of Spinoni et al. (2015a), who identified a significant increase in late-winter thermal extremes and shifting heat/cold wave frequencies within the Carpathian region.

Beyond the late-winter shift, the transitions of mid-spring (April) and autumn (September to November) reveal high spatial heterogeneity. The network indicators do not show a uniform basin-wide trend; instead, northwestern and lowland plain locations exhibit increased fragmentation during these shoulder months, whereas southeastern foothill sites and sheltered intra-mountain depressions show stable or even decreasing entropy. This localized divergence underscores the critical role of topographic controls in modulating regional climate change impacts, as highlighted by Spinoni et al. (2015b). The open, lowland landscapes of the Pannonian Basin are highly susceptible to shifting advective regimes and moisture fluctuations, leading to highly variable transitional states. Conversely, the weaker or more spatially variable changes observed at mountain-influenced locations may be partly related to topographic control, but this interpretation remains tentative. E-OBS represents grid-cell-scale climatic conditions and may smooth elevation gradients, valley inversions, cold-air pooling and local orographic precipitation. The apparent contrast between lowland and mountain-influenced sites should therefore be interpreted as a regional grid-scale pattern rather than as direct evidence of local microclimatic buffering. These complex local responses confirm that broad geographical generalizations are insufficient for tracking seasonal architecture, aligning with the highly localized variations in regional climate indices modelled by Megyeri-Korotaj et al. (2023).

The prototype similarity matrices provide a direct look into the nature of this structural mixing, uncovering off-diagonal relationships between entirely different parts of the annual cycle. The high multi-dimensional similarity observed between early spring (April/May) and mid-to-late autumn (September/October) indicates that the climatic profiles of these shoulder periods are increasingly overlapping. This cross-seasonal convergence suggests a flattening of the transition gradients within the basin. As shoulder seasons expand and increasingly mimic one another, the distinct meteorological identities of spring and autumn become blurred. This systemic blending of transitional states could have important implications for regional water cycles, agricultural growing windows, and environmental stability, corroborating the compounding hydrological tendencies discussed by Bartholy and Pongrácz (2007) and Jánosi et al. (2023).

The applied relevance of this seasonal reorganisation is also apparent in mountain recreation and geoheritage management. In Harghita County, trail-hazard assessment has been conceptualised as a combination of static topographic properties and dynamic environmental factors, including rain, fog, wind and storms, for which regularly updated observations are required (Magyari-Sáska, 2014). Regional geomorphosite research has likewise evaluated volcanic landforms through a combination of scientific, landscape, cultural-historical, ecological and socio-economic values in order to support their classification and geotourism use (Irimuș et al., 2015). More recently, a quantitative geopark-attractiveness framework has explicitly incorporated extreme temperature as a natural-hazard attribute within its safety and risk component (Nyulas et al., 2024). The climate-network results presented here do not directly quantify trail danger, visitor demand or destination attractiveness. Nevertheless, the increasing ambiguity of late winter and the stronger similarity between spring and autumn states indicate that fixed calendar-based assumptions about outdoor-activity seasons may become progressively less reliable. This interpretation is consistent with research showing that hiking suitability depends on multiple atmospheric conditions and that climate change may redistribute both opportunities and constraints across summer and shoulder seasons (Martínez Ibarra et al., 2019; Pröbstl-Haider et al., 2021). In geotourism, such changes may also affect visitor comfort, site accessibility and exposure to climate-related natural hazards (Gordon, 2023). Time-based climate networks could therefore provide a regional climatic layer for updating trail information, risk communication and geopark planning, especially in mountain-influenced locations.

The percolation analysis qualifies these findings by demonstrating that this internal restructuring did not cause a major degradation of global network connectivity. The mean percolation index remained close to zero across the basin, with subtle localized shifts toward fragility or robustness depending on the site's physiographic setting. This behaviour shows that a climate network can experience enhanced internal overlap and weaker community boundaries at its boundaries while maintaining the absolute stability of its core structural backbone.

From a methodological perspective, adapting a temporal-node framework to climate networks provides a valuable complement to conventional trend and anomaly analyses. Traditional grid-cell networks excel at highlighting spatial teleconnections and regional coupling, but they obscure the internal structural relationships between temporal states. By treating individual month-year observations as distinct multidimensional vectors, this approach successfully captures changes in the systemic architecture of seasonality that are invisible when variables are analysed in isolation.

Three methodological settings are relevant when considering the robustness of the analysis: the number of retained PCA components, the target average degree used for network pruning, and the resolution parameter of the Leiden community-detection algorithm. These settings were defined prior to the comparison and were applied identically to all locations and both periods. The retention of two principal components was supported by the high cumulative proportion of variance explained by the first two components, which ranged from 91.5% (Gheorgheni) to 93.7% (Kecskemét) across the ten locations. The two-dimensional PCA representation therefore preserved the dominant structure of the six climatic variables, while also providing a consistent and parsimonious similarity space. The use of additional components would introduce only a comparatively limited amount of residual variance and would reduce the interpretability of the common distance space.

The target average degree was likewise not selected as an arbitrary tuning parameter, but was derived analytically from the expected seasonal neighbourhood of each node. In a 30-year period, each year–month observation can be associated with the other 29 occurrences of the same calendar month and with the 30 occurrences of each adjacent month, resulting in a target average degree of $29 + 30 + 30 = 89$. Changing this value would therefore imply a different assumption about the temporal extent of the seasonal neighbourhood rather than a minor adjustment of network density. Finally, the Leiden resolution parameter was set to its standard value of 1.0, corresponding to the conventional weighted-modularity formulation. It was not optimised separately by location or period, thereby avoiding a posteriori adjustment of community granularity. Although alternative resolution values may affect the exact number or boundaries of detected communities, the use of a common standard setting, together with the recurrence of the main patterns across locations and across complementary indicators, supports the internal consistency of the comparison. This does not imply complete parameter invariance, but it reduces the likelihood that the principal conclusions are artefacts of location- or period-specific parameter tuning.

Several limitations must be considered when interpreting these outcomes. The analysed E-OBS values are spatially interpolated grid-cell estimates rather than direct observations at the selected cities. Interpolation uncertainty varies with station density and may also change through time as the underlying observational network changes. Previous evaluations have shown that gridded estimates are generally less reliable for spatially heterogeneous variables, particularly precipitation, and in regions characterised by sparse observations or complex terrain (Hofstra et al., 2009; Cornes et al., 2018). At the 0.1° grid scale, local elevation contrasts, slope exposure, valley inversions, cold-air pooling and fine-scale orographic precipitation cannot be fully represented. This limitation is particularly relevant for Gheorgheni and Brașov and, to a lesser extent, for the other foothill and basin locations. Consequently, the location-specific results should be interpreted as regional grid-cell-scale signals rather than as exact descriptions of urban or valley-floor microclimates. Monthly aggregation and the consistent use of the same grid cells in both periods may reduce the influence of short-term random interpolation errors, but they do not eliminate systematic topographic smoothing, temporal changes in station density or possible inhomogeneities in the input observations.

Because the analysis parameters were held strictly constant across both analysis intervals, the comparative validity between the periods remains robust. However, the 30-year snapshot comparison is inherently static; it identifies clear structural differences between the two blocks but cannot trace the exact timing, velocity, or continuity of the transition. Integrating moving-window network formulations and comprehensive sensitivity testing represents a highly promising avenue for future extensions of this research.

6. CONCLUSIONS

This study used a time-based climate-network approach to compare the seasonal organisation of climate in the Carpathian Basin during 1961–1990 and 1995–2024. The annual cycle remained recognisable in the later period: winter and summer cores persisted, while seasonal communities became less clearly separated at all ten locations.

The strongest reorganisation affected transition months. February became more fragmented at nine locations, whereas March became more coherent everywhere. April showed increased fragmentation at Győr, Košice, Cluj-Napoca and Deva, but decreases at Kecskemét, Pécs and Brașov. October became more fragmented at Győr, Kecskemét, Keszthely and Oradea, while Košice and Brașov showed decreases. September remained a persistent boundary month, and at Pécs strong off-diagonal prototype similarities confirmed greater overlap between spring and autumn climatic states.

Percolation results indicate that these changes did not produce a general loss of network robustness. Brașov and Deva showed the clearest weakening, with smaller negative shifts at Pécs, Košice, Kecskemét and Cluj-Napoca. Győr remained essentially unchanged, whereas Gheorgheni, Oradea and Keszthely showed modest gains. The findings indicate a moderate reorganisation rather than a collapse of seasonality. Climate change altered the relationships between monthly climatic states mainly at seasonal boundaries, while the core annual structure remained intact. Time-based climate networks therefore complement conventional trend analysis by revealing structural changes not captured by individual climatic variables alone.

REFERENCES

Bartholy, J. and Pongrácz, R. (2007) Regional analysis of extreme temperature and precipitation indices for the Carpathian Basin from 1946 to 2001, *Global and Planetary Change*, 57(1–2), pp. 83–95. doi: 10.1016/j.gloplacha.2006.11.002.

Donges, J.F., Zou, Y., Marwan, N. and Kurths, J. (2009) Complex networks in climate dynamics, *The European Physical Journal Special Topics*, 174, pp. 157–179. doi: 10.1140/epjst/e2009-01098-2.

Fan, J., Meng, J., Ashkenazy, Y., Havlin, S. and Schellnhuber, H.J. (2018) Climate network percolation reveals the expansion and weakening of the tropical component under global warming, *Proceedings of the National Academy of Sciences of the United States of America,* 115(52), pp. E12128–E12134. doi: 10.1073/pnas.1811068115.

Gordon, J.E. (2023) Climate change and geotourism: impacts, challenges, and opportunities, *Tourism and Hospitality*, 4(4), pp. 514–538. doi: 10.3390/tourhosp4040032

Hajek, O.L. and Knapp, A.K. (2022) Shifting seasonal patterns of water availability: ecosystem responses to an unappreciated dimension of climate change, *New Phytologist,* 233(1), pp. 119–125. doi: 10.1111/nph.17728.

Holme, P. and Rocha, J.C. (2023) Networks of climate change: connecting causes and consequences, *Applied Network Science,* 8(1), article 10, pp. 1–20. doi: 10.1007/s41109-023-00536-9.

Holme, P. and Saramäki, J. (2012) Temporal networks, *Physics Reports,* 519(3), pp. 97–125. doi: 10.1016/j.physrep.2012.03.001.

Irimuș, I.A., Bálint-Bálint, L., Dombay, Ș., Crișan, H.F. and Magyari-Sáska, Z. (2015) Classification and evaluation criteria for volcanic geomorphosites in Harghita Mountains, *15th International Multidisciplinary Scientific GeoConference SGEM 2015, Conference Proceedings, Volume I: Geology, Mineral Processing, Oil and Gas Exploration*, pp. 77–84.

Jánosi, I.M., Bíró, T., Lakatos, B.O., Gallas, J.A.C. and Szöllősi-Nagy, A. (2023) Changing water cycle under a warming climate: Tendencies in the Carpathian Basin, *Climate,* 11(6), article 118. doi: 10.3390/cli11060118.

Ludescher, J., Bunde, A. and Schellnhuber, H.J. (2023) Forecasting the El Niño type well before the spring predictability barrier, *npj Climate and Atmospheric Science,* 6, article 196. doi: 10.1038/s41612-023-00519-8.

Magyari-Sáska, Z. (2014) Quantifying threats along tourist trails: an initial approach, *Geographia Technica*, 9(1), pp. 78–86.

Martínez Ibarra, E., Gómez Martín, M.B., Armesto López, X.A. and Pardo Martínez, R. (2019) Climate preferences for tourism: perceptions regarding ideal and unfavourable conditions for hiking in Spain, *Atmosphere*, 10(11), article 646. doi: 10.3390/atmos10110646

Megyeri-Korotaj, O.A., Bán, B., Suga, R., Allaga-Zsebeházi, G. and Szépszó, G. (2023) Assessment of climate indices over the Carpathian Basin based on ALADIN5.2 and REMO2015 regional climate model simulations, *Atmosphere,* 14(3), article 448. doi: 10.3390/atmos14030448.

Mucha, P.J., Richardson, T., Macon, K., Porter, M.A. and Onnela, J.-P. (2010) Community structure in time-dependent, multiscale, and multiplex networks, *Science,* 328(5980), pp. 876–878. doi: 10.1126/science.1184819.

Newman, M.E.J. (2006) Modularity and community structure in networks, *Proceedings of the National Academy of Sciences of the United States of America,* 103(23), pp. 8577–8582. doi: 10.1073/pnas.0601602103.

Nyulas, J., Dezsi, Ș., Haidu, I., Magyari-Sáska, Z. and Niță, A. (2024) Attractiveness assessment model for evaluating an area for a potential geopark – Case study: Hațeg UNESCO Global Geopark (Romania), *Land*, 13(2), article 148. doi: 10.3390/land13020148

Pröbstl-Haider, U., Hödl, C., Ginner, K. and Borgwardt, F. (2021) Climate change: impacts on outdoor activities in the summer and shoulder seasons, *Journal of Outdoor Recreation and Tourism*, 34, article 100344. doi: 10.1016/j.jort.2020.100344

Shannon, C.E. (1948) A mathematical theory of communication, *The Bell System Technical Journal,* 27(3), pp. 379–423, 623-656. doi: 10.1002/j.1538-7305.1948.tb01338.x.

Spinoni, J., Lakatos, M., Szentimrey, T., Bihari, Z., Szalai, S., Vogt, J. and Antofie, T. (2015a) Heat and cold waves trends in the Carpathian Region from 1961 to 2010, *International Journal of Climatology,* 35(14), pp. 4197–4209. doi: 10.1002/joc.4279.

Spinoni, J., Szalai, S., Szentimrey, T., Lakatos, M., Bihari, Z., Nagy, A., Németh, Á., Kovács, T., Mihic, D., Dacic, M., Petrovic, P., Kržič, A., Hiebl, J., Auer, I., Milkovic, J., Štepánek, P., Zahradníček, P., Kilar, P., Limanowka, D., Pyrc, R., Cheval, S., Birsan, M.-V., Dumitrescu, A., Deak, G., Matei, M., Antolovic, I., Nejedlik, P., Štastný, P., Kajaba, P., Bochníček, O., Galo, D., Mikulová, K., Nabyvanets, Y., Skrynyk, O., Krakovska, S., Gnatiuk, N., Tolasz, R., Antofie, T. and Vogt, J. (2015b) Climate of the Carpathian Region in the period 1961–2010: climatologies and trends of 10 variables, *International Journal of Climatology,* 35(7), pp. 1322–1341. doi: 10.1002/joc.4059.

Stine, A.R., Huybers, P. and Fung, I.Y. (2009) Changes in the phase of the annual cycle of surface temperature, *Nature*, 457, pp. 435–440. doi: 10.1038/nature07675.

Stine, A.R. and Huybers, P. (2012) Changes in the seasonal cycle of temperature and atmospheric circulation, *Journal of Climate*, 25(21), pp. 7362–7380. doi: 10.1175/JCLI-D-11-00470.1.

Traag, V.A., Waltman, L. and van Eck, N.J. (2019) From Louvain to Leiden: guaranteeing well-connected communities, *Scientific Reports,* 9, article 5233. doi: 10.1038/s41598-019-41695-z.

Tsonis, A.A. and Roebber, P.J. (2004) The architecture of the climate network, *Physica A: Statistical Mechanics and its Applications,* 333, pp. 497–504. doi: 10.1016/j.physa.2003.10.045.

Tsonis, A.A., Swanson, K.L. and Roebber, P.J. (2006) What do networks have to do with climate?, *Bulletin of the American Meteorological Society,* 87(5), pp. 585–596. doi: 10.1175/BAMS-87-5-585.

STATISTICAL AND OPERATIONAL ASSESSMENT OF FOG-WATER HARVESTING UNDER COMMUNITY-BASED MONITORING IN SEMI-ARID NORTHERN CHILE: FIVE-YEAR EVIDENCE FROM PEÑA BLANCA

Marilyn CEPEDA-VELASTEGUI [1] & Nicolás SCHNEIDER [2]*

DOI: 10.21163/GT_2026.213.13

ABSTRACT

This study evaluates the statistical and operational performance of fog-water harvesting in the Peña Blanca Agricultural Community, Coquimbo Region, semi-arid northern Chile, using community-based monitoring records from 2020 to 2025. Standard Fog Collectors equipped with Raschel 35% double-layer and Kimre meshes were analyzed through paired comparisons, non-parametric seasonal tests, precipitation-based sensitivity analysis, and correlation analyses with monthly precipitation from a reference meteorological station. Kimre consistently outperformed Raschel 35% double-layer mesh under the local operational conditions analyzed, with an average relative advantage of approximately 25% and statistically significant differences in both parametric and non-parametric tests. This advantage persisted after excluding months with precipitation above 20 mm and under dry or negligible-precipitation conditions, where the relative advantage reached 27.4%. Correlation analyses showed no positive association between monthly precipitation and fog-water collection. Fog-water collection also showed marked seasonal variability, with higher values during spring and summer and lower values toward autumn and winter. These findings provide five-year statistical and operational evidence from a functioning community-managed system, highlighting the relevance of mesh selection, seasonal planning, and sustained monitoring for fog-water harvesting under real field conditions.

Keywords: *Atmospheric water; Fog-water harvesting; Standard Fog Collector; Fog-collector mesh performance; Semi-arid coastal environments.*

1. INTRODUCTION

Arid and semi-arid coastal regions face increasing challenges in securing reliable water supplies due to climatic variability, strong seasonality of precipitation, and growing pressure on conventional water sources (Qadir et al., 2021). In semi-arid northern Chile, these conditions are particularly relevant in rural and dispersed settlements, where water availability is constrained by both hydroclimatic variability and structural limitations in access to water (Montecinos et al., 2016; Nicolas-Artero & Blanco-Wells, 2025). At the same time, the interaction between the Pacific Ocean, coastal relief, and atmospheric circulation favors recurrent fog occurrence, creating opportunities to explore fog water harvesting as a complementary water source in areas affected by water scarcity (Schemenauer & Cereceda, 1994; Klemm et al., 2012; Montecinos et al., 2018).

Fog water harvesting is commonly described as a passive water-supply technique in which suspended fog droplets are intercepted by vertical mesh collectors and then drained into a storage system (Schemenauer & Cereceda, 1994; Klemm et al., 2012). Standard Fog Collectors (SFCs) have been widely used to quantify fog-water yield and compare collection potential across sites (Schemenauer & Cereceda, 1994).

----

[1]Heidelberg Center for Latin America, Santiago de Chile, Chile, geociencia@heidelbergcenter.cl*
[2] Fundación Un Alto en el Desierto, Ovalle, Chile, nicolas.schneider@unaltoeneldesierto.cl

Previous research in Chile and other dryland environments has shown that fog collection depends not only on fog occurrence, but also on local meteorological variables, including wind speed and direction, relative humidity, dew point depression, and the design and material properties of the collecting mesh (Klemm et al., 2012; Montecinos et al., 2018; Fernandez et al., 2018). These factors generate high temporal variability in fog-water yield and make long-term field observations essential for understanding the operational behavior of fog harvesting systems.

In Chile, several studies have demonstrated the potential of fog collection in coastal desert and semi-arid environments (Cereceda et al., 1992; Osses et al., 1998; Larraín et al., 2002; Farías et al., 2005). More recent contributions have advanced from field-based monitoring to spatial and climatic modeling approaches, allowing fog-water potential to be estimated at broader territorial scales (Montecinos et al., 2018; Lobos-Roco et al., 2025; Carter et al., 2025). However, despite these advances, long-term operational assessments under community-managed conditions remain relatively limited. This gap is relevant because the performance and continuity of fog harvesting systems depend not only on atmospheric suitability and technical efficiency, but also on maintenance, local monitoring capacity, and the practical conditions under which systems operate over time (Fessehaye et al., 2014; Qadir et al., 2021; Ait el Kadi et al., 2024; Rivera et al., 2026).

The Peña Blanca Agricultural Community, located in the Coquimbo Region of semi-arid northern Chile, provides a relevant case for analyzing fog-water harvesting under real operational conditions. In this territory, fog collection is embedded in a community-managed system where local knowledge, site selection, monitoring practices, and maintenance routines support the continuity of the infrastructure. From a technical perspective, the available five-year monitoring record offers an opportunity to evaluate standardized daily fog-water collection, compare the performance of Raschel 35% double-layer and Kimre meshes under paired field conditions, and assess whether the observed mesh-performance patterns are robust across monthly precipitation conditions.

This study provides a statistical and operational assessment of fog-water harvesting in the Peña Blanca Agricultural Community between 2020 and 2025. Drawing on community-based monitoring records, the article analyzes paired mesh-performance differences, applies precipitation-based sensitivity analysis, evaluates monthly precipitation–collection patterns, and characterizes seasonal variability. In doing so, it provides original site-specific evidence from a functioning community-managed fog harvesting system and contributes to understanding the role of fog harvesting as a strategic complementary water source in semi-arid coastal environments.

2. STUDY AREA

The study was conducted in the Peña Blanca Agricultural Community, located in the municipality of Ovalle, Coquimbo Region, semi-arid northern Chile. This territory forms part of a coastal semi-arid environment where the interaction between the Pacific Ocean, coastal relief, and local atmospheric circulation favors the recurrent occurrence of advective fog, supporting the potential use of fog water harvesting as a complementary water source (Klemm et al., 2012; Montecinos et al., 2016; del Río et al., 2018).

The monitoring site is situated in the Cerro Grande Ecological Reserve, a community-owned area where fog harvesting infrastructure has been developed over time. The area represented in **Fig.1** shows marked topographic contrasts, with elevations ranging approximately from 232 to 673 m a.s.l. These relief conditions are relevant because coastal topography can influence fog interception by modifying exposure to marine air masses and low-cloud advection.

The SFC monitoring point is located inside the reserve and is connected to the surrounding territory through local access roads. This setting makes Peña Blanca a relevant case for evaluating fog water harvesting under real operational conditions, since the monitoring system is embedded in a locally managed territory where access, maintenance, and measurement routines contribute to the continuity of the infrastructure.

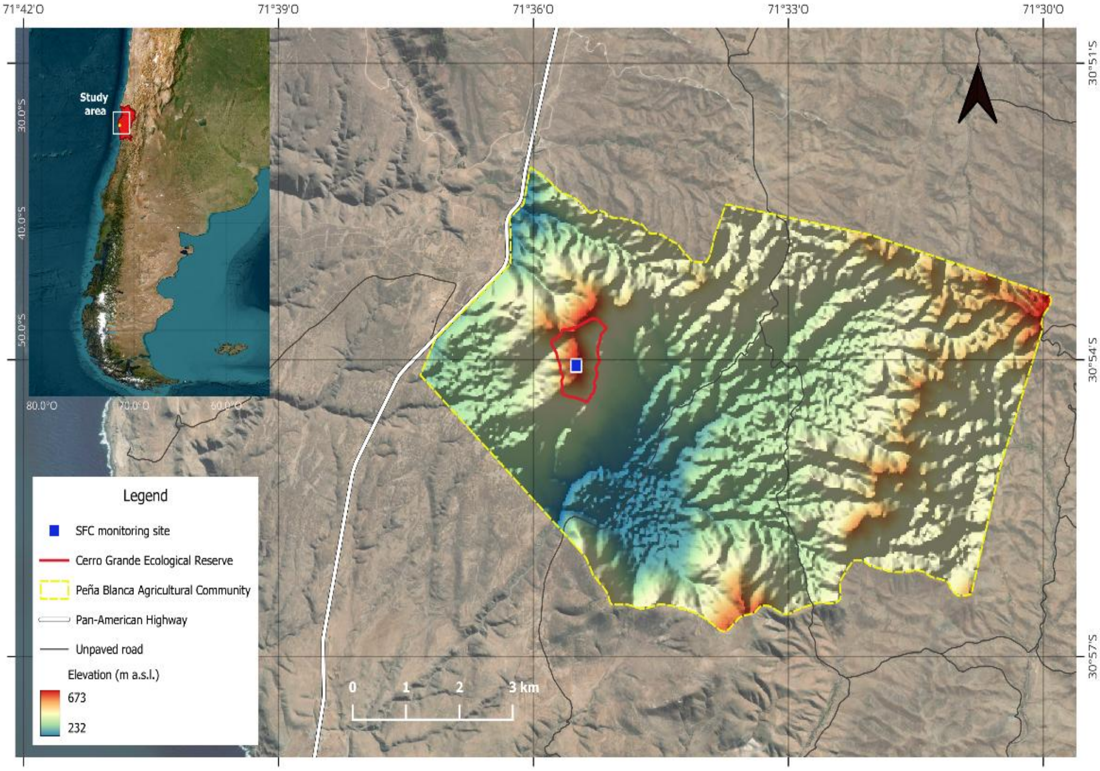

Fig. 1. Location of the study area in the Peña Blanca Agricultural Community, Coquimbo Region, semi-arid northern Chile.

3. DATA AND METHODS

3.1. Fog collectors and mesh materials

Fog-water collection was measured using Standard Fog Collectors, which are widely used to quantify fog-water yield on vertical collecting surfaces and to facilitate comparisons between sites (Schemenauer & Cereceda, 1994). Each SFC had an effective collecting area of 1 m², with the collecting mesh installed approximately 2 m above ground level. A lower gutter directed the collected water into a storage container.

Two mesh materials were monitored: Raschel 35% and Kimre. The collectors were installed in the same monitoring sector, approximately two meters apart, allowing their performance to be compared under similar local exposure and atmospheric conditions. The Raschel 35% collector used a double layer of 35% shade-coefficient Raschel mesh, consistent with the standard SFC configuration proposed by Schemenauer and Cereceda (1994). Raschel 35% is a Raschel-woven mesh commonly used in fog collection systems. It consists of high-density polyethylene filaments with UV protection and a triangular weave; the 35% value refers to the nominal shade coefficient of the mesh, which describes its degree of shading or obstruction.

This parameter is relevant because mesh structure and openness influence airflow through the collector, droplet interception, and drainage behavior (Schemenauer & Cereceda, 1994; Rivera, 2011; Fernandez et al., 2018). Kimre, by contrast, is a structured three-dimensional mesh made of interlocking thermoplastic monofilaments. Its volumetric configuration provides a larger contact surface than a flat mesh and was included to evaluate whether differences in mesh structure affect standardized operational collector yield under the same field conditions.

3.2. Operational monitoring and data standardization

Fog-water collection was evaluated from operational monitoring records covering the period 2020–2025. Field readings of accumulated water volume were carried out approximately every 10 days, depending on site access and operational conditions.

The monitoring process was supported by a local community operator, who conducted field measurements and periodic inspection of the collectors. To ensure temporal comparability, accumulated volumes measured between field visits were converted into standardized daily fog-water collection, expressed in $L \cdot m^{-2} \cdot day^{-1}$, following the standard area- and time-normalized reporting convention used in fog-collector studies (Schemenauer & Cereceda, 1994; Klemm et al., 2012) (Eq. 1).

$$q_i = \frac{V_i}{A \cdot \Delta t_i} \tag{1}$$

where q_i is the daily fog-water collection for period i ($L \cdot m^{-2} \cdot day^{-1}$), V_i is the accumulated volume between two consecutive readings (L), A is the effective collector area (1 m^2), and Δt_i is the number of days between consecutive readings.

3.3. Precipitation data

Monthly accumulated precipitation data were obtained from the nearest available CEAZAMET meteorological station, "Peña Blanca", operated by the Centro de Estudios Avanzados en Zonas Áridas (CEAZA, 2019). The station is located approximately 7 km from the SFC monitoring site and was used as a monthly precipitation reference for the study area. Precipitation was expressed as monthly totals in millimeters (mm) and used as auxiliary information for the precipitation-based sensitivity analysis and for evaluating monthly precipitation–collection patterns. Monthly precipitation records were paired by year and month with the corresponding monthly mean daily fog-water collection values.

3.4. Statistical analysis

Statistical analysis focused on mesh-performance differences, precipitation-based sensitivity analysis, the relationship between monthly precipitation and fog-water collection, and seasonal variability. The main comparative analysis was based on simultaneous observations for Raschel 35% and Kimre, in order to maintain a paired design and control for shared temporal variability. Standardized daily fog-water collection was aggregated by year and month to support precipitation-related and seasonal analyses.

The comparison between Raschel 35% and Kimre was performed using simultaneous observations available for both meshes. For each paired observation, the absolute difference was calculated as:

$$D_i = q_{K,i} - q_{R,i} \tag{2}$$

where D_i is the paired difference for observation i, $q_{K,i}$ is the Kimre standardized daily fog-water collection, and $q_{R,i}$ is the Raschel 35% standardized daily fog-water collection.

The relative performance ratio was calculated as:

$$G_i = \frac{q_{K,i}}{q_{R,i}} \tag{3}$$

where G_i represents the relative performance ratio of Kimre compared with Raschel 35% for each paired observation.

The hypothesis that Kimre yielded higher standardized daily fog-water collection than Raschel 35% was evaluated using a paired Student's t-test. As a non-parametric alternative, the Wilcoxon signed-rank test was also applied to assess whether the paired differences were consistently positive. In addition to statistical significance, effect size was reported using Cohen's d (Eq. 4) for paired samples (Cohen, 1988).

$$d = \frac{\bar{D}}{s_D} \tag{4}$$

where $\bar{D}$ is the mean paired difference and s_D is the standard deviation of the paired differences. This allowed the practical magnitude of the difference between mesh materials to be interpreted beyond the p-value.

To assess whether mesh-performance differences were sensitive to monthly precipitation conditions, a precipitation-based sensitivity analysis was conducted using precipitation records from the CEAZAMET Peña Blanca station. The paired Kimre–Raschel comparison was repeated under three precipitation-screening scenarios: all paired months with available precipitation data, after excluding months with precipitation above 20 mm, and considering only dry or negligible-precipitation months with precipitation equal to or below 5 mm. These thresholds were used to screen records according to monthly precipitation conditions, distinguishing months with higher precipitation from months with low or minimal precipitation. For each scenario, mean Raschel and Kimre fog-water collection rates, mean paired differences, relative advantage, paired t-tests, Wilcoxon signed-rank tests, and Cohen's d were calculated.

For the relationship between monthly precipitation and standardized daily fog-water collection, monthly accumulated precipitation totals were paired by year and month with the corresponding monthly mean daily fog-water collection. Pearson's correlation coefficient (Eq. 5) was used to evaluate the linear association between both variables:

$$r = \frac{\sum_{i=1}^{n}(P_i-\bar{P})(q_i-\bar{q})}{\sqrt{\sum_{i=1}^{n}(P_i-\bar{P})^{2}}\sqrt{\sum_{i=1}^{n}(q_i-\bar{q})^{2}}} \tag{5}$$

where P_i is monthly precipitation, q_i is monthly mean daily fog-water collection, and $\bar{P}$ and $\bar{q}$ are their respective means.

Spearman's rank correlation coefficient (Eq. 6) was also calculated as a non-parametric measure of monotonic association, appropriate when the relationship between variables may not be linear or when the data do not meet normality assumptions (Hollander et al., 2013):

$$\rho = \frac{\sum_{i=1}^{n}(R(P_i)-\overline{R(P)})(R(q_i)-\overline{R(q)})}{\sqrt{\sum_{i=1}^{n}(R(P_i)-\overline{R(P)})^{2}}\sqrt{\sum_{i=1}^{n}(R(q_i)-R(\bar{q})^{2}}} \tag{6}$$

where $R(P_i)$ and $R(q_i)$ are the ranks of monthly precipitation and monthly mean daily fog-water collection, respectively, and the overbars indicate their mean ranks.

In addition, monthly mean daily fog-water collection was explored across precipitation ranges of 0–5 mm, 5–20 mm, and >20 mm to identify whether collection rates varied systematically under different monthly precipitation conditions.

Seasonal variability was analyzed by calendar month and by austral seasons: summer (December–February), autumn (March–May), winter (June–August), and spring (September–November). For the seasonal analysis, monthly mean daily fog-water collection was calculated by aggregating the operational records by year and month. Accumulated volumes assigned to each month were summed and divided by the number of days in the corresponding month, producing monthly values expressed in $L \cdot m^{-2} \cdot day^{-1}$. These monthly values were used to compare seasonal behavior among months and seasons. Seasonal differences were tested separately for each mesh using the Kruskal–Wallis test, given that fog-water collection records may show asymmetric distributions, heteroscedasticity, and unequal data availability among seasonal groups.

For this reason, a non-parametric test that does not require the assumption of normality was preferred (Kruskal & Wallis, 1952). The Kruskal–Wallis statistic was expressed as:

$$H = \frac{12}{N(N+1)} \sum_{j=1}^{k} \frac{R_j^2}{n_j} - 3(N+1) \quad (7)$$

where N is the total number of observations, k is the number of seasonal groups, R_j is the sum of ranks for group j, and n_j is the number of observations in group j.

The main paired mesh comparison included all simultaneous Kimre–Raschel observations, whereas precipitation-based analyses were restricted to paired observations with available monthly precipitation records. All analyses were conducted using complete cases for the variables required in each specific test, and statistical significance was assessed at $\alpha = 0.05$.

4. RESULTS AND DISCUSSIONS

4.1. Mesh performance and paired comparison

Considering all simultaneous observations available for both meshes, Kimre showed a higher standardized daily fog-water collection than Raschel 35% double-layer mesh (**Table 1**). Raschel 35% recorded a mean value of 6.82 $L \cdot m^{-2} \cdot day^{-1}$, while Kimre reached 8.51 $L \cdot m^{-2} \cdot day^{-1}$. The mean paired difference was 1.69 $L \cdot m^{-2} \cdot day^{-1}$ in favor of Kimre, corresponding to an average relative advantage of 24.8%. The effect size was $d = 0.75$, indicating a moderate to relevant difference between mesh materials.

The hypothesis tests confirmed this difference. The paired t-test showed statistically significant differences between meshes, with $t = 6.07$ and $p = 3.70 \times 10^{-8}$ for the one-tailed test. The Wilcoxon signed-rank test produced consistent results, with $W = 1860$ and $p = 7.19 \times 10^{-7}$. These results indicate that Kimre performed significantly better than Raschel 35% double-layer mesh under the operational conditions analyzed.

Table 1.

Paired comparison of standardized daily fog-water collection ($L \cdot m^{-2} \cdot day^{-1}$) between Raschel 35% double-layer and Kimre meshes during 2020–2025.

Descriptive statistics				
Paired monthly observations *n*	**Mean Raschel 35% collection**	**Mean Kimre collection**	**Mean difference Kimre – Raschel**	**Cohen's *d***
66	6.82	8.51	1.69	0.75

Hypothesis tests		
Test	**Statistic**	***p*-values**
Paired t-test	$t = 6.07$	3.70×10^{-8}
Wilcoxon signed-rank test	$W = 1860$	7.19×10^{-7}

Note: *Collection values and mean differences are expressed in $L \cdot m^{-2} \cdot day^{-1}$, p-values correspond to one-tailed tests for the hypothesis Kimre > Raschel.*

The paired pattern is further illustrated in **Fig. 2**, where simultaneous Raschel 35% double-layer and Kimre observations are compared against the 1:1 line. Points above this line indicate higher standardized daily fog-water collection for Kimre, while points below it indicate higher values for Raschel 35% double-layer mesh. Most observations are located above the line, showing that the higher mean value of Kimre reflects a recurrent pattern across paired measurements rather than a few isolated cases.

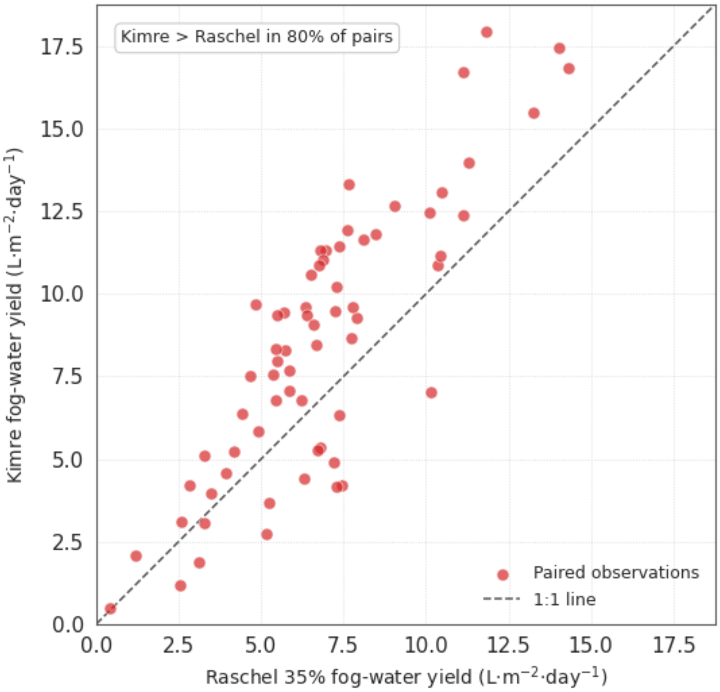

Fig. 2. Paired comparison of standardized daily fog-water collection between Raschel 35% double-layer and Kimre meshes during simultaneous observations.

The higher standardized daily fog-water collection observed for Kimre shows that mesh material can substantially influence collector performance under local operational conditions. In Peña Blanca, the paired design allowed both meshes to be compared during the same monitoring periods and in the same sector, reducing the influence of temporal variability in fog occurrence and minimizing differences in local exposure conditions.

This result is consistent with previous studies showing that fog-water collection depends not only on fog occurrence, but also on collector design and mesh properties. The Standard Fog Collector has traditionally used Raschel-type mesh because of its availability, low cost, and usefulness for comparisons among sites (Schemenauer & Cereceda, 1994; Klemm et al., 2012). However, collection efficiency can vary according to mesh geometry, filament arrangement, aerodynamic collection efficiency, droplet interception, and drainage behavior (Rivera, 2011; Fernandez et al., 2018).

From an applied perspective, the contrast between meshes has implications for the design and operation of fog harvesting systems in semi-arid coastal environments. Where water availability is limited, sustained increase in fog-water collection may improve the contribution of fog harvesting without necessarily increasing the number of collectors. However, material selection should not be based only on collection rates. Durability, cost, local availability, maintenance requirements, and long-term operational feasibility should also be considered, particularly in community-managed systems where technical performance must be compatible with local capacities and maintenance routines (Rivera, 2011; Fernandez et al., 2018).

4.2. Precipitation-based sensitivity analysis and monthly precipitation–collection patterns

The precipitation-screening analysis showed that the higher performance of Kimre persisted across all evaluated scenarios (**Table 2**). Monthly precipitation during the monitoring period was generally low and episodic within the paired dataset. Among the 63 paired monthly observations with available precipitation data, 46 months recorded 0–5 mm, six months recorded 5–20 mm, and eleven months exceeded 20 mm.

After excluding these eleven higher-precipitation months, 52 paired observations remained for the sensitivity analysis. This distribution is consistent with the broader semi-arid coastal context of northern Chile, where fog harvesting has been studied as a complementary water source in areas with limited conventional freshwater availability (Garreaud et al., 2008; del Río et al., 2018; Lobos-Roco et al., 2025).

Results obtained from the 63 paired months with available monthly precipitation data were very similar to those from the full paired mesh dataset: Raschel 35% double-layer mesh recorded a mean value of 6.88 $L \cdot m^{-2} \cdot day^{-1}$, while Kimre reached 8.56 $L \cdot m^{-2} \cdot day^{-1}$. The mean paired difference was 1.68 $L \cdot m^{-2} \cdot day^{-1}$ in favor of Kimre, corresponding to a relative advantage of 24.4%.

After excluding months with precipitation above 20 mm, 52 paired observations remained. In this subset, Kimre continued to show higher standardized daily fog-water collection than Raschel, with mean values of 8.98 and 7.18 $L \cdot m^{-2} \cdot day^{-1}$, respectively. The mean paired difference remained positive at 1.80 $L \cdot m^{-2} \cdot day^{-1}$, corresponding to a relative advantage of 25.0%. Under dry or negligible-precipitation conditions ($P \leq 5$ mm), the difference was also maintained, reaching 2.00 $L \cdot m^{-2} \cdot day^{-1}$, with Kimre averaging 9.29 $L \cdot m^{-2} \cdot day^{-1}$ compared with 7.29 $L \cdot m^{-2} \cdot day^{-1}$ for Raschel, corresponding to a relative advantage of 27.4%.

Across all precipitation-screening scenarios, the paired t-tests and Wilcoxon signed-rank tests remained statistically significant. The Kimre advantage was maintained after excluding the eleven months with precipitation above 20 mm and under dry or negligible-precipitation conditions. This consistency supports the robustness of the paired mesh comparison under the operational monitoring conditions analyzed.

Table 2.

Sensitivity analysis of Kimre–Raschel 35% double-layer performance differences under monthly precipitation-screening scenarios.

Precipitation-screening scenario	*n*	Mean Raschel 35%	Mean Kimre	Mean difference Kimre–Raschel	Relative advantage (%)	Cohen's *d*	Paired *t*-test *p*	Wilcoxon *p*
All paired months with precipitation data	63	6.88	8.56	1.68	24.4	0.73	1.38×10^{-7}	1.91×10^{-6}
Excluding months with P > 20 mm	52	7.18	8.98	1.80	25.0	0.78	3.96×10^{-7}	5.45×10^{-6}
Dry/negligible-precipitation months, P ≤ 5 mm	46	7.29	9.29	2.00	27.4	0.92	7.46×10^{-8}	4.34×10^{-7}

Note: *Collection values and mean differences are expressed in* $L \cdot m^{-2} \cdot day^{-1}$. *P refers to monthly precipitation recorded at the CEAZAMET Peña Blanca station. p-values correspond to one-tailed paired tests for the hypothesis Kimre > Raschel.*

To complement the precipitation-based sensitivity analysis, the association between monthly precipitation recorded at the CEAZAMET Peña Blanca station and monthly mean daily fog-water collection was evaluated. The association was weak and negative for both meshes: Pearson's correlation coefficient was r = −0.180 for Raschel 35% double-layer mesh and r = −0.187 for Kimre, suggesting the absence of a positive linear relationship between monthly precipitation and fog-water collection (**Fig. 3a**). These correlations were not statistically significant for either mesh, with p = 0.158 for Raschel 35% and p = 0.143 for Kimre.

Spearman's rank correlations were also negative. For Raschel 35%, Spearman's correlation was ρ = −0.261 with p = 0.039, while for Kimre it was ρ = −0.357 with p = 0.004. These results indicate that, at the monthly scale, higher precipitation values recorded at the reference station did not correspond to higher fog-water collection. Rather, the ranked data suggest a weak to moderate negative monotonic association, particularly for Kimre.

The boxplots show the distribution of monthly mean daily fog-water collection for Raschel 35% and Kimre after grouping months into three precipitation ranges: 0–5 mm, 5–20 mm, and >20 mm.

The overlap between distributions and the similarity of the medians suggest that months with higher precipitation did not show, on average, a systematic increase in fog-water collection compared with drier months (**Fig. 3b**). This pattern is consistent with the weak Pearson correlations and the negative Spearman associations observed.

The sensitivity analysis, correlation results, and precipitation-range comparison indicate that monthly precipitation records are useful for contextualizing the monitoring series, but the observed Kimre–Raschel performance difference was robust across the evaluated precipitation subsets. This supports the use of fog-specific monitoring to assess collector performance in semi-arid coastal environments as a complementary water source.

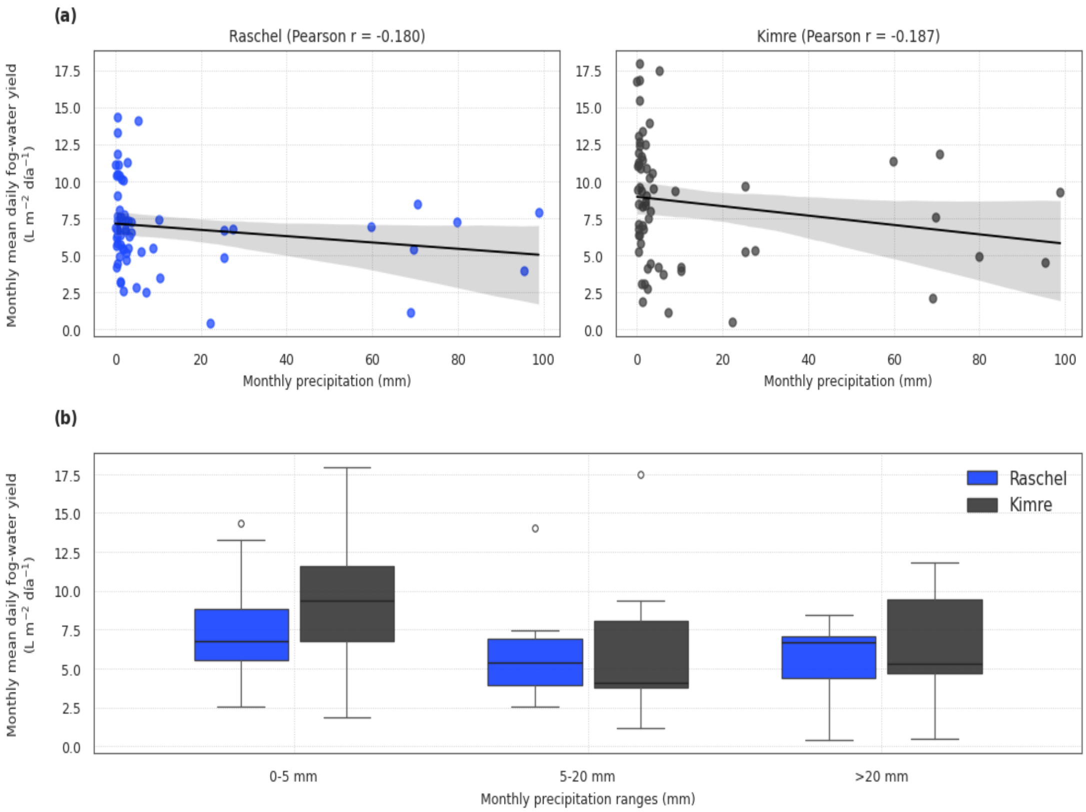

Fig. 3. Relationship between monthly precipitation and monthly mean daily fog-water collection ($L \cdot m^{-2} \cdot day^{-1}$) for Raschel 35% double-layer and Kimre meshes during 2020–2025: **(a)** scatterplots with linear trends; **(b)** boxplots of fog-water collection by monthly precipitation ranges.

4.3. Seasonal variability of fog-water collection

Fog-water collection showed a marked seasonal pattern in both meshes (**Fig. 4**). For Raschel 35% double-layer mesh, seasonal means were higher in spring (8.64 ± 3.31 $L \cdot m^{-2} \cdot day^{-1}$) and summer (7.62 ± 2.62 $L \cdot m^{-2} \cdot day^{-1}$), and lower in autumn (5.90 ± 2.70 $L \cdot m^{-2} \cdot day^{-1}$) and winter (5.64 ± 1.94 $L \cdot m^{-2} \cdot day^{-1}$). Kimre showed a similar seasonal behavior, with higher values in spring (11.36 ± 3.89 $L \cdot m^{-2} \cdot day^{-1}$) and summer (10.43 ± 3.90 $L \cdot m^{-2} \cdot day^{-1}$), and lower values in autumn (6.40 ± 3.63 $L \cdot m^{-2} \cdot day^{-1}$) and winter (6.66 ± 2.98 $L \cdot m^{-2} \cdot day^{-1}$).

Seasonal differences were statistically significant for both meshes according to the Kruskal–Wallis test. For Raschel 35%, the test yielded $H = 10.34$ and $p = 0.0159$, while for Kimre it yielded $H = 17.98$ and $p = 0.0004$. These results indicate that fog-water collection varied significantly throughout the year, with the highest values generally observed during spring and summer and the lowest values toward late autumn and early winter.

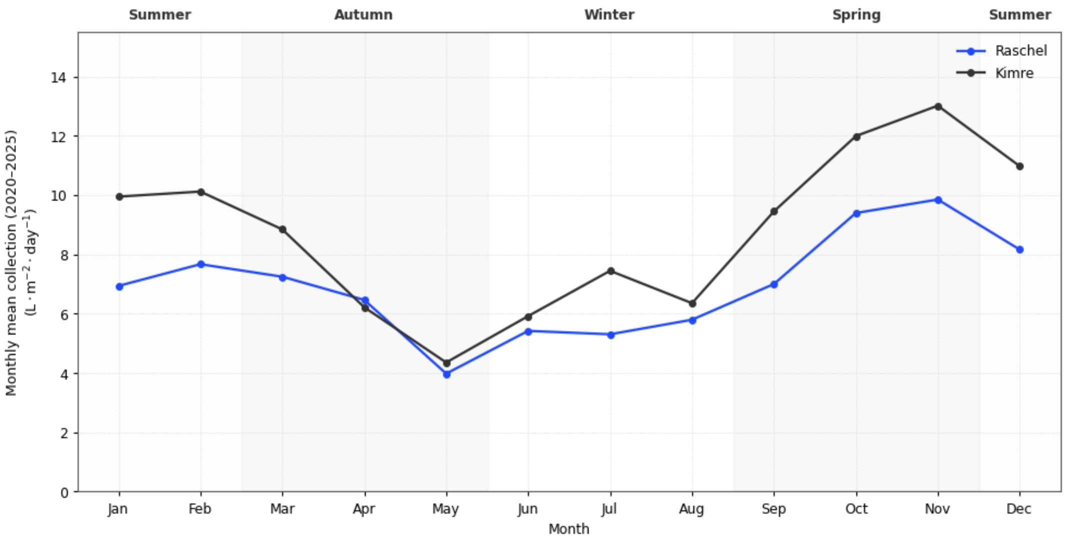

Fig. 4. Monthly mean daily fog-water collection for Raschel 35% double-layer and Kimre meshes during 2020–2025. Austral seasons are indicated above the monthly axis.

The seasonal pattern observed in Peña Blanca is consistent with the high temporal variability of coastal fog systems in semi-arid Chile and with the seasonality documented in Standard Fog Collector measurements (Klemm et al., 2012; Montecinos et al., 2018). In this case, the five-year operational record provides site-specific evidence for a community-managed fog harvesting system, where seasonal differences are directly relevant for water-use planning, storage capacity, maintenance schedules, and operational management during the months of higher production (Klemm et al., 2012; Carter et al., 2025).

This seasonal contrast indicates that fog harvesting does not provide a constant supply throughout the year, but rather a contribution concentrated in specific temporal windows. Therefore, the seasonal cycle of fog-water collection should be considered explicitly when evaluating the role of fog harvesting as a complementary water source in semi-arid coastal environments.

4.4. Fog harvesting as a complementary water source

The Peña Blanca case shows that fog harvesting can constitute a strategic complementary water source in semi-arid coastal environments, particularly where conventional freshwater availability is limited and local communities require diversified water practices. Its contribution should not be understood only in terms of isolated collection volumes, but also in relation to its capacity to support local water management when the system is continuously monitored, maintained, and integrated into community-based operational routines (Fessehaye et al., 2014; Qadir et al., 2021; Ait el Kadi et al., 2024).

A central contribution of this study is that it provides original site-specific evidence from a locally sustained operational monitoring experience in Peña Blanca. This operational perspective is relevant because long-term records from functioning community-managed fog harvesting systems are necessary to understand not only collection rates, but also the practical conditions that shape their continuity, maintenance, and performance over time.

Additionally, these findings have practical implications for the design and operation of fog harvesting systems in semi-arid coastal environments. The higher performance observed for Kimre suggests that mesh selection can improve fog-water collection under local operational conditions. However, in community-managed systems, material selection should not be based only on collection rates, but also on maintenance requirements, durability, local availability, storage capacity, and community management capacity, particularly in long-term operational systems (Fessehaye et al., 2014; Qadir et al., 2021; Ait el Kadi et al., 2024).

Likewise, the marked seasonal variability observed in Peña Blanca indicates that fog harvesting requires planning around periods of higher and lower production, rather than assuming a constant supply throughout the year (Klemm et al., 2012; Montecinos et al., 2018; Carter et al., 2025). In this sense, fog harvesting in Peña Blanca should be understood as both a technical and operational practice. Its potential contribution is shaped by the interaction between measured fog-water collection, mesh performance, storage possibilities, maintenance routines, local monitoring capacity, and community organization. This interpretation is consistent with recent work on Peña Blanca that highlights the role of collective action and territorial organization in local water practices (Di Tullio & Zannini, 2025).

5. CONCLUSIONS

This study evaluated the operational performance of fog-water harvesting in the Peña Blanca Agricultural Community, semi-arid northern Chile, using five years of locally sustained monitoring records from 2020 to 2025. The results provide original site-specific evidence from a functioning community-managed fog harvesting system and show that standardized daily fog-water collection varies according to mesh configuration and seasonal conditions under real operational monitoring.

The paired comparison showed that Kimre consistently outperformed Raschel 35% double-layer mesh under the local operational conditions analyzed. This difference was statistically significant in both parametric and non-parametric tests and represented an average relative advantage of approximately 25% in favor of Kimre. The precipitation-based sensitivity analysis reinforced this pattern: after excluding months with precipitation above 20 mm, Kimre maintained a relative advantage of 25.0%, and the advantage also persisted under dry or negligible-precipitation conditions, reaching 27.4%. In addition, the correlation analyses showed no positive association between monthly precipitation and fog-water collection. These findings indicate that the observed difference between meshes was robust across the evaluated monthly precipitation subsets and support the relevance of mesh selection for improving collector performance under community-based operational conditions.

Fog-water collection in Peña Blanca also showed marked seasonal variability, with higher values during spring and summer and lower values toward autumn and winter. This seasonal pattern indicates that fog harvesting should not be understood as a uniform supply throughout the year, but rather as a complementary contribution concentrated in specific production windows. Therefore, storage capacity, maintenance schedules, water-use planning, and local management routines are essential for sustaining its contribution over time.

The Peña Blanca case demonstrates that fog harvesting can constitute a strategic complementary water source in semi-arid coastal environments when its technical performance is evaluated together with long-term monitoring, seasonal variability, and local operational conditions. The study highlights that mesh selection, sustained data collection, seasonal planning, and local institutional and community capacity are key dimensions for improving the design, assessment, and continuity of fog harvesting systems under real field conditions.

ACKNOWLEDGEMENTS

This work is the result of the sustained efforts of several people in the Peña Blanca Agricultural Community, Ovalle, whose trust, collaboration, and commitment made it possible to document and share this community-based monitoring experience. The authors gratefully acknowledge the community members and *Fundación Un Alto en el Desierto*, whose joint work has supported the continuity of field measurements, maintenance routines, operational follow-up, and care of the fog-water harvesting system. Their contribution has made it possible to generate and share scientific evidence on community-based fog-water harvesting as a complementary response to water scarcity in semi-arid territories.

REFERENCES

Ait el Kadi, M., Bouchaou, L., Castelli, G., Re, V., Çakmakçı, Y., Bresci, E. & Hssaissone, M. (2024) Multi-aspect assessment of operational fog collection systems: A rural development perspective, insights from the Sidi Ifni project in Morocco. *Journal of Arid Environments*, 222, 105174. https://doi.org/10.1016/j.jaridenv.2024.105174

Carter, V., Verbrugghe, N., Lobos-Roco, F., del Río, C., Albornoz, F. & Khan, A. Z. (2025) Unlocking the fog: Assessing fog collection potential and need as a complementary water resource in arid urban lands–the Alto Hospicio, Chile case. *Frontiers in Environmental Science*, 13, 1537058. https://doi.org/10.3389/fenvs.2025.1537058

Cereceda, P., Schemenauer, R. S. & Suit, M. (1992) An alternative water supply for Chilean coastal desert villages. *International Journal of Water Resources Development*, 8, 53–59.

Centro de Estudios Avanzados en Zonas Áridas (CEAZA) (2019) *CEAZAmet*. Available at: https://www.ceazamet.cl

Cohen, J. (1988) *Statistical power analysis for the behavioral sciences*. 2nd edn. Lawrence Erlbaum Associates.

del Río, C., Garcia, J. L., Osses, P., Zanetta, N., Lambert, F., Rivera, D., Siegmund, A., Wolf, N., Cereceda, P., Larraín, H. & Lobos, F. (2018) ENSO influence on coastal fog-water yield in the Atacama Desert, Chile. *Aerosol and Air Quality Research*, 18, 127–144. https://doi.org/10.4209/aaqr.2017.01.0022

Di Tullio, V. & Zannini, L. (2025) Unveiling hydrosocial dynamics: Discourse and power in Peña Blanca. *Frontiers in Environmental Science*, 12, 1502191. https://doi.org/10.3389/fenvs.2024.1502191

Farías, M., Cereceda, P., Osses, P. & Núñez, R. (2005) Comportamiento espacio-temporal de la nube estratocúmulo, productora de niebla en la costa del desierto de Atacama (21° lat. S., 70° long. W.), durante un mes de invierno y otro de verano (in Spanish). *Investigaciones Geográficas*, 56, 43–61. https://doi.org/10.14350/rig.30096

Fernandez, D. M., Torregrosa, A., Weiss-Penzias, P. S., Zhang, B. J., Sorensen, D., Cohen, R. E., McKinley, G. H., Kleingartner, J., Oliphant, A. & Bowman, M. (2018) Fog water collection effectiveness: Mesh intercomparisons. *Aerosol and Air Quality Research*, 18(1), 270–283. https://doi.org/10.4209/aaqr.2017.01.0040

Fessehaye, M., Abdul-Wahab, S. A., Savage, M. J., Kohler, T., Gherezghiher, T. & Hurni, H. (2014) Fog-water collection for community use. *Renewable and Sustainable Energy Reviews*, 29, 52–62. https://doi.org/10.1016/j.rser.2013.08.063

Garreaud, R., Barichivich, J., Christie, D. A. & Maldonado, A. (2008) Interannual variability of the coastal fog at Fray Jorge relict forests in semiarid Chile. *Journal of Geophysical Research: Biogeosciences*, 113(G4), G04011. https://doi.org/10.1029/2008JG000709

Hollander, M., Wolfe, D. A. & Chicken, E. (2013) *Nonparametric statistical methods*. 3rd edn. John Wiley & Sons.

Klemm, O., Schemenauer, R. S., Lummerich, A., Cereceda, P., Marzol, V., Corell, D., van Heerden, J., Reinhard, D., Gherezghiher, T., Olivier, J., Osses, P., Sarsour, J., Frost, E., Estrela, M. J., Valiente, J. A. & Fessehaye, G. M. (2012) Fog as a fresh-water resource: Overview and perspectives. *AMBIO*, 41(3), 221–234. https://doi.org/10.1007/s13280-012-0247-8

Kruskal, W. H. & Wallis, W. A. (1952) Use of ranks in one-criterion variance analysis. *Journal of the American Statistical Association*, 47(260), 583–621. https://doi.org/10.1080/01621459.1952.10483441

Larraín, H., Velásquez, F., Espejo, R., Pinto, R., Cereceda, P., Osses, P. & Schemenauer, R. S. (2002) Fog measurements at the site “Falda Verde, North of Chañaral”, compared with other north Chilean fog stations. *Atmospheric Research*, 64, 271–284. https://doi.org/10.1016/S0169-8095(02)00098-4

Lobos-Roco, F., Vilà-Guerau de Arellano, J. & del Río, C. (2025) Observation-driven model for calculating water-harvesting potential from advective fog in (semi-)arid coastal regions. *Hydrology and Earth System Sciences*, 29, 109–125. https://doi.org/10.5194/hess-29-109-2025

Montecinos, S., Cereceda, P. & Rivera, D. (2018) Fog collection and its relationship with local meteorological variables in a semiarid zone in Chile. *Atmósfera*, 31(2), 143–153. https://doi.org/10.20937/ATM.2018.31.02.03

Montecinos, S., Gutiérrez, J. R., López-Cortés, F. & López, D. (2016) Climatic characteristics of the semi-arid Coquimbo Region in Chile. *Journal of Arid Environments*, 126, 7–11. https://doi.org/10.1016/j.jaridenv.2015.09.018

Nicolas-Artero, C. & Blanco-Wells, G. (2025) *Camiones aljibe como sustentadores de un sistema que debe repensarse* (in Spanish). Policy Brief CR2 25. Centro de Ciencia del Clima y la Resiliencia (CR2). Available at: https://www.cr2.cl/wp-content/uploads/2025/07/Policy-brief-25-Camiones-aljibe.pdf

Osses, P., Cereceda, P., Larraín, H. & Schemenauer, R. S. (1998) Influence of relief on the origin and behaviour of fog at Tarapacá, Chile. In *Conference on Fog and Fog Collection*, pp. 245–247.

Qadir, M., Jiménez, G. C., Farnum, R. L. & Trautwein, P. (2021) Research history and functional systems of fog water harvesting. *Frontiers in Water*, 3, 675269. https://doi.org/10.3389/frwa.2021.675269

Rivera, J. D. (2011) Aerodynamic collection efficiency of fog water collectors. *Atmospheric Research*, 102(3), 335–342. https://doi.org/10.1016/j.atmosres.2011.08.005

Rivera, D., Del Río, C., Carter, V., Donoso, G., Pimentel, P. & Aguirre, C. (2026) Regulation, governance and management of fog water in Chile: Challenges in a territory of scarcity. *International Journal of Water Resources Development*, 42(1), 72–93. https://doi.org/10.1080/07900627.2025.2553140

Schemenauer, R. S. & Cereceda, P. (1994) A proposed standard fog collector for use in high-elevation regions. *Journal of Applied Meteorology*, 33(11), 1313–1322. https://doi.org/10.1175/1520-0450(1994)033%3C1313:APSFCF%3E2.0.CO;2

Geographia Technica, Vol. 21, Issue 3, 2026, pp 209 to 223

DIGITAL TWINNING FOR A SAFE COASTAL NAVIGATION: GNSS INTEGRITY REAL-TIME ANALYSIS IN WEBGIS WITH LOW-COST EQUIPMENT

Marcello LA GUARDIA [1*]***, Giuseppe MUSSUMECI*** [1] ***& Antonio ANGRISANO*** [1]

DOI: 10.21163/GT_2026.213.14

ABSTRACT

The real-time analysis of Global Navigation Satellite System (GNSS) integrity information is a precious requirement for the enhancement of safety in coastal navigation. At the same time the spread of open-source WebGIS technologies and low-cost Internet of Things (IoT) hardware equipment opened new scenarios for dynamic analyses into geospatial web visualization platforms. The focus of the paper is addressed on the generation of a low-cost WebGIS visualization platform for the real-time analysis of the GNSS integrity information during coastal navigation of ships. The framework is composed of a WebGIS platform connected with a computation module inside Anaconda Python platform, that real-time analyzes the GNSS integrity from a low cost GNSS IoT receiver. This application can be useful for improving the safety of navigation and the effectiveness of rescue operations at sea. The use of JavaScript opensource libraries and Python language and low-cost smartphone sensors allowed us to produce a low-cost digital twinning solution for the improvement of safeness in coastal navigation, available for municipalities and private companies. Future improvements may consider the integration of further modules that can optimize the quality of integrity calculation and the extension of the application offshore.

Keywords: *GNSS; integrity; WebGIS; IoT; Coastal navigation; Opensource.*

1. INTRODUCTION

Safety in maritime navigation is a sensitive issue, and accurate and reliable positioning has a key role in maintaining and increasing it. IMO (International Maritime Organization) specifies the performance requirements that a radio-navigation system must meet (IMO, 2011). The requirements are expressed in terms of accuracy, integrity, availability and continuity, and refer to different navigation phases, i.e. in ocean waters and in harbor entrance, harbor approaches, and coastal waters; of course, according to the cases, the requirements are more stringent. In this scenario, the integration of artificial intelligence and automation allowed the navigation of Maritime Autonomous Surface Ships (MASS) refining collision-avoidance navigation (Zhang et al., 2021).

Global Navigation Satellite System (GNSS) are navigation systems based on constellations of artificial satellites and are able to provide Position, Velocity and Timing (PVT) to a potentially endless number of users, worldwide and in all weather conditions (Kaplan & Hegarty, 2017). GNSS includes four systems: GPS, Glonass, Galileo and BeiDou (Jin et al., 2024). They are very similar to each other, and they are conceived to be compatible and interoperable.

GNSS are currently used in many fields, in terrestrial, air and maritime context, for technical, business or personal applications (Hassien et al., 2024). In maritime, the required performance of GNSS is detailed in (IMO, 2001), also in this case expressed in terms of accuracy, integrity, availability and continuity. Accuracy is the degree of conformance between the estimated or measured parameters of a craft at a given time and its true parameters at that time.

[1]*Department of Engineering, University of Messina, Contrada di Dio, 98158 Sant'Agata, Messina ME, Italy.*
[*]*Corresponding author: marcello.laguardia@unime.it; giuseppe.mussumeci@unime.it, antonio.angrisano@unime.it.*

Integrity is the ability to provide users with warnings within a specified time when the system should not be used for navigation. Availability is the percentage of time that an aid, or system of aids, is performing a required function under stated conditions; availability consists in signal availability, i.e. availability of a radio signal in a specified coverage area, and system availability, i.e. availability of a system to a user. Continuity is the probability that having a fault-free receiver, a user will be able to determine position with specified accuracy and to monitor the integrity of the determined position over the (short) time interval applicable for a particular operation within a limited part of the coverage area.

The most critical requirement for GNSS concerns the integrity; indeed, GNSSs are not able to deliver information about the integrity of the provided data. This shortcoming is particularly felt in safety-of-life applications such as aviation, and precisely in this context there was the development of augmentation systems which can fill the GNSS gaps. To provide integrity in the aviation context, three augmentation systems have been developed: Aircraft-Based Augmentation System (ABAS), Satellite-Based Augmentation System (SBAS) and Ground-Based Augmentation System (GBAS).

SBAS and GBAS need complex space and/or terrestrial infrastructures, such as GNSS reference stations at ground and additional artificial satellites; on the other hand, ABAS only uses information available onboard. Although the augmentation systems have been developed to meet the stringent integrity requirements of civil aviation, they have been successfully adapted to work in other contexts such as maritime or urban applications.

Two ABAS implementations are possible: Receiver Autonomous Integrity Monitoring (RAIM) and Aircraft Autonomous Integrity Monitoring (AAIM).

RAIM is based only on GNSS measurements, while in AAIM, GNSS measurements are merged with other onboard available sources, such as compass, inertial sensors, altimeters or clocks.

RAIM can provide a valuable contribution to safety in maritime navigation; indeed, RAIM is able to detect the presence of anomalous measurements, often referred to as blunders or outliers, alerting the user about the reliability of the PVT solution provided by the GNSS (Sturza, 1988; Brown, 1996; Brown & Chin, 1997). RAIM can detect anomalous solutions and also identify outliers, in order to reject them, allowing improvements in accuracy and a continuous positioning service. RAIM techniques consist of checking the self-consistency of redundant measurements; an inconsistency among the measurements indicates the presence on anomalous measurements. The use of multiple GNSS systems increases noticeably redundancy, in turn improving the RAIM ability of identifying anomalous measurements. RAIM techniques are finally able to provide Protection Levels (PLs), which define a region of the space containing the true position of the receiver with a fixed probability. PLs are compared with suitable threshold values, called Alarm Limits (ALs), defined in accordance with the considered application; in case PL exceeds AL, the GNSS solution is considered not reliable by RAIM.

RAIM was developed for aviation, but subsequently its performance has been largely analyzed outside the aviation context; for instance, in (Kuusniemi et al., 2004; Kuusniemi et al., 2007; Castaldo et al., 2014; Angrisano et al., 2013) RAIM is profitably applied to signal-degraded scenarios. Also in maritime domain, RAIM has been applied, demonstrating good results (Mink, 2016; Zalewski, 2019; Porretta et al., 2016, Gaglione et al., 2017). In maritime navigation, ad hoc RAIM algorithms should be used considering the context concerned. In particular, it should be considered that maritime navigation is mainly carried out in a good visibility scenario with a good amount of available GNSS satellites; this allows a satisfying redundancy, favorable for RAIM applications. The anomalous measurements, in this context, are mainly related to multipath from sea or, more rarely, to anomalies in the satellite clock or ephemeris; it is possible setting consequently the RAIM parameters, such as the probability of false alarm and of missed detection, or the a priori uncertainties of the measurements.

In maritime navigation, GNSS supported by RAIM can provide great benefits to the safety aspects, mainly because RAIM provides the PL, which define the boundaries of a volume surrounding the ship, where the ship itself is, with known probability; this information can be used by the authorities for the traffic management or by the ship commander for improving the separation among the ships, increasing safety and optimizing the traffic.

Considering the possibility of sharing geospatial information, the diffusion of Geographic Information Systems (GIS) and their web applications (WebGIS) allowed specialists to store, visualize and manage combinations of raster and vectorial geometric dataset and semantic information (Van Oosterom et al., 2002). In this way, the spread of geospatial information on the web through the development of WebGIS, diffusing this kind of application in numerous fields of research, has enabled the management of geospatial data in various fields of application including the management of urban transportation infrastructures (Santoso et al., 2019), the analysis of air pollution (Yakubailik et al., 2018), monitoring of forest damage (Piragnolo et al., 2021), improvement of energy efficiency in urban areas (Amado et al., 2018), valorization of touristic cultural heritage itineraries (Scianna et al., 2021), acoustic mapping of the vehicular traffic (Dardanelli et al., 2017), etc.

Considering this scenario, the parallel spread of low-cost sensor applications in electronics, based on IoT technologies, offered a fundamental contribution to WebGIS applications, introducing the possibility of making real-time spatial data analysis, processing the IoT acquisitions into WebGIS structures (Congiu et al., 2023; D'Ippolito et al., 2026). The IoT integration inside WebGIS structures opened new possibilities related to territorial analysis in many fields of research: localization of power plants related to renewable energy solutions (La Guardia & D'Ippolito, 2024), spatial and temporal WebGIS visualization of water quality (Balla et al., 2022), visualization of seismic risk in infrastructures (Mazzei & Quaroni, 2022), real-time dispatching and control of power grids (He et al., 2021). The possibility of obtaining real-time data acquisition from the real environment using low-cost IoT solutions offered specialists the opportunity to expand the research on Digital Twin (DT) applications, where the geospatial representation integrates the real-time behavior of the visualized system (Tomko & Winter, 2018). The idea of DT started in the field of robotics and automation engineering some decades ago and considers the development of a replica of a real model, that allows to control the behavior of its counterpart in real-time (Singh et al., 2021). This concept was recently applied to territorial analysis fields, creating the Urban Digital Twins (UDT), where the real-time analysis is processed in GIS (Weil et al., 2023). Furthermore, though the Geospatial Science presence in DT is not explicit, a considerable percentage of DT case studies contain elements of Geospatial discipline (Metcalfe et al., 2024).

The evolution of UDT applications generated the new concept of City Information Models (CIM) (Xue et al., 2021) extending the spread of to digital twin cities (Deng et al., 2021; Martella et al., 2023). The spread of CIM applications allowed experts to improve the quality of urban planning operations, but, at the same time, led new challenges regarding the quality of data to adopt, the not simple interoperability between different sources of dataset and the limited computing resources (Bigorra et al., 2022). In this scenario the development of digital twinning applications developed with opensource technology seems to be a valid strategy for a wide diffusion of these applications for municipalities and private companies (La Guardia et al., 2024).

In maritime navigation, considering the domain of surface ships, the DT concept was introduced in the early 2000s expressing great potential but initial slow trend of progress due to the lack of hardware and software solutions, remote sensing technologies, satellite communication facilities and other components not sufficiently developed at that time (Innac et al., 2021; Madusanka et al., 2023). Recent technological advancements allowed experts to focus their interest on the development of ship digital twinning applications finalized to autonomous navigation (Kinaci, 2023), to improve the safety on board (Briguglio & Crupi, 2024), or to help ship operations in seaways predicting hydrodynamic performances for the maneuvers (Lee et al., 2022). The possibility to generate realistic simulation in a virtual environment offered by DT applications allowed to improve the safety and sustainability of maritime operations using Autonomous Surface Vessels (ASVs) experimentations, identifying different ranges of complexity in digital twinning functionalities (Menges, & Rasheed, 2024).

In this scenario, our experimentation is based on a low-cost digital twinning application for coastal ship navigation finalized to the dynamic online WebGIS visualization of the horizontal PL surrounding the ship, based on the real-time GNSS integrity analysis. The experimentation was performed along the coast of Messina (Italy), using a low-cost GNSS equipment, inside a smartphone device, to acquire GNSS signals and integrating a Python module to perform real-time integrity calculations and a WebGIS visualization system based on the open-source Leaflet libraries (JavaScript). This solution was conceived as a DT module that can be implemented in all coastal navigation frameworks aimed at improving the quality of navigation avoiding expensive solutions. Preliminary approaches to this research were recently presented in (La Guardia et al., 2025).

The paper is organized as follows: Section 2 illustrates the framework of the DT application, Section 3 describes the functionalities of the WebGIS platform, Section 4 analyzes strengths and weaknesses of the adopted solution, and, finally, Section 5 makes an overall analysis of the work with some indications of possible future improvements.

2. MATERIALS AND METHODS

The developed platform is based on the integration of different modules (**Fig.1**), real-time connected to providing the WebGIS visualization of the protection level during navigation.

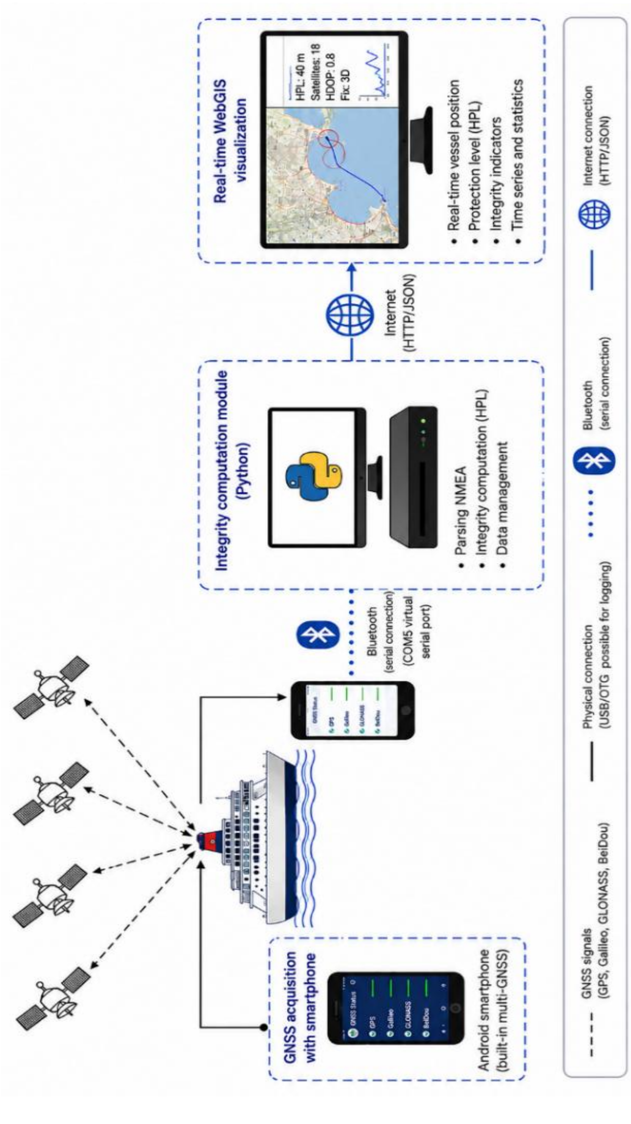

Fig. 1. The general framework.

The core of the structure is represented by the GNSS integrity computation module, that allows us to calculate the horizontal PL on the basis of the real-time data acquired from the low cost GNSS equipment that caught the signal provided by satellites. The GNSS integrity computation module was incapsulated in a Python module and connected on one side to the IoT GNSS equipment, and on the other side to a WebGIS + database structure to provide the real-time web visualization of the computation in a geospatial environment.

2.1. The GNSS integrity module

RAIM algorithms are able to provide PLs, defining a region of the space which includes the true receiver position with a fixed probability; in particular, HPL is the radius of a circle, which contains the true horizontal position with defined probabilities of false alert and missed detection. The most widespread computation of HPL from RAIM is detailed in (Brown & Chin, 1997), where HPL expression is:

$$HPL = MDB * Slope_{max}$$

MDB is the minimum detectable bias and depends on the probabilities of false alarm and missed detection, on the measurement redundancy (i.e. the difference between number of measurements and unknowns), and on the measurement uncertainty.

The "slope" is defined as the ratio between the horizontal position error and the magnitude of the residuals, assuming the absence of noise and the presence of a bias affecting only one measurement. $Slope_{max}$ is the maximum slope and it is associated with the most insidious measurement, for which a low residual corresponds to a large position error. Such parameter depends only on the design matrix of the equations system, in turn related to the receiver-satellites geometry.

The design matrix can be expressed in terms of elevation and azimuth of the satellites with respect to receiver; naming El_i and Az_i respectively the elevation and the azimuth of the i^{th} satellite, the design matrix H can be expressed as:

$$H = \begin{bmatrix} & & \cdots & \\ -\cos El_i * \sin Az_i & -\cos El_i * \cos Az_i & -\sin El_i & 1 \\ & & \cdots & \end{bmatrix}$$

The size of matrix H is mx4, with m number of available satellites and 4 number of unknowns in GPS-only case.

2.2. The structure of the real-time WebGIS platform

The developed framework was based on the integration of a low-cost GNSS acquisition device, a Python-based integrity computation module, a PostgreSQL database, and a WebGIS visualization environment (**Fig.2**). Unlike the preliminary prototype based on a dedicated Mini NEO-6M GNSS board, the experimental campaign presented in this paper employed a commercial Android smartphone acting as a multi-constellation GNSS receiver.

The smartphone used during the experiment was a Xiaomi 11T device running Android 15. The embedded GNSS chipset was able to simultaneously track signals from multiple satellite constellations, including GPS, Galileo, GLONASS, and BeiDou. The developed platform allowed us to export in real-time GNSS observations using the open-source application GPS NMEA Tether, which allowed the transmission of National Marine Electronics Association (NMEA) messages from the smartphone to the processing workstation through a local Bluetooth Serial Port Profile (SPP) connection.

The transmitted NMEA stream included standard GNSS sentences such as GGA, RMC, GSA and GSV. These messages provided real-time information about receiver coordinates, satellite geometry, signal quality indicators and satellite visibility. The communication between the smartphone and the workstation was established through a local wireless network, avoiding the need for dedicated GNSS hardware interfaces.

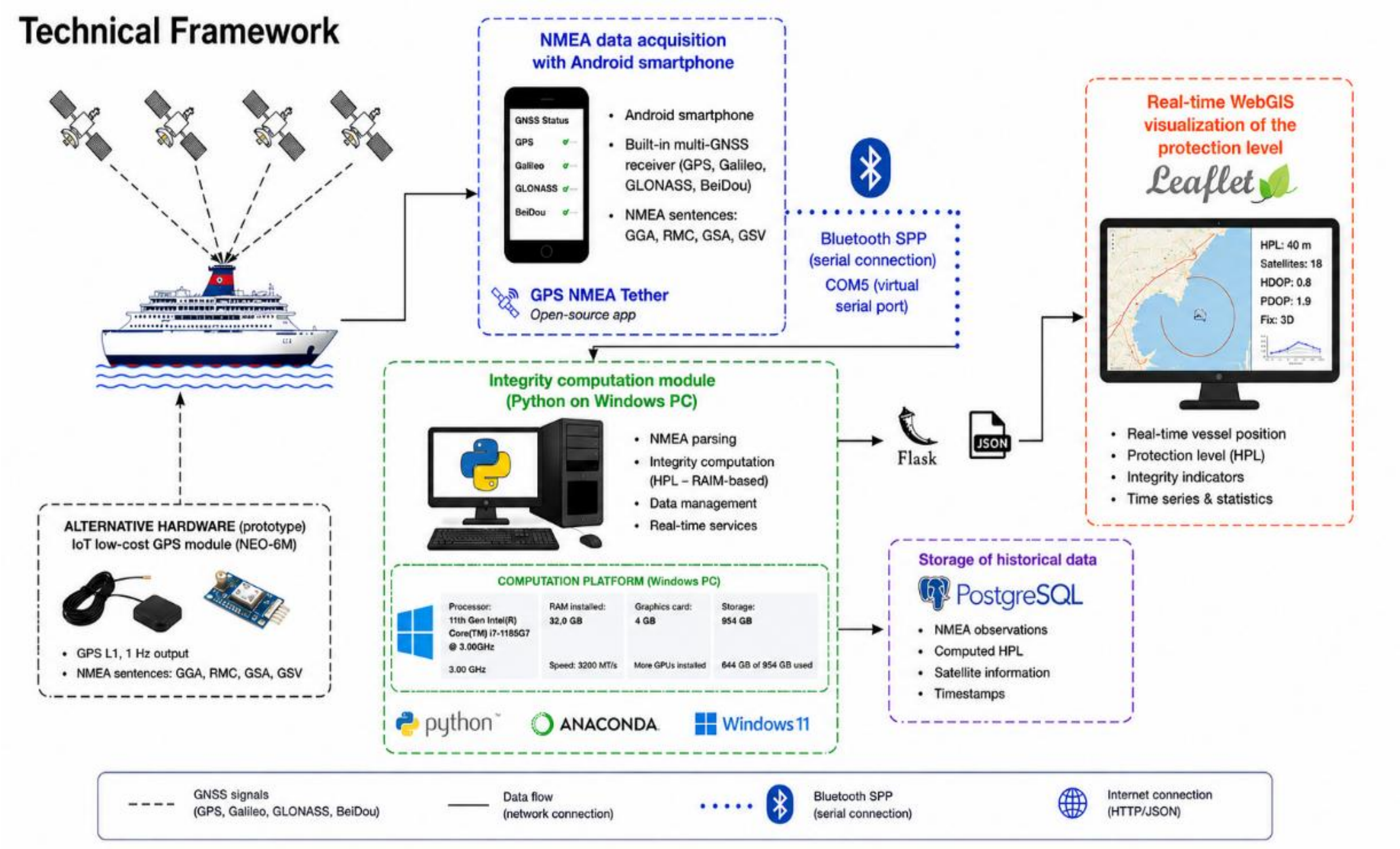

Fig. 2. All the software and hardware components involved in the platform.

The integrity computation module was executed within an Anaconda Python environment running on a Windows 11 Pro workstation equipped with an 11th Generation Intel® Core™ i7-1185G7 processor operating at 3.00 GHz, 32 GB of RAM, a 4 GB graphics card, and a 954 GB SSD storage unit. The module continuously received NMEA observations from the smartphone, extracted the information required for the integrity analysis, and computed the Horizontal Protection Level (HPL) at a frequency of 1 Hz. Flask open-source libraries were employed to expose the integrity results through JavaScript Object Notation (JSON) services, while the psycopg2 adapter was used to store historical observations within a PostgreSQL database.

The processing workstation communicated with an Apache web server hosting the WebGIS visualization environment. The WebGIS interface was developed using Leaflet open-source JavaScript libraries and was designed to provide real-time visualization of the vessel position and the associated Horizontal Protection Level. The HPL was represented as a circle centred on the vessel position, while historical observations were stored and queried from PostgreSQL.

The complete architecture was entirely based on open-source technologies, including Android 15 GNSS utilities, GPS NMEA Tether 1.1.0, Python 3.12, Flask 3.1.3, PostgreSQL 18.1, Apache Web Server 2.0, and Leaflet 1.9.4 libraries. This approach allowed the development of a low-cost digital twinning framework suitable for real-time coastal navigation monitoring without requiring professional maritime GNSS infrastructures.

2.3. Experimental dataset

A real-world navigation experiment was conducted to evaluate the operational capabilities of the proposed GNSS integrity framework. The test was performed aboard a ferry operating along the Strait of Messina. During the navigation, GNSS observations were continuously acquired using the Android smartphone described in Section 2.2. The system allowed the real-time transmission of NMEA information to the integrity computation module through the GPS NMEA Tether application.

The acquisition system generated standard NMEA 0183 messages, including GGA, RMC, GSA, and GSV sentences, at a nominal frequency of 1 Hz. The resulting NMEA stream was processed in real-time by the Python-based integrity module and simultaneously stored within the PostgreSQL database for subsequent analyses. The experiment produced 1,877 valid GNSS epochs collected over a period of 31 minutes and 17 seconds. The navigation scenario included both harbour manoeuvres and open-water navigation conditions, providing a representative dataset for evaluating the behaviour of the proposed integrity framework under realistic maritime operational conditions.

Table 1 summarizes the main characteristics of the experimental dataset used for the validation of the proposed architecture.

Table 1.

The experimental navigation dataset.

Parameter	**Value**
Navigation scenario	ferry navigation
Acquisition date	18 June 2026
Acquisition duration	31 min 17 s
Acquisition frequency	1 Hz
Valid GNSS epochs	1,877
GNSS receiver	Android smartphone (Xiaomi 11T)
Android version	Android 15
Data transmission	Bluetooth SPP connection
Transmission software	GPS NMEA Tether
NMEA protocol	NMEA 0183
Available messages	GGA, RMC, GSA, GSV
Processing platform	Python (Anaconda) on Windows 11
Database	PostgreSQL
WebGIS framework	Leaflet

3. RESULTS

The functionalities of the proposed platform were validated through a real-world maritime navigation experiment conducted aboard a ferry operating between Villa San Giovanni and Messina (Italy). During the navigation, GNSS observations, acquired by an Android smartphone, were transmitted and the platform enabled the dynamic Bluetooth SPP connection to the integrity computation module implemented in Python within the Anaconda environment. The incoming NMEA stream was processed at a frequency of 1 Hz, allowing the continuous computation of the Horizontal Protection Level (HPL), satellite geometry indicators, and navigation quality parameters.

The processed information was remotely visualized through a WebGIS platform developed using Leaflet JavaScript libraries (**Fig. 3**).

The interface provided a real-time representation of the vessel position together with the associated protection level. The current HPL was displayed as a circle centred on the vessel position, whose radius was dynamically updated according to the integrity computation results. In addition, the platform continuously generated and displayed the complete navigation trajectory, allowing users to monitor both the current position and the historical evolution of the route.

The WebGIS interface was further enhanced by integrating real-time quality indicators derived from the GNSS observations. In particular, the Horizontal Dilution of Precision (HDOP), Position Dilution of Precision (PDOP), number of available satellites, and HPL values were continuously updated during the navigation and made available to the end user. This information provided an immediate assessment of both positioning geometry and navigation integrity conditions.

Simultaneously, all observations and integrity indicators were archived within a PostgreSQL database. The historical acquisition component enabled the visualization and retrieval of previously processed observations, supporting post-processing analyses and integrity performance assessment. The complete acquisition-processing-storage-visualization chain operated continuously throughout the experiment, demonstrating the capability of the proposed architecture to support dynamic integrity monitoring under actual maritime navigation conditions.

The map was automatically centred on the vessel position according to the update frequency of the navigation solution, allowing continuous visualization of the navigation scenario. The flexibility of the Leaflet environment also enables the future integration of additional geospatial layers and external geospatial services, including OGC-compliant Web Map Services (WMS) and Digital Twin components. The adoption of exclusively open-source technologies allowed the implementation of the complete framework without licensing costs, improving its reproducibility and facilitating future developments for low-cost maritime navigation monitoring applications.

The proposed framework was evaluated through a real-world navigation experiment conducted aboard a ferry operating between Villa San Giovanni and Messina. **Fig. 4** reports the temporal evolution of the Horizontal Protection Level (HPL), Horizontal Dilution of Precision (HDOP), and Position Dilution of Precision (PDOP) computed from the acquired NMEA observations. The HPL values were derived according to the RAIM-inspired methodology described in Section 2, based on the SLOPE parameter computed from the satellite geometry matrix and the adopted pseudorange standard deviation.

The obtained results highlight the overall stability of the GNSS geometry during the entire navigation experiment. HDOP values remained consistently below 1.0, with an average value close to 0.5, while PDOP values were generally lower than 1.5. Such indicators denote favourable satellite visibility conditions and a well-conditioned positioning geometry throughout the navigation route.

The computed HPL exhibited limited fluctuations along the trajectory, with average values of approximately 35 m and maximum peaks below 85 m. The observed variations were mainly associated with changes in satellite geometry related to modifications in constellation visibility occurring during different phases of the navigation. Nevertheless, no significant degradation of integrity performance was detected, and the HPL remained within a relatively narrow operational range for the entire duration of the experiment.

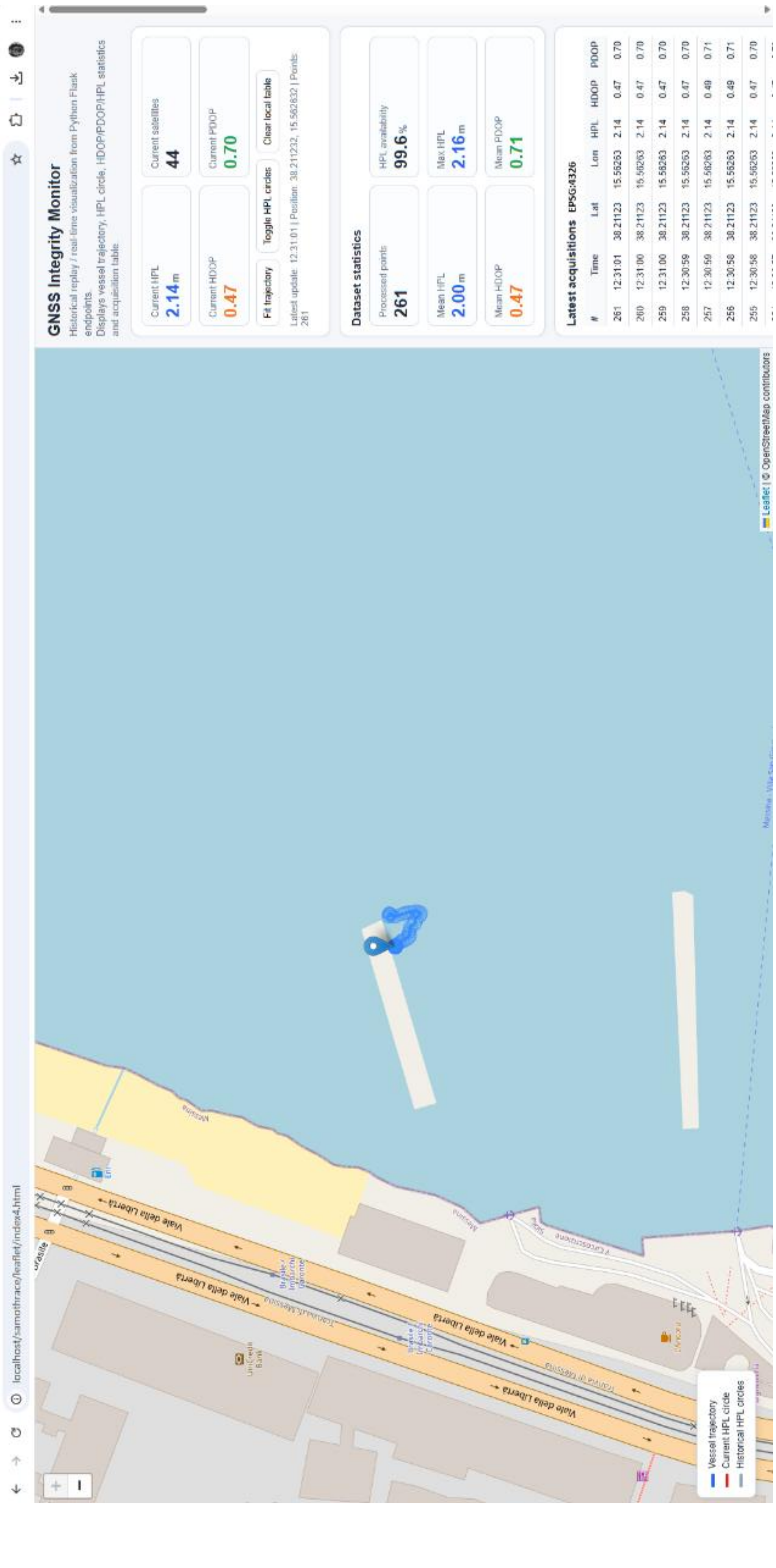

Fig. 3. Real-time WebGIS visualization of the proposed integrity monitoring framework. The interface displays the vessel trajectory, the current Horizontal Protection Level (HPL) represented by the blue protection circle, and the real-time integrity indicators (HDOP, PDOP, satellite availability, and HPL statistics) derived from the GNSS observations acquired during the Villa San Giovanni –Messina navigation experiment in WGS84 – EPSG:4326 .

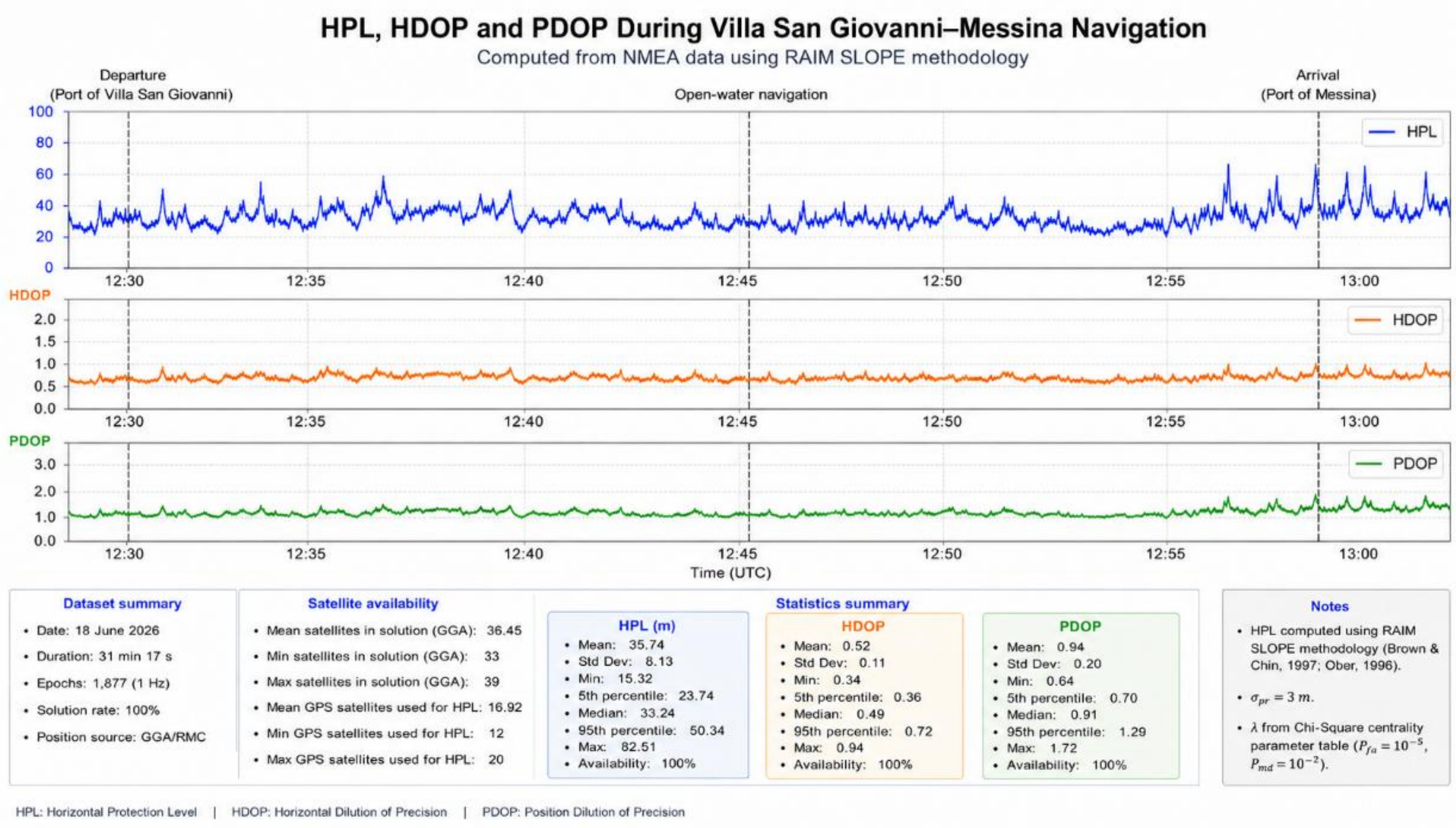

Fig. 4. The timeline of HPL, HDOP, PDOP trend during the test of navigation.

4. DISCUSSION

The real-time tracking of ships using GNSS and WebGIS together represents useful technology for the real-time monitoring of boating activities (Yen et al., 2009). Recent applications considered also the integration of low-cost bathymetric acquisition to extract ship motion data and correct depths in dynamic shallow water systems (Bio et al., 2020). In our case, the proposed solution integrates the real-time visualization of the horizontal protection level, which contains the estimated horizontal position of the ship, into a WebGIS platform.

The entire structure is developed using low-cost GNSS hardware equipment and open-source software solutions to provide an instrument widely suitable for municipalities and private companies. Although the proposed framework demonstrated stable behaviour during the real navigation experiment, the validation presented in this work was intentionally focused on assessing the feasibility of the complete real-time integrity monitoring architecture rather than on benchmarking positioning performance against professional maritime GNSS equipment. A comparison with geodetic-grade or certified maritime GNSS receivers would allow a more rigorous assessment of both positioning accuracy and the computed Horizontal Protection Level (HPL). Such an experimental campaign was outside the scope of the present work due to the unavailability of professional reference instrumentation during the navigation tests. Nevertheless, the developed platform has been specifically designed to be hardware-independent, making future comparative experiments with professional GNSS receivers straightforward without requiring modifications to the integrity computation or WebGIS architecture.

Considering the economic impact of the framework, the costs are limited to the low cost GNSS receiver. In fact, the platform employs only open-source technology compliant with Windows, Linux, and macOS (Apple), using the Anaconda platform for Python computation, the PostgreSQL database for the storage of position information, and Leaflet JavaScript libraries for the WebGIS design.

If on the one hand the opensource nature of the platform allows the spread of the application, on the other hand it requires programming skills for developing and integrating the different modules that compose its structure (low cost GNSS module, Integrity computation module, Database, real-time WebGIS visualization). Another challenge is the limitation of use to coastal navigation due to the need for data transmission over the 4G network between the integrity calculation module and the WebGIS+database structure.

However, it is necessary to underline that this kind of application is very useful for coastal navigation due to the intensive traffic of ships that characterizes the harbors and their neighborhoods where a valid integrity computation can be precious especially in adverse weather conditions.

Similar recent experimentations were considered for the development of vehicle live tracking systems for public transport in urban areas (Amer et al., 2024), or for real-time metro rail localization (Aggarwal et al., 2023) allowing a WebGIS real-time visualization of GPS integrity location data based on Flutter Google open-source framework. These solutions are compliant with iOS and Android platforms and represent a valid possibility if we want the implementation of the platform in a mobile application instead of a web browser navigation.

An interesting aspect emerging from the analysis is the correspondence between local increases in HDOP/PDOP and the occurrence of higher HPL values. This behaviour is consistent with the adopted integrity model, since both dilution of precision indicators and protection levels are directly influenced by the underlying satellite geometry. The results therefore confirm the capability of the proposed framework to dynamically reflect changes in GNSS observation conditions and to provide meaningful integrity information to the end user.

The experiment also demonstrated the operational robustness of the complete acquisition-processing-storage-visualization chain. During the 31-minute navigation campaign, 1,877 valid GNSS epochs were processed without interruptions, achieving continuous integrity monitoring, real-time WebGIS dissemination, and persistent storage of all navigation observations within the PostgreSQL database. These results validate the feasibility of employing low-cost commercial devices and open-source software components for real-time maritime integrity monitoring applications.

In fact, the main contribution of this research is not limited to the implementation of a GNSS integrity algorithm but consists in the development and validation of a complete real-time open-source framework that seamlessly integrates GNSS acquisition, integrity computation, database management, and WebGIS dissemination within a unified Digital Twin-oriented architecture for maritime navigation.

5. CONCLUSIONS AND OPEN SCENARIOS

This work presented a low-cost open-source framework for real-time GNSS integrity monitoring and WebGIS visualization designed for coastal maritime navigation. The proposed architecture integrates commercial GNSS hardware, Python-based integrity computation, PostgreSQL data storage, and a WebGIS dashboard developed with open-source technologies, providing a complete acquisition-processing-storage-visualization workflow.

The experimental validation was performed during a real navigation campaign aboard a ferry operating between Villa San Giovanni and Messina (Italy). GNSS observations were continuously acquired using an Android smartphone and transmitted through a local Bluetooth SPP connection to the integrity computation module. The developed framework successfully computed the Horizontal Protection Level (HPL) at a frequency of 1 Hz while simultaneously storing all observations within a PostgreSQL database and publishing the integrity information through the WebGIS interface. The experimental results demonstrated the operational stability of the proposed architecture during the entire navigation, confirming the capability of the framework to support continuous integrity monitoring under realistic maritime conditions.

Compared with the preliminary prototype, the developed platform provides a significantly enhanced monitoring environment. In addition to the real-time visualization of the protection level, the WebGIS now integrates the complete vessel trajectory together with navigation quality indicators such as HDOP, PDOP, satellite availability, and historical integrity statistics. These functionalities transform the WebGIS from a simple visualization interface into an operational integrity monitoring dashboard capable of supporting both real-time situational awareness and post-processing analyses.

The exclusive adoption of open-source software components considerably reduces implementation and maintenance costs, making the proposed solution suitable for research activities, public administrations, and private organizations interested in developing low-cost Digital Twin applications for maritime navigation. Although the current implementation focuses on coastal navigation scenarios, the modular architecture allows straightforward integration with additional geospatial services, IoT sensors, and external environmental information.

Future developments will focus on extending the integrity computation to full multi-constellation GNSS processing, integrating additional navigation and environmental sensors, and implementing satellite communication technologies to remove dependency on terrestrial wireless networks during offshore navigation. Furthermore, future research will investigate the integration of predictive integrity models and Digital Twin functionalities capable of supporting decision-making processes through continuous monitoring and forecasting of navigation conditions.

To encourage reproducibility and further developments by the scientific community, a demonstration version of the developed framework is publicly available at: https://github.com/marcellolg1987/realtime_PL_WebGIS_analyzer.

Another promising research direction concerns interoperability with emerging geospatial IoT standards. Although the current implementation relies on lightweight JSON services for real-time communication, future versions of the framework will investigate the adoption of OGC SensorThings API to standardize the management and dissemination of GNSS observations and integrity indicators. Such an evolution would facilitate interoperability with heterogeneous sensor networks, Digital Twin platforms, and Smart City infrastructures, while improving scalability and compliance with internationally recognized geospatial standards

REFERENCES

Aggarwal, A., Kumar, R., Singh Jakhar, N. & Gouthaman, P. (2023) Live Tracking of Metro Rail Using Internet of Things. In *2023 International Conference on Recent Advances in Science and Engineering Technology (ICRASET)*, 1‑5. DOI: 10.1109/ICRASET59632.2023.10420289.

Amado, M., Poggi, F., Ribeiro Amado, A. & Breu, S. (2018) E-City Web Platform: A Tool for Energy Efficiency at Urban Level. *Energies*, 11(7), 1857. DOI: 10.3390/en11071857.

Amer, E.S., Darwish, S., Fahim, N.N., Mohmed EL-Qabbary, M.M., Ghaly, K.B. & Ramdan, A.S. (2024) Vehicle Live Tracking System Based on GPS and GSM. In *2024 International Telecommunications Conference* (ITC-Egypt), 237‑244. DOI: 10.1109/ITC-Egypt61547.2024.10620479.

Angrisano, A., Gioia, C., Gaglione, S. & del Core, G. (2013) GNSS Reliability Testing in Signal-Degraded Scenario. *International Journal of Navigation and Observation*, 2013, 1‑12.

Balla, D., Zichar, M., Kiss, E., Szabó, G. & Mester, T. (2022) Possibilities for Assessment and Geovisualization of Spatial and Temporal Water Quality Data Using a WebGIS Application. *ISPRS International Journal of Geo-Information*, 11, 108. DOI: 10.3390/ijgi11020108.

Bigorra, J.F., Casals, M. & Gangolells, M. (2022) The Adoption of Urban Digital Twins. *Cities*, 131, 103905. DOI: 10.1016/j.cities.2022.103905.

Bio, A., Gonçalves, J.A., Magalhães, A., Pinheiro, J. & Bastos, L. (2020) Combining Low-Cost Sonar and High-Precision Global Navigation Satellite System for Shallow Water Bathymetry. *Estuaries and Coasts*, 45, 1000‑1011. DOI:10.1007/s12237-020-00703-6

Briguglio, G. & Crupi, V. (2024) Review on Sensors for Sustainable and Safe Maritime Mobility. *Journal of Marine Science and Engineering*, 12, 353. DOI: 10.3390/jmse12020353.

Brown, R.G. & Chin, G.Y. (1997) Calculation of Thresholds and Protection Radius Using Chi Square Methods– A Geometric Approach. *Navigation*, 5, 155‑179.

Brown, R.G. (1996) Receiver Autonomous Integrity Monitoring. In: Parkinson, B.W. & Spilker, J.J. Jr. (Eds.) Global Positioning System: Theory and Applications. American Institute of Aeronautics and Astronautics, National Harbor, MD, USA, Volume II, 143‑165.

Castaldo, G., Angrisano, A., Gaglione, S. & Troisi, S. (2014) P-RANSAC: An Integrity Monitoring Approach for GNSS Signal Degraded Scenario. *International Journal of Navigation and Observation*, 2014, e173818. DOI:10.1155/2014/173818

Congiu, E., Desogus, G., Frau, C., Gatto, G. & Pili, S. (2023) Web-Based Management of Public Buildings: A Workflow Based on Integration of BIM and IoT Sensors with a Web‑GIS Portal. *Buildings*, 13(5), 1327. DOI: 10.3390/buildings13051327.

Dardanelli, G., Marretta, R., Sansone Santamaria, A., Streva, A., Lo Brutto, M., Maltese, A. (2017) Analysis of Technical Criticalities for GIS Modelling an Urban Noise Map. *Geogr. Tech.*, *12*, 41–61.

Deng, T., Zhang, K. & Shen, Z. (2021) A Systematic Review of a Digital Twin City: A New Pattern of Urban Governance toward Smart Cities. *Journal of Management Science and Engineering*, 6(2), 125‑134. DOI: 10.1016/j.jmse.2021.03.003.

D'Ippolito, F.; Garraffa, G.; La Guardia, M. & Sferlazza, A. (2026) An Open-Source, Low-Cost Framework for Real-Time IoT–WebGIS Integration. *Distributed Monitoring and Automation System*. *Control and Robotics Express Communications*, 1 (1), 3.

Gaglione, S., Del Pizzo, S., Innac, A. & Troisi, S. (2017) The SMILE Project: Satellite Multi-Constellation Identification Techniques for Liable Enhanced Applications. In *Marine Navigation*. CRC Press, 137‑141. DOI:10.1201/9781315099132

Hassinen, S., Ojala, A. & Kuusniemi, H. (2024) The Commercial Aspects of Navigation Satellites: A Systematic Literature Review. *Space Business*, 81‑109. DOI: 10.1007/978-981-97-3430-6_4.

He, Y., Zhang, Y., Zhang, Y., Fang, C., Huang, K. & Han, X. (2021) Design and Implementation of Real-Time Power Grid WebGIS Visualization Framework Based on New Generation Dispatching and Control System. *Journal of Physics: Conference Series*, 2087, 012073. DOI: 10.1088/1742-6596/2087/1/012073.

IMO (2001) A.915(22), Revised Maritime Policy and Requirements for A Future GNSS. International Maritime Organization, London, UK.

IMO (2011) A.1046(27), World Wide Radionavigation System. International Maritime Organization, London, UK.

Innac, A., Angrisano, A., Dardanelli, G., Corte, V., Martellato, E., Rotundi, A., Ferraioli, G., Palumbo, P.; Gaglione, S. (2020) A Kalman filter single point positioning for maritime applications using a smartphone. *Geogr. Tech.*, *16*, 29. DOI: 10.21163/GT_2021.163.02

Jin, S., Meng, X., Dardanelli, G., & Zhu, Y. (2024). Multi-Global Navigation Satellite System for Earth Observation: Recent Developments and New Progress. *Remote Sensing*, *16*(24), 4800. https://doi.org/10.3390/rs16244800

Kaplan, E.D. & Hegarty, C. (Ed.) (2017) Understanding GPS/GNSS: Principles and Applications. Artech House.

Kinaci, O.K. (2023) Ship Digital Twin Architecture for Optimizing Sailing Automation. *Ocean Engineering*, 275, 114128. DOI: 10.1016/j.oceaneng.2023.114128.

Kuusniemi, H., Lachapelle, G. & Takala, J. (2004) Position and Velocity Reliability Testing in Degraded GPS Signal Environments. *GPS Solutions*, 8, 226–237. DOI: 10.1007/s10291-004-0113-7

Kuusniemi, H., Wieser, A., Lachapelle, G. & Takala, J. (2007) User-Level Reliability Monitoring in Urban Personal Satellite-Navigation. *IEEE Transactions on Aerospace and Electronic Systems*, 43, 1305–1318. DOI: 10.1109/TAES.2007.4441741

La Guardia, M. & D’Ippolito, F. (2024) WebGIS Open-Source Platform for Localizations of New P2G Plants in Sicily. *Geomatics and Environmental Engineering*, 18(4), 5–25. DOI: 10.7494/geom.2024.18.4.5.

La Guardia, M., Koeva, M., Díaz-Vilariño, L. & Nourian, P. (2024) Open-Source Solutions for Real-Time 3D Geospatial Web Integration. *International Archives of the Photogrammetry, Remote Sensing and Spatial Information Sciences*, XLVIII-4-2024, 289–295. DOI: 10.5194/isprs-archives-XLVIII-4-2024-289-2024.

La Guardia, M., Mussumeci, G., Angrisano, A. (2025) A Prototypal Dynamic GNSS Integrity Framework for Coastal Navigation in WebGIS. *Progress in Marine Science and Technology,* Vol. 10. Vol. 10. IOS Press BV, 2025. 606-613. https://doi.org/10.3233/PMST250073

Lee, J.H., Nam, Y.S., Kim, Y., Liu, Y., Lee, J. & Yang, H. (2022) Real-Time Digital Twin for Ship Operation in Waves. *Ocean Engineering*, 266, 112867. DOI: 10.1016/j.oceaneng.2022.112867.

Madusanka, N.S., Fan, Y., Yang, S. & Xiang, X. (2023) Digital Twin in the Maritime Domain: A Review and Emerging Trends. *Journal of Marine Science and Engineering*, 11, 1021. DOI: 10.3390/jmse11051021.

Martella, A., Ramadan, A.I.H.A., Martella, C., Patano, M. & Longo, A. (2023) State of the Art of Urban Digital Twin Platforms. In: D.L.T., A.P. & S.M. (Eds.) Extended Reality. XR Salento 2023. *Lecture Notes in Computer Science*, Volume 14218. Springer, Cham. DOI: 10.1007/978-3-031-43401-3_20.

Mazzei, M. & Quaroni, D. (2022) Development of a 3D WebGIS Application for the Visualization of Seismic Risk on Infrastructural Work. *ISPRS International Journal of Geo-Information*, 11, 22. DOI: 10.3390/ijgi11010022.

Menges, D. & Rasheed, A. (2024) Digital Twin for Autonomous Surface Vessels: Enabler for Safe Maritime Navigation. *arXiv*, 2411.03465. DOI: 10.48550/arXiv.2411.03465.

Metcalfe, J., Ellul, C., Morley, J. & Stoter, J. (2024) Characterizing the Role of Geospatial Science in Digital Twins. *ISPRS International Journal of Geo-Information*, 13, 320. DOI: 10.3390/ijgi13090320.

Mink, M. (2016) Performance of Receiver Autonomous Integrity Monitoring (RAIM) for Maritime Operations. PhD Thesis, Karlsruher Institut für Technologie (KIT).

Piragnolo, M., Pirotti, F., Zanrosso, C., Lingua, E. & Grigolato, S. (2021) Responding to Large-Scale Forest Damage in an Alpine Environment with Remote Sensing, Machine Learning, and Web-GIS. *Remote Sensing*, 13(8), 1541. DOI: 10.3390/rs13081541.

Porretta, M., Jimenez-Banos, D., Crisci, M., Solari, G., Fiumara, A. & Hein, G. (2016) GNSS Evolutions for Maritime: An Incremental Approach. InsideGNSS Working Paper, May/June 2016. Available online: https://insidegnss-com.exactdn.com/wp-content/uploads/2018/01/mayjune16-WP.pdf (accessed on 10 January 2025).

Santoso, M.I., Gumelar, R.G. & Irawan, B. (2019) Development of the WebGIS Application for Transport Infrastructure Management in the City of Serang. In *Proceedings of the IOP Conference Series: Materials Science and Engineering*, Bali, Indonesia, 7–8 August 2019. IOP Publishing, Bristol, UK, Volume 673, 012072. DOI: 10.1088/1757-899X/673/1/012072

Scianna, A., Gaglio, G.F., La Guardia, M. & Nuccio, G. (2021) Development of a Virtual CH Path on WEB: Integration of a GIS, VR, and Other Multimedia Data. In: I.M., F.E., C.L. & C.E. (Eds.) Digital Heritage.

Progress in Cultural Heritage: Documentation, Preservation, and Protection. EuroMed 2020. *Lecture Notes in Computer Science*, Volume 12642. Springer, Cham. DOI: 10.1007/978-3-030-73043-7_15.

Singh, M., Fuenmayor, E., Hinchy, E.P., Qiao, Y., Murray, N. & Devine, D. (2021) Digital Twin: Origin to Future. *Applied System Innovation*, 4(2), 36. DOI: 10.3390/asi4020036.

Sturza, M.A. (1988) Navigation System Integrity Monitoring Using Redundant Measurements. *Navigation*, 35, 483‑501. DOI: 10.1002/j.2161-4296.1988.tb00975.x.

Tomko, M. & Winter, S. (2018) Beyond Digital Twins−A Commentary. *Environment and Planning B: Urban Analytics and City Science*, 46, 395‑399. DOI: 10.1177/2399808318816992.

Van Oosterom, P., Stoter, J., Quak, W. & Zlatanova, S. (2002) The Balance between Geometry and Topology. In: Richardson, D.E. & van Oosterom, P. (Eds.) Advances in Spatial Data Handling. Springer, Berlin/Heidelberg, Germany, 209‑224. DOI: 10.1007/978-3-642-56094-1_16.

Weil, C.G., Bibri, S.E., Longchamp, R., Golay, F. & Alahi, A. (2023) Urban Digital Twin Challenges: A Systematic Review and Perspectives for Sustainable Smart Cities. *Sustainable Cities and Society*, 99, 104862. DOI: 10.1016/j.scs.2023.104862.

Xue, F., Wu, L. & Lu, W. (2021) Semantic Enrichment of Building and City Information Models: A Ten-Year Review. *Advanced Engineering Informatics*, 47, 101245. DOI: 10.1016/j.aei.2020.101245.

Yakubailik, O.E., Kadochnikov, A.A. & Tokarev, A.V. (2018) WEB Geographic Information System and the Hardware and Software Ensuring Rapid Assessment of Air Pollution. Optoelectronics Instrumentation and Data Processing, 54, 243‑249. DOI: 10.3103/S8756699018030056.

Yen, C.C., Chien, L.K., Feng, T.S. & Lee, B.C. (2009) Establishment and Application of Global Satellite Tracking Web Geographical Information System. In *ISOPE International Ocean and Polar Engineering Conference*. ISOPE.

Zalewski, P. (2019) GNSS Integrity Concepts for Maritime Users. In Proceedings of the 2019 European Navigation Conference (ENC), Warsaw, Poland, 9‑12 April 2019, 1‑10. DOI: 10.1109/EURONAV.2019.8714188

Zhang, X., Wang, C., Jiang, L., An, L. & Yang, R. (2021) Collision-Avoidance Navigation Systems for Maritime Autonomous Surface Ships: A State-of-the-Art Survey. *Ocean Engineering*, 235, 1‑22. DOI: 10.1016/j.oceaneng.2021.109380.

Aims and Scope

Geographia Technica is a journal devoted to the publication of all papers on all aspects of the use of technical and quantitative methods in geographical research. It aims at presenting its readers with the latest developments in G.I.S technology, mathematical methods applicable to any field of geography, territorial micro-scalar and laboratory experiments, and the latest developments induced by the measurement techniques to the geographical research.

Geographia Technica is dedicated to all those who understand that nowadays every field of geography can only be described by specific numerical values, variables both oftime and space which require the sort of numerical analysis only possible with the aid of technical and quantitative methods offered by powerful computers and dedicated software.

Our understanding of ***Geographia Technica*** expands the concept of technical methods applied to geography to its broadest sense and for that, papers of different interests such as: G.I.S, Spatial Analysis, Remote Sensing, Cartography or Geostatistics as well as papers which, by promoting the above mentioned directions bring a technical approach in the fields of hydrology, climatology, geomorphology, human geography territorial planning are more than welcomed provided they are of sufficient wide interest and relevance.

Targeted readers:

The publication intends to serve workers in academia, industry and government.
Students, teachers, researchers and practitioners should benefit from the ideas in the journal.

Guide for Authors

Submission

Articles and proposals for articles are accepted for consideration on the understanding that they are not being submitted elsewhere.

The publication proposals that satisfy the conditions for originality, relevance for the new technical geography domain and editorial requirements, will be sent by email to the address editorial-secretary@technicalgeography.org.

This page can be accessed to see the requirements for editing an article, and also the articles from the journal archive found on www.technicalgeography.org can be used as a guide.

Content

In addition to full-length research contributions, the journal also publishes Short Notes, Book reviews, Software Reviews, Letters of the Editor. However the editors wish to point out that the views expressed in the book reviews are the personal opinion of the reviewer and do not necessarily reflect the views of the publishers.

Each year two volumes are scheduled for publication. Papers in English or French are accepted. The articles are printed in full color. A part of the articles are available as full text on the www.technicalgeography.org website. The link between the author and reviewers is mediated by the Editor.

Peer Review Process

The papers submitted for publication to the Editor undergo an anonymous peer review process, necessary for assessing the quality of scientific information, the relevance to the technical geography field and the publishing requirements of our journal.

The contents are reviewed by two members of the Editorial Board or other reviewers on a simple blind review system. The reviewer's comments for the improvement of the paper will be sent to the corresponding author by the editor. After the author changes the paper according to the comments, the article is published in the next number of the journal.

Eventual paper rejections will have solid arguments, but sending the paper only to receive the comments of the reviewers is discouraged. Authors are notified by e-mail about the status of the submitted articles and the whole process takes about 3-4 months from the date of the article submission.

Indexed by: **CLARIVATE ANALYTICS**
SCOPUS
GEOBASE
EBSCO
SJR
CABELL

ISSN: 1842 - 5135 (Print)
ISSN: 2065 - 4421 (Online)